5. AUTOMOTIVE METALS—STEEL

A. High-Strength Steel Joining Technologies

Project Manager: Michael S. Bzdok
Auto/Steel Partnership
2000 Town Center, Suite 320
Southfield, MI 48075-1123
(248) 945-4778; fax: (248) 356-8511; e-mail: mbzdok@a-sp.org

Co-chair: John C. Bohr
General Motors Corporation—Conveyors, Controls, Robotics, and Welding
30300 Mound Road, Mail Code 480-109-164
Warren, MI 48090-9015
(810) 602-8276; fax: (586) 947-1039; e-mail: johnc.bohr@gm.com

Co-chair: Eric Pakalnins
Chrysler LLC
800 Chrysler Drive, CTC-CIMS 482-00-11
Auburn Hills, MI 48326-2757
(248) 576-7454; fax: (248) 576-7490; e-mail: ep18@chrysler.com

Technology Area Development Manager: Joseph A. Carpenter
(202) 586-1022; fax: (202) 586-1600; e-mail: joseph.carpenter@ee.doe.gov

Field Project Officer: Aaron D. Yocum
(304) 285-4852; fax (304) 285-4403; e-mail: aaron.yocum@netl.doe.gov

Contractor: United States Automotive Materials Partnership (USAMP)
Contract No.: DE-FC05-02OR22910 through the National Energy Technology Laboratory

Objective

- Provide welding and joining expertise to support Auto/Steel Partnership (A/SP) project teams in developing lightweight automotive body structures.
- Supplement the existing welding and joining technical knowledge with applied research to facilitate an increased use of Advanced High-Strength Steel (AHSS).
- Utilize A/SP research data to prepare industry weldability and weld quality acceptance standards.

Approach

- Anticipate needs of the A/SP lightweighting projects and conduct applied research to address identified technology gaps.
- Determine welding parameters to produce quality welds, then statically and dynamically test welds produced at these parameters to quantify individual weld structural performance (see Figure 1). Tensile shear strength, impact energy and fatigue life are typically evaluated.

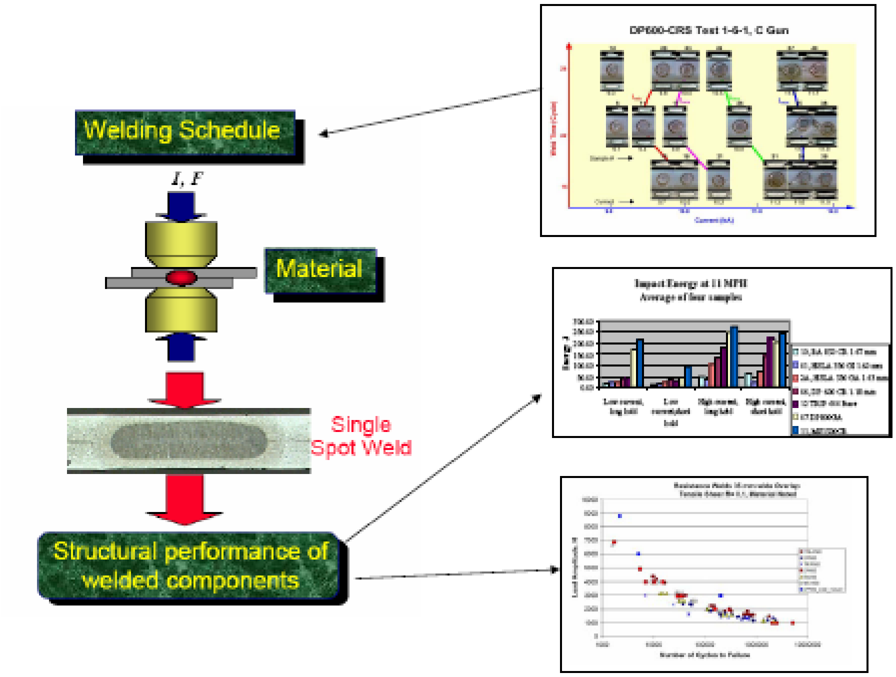

Figure 1. Resistance spot welding (RSW).

- Utilize commercially-available equipment or equipment typically found in existing manufacturing facilities for AHSS feasibility assessments. Utilize other, new technologies as necessary for lightweighting implementation.
- Focus on materials classified as Group 3 and 4 (see Figure 2) as well as specific materials recommended by the A/SP member companies.

Group: Tensile Strength (MPa)	**1. Low Strength < 350**	**2. Intermediate Strength 350–500**	**3. High Strength > 500–800**	**4. Ultra High Strength > 800**
Typical Materials	**Mild 140YS/270TS** **BH 180YS/300TS** **BH 210YS/320TS** **BH 240YS/340TS**	**BH 260YS/370TS** **HSLA 280YS/350TS** **HSLA 350YS/450TS** **DP 300YS/500TS**	**DP 350YS/600TS** **TRIP 350YS/600TS** **DP 500YS/800TS** **TRIP 500YS/800TS** **CP 700YS/800TS**	**DP 700YS/1000TS** **MS 950YS/1200TS** **MS 1150YS/1400TS** **MS 1250YS/1520TS** **HS 950YS/1300TS**

Note: Steels with a minimum tensile strength above 500 MPa (Groups 3 and 4) are generally considered advanced high-strength steels (AHSSs).

Acronyms: YS = yield strength, TS = tensile strength, BH = bake hardenable, DP = dual phase, HSLA = high-strength, low-alloy, TRIP = transformation-induced plasticity, MS = martensitic steel, CP = complex phase.

Source: International Iron and Steel Institute (IISI), *Advanced High Strength Steel (AHSS) Application Guidelines, 6 June 2006*

Figure 2. IISI steel classifications for welding.

- Investigate the use of process finite-element modeling to predict weld quality characteristics and optimize weld process parameters (see Figure 3). Utilize simulation for future projects to develop weld process optimization and weldability assessments. Validate simulation results with experimental data.

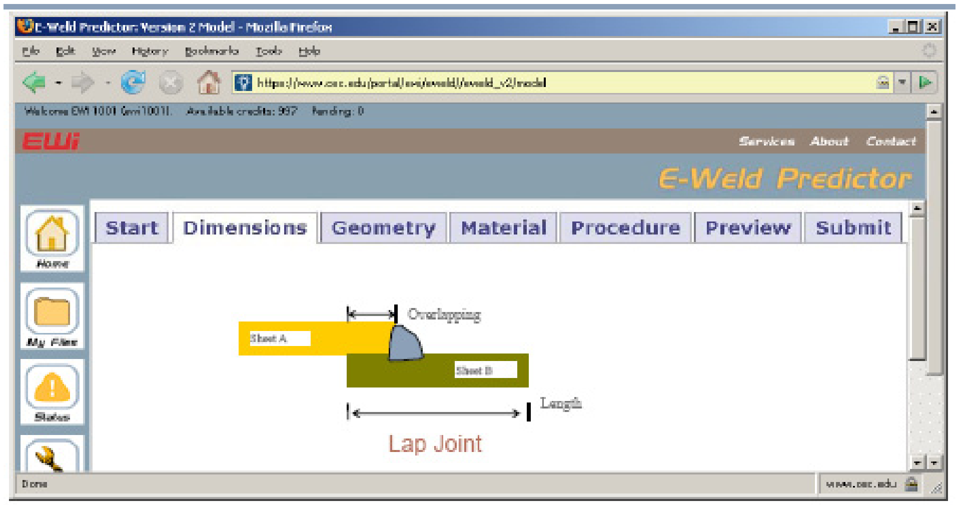

E-Weld Predictor: Version 2 Model - Mozilla Firefox

https://www.osc.edu/portal/ewi/eweld/eweld_v2/model

Welcome EWI 1001 (ewi1001). Available credits: 997 Pending: 0

File
Edit
View
History
Bookmarks
Tools
Help
EWi
Services
About
Contact
E-Weld Predictor
Home
My Files
Status
Start
Dimensions
Geometry
Material
Procedure
Preview
Submit
Overlapping
Sheet A
Sheet B
Length
Lap Joint
Done
www.osc.edu

Figure 3. Gas metal arc weld (GMAW) process simulation input.

Accomplishments

- Completed a comprehensive study on joint efficiency that will allow joining process comparisons for weld repair or substitution. Joint efficiency is defined as joint strength/parent material strength. The Joint Efficiency project is intended only to compare processes. Data are also available for energy comparisons and for stiffness comparisons (see Figure 4).

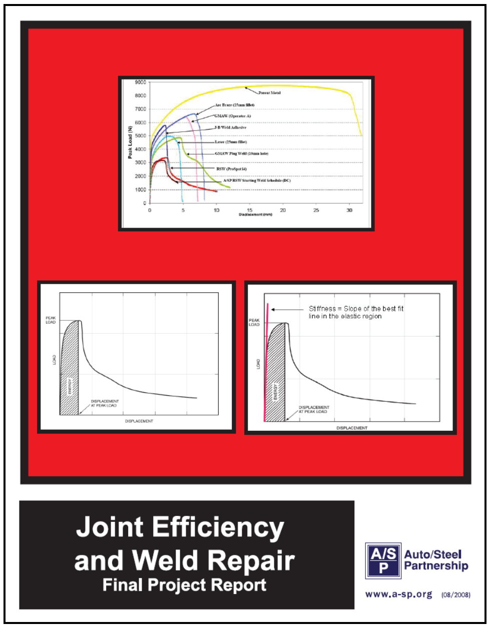

Joint Efficiency and Weld Repair

Final Project Report

A/S P Auto/Steel Partnership

www.a-sp.org (08/2008)

Peak Load (N)
Displacement (mm)
Parent Metal
Arc Braze (25mm fillet)
GMAW (Operator A)
J-B Weld Adhesive
Laser (25mm fillet)
GMAW Plug Weld (10mm hole)
RSW (ProSpot i4)
A/SP RSW Starting Weld Schedule (DC)
PEAK LOAD
LOAD
DISPLACEMENT AT PEAK LOAD
DISPLACEMENT
Stiffness = Slope of the best fit line in the elastic region

Figure 4. A/SP Joint Efficiency—Phase I final report.

- Created and published a set of arc weld design rules for the Lightweight Chassis Project Team (see Figure 5).

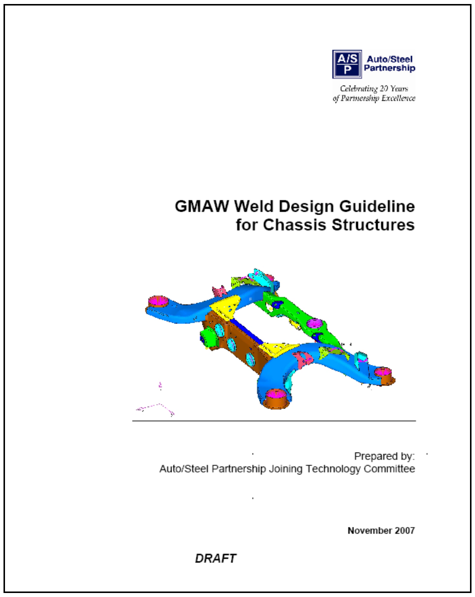

A/S P Auto/Steel Partnership
Celebrating 20 Years of Partnership Excellence

GMAW Weld Design Guideline
for Chassis Structures

Prepared by:
Auto/Steel Partnership Joining Technology Committee

November 2007

DRAFT

Figure 5. GMAW Weld Design Guideline for Chassis Structures.

- Supported development of an automotive industry AHSS resistance spot weld material characterization [American Welding Society (AWS) D8.9M:200X] and provided technical support for development of a software application to support common deployment and analysis of the AHSS Design of Experiment test method. This American National Standard has started the balloting process heading towards publication (see Figure 6).

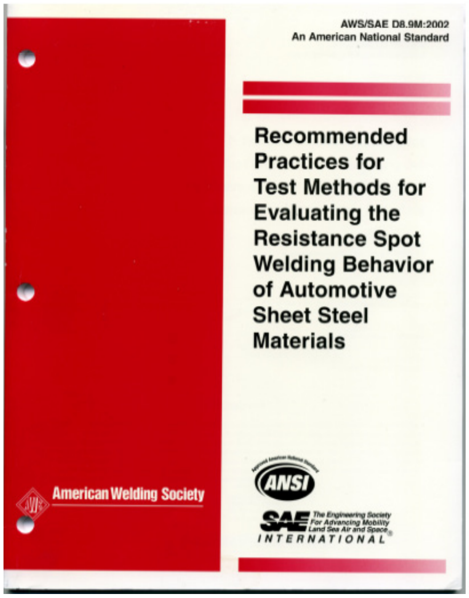

AWS/SAE D8.9M:2002
An American National Standard

Recommended Practices for Test Methods for Evaluating the Resistance Spot Welding Behavior of Automotive Sheet Steel Materials

American Welding Society

ANSI

SAE The Engineering Society For Advancing Mobility Land Sea Air and Space
INTERNATIONAL

Figure 6. AWS D8.9M:200X.

- Created and published Weld Bond Adhesive Guidelines for the Lightweight Chassis Project Team (see Figure 7).

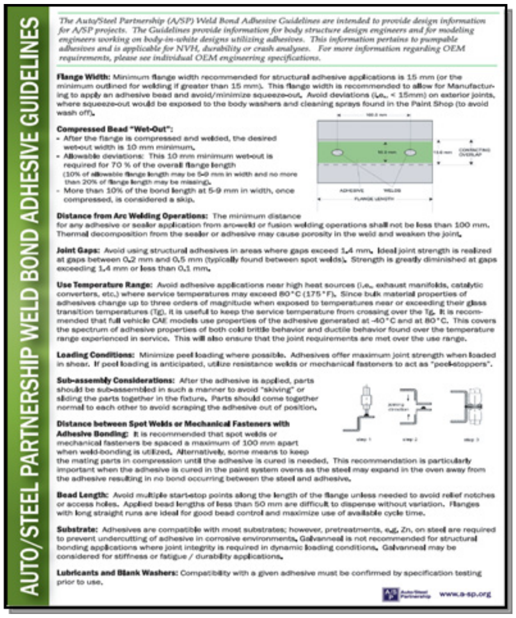

AUTO/STEEL PARTNERSHIP WELD BOND ADHESIVE GUIDELINES

The Auto/Steel Partnership (A/SP) Weld Bond Adhesive Guidelines are intended to provide design information for A/SP projects. The Guidelines provide information for body structure design engineers and for modeling engineers working on body-in-white designs utilizing adhesives. This information pertains to pumpable adhesives and is applicable for NVH, durability or crash analyses. For more information regarding OEM requirements, please see individual OEM engineering specifications.

Flange Width: Minimum flange width recommended for structural adhesive applications is 15 mm (or the minimum outlined for welding if greater than 15 mm). This flange width is recommended to allow for Manufacturing to apply an adhesive bead and avoid/minimize squeeze-out. Avoid deviations (i.e., < 15mm) on exterior joints, where squeeze-out would be exposed to the body washers and cleaning sprays found in the Paint Shop (to avoid wash off).

Compressed Bead "Wet-Out":
- After the flange is compressed and welded, the desired wet-out width is 10 mm minimum.
- Allowable deviations: This 10 mm minimum wet-out is required for 70 % of the overall flange length (10% of allowable flange length may be 5-9 mm in width and no more than 20% of flange length may be missing).
- More than 10% of the bond length at 5-9 mm in width, once compressed, is considered a skip.

Distance from Arc Welding Operations: The minimum distance for any adhesive or sealer application from arc-weld or fusion welding operations shall not be less than 100 mm. Thermal decomposition from the sealer or adhesive may cause porosity in the weld and weaken the joint.

Joint Gaps: Avoid using structural adhesives in areas where gaps exceed 1.4 mm. Ideal joint strength is realized at gaps between 0.2 mm and 0.5 mm (typically found between spot welds). Strength is greatly diminished at gaps exceeding 1.4 mm or less than 0.1 mm.

Use Temperature Range: Avoid adhesive applications near high heat sources (i.e., exhaust manifolds, catalytic converters, etc.) where service temperatures may exceed 80°C (175°F). Since bulk material properties of adhesives change up to three orders of magnitude when exposed to temperatures near or exceeding their glass transition temperatures (Tg), it is useful to keep the service temperature from crossing over the Tg. It is recommended that full vehicle CAE models use properties of the adhesive generated at -40°C and at 80°C. This covers the spectrum of adhesive properties of both cold brittle behavior and ductile behavior found over the temperature range experienced in service. This will also ensure that the joint requirements are met over the use range.

Loading Conditions: Minimize peel loading where possible. Adhesives offer maximum joint strength when loaded in shear. If peel loading is anticipated, utilize resistance welds or mechanical fasteners to act as "peel-stoppers".

Sub-assembly Considerations: After the adhesive is applied, parts should be sub-assembled in such a manner to avoid "skiving" or sliding the parts together in the fixture. Parts should come together normal to each other to avoid scraping the adhesive out of position.

Distance between Spot Welds or Mechanical Fasteners with Adhesive Bonding: It is recommended that spot welds or mechanical fasteners be spaced a maximum of 100 mm apart when weld-bonding is utilized. Alternatively, some means to keep the mating parts in compression until the adhesive is cured is needed. This recommendation is particularly important when the adhesive is cured in the paint system ovens as the steel may expand in the oven away from the adhesive resulting in no bond occurring between the steel and adhesive.

Bead Length: Avoid multiple start-stop points along the length of the flange unless needed to avoid relief notches or access holes. Applied bead lengths of less than 50 mm are difficult to dispense without variation. Flanges with long straight runs are ideal for good bead control and maximize use of available cycle time.

Substrate: Adhesives are compatible with most substrates; however, pretreatments, e.g. Zn, on steel are required to prevent undercutting of adhesive in corrosive environments. Galvanneal is not recommended for structural bonding applications where joint integrity is required in dynamic loading conditions. Galvanneal may be considered for stiffness or fatigue / durability applications.

Lubricants and Blank Washers: Compatibility with a given adhesive must be confirmed by specification testing prior to use.

www.a-sp.org

Figure 7. A/SP Weld Bond Adhesive Guidelines.

- Completed extensive finite-element modeling (FEM) and laboratory experimentation to develop and validate starting resistance spot weld schedules for advanced high strength steel applications (see Figure 8).

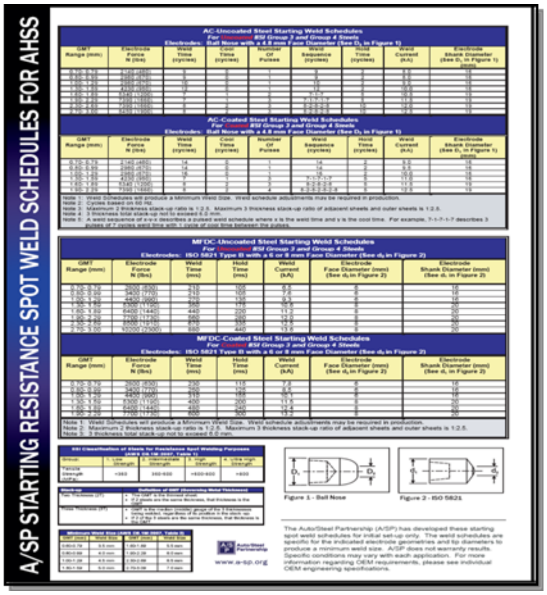

A/SP STARTING RESISTANCE SPOT WELD SCHEDULES FOR AHSS

Figure 8. Starting RSW Weld Schedules for AHSS.

Future Direction

- Future team activities include supporting welding development for the A/SP AHSS Application Guidelines Project Team and developing welding parameter and joint performance data for specific applications on AHSS automotive body prototypes. Future project work also includes:
- Develop arc weld procedures for various weld filler metals and AHSS joints, including determining the hot-cracking susceptibility and filler metal compatibility of sheet AHSS materials.
- Develop an FEM application for automotive arc welding utilizing the E-Weld Predictor tool developed by the Edison Welding Institute and the Ohio Super-Computer Center.
- Initiate a weld bonding applied research project to study adhesive effects on between spot weld buckling.
- Initiate a Phase 2 of the Weld Repair and Joint Efficiency Study to expand the assessment of the various joining processes in coach peel applications.

Introduction

The purpose of this project is to evaluate the weldability of the new AHSS currently being considered by the automotive companies as a solution to lightweighting without compromising cost or structural strength. The project intent is to evaluate various grades, thicknesses, and joining processes.

Initially, resistance welding was evaluated. Subsequent projects extended to Metal Inert Gas (MIG), laser-assisted MIG, and plasma- assisted MIG joining processes. Additional evaluations have included projection nut welding and drawn arc stud and nut welding to AHSS.

Weld Repair and Joint Efficiency Project

A study of joint efficiency for various joining processes does not currently exist for AHSS. These materials are considered for future automotive production. The objective of this project is to demonstrate weldability and joinability of AHSS by various processes. This work is a comprehensive study on various grades of steels, which quantifies peak load, joint efficiency, energy up-to-peak load, and joint stiffness for a variety of joining methods. The data allow comparisons to be made for production welding/joining processes and repair substitutions. Processes studied include:

- Resistance spot welding (RSW)
- Conventional, alternating current (ac) and direct current (dc) schedules, RSW with adhesives
- Gas metal arc welding (GMAW)
- Lap fillet, plug weld, fillet in slot, arc spot, cold metal transfer
- Gas metal arc brazing (GMAB)
- Lap fillet, plug weld, fillet in slot
- Laser welding/brazing
- Lap, lap fillet, laser/MIG, braze, staple geometry mechanical fasteners
- Hemlok rivet, Henrob self-pierce rivet, Tog-L-Loc mechanical clinch, rivet with adhesive bonding
- Dow Betamate 1484, Henkel 4555B, Henkel 5087, JB Weld, 3M VHB tape
- Other processes including Arplas, Spot Fast, Supersonic Spray Transfer, Fronius Delta Spot, Friction Stir Spot Welding

Welding/joining processes were performed on mild steel and four advanced high strength steels.

Materials:

- 0.7 mm electro-galvanized mild steel
- 1.2 mm hot-dip galvannealed 590R
- 1.2 mm hot-dip galvanized Dual Phase (DP) 600
- 1.15 mm hot-dip galvannealed DP 780
- 1.0 mm electro-galvanized TRIP 800

Tensile shear tests were performed for a minimum of two test specimens for each material/process combination. If the variation in peak load of the first two samples was within 5%, a third sample was not tested. Load/displacement curves were generated using an MTS 810 Material Test System. Joint efficiency was calculated as the peak load of the joint divided by the peak load of the parent material, expressed as a percentage. Energy was calculated as the area under the load/displacement curve up to the peak load. Joint stiffness was calculated as the slope of the best fit line in the elastic region of the load/displacement curve. Normalized stiffness was calculated as the joint stiffness divided by the parent material stiffness, expressed as a percentage. Normalized energy was calculated as the joint energy divided by the parent material energy, expressed as a percentage.

The average joint efficiency for all material/joining combinations was 48%. The average normalized energy for all material/joining combinations was 6%. Several observations can be made regarding joint efficiencies and normalized energy for all categories of welding/joining processes studied.

- Joint efficiencies for resistance spot welds ranged from 29% to 54%. Normalized energies ranged from 2% to 9%.
- GMAW and laser processes generally produced higher joint efficiencies than resistance spot welds for all materials.
- The highest joint efficiency for GMAW processes was obtained with the double fillet weld in a slot. Joint efficiency ranged from 61% to 90%. This process also produced the highest normalized energy for AHSS within GMAW welds.
- The laser staple geometry generally produced some of the highest joint efficiencies and normalized energies for all materials. Joint efficiencies ranged from 61% to 73%. Normalized energies ranged from 9% to 23%.
- Very high joint efficiencies were obtained with several fracture toughened adhesive/rivet combinations, which produced joint efficiencies between 51% and 87% and normalized energies between 2% and 18%. Normalized energy was exceptionally high for mild steel, but relatively low for AHSS.

It is observed that AHSS are weldable and joinable by all of the processes studied in this project. Several processes had joint efficiencies less than 10% and energies of almost 0% for AHSS, which may limit their applications in automotive structures.

Various joining processes result in different strength metrics. There appears to be no correlation between joint efficiency, energy, and stiffness for the material/process combinations tested. Processes which produce high joint efficiency can produce very low energy values. Processes producing similar joint efficiencies can result in very low or very high energies. For mild steel, an AWS D8.1M resistance spot weld produced a joint efficiency of 34% and normalized energy of 3%. A Hemlok Rivet in mild steel produced a joint efficiency of 27%, and normalized energy of 11%, which is almost four times greater than that of the spot-welded joint. Similar observations can be made for a number of material/process combinations for both mild and AHSS.

It is observed that joint efficiency decreases as material strength increases for most processes studied. This shows that peak load and corresponding joint strength does not generally increase in proportion to parent material strength increase.

For most processes, normalized stiffness tends to increase from mild to advanced high strength steels. Within the AHSS, normalized stiffness does not vary significantly.

Joint energy in this study is considered only up to peak load. In general, the entire area under the load/displacement curve is equal to the energy input required to cause joint fracture. A joint may have high tensile strength but short displacement under load. High tensile strength increases the peak load and, therefore, joint efficiency. Shorter displacement corresponds to low energy input. This is observed by the decreased area under the load/displacement curve. Increasing the energy required to cause fracture may improve joint performance under various loading conditions. Because joints may have very different efficiencies and energies depending on material and process, all factors should be considered when choosing joining processes. For both mild and advanced high strength steels, acceptable welding and joining processes can be selected from those tested in this project, based on application and loading requirements.

Lightweight Rear Chassis and Arc Weld Design Guidelines

The Lightweight Rear Chassis team of the A/SP requested assistance in welding a lightweight design from DP 600, 800, and 980 materials. After obtaining the various materials, the Joining Team proceeded to evaluate the weldability of these materials, and to test weld the combinations prescribed for a rear-end structure. The Joining Team established the weld parameters, and assisted the prototype source in making the structure. Weld parameters were delivered to the Lightweight Rear Chassis Team along with mechanical and chemical properties of the test materials.

The Lightweight Rear Chassis team requested assistance for developing future designs requiring arc welded joints. The Joining Team then established a project to do the following.

- Develop and publish an A/SP GMAW Weld Design Guideline for Chassis Structures.
- Utilize a methodology to use existing Original Equipment Manufacturer (OEM) Design Standards to create a comparison matrix of product design rules applicable to arc welded chassis structures.
- Utilize the comparison matrix, assess requirements, and create a consensus set of A/SP design guidelines applicable to arc-welded chassis structures.

The results of the project are published as the GMAW Weld Design Guideline for Chassis Structures by the Auto/Steel Partnership.

Evaluation of Starting Resistance Spot Weld Schedules

The OEM's currently have starting point resistance spot weld (RSW) schedule matrices for resistance spot welding mild and High-Strength Low Alloy (HSLA) production materials (steels classified as IISI Groups 1 and 2) that are based on Governing Metal Thickness (GMT) and type of material coating. These starting-point weld schedules are used for material weldability testing as well as during product launch for set-up of resistance spot welding equipment.

The purpose of this A/SP Joining Technologies Project was to determine whether these existing ac and dc weld schedules were suitable for Advanced High Strength Steels (AHSS) classified as IISI Group 3 and 4 materials. Verification of these weld schedules for Group 3 and 4 steels was accomplished by

1. finite-element modeling via Simulation and Optimization of Resistance Projection and Spot Welding Processes (SORPAS), Version 7.0, software and
2. limited welding of two-thickness (2T) and three-thickness (3T) stack-ups with available material.

2T and 3T stack-up combinations were considered. The IISI Group 3 and Group 4 steels included; TRIP 800, DP 600, DP 980, and uncoated hot-stamped boron. Mild steels were used in 3T stack-up modeling including AISI 1006 and BH 210. Finite- element modeling for both ac and dc RSW consisted of the following 3 types of thickness combinations:

1. 2T stack-up, Group 3 and 4 steel welded to itself.
2. 2T stack-up, Group 3 and 4 steel welded to itself with a thickness ratio of 1:2.5.
3. 3T stack-up, Group 3 and 4 steel welded to itself along with a 0.64 to 1.08 mm mild steel.

The test constraints for verification were as follows: maximum 6.0 mm total stack-up thickness, 2.1 mm maximum gage for a coated steel, 3.0 mm for uncoated steel, and a worst-case thickness ratio equal to 1 to 2.5. The governing metal thickness was the 2nd thickest sheet. Additionally, for 3T stack-ups, the worst-case welding situation was thin to thick to thick. The criteria was that the Minimum Weld Size (MWS) as per AWS D8.1M:2007 (Specification for Automotive Weld Quality-Resistance Spot Welding of Steel) was obtained.

The results from finite-element modeling indicated that the ac starting-point weld schedules met the MWS requirement stated above. The initial dc weld schedules proved to be "hot" and required adjustments which were then simulated. The final dc weld schedules also met the MWS requirement.

The following materials at various gages were scheduled to be welded using the ac and dc weld schedules that were verified through finite element modeling: DP 600, DP 590R, DP 750, DP780, DP 980, and TRIP 800. Welding with actual steel consisted of the following:

1. 2T stack-up, Group 3 and 4 steel welded to itself.
2. 2T stack-up, Group 3 and 4 steel welded to itself at different thicknesses.
3. 3T stack-up, Group 3 and 4 steel welded to itself along with thinner mild steel.

Testing of the welded samples included destructive peel, shear tension, cross tension, and metallography. Results were compared to the requirements of AWS D8.1M:2007.

The results will be published as a one-page set of tables entitled, "A/SP Starting Resistance Spot Weld Schedules."

Conclusions

Additional welding issues will be addressed during 2009, by the Joining Technologies Team, funded by USAMP Lightweighting Initiatives and as member company in-kind contributions.

Presentations and Publications

1. John C. Bohr, General Motors Corporation, "Joint Efficiency of Advanced High-Strength Steel Joints made by Various Joining Processes," *Presented at the Sheet Metal Welding Conference in Livonia, Michigan on May 14–16, 2008.*
2. Chonghua Jiang, AET Integration, "Resistance Spot Welding of Advanced High-Strength Steel (AHSS); A Comparative Study of Joint Efficiency" *Presented at the 5th International Seminar on Advances in Resistance Welding in Toronto, Ontario, Canada on September 24–26, 2008.*
3. Michael L. Kuntz, University of Waterloo, "Development of Starting Weld Schedules for AHSS—SORPAS Modeling of Starting Point Weld Schedules with Experimental Evaluation and Validation," *Presented at the 5th International Seminar on Advances in Resistance Welding in Toronto, Ontario, Canada on September 24–26, 2008.*

B. Hydroforming Materials and Lubricants

Project Manager: Bart Clark
Auto/Steel Partnership
2000 Town Center, Suite 320
Southfield, Michigan 48075-1123
(248) 945-4776; fax: (248) 356-8511; e-mail: bclarke@a-sp.org

Chairperson: Ronald Soldaat
ArcelorMittal USA
1330 Burlington Street East
P.O. Box 2460
Hamilton, Ontario, Canada L8N 3J5
(905) 548-7200 ext. 2664; fax: (905) 548-4250; e-mail: ronald.soldaat@arcelormittal.com

Technology Area Development Manager: Joseph A. Carpenter
(202) 586-1022; fax: (202) 586-1600; e-mail: joseph.carpenter@ee.doe.gov

Field Project Officer: Aaron D. Yocum
(304) 285-4852; fax (304) 285-4403; e-mail: aaron.yocum@netl.doe.gov

Contractor: United States Automotive Materials Partnership (USAMP)
Contract No.: DE-FC05-02OR22910 through the National Energy Technology Laboratory

Objective

- Develop mechanical test procedures and forming limit diagrams (FLDs) for tubes.
- Improve the accuracy and confidence in finite-element modeling (FEM) of tubular hydroforming.
- Investigate the fabricating and performance characteristics of tailor-welded tubes (TWTs).
- Develop an understanding of steel and lubricant requirements for hydroforming using a combination of experiments and FEM.
- Develop an improved understanding of the structural and cost benefits of hydroformed components.
- Support the work of other Auto/Steel Partnership (A/SP) project teams when they investigate hydroformed structural components.
- Validate the performance benefits of hydroforming in automotive structures.

Approach

The approach taken on this project is to initially gain a basic understanding of the hydroforming process and potential issues and to then extend learning to real-world applications of increasing complexity. The investigation encompasses various steel grades with a focus on Advanced High Strength Steel (AHSS) and gauges of steel tubing, including TWTs, in free expansion and corner-fill processes using several types of lubricants. Project plans are developed based on identified knowledge gaps, barriers to implementation and technology needs as follows.

- Limited in-depth understanding of hydroforming and associated processes.
  - Effect of process variables such as lubrication at each operation on subsequent operations. Forming operations prior to hydroforming include tube making, prebending and preforming.
  - Forming limits (e.g., FLDs) and other failure criteria.

- Limited experience with AHSS in hydroforming applications.
- Attitude is conservative toward new materials and envelope-pushing applications.
  - Need to demonstrate the benefits of tube hydroforming through projects focused on real-world applications.
- Limited computer modeling knowledge and lack of validated tools for automotive design process.

Accomplishments

During the report period from October 1, 2007, to September 30, 2008, the following objectives were accomplished.

- Hydroforming of DP600 and Interstitial Free (IF) Steel Bent Tubes with Welded End Caps
  - Completed work on the final report on the Influence of Bending parameters on Hydroforming of IF and DP600 Tubes.
- Technology Transfer Deliverables and Rewrites of FLD and Influence of Bending on Hydroforming Reports
  - Completed technology transfer of FLD and Influence of Bending on Hydroforming reports and presentations to be used for dissemination of the learning.
- Study on the Forming Characteristics of TWTs.
  - Completed a project to obtain strain and thickness measurements during the hydroforming process of the above TWTs.
  - The final report has been prepared and is being reviewed by the A/SP Hydroform team.
- AHSS Hydroform TWT Lightweight Front Rails
  - In March 2005 the team was challenged to demonstrate the manufacturability of AHSS hydroform TWT lightweight automotive front rails.
  - Successfully completed bending the TWTs to fit in the hydroform dies. This process proved to be a significant challenge due to the high strength, multiple thicknesses and high diameter to thickness (d/t) ratio. Wrinkling and splitting of the tubes was a major problem. Various experts from the industry were recruited to assist in resolving the tube bending issues. Bending issues have been resolved. Tubes have been successfully bent.
  - Hydroform dies remain ready for use at Schuler, Inc. These dies are being used by Schuler to pursue the next phase of the project, hydroforming tailor-welded front rails.
  - Technical issues pertaining to the hydroforming process have been encountered and are being pursued by Schuler.
  - In light of the difficult technical issues encountered throughout the project, the team is evaluating whether or not the expenditure of further cost and effort on this project is warranted.
- Investigation of Fabricating Dual Phase and Transformation-Induced Plasticity (TRIP) Steel Tube from an Electric Resistance Welding (ERW) Production Line
  - This project has been undertaken by CANMET using their laboratory high-frequency induction tube welding draw bench. Work on this project is on schedule and is nearing completion.
- Investigation of Fabricating Dual Phase and TRIP Steel Tube from a Laser Production Line
  - This project has been deleted.
- Numerical Modeling of Straight TWT Hydroforming and Pre-Bent Tubular Hydroforming
  - This project has been deleted.
- Characterizing Material Response during Tube Hydroforming
  - The costs of proposals received for an initial demonstration project were greater than expected. The Statement of Work (SOW) was revised to include more test conditions, but fewer repeats.
  - A revised Request for Quotation (RFQ) was issued and revised bids were received.

  - Further evaluation of this project led to the conclusion that it would be more appropriate for this project to be undertaken by a new, stand-alone A/SP project team rather than have the Hydroform Team continue with it. A new project team is being formed. If sufficient support for this project can be generated, then the new project team will be formalized and will begin work.

Future Direction

During fiscal year (FY) 2009, the Hydroforming Materials and Lubricant Team plans to accomplish the following.

- Continue work to fabricate the Hydroformed Lightweight Front Rails project which was initially undertaken in support of the Lightweight Front Structure project, A/SP110.
  - Evaluate the components and quantify the manufacturing parameters of the hydroformed components.
  - If the rails can be successfully manufactured, they will be further tested by the Strain Rate Characterization project, A/SP190 (see report 5.F).
  - Summarize lessons learned from the fabricating, bending and hydroforming work done on the front rail components.
- Transfer the revised project Characterize Material Response During Hydroforming to a new A/SP project team if there is sufficient support for the project.
- Issue the final report on the Hydroforming of DP600 and IF Bent Tubes with Welded End Caps and take appropriate technology transfer steps.
- Complete the project, “Investigation of Fabricating Dual Phase and TRIP Steel Tube from an ERW Production Line” and take appropriate technology transfer actions.
- It is anticipated that after the Hydroform Materials and Lubricants project team completes their current projects, the team will disband in FY 2009.

Introduction

Hydroformed steel tubes have been used in the automotive industry to form components that meet structural objectives, particularly strength and rigidity, at optimal mass. One of the most significant advantages of tubes is that they are monolithic closed sections and, as such, exhibit many times more stiffness in torsion than conventional open sections, such as “C” and “hat” shapes. Their use is limited largely by a lack of knowledge about the capabilities and parameters of hydroforming processes and the effects of the processes on the tubes.

This project was undertaken to investigate and quantify the capabilities and parameters of various hydroforming processes so that automotive designers and engineers can utilize the tube configurations that are available and predict the performance of components made by hydroforming. Hydroformed tubes and TWTs made from high-strength steel and AHSS are of particular interest because of the potential reduction of mass associated with materials of higher strength and optimal thickness.

The Hydroforming Process

Hydroforming is a process in which a tube is placed into a die which is shaped to develop the desired configuration of the tube. Water is introduced into the tube under very high pressure causing the tube to expand inside the die. The tube ends can be held stationary or moved inward during the process to end feed material into the die cavity.

The process has two distinct stages, shown in Figure 1. The first stage is free expansion, [Figure 1(a)]. The free expansion phase continues until the tube contacts the die wall [Figure 1(b)]. In the second stage, the corner filling phase, the tube is in contact with the surface of the die which constrains subsequent deformation [Figure 1(c)]. During this stage, the tube expands into the corners of the cavity, accomplishing corner fill. A tube that has been hydroformed is shown with the die in Figure 2. Note that the test was continued until the tube failed.

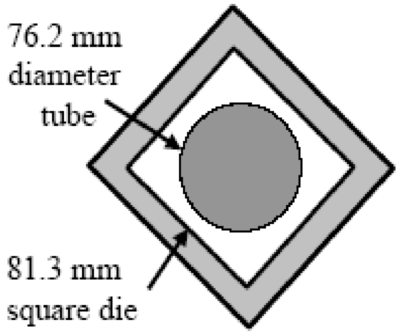

a) Free expansion

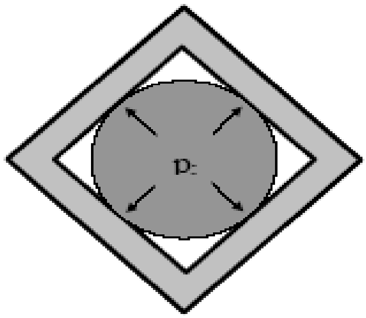

b) Contact with die wall

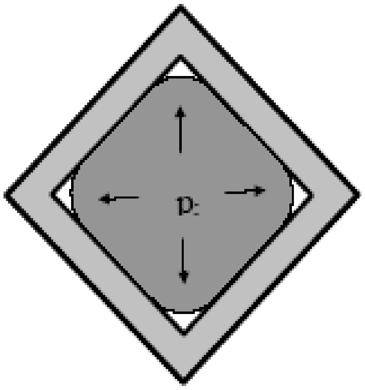

c) Corner filling

Figure 1. (a) Free expansion stage, (b) contact with the die wall, and (c) corner filling.

During corner fill, the tube slides against the die. Friction between the tube and die affects the process. The lubricant used in the process is a significant parameter.

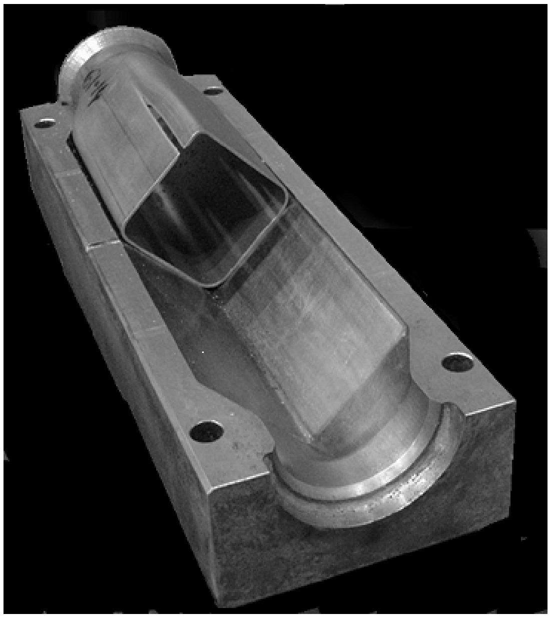

Figure 2. Hydroformed Tube and Die (the test was run to failure of the tube).

During both stages, the tube undergoes plastic strain. The amount of plastic strain that can occur before the material fractures is predicted in stamping processes that utilize flat sheet steel by using a FLD. The FLD is determined by the properties of the material. The hydroforming process is preceded by tube forming and sometimes pre-bending of the tube, both of which induce strains in the material and alter its properties. Before an FLD can be developed for the hydroforming process, the strain history, that is, the strain induced in the material prior to hydroforming, must be known.

Project Discussion

Tailor-Welded Tubes

Tailor-welded blanks are used for sheet steel stampings in numerous automotive applications. Their use enables the development of components with varying material thicknesses and mechanical properties to achieve the required structural performance at optimal mass. These same advantages can be achieved in tubes by utilizing the expertise currently available for producing tailor-welded blanks.

The Hydroforming Team recognized that optimal performance can be achieved only when the parameters of fabricating and hydroforming tubes with varying thicknesses and/or material properties are understood. For example, when a sheet steel blank of a given thickness and grade is joined to a blank with greater thickness and/or strength, the former sheet will tend to expand farther than the latter. The tendency for differential expansion imposes loads on the interface of the sheets, namely, the weld, where there can be no differential expansion.

Tubes are usually formed before hydroforming in bending operations which progressively bend the tube to the desired radius along its length. Bending parameters may need to be adjusted to move progressively over tube sections with varying thickness and material properties.

To assess the parameters associated with these conditions, the Hydroforming Team developed a test plan that will allow direct comparison of TWT characteristics by forming five sets of tubes, 12 tubes per set. The first set is a baseline tube made from one blank. The other four are made from two laser-welded blanks, as follows.

1. One-piece tube as a baseline: 1.5 mm DP 600.
2. Same material, same thickness: 1.5 mm DP 600 welded to 1.5 mm DP 600.
3. Same material, different thickness: 1.2 mm DP 600 welded to 1.5 mm DP 600.
4. Different material, same thickness: 1.5 mm HSLA 350 welded to 1.5 mm DP 600.
5. Different material, different thickness: 1.5 mm HSLA 350 welded to 1.2 mm DP 600.

Hydroforming with Welded End Caps

During hydroforming operations, expansion of the tubes causes “end feeding”, wherein the ends of the tube move inward toward the expanding area due to metal flow in the workpiece. End feeding affects the strain patterns in the tube. In some hydroforming operations, deliberate end feeding is performed under controlled parameters in relationship to other parameters, such as water pressure, to enhance metal flow. End feeding can be prevented by welding the tubes to the end caps (interface between the tube and the area where water is introduced) and fixing the caps rigidly in the hydroforming tool. The Hydroforming Team determined that the effects of end feeding on strain patterns in the hydroformed tubes could be better understood by performing tests with no end feeding. Welded end caps were used in all tests.

Conclusions

Work conducted during this reporting period indicated the following:

- the interior surface condition of dies to be used in hydroforming is an important characteristic,
- tooling used to fabricate the TWTs must be carefully tuned to achieve acceptable circularity of the tubes,
- tooling used to bend TWTs into the desired shapes for hydroforming must take into account the differing tube metal thicknesses, and
- hydroforming TWTs presents many significant engineering challenges.

Presentations and Publications

1. “Hydroforming Group,” Auto/Steel Partnership Program Review, Department of Energy, September 21, 2005.

2. “Hydroforming Committee,” A/SP SPARC financial planning review, July 18, 2006.

3. “Hydroforming Materials and Lubricants,” Auto/Steel Partnership Department of Energy Peer Review meeting was conducted on Friday, December 1, 2006.

4. “Influence of Lubricant in Bending & Hydroforming Evaluations” presentation by Jean Reid at ASTM D02 Petroleum Products and Lubricants Committee workshop/ symposium on Tribological Challenges of Metal Deformation Fluids, Florida, June 17, 2007.

5. “Tube Hydroforming Phase V: Experimental Forming Limits of Steel Tubes” IRDI report, March 2007 (awaiting publication by A/SP Technology Transfer Team).

6. “Influence of Bending Parameters on the Hydroforming of IF and DP 600 Tubes” IRDI report, March 2007 (awaiting publication by A/SP Technology Transfer Team).

7. “Hydroforming Materials and Lubricants (A/SP060)—Project Description Sheet, Statement of Project Objectives and Presentation,” A/SP Project Review and Budget meeting, July 17, 2007.

8. “Hydroforming Materials and Lubricants (A/SP060)—Project Description Sheet, Statement of Project Objectives and Presentation,” A/SP Project Review and Budget meeting, August 19, 2008.

C. Sheet Steel Fatigue Characteristics (A/SP160*)

Project Manager: Bart Clark
Auto/Steel Partnership
2000 Town Center, Suite 320
Southfield, Michigan 48075-1123
(248) 945-4776; fax: (248) 356-8511; e-mail: bclark@a-sp.org

Chair: Raj Mohan Iyengar, PhD.
Severstal North America Inc
3001 Miller Road
P.O. Box 1631
Dearborn, MI 48121-1631
(313) 317-1303; fax: (313) 337-9372; e-mail: rmohan@severstalna.com

Technology Area Development Manager: Joseph A. Carpenter
(202) 586-1022; fax: (202) 586-1600; e-mail: joseph.carpenter@ee.doe.gov

Field Project Officer: Aaron D. Yocum
(304) 285-4852; fax: (304) 285-4403; e-mail: aaron.yocum@netl.doe.gov

---

Contractor: United States Automotive Materials Partnership (USAMP)
Contract No.: DE-FC05-02OR22910 through the National Energy Technology Laboratory

---

Objectives

- Compile the test data generated in the previous phases of the program into a user-friendly database that can be used in all phases of design and structural analysis of sheet steel vehicle bodies.
- Investigate the fatigue life of joints formed by spot welding, adhesive bonding and weld bonding (a combination of spot welding and adhesive bonding).
- Explore the fatigue response of advanced high-strength steels (AHSSs) after being subjected to metal inert gas (MIG) and laser-welded joining and compare this behavior with that of standard automotive steels.
- Assist the Joining Technology team in identifying the optimum welding parameters for laser and MIG welded joints, and develop a fatigue test program.
- Study durability issues pertaining to the use of AHSS in automotive applications

Approach

- Investigate the fatigue characteristics of resistance spot welding, a fusion process in which the metal pieces to be joined are melted and re-solidified via a brief high voltage electrical pulse, forming an alloy with a distinctly different microstructure than that of the parent metals. At the intersection of the weld nugget, or button, and the faying surfaces a crack-like discontinuity is formed which is often the site of initial crack growth. In addition, the weld nugget itself may contain discontinuities (such as porosity), which can also become sites at which fatigue cracks form. The amount and type of discontinuities, and thus the fatigue properties, can be affected to a

---

[*] Denotes Project 160 of the Auto/Steel Partnership (A/SP), the automotive-focus arm of the American Iron and Steel Institute (AISI) (see www.a-sp.org). The A/SP cofunds projects with DOE through a cooperative agreement between DOE and the United States Automotive Materials Partnership, one of the formal consortia of the United States Council for Automotive Research set up by Chrysler, Ford, and General Motors to conduct joint, precompetitive research and development (see www.uscar.org).

considerable extent by the welding process. The microstructures of the joined metals are also changed in the area adjacent to the weld, which is known as the heat-affected zone (HAZ).

- Investigate the fatigue characteristics of adhesive bonding, which substitutes an entirely different material in place of the weld to act as the load-bearing connection. The adhesive must adhere to the metals being joined and resist interfacial fatigue failure at the adhesive/metal interface and within itself (cohesive failure).
- Investigate the fatigue characteristics of weld bonding, which is a combination of adhesive bonding and spot welding.
- Investigate the previously unknown, or at best little known, factors that are expected either to improve impact durability or facilitate their modeling and simulation.
- Reduce the spot weld, adhesive bonded and weld bonded test data to a form that is useful to design engineers who perform vehicle structural analysis.
- Develop a test program to investigate the fatigue performance of gas metal arc welding (GMAW) – a fusion welding process which results in continuous joints. However, under GMAW or MIG welding, a third “filler” metal is introduced under an arc and shielding gas, and, akin to spot-welding, alloys and microstructures are formed which are different from the metals being joined.
- Identify the parameters, including metal grades, metal thicknesses, coatings, and joint configurations that impact the fatigue performance of GMAW welded joints.
- Evaluate durability performance of AHSS components in automotive applications.

Accomplishments

- Completed testing of spot welds in mild steel and ultrahigh strength boron steel, and placed online the knowledge base developed from the results.
- Completed a detailed study of effect of geometric parameters on fatigue lives of spot-welded specimens.
- Developed a specification for fabricating MIG and laser-weld specimens, submitted a request for quotation, selected a contactor and awarded a contract.
- Completed fatigue testing of MIG welded specimens created by the Joining Technologies Team, A/SP070 (see report 5.A).
- Completed fabrication of test specimens for Phase 1A MIG weld fatigue testing.
- Completed weld fatigue testing for MIG welded Phase 1A test specimens. The team is evaluating the results of the testing.
- Began work to resolve technical questions pertaining to test specimens for Phase 1B fusion weld fatigue testing.

Future Direction

- Specimens for Phase 1B testing will be designed and fabricated.
- The project team will complete the Phase 1B of its program of fatigue testing MIG and laser welds in fiscal year (FY) 2009.
- Detailed analyses and interpretations of the test results will be conducted to develop appropriate parameters that capture the effect of weld and specimen geometry on fatigue performance.
- Preliminary projects will be undertaken to determine if there is sufficient support for the Fatigue Team to shift their focus to durability studies. If so, then subsequent projects will focus more deeply into understanding durability issues with the use of AHSS in automotive applications.

Introduction

Future and near-future vehicle designs are faced with several stringent requirements that impose conflicting demands on the vehicle designers. Safety, particularly crash-energy management, must be improved while vehicle mass and cost are contained.

AHSSs, judiciously selected and applied, are currently the best candidates to achieve a low-cost solution, compared with aluminum, magnesium, and plastics that meets these mandates. As structural components are optimized and thinner gauge, higher strength materials are assessed, the fatigue lives of the areas where loads are transferred become increasingly important considerations. To assess the performance of a component in the design phase, the fatigue characteristics of not only the base material but the joints, where loads are transferred, must be known. This project has essentially completed testing various grades of steel and steel coupons that have been spot welded, adhesively bonded, and weld bonded. Testing of GMAW and laser-welded joints is under way.

Discussion

The effort to evaluate the fatigue characteristics of spot-welds began in the 2002 fiscal year with presentations by key researchers on the current state of the work at Chrysler Corporation, Ford Motor Company, and General Motors Corporation. Based on these presentations, the Sheet Steel Fatigue Project Team has produced results beneficial to all three companies in achieving light weight designs. Early in the planning, the Auto/Steel Partnership (A/SP) Joining Technologies Team was consulted and that team prepared the samples that were tested. This interaction ensured that the samples were joined using consistent procedures that were properly controlled and in adherence to the best current practices in sheet metal joining in the automotive industry.

The following fatigue test parameters were agreed upon and carried out:

- Two modes of testing: tensile shear (Figure 1) and coach peel (Figure 2).

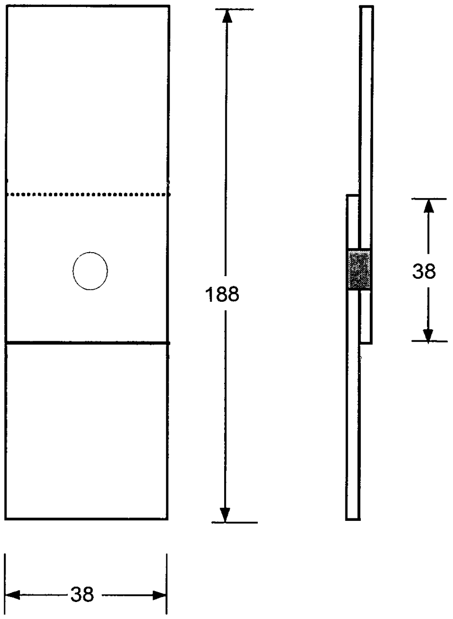

Figure 1. Spot-welded lap shear test specimen (dimensions in millimeters).

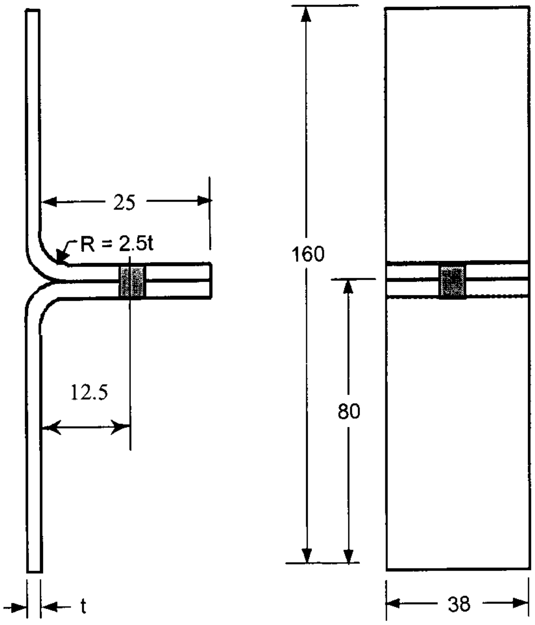

Figure 2. Coach peel test specimen (dimensions in millimeters).

- A single thickness (1.6 mm) was selected to ensure that results were comparable between steel grades. A thinner gage (0.8mm) was selected for a small satellite study [one AHSS and one high-strength low-alloy (HSLA)] on the effect of gage thickness on fatigue.

- Because no such data was available for advanced high strength steels, several grades in this class were tested.
- Testing was done at two R ratios: 0.1 and 0.3. The stress ratio R is defined as the ratio of the minimum stress to the maximum stress in the test cycle. Maximum and minimum values are algebraic, with tension designated as positive and compression negative.
- Eleven steel grades were tested.
- While the majority of testing was performed on spot welded joints, the fatigue performance of adhesive-bonded and weld-bonded joints was explored in several tests series.

Two testing sources, of the nine invited to submit testing proposals, were selected to perform the fatigue experiments: The University of Missouri at Columbia, Missouri, and Westmoreland Mechanical Testing and Research, Inc. in Youngstown, Pennsylvania.

As the testing progressed and results were analyzed, the following tests were added for comparison purposes:

1. Testing at specified R ratios means that the maximum and minimum loads are constant throughout a given test. However, as the maximum load is increased to generate fatigue curve data, the minimum loads also increase. This process is valuable for establishing baseline data. However, in the real world, loads amplitudes can be expected to be variable. For this reason, automotive spectrum load tests, set to two different predetermined scalings, were run.
2. To investigate the effect of button size, fatigue studies were performed on specimens with a welding schedule that produced a smaller weld button.
3. At the request of the Joining Technologies Team, three test series were run using wide samples (125 mm vs. the standard 38 mm). The wider samples minimize rotation of the weld under load and allow negative R-ratios to be explored.

Gas Metal Arc Welded (GMAW) Joints

GMAW welding is the second most common welding process used on vehicle structures, with the rate of applications increasing yearly. GMAW or MIG welds are used not only on body members and sub-frames in passenger cars, but also in frames for larger passenger vehicles, light trucks and Sport-Utility Vehicles (SUVs). Therefore, the test samples will be made from two thickness groups: a thinner gage of 1.6 mm for body applications and a thicker gage of 3.4 mm for frame applications. These target thicknesses, primarily based on material availability, represent typical as-welded material thicknesses found in body and frame applications, respectively.

Frame members do not generally require as much formability as do body members and they offer excellent opportunities for mass reduction through downgaging. Therefore, tests on frame joints will ultimately employ higher strength materials than those specific to body members, but often result in similar numbers of welds and amount of weld area.

The team agreed to four specimen designs for testing. Each explores a different loading mode and reveals different information about the material/joint performance: butt weld (Figure 3), single lap shear (Figure 4), double lap shear (Figure 5), and perch mount (Figure 6).

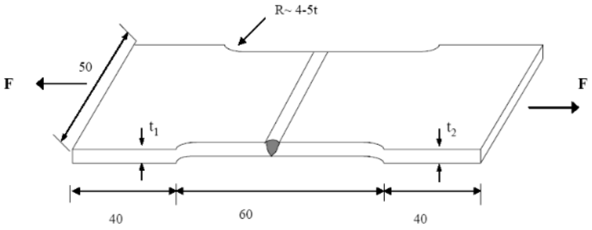

Figure 3. MIG butt-welded specimen (dimensions in millimeters).

Results—Spot Welds

Plotted in Figure 7 are all the tensile shear and coach-peel fatigue results for all nominal 1.6 mm gage materials with 7 mm diameter spot weld, conventional steels and AHSS included. Data labels ending in R0.1 indicate R=0.1 loading and data labels ending R0.3 indicate R=0.3 loading.

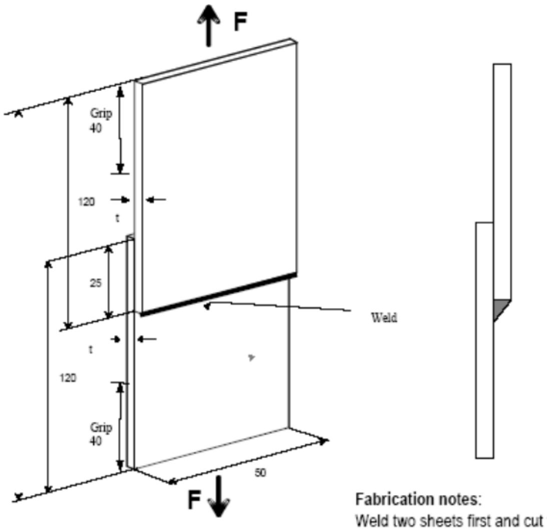
F
Grip
40
120
t
25
Weld
t
120
Grip
40
50
F

Fabrication notes:
Weld two sheets first and cut to specimen size to obtain consistent weld end conditions

Figure 4. MIG welded single-lap shear specimen (dimensions in millimeters).

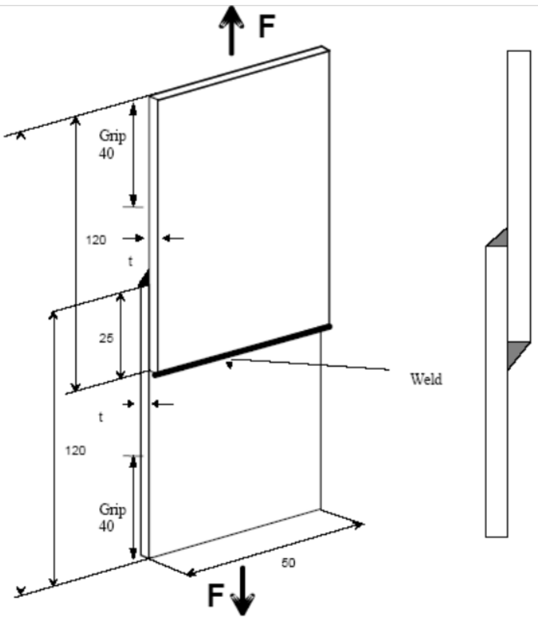
F
Grip
40
120
t
25
Weld
t
120
Grip
40
50
F

Figure 5. MIG welded double-lap shear specimen (dimensions in millimeters).

Runouts are plotted but not otherwise indicated in this figure.

Two thicknesses of HSLA340 (1.0 mm and 1.78 mm) and two thicknesses of DP600 (1.53 mm and 0.83 mm) are compared in Figure 8. The nominal button size for all specimens was 7.0 mm, and the welding parameters were held as similar as possible between the gages/grades without

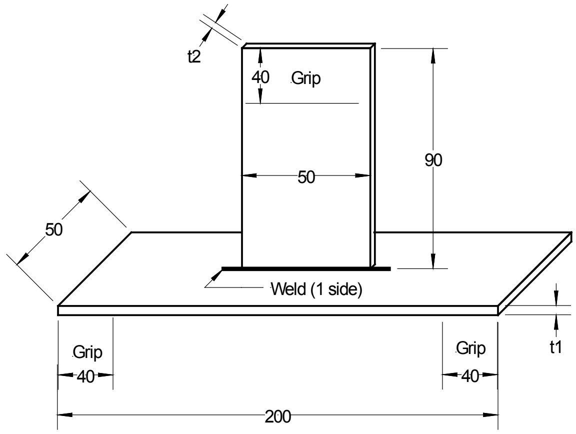
t2
40
Grip
50
90
50
Weld (1 side)
Grip
40
Grip
40
t1
200

Figure 6. MIG welded perch mount specimen (dimensions in millimeters).

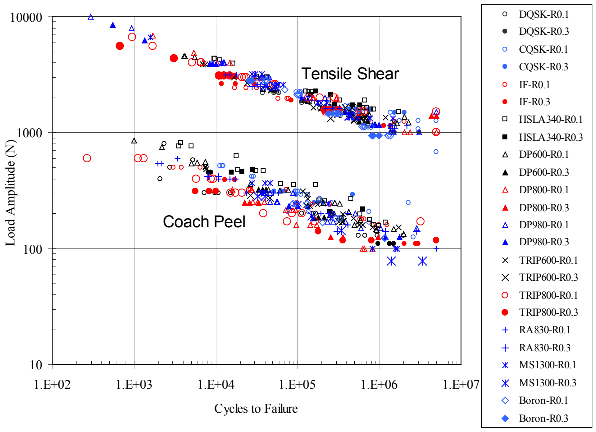

Figure 7. Fatigue results for all 1.6 mm thick, 7 mm diameter nugget spot-welded materials.

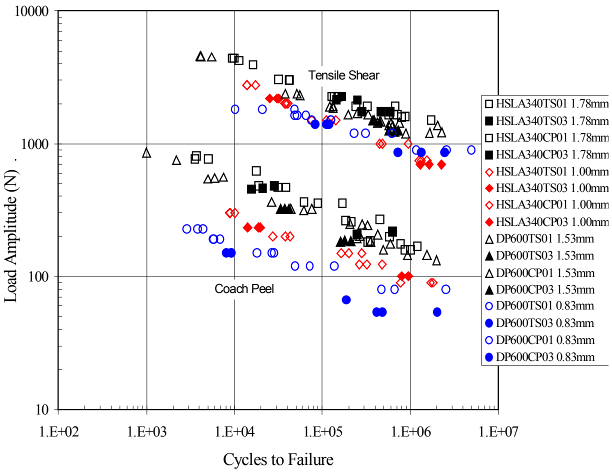

Figure 8. Effect of thickness on fatigue performance.

compromising strength. It was expected that the thinner gages would show shorter life because of the intrinsically higher stresses in the joint, and this result was indeed found in both materials.

Results—Fusion Welds

Fatigue testing of specimens containing the fusion weld-line within the width of the specimen was conducted to assist the Joining Technology team in identifying the optimum welding parameters for laser and MIG welded joints. The dimensions of the specimens are shown in Figure 9a and 9b. The weld location was centered between the edges of the sample and the robot travel was 25 mm total. This produced a weld with a start and a stop within the gage section of each specimen. GMAW welding of the DP780 AHSS was performed with 70 ksi and 90 ksi filler wires while GMAW welding of the DP600 AHSS was performed with only 70 ksi filler wire. No filler was used with the laser welds.

The DP600 results of the fatigue, shown in Figure 10a, indicate no significant difference in performance between the alternating current (ac), direct current (dc) or laser-assisted GMAW welding processes. Similarly, the performance of the DP780 GMAW welds (Figure 10d) was not influenced by either the process type or the strength of the filler material used. Similar observations may be made concerning the laser processing presented in Figure 10b and 10c. The mean stress appears to be an insignificant factor in the fatigue performance of fusion welded joints. This behavior can be seen in all of the graphs in Figure 10.

Conclusions

Analysis of test results indicates that, for the specimen geometries and steel grades selected for this study, the fatigue performance of a spot weld is independent of the base metal strength. This finding supports the initial understanding that the melting and resolidifying processes associated with spot welding form new alloys and make the properties and coating of the material(s) being joined, and the welding parameters, insignificant contributors to fatigue performance.

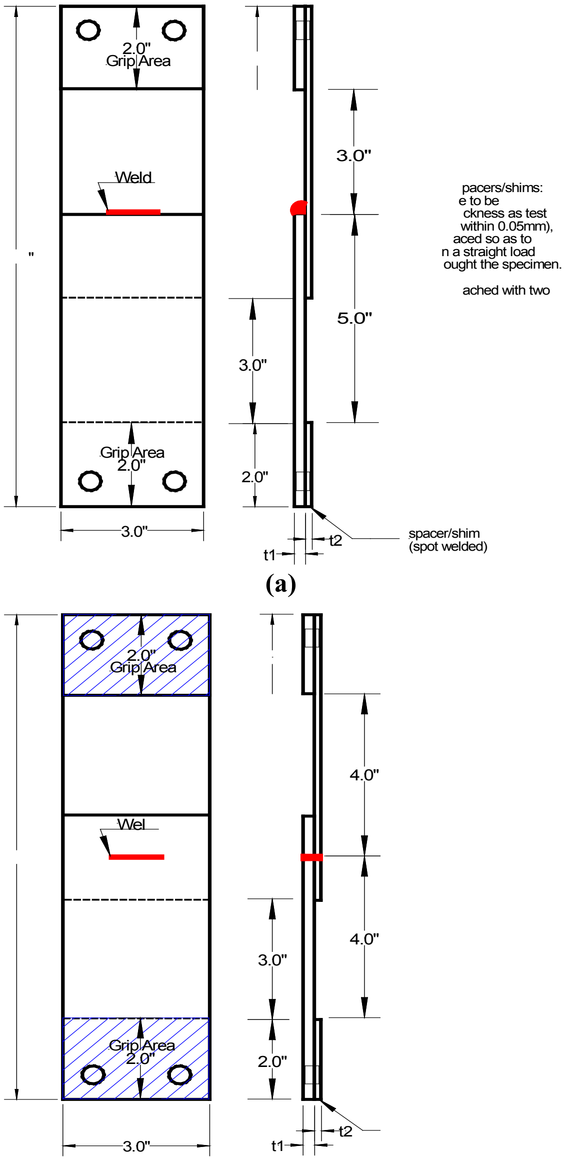

(a)

(b)

Figure 9. (a) Schematic of specimens for GMAW (dimensions in mm) and (b) Schematic of specimens for laser weld fatigue tests (dimensions in millimeters).

Similarly, the results clearly indicate that, within either the GMAW or laser weld groups, the type of weld does not seem to influence the fatigue performance (e.g., for GMAW it does not matter if the weld is ac, dc, or laser-assisted).

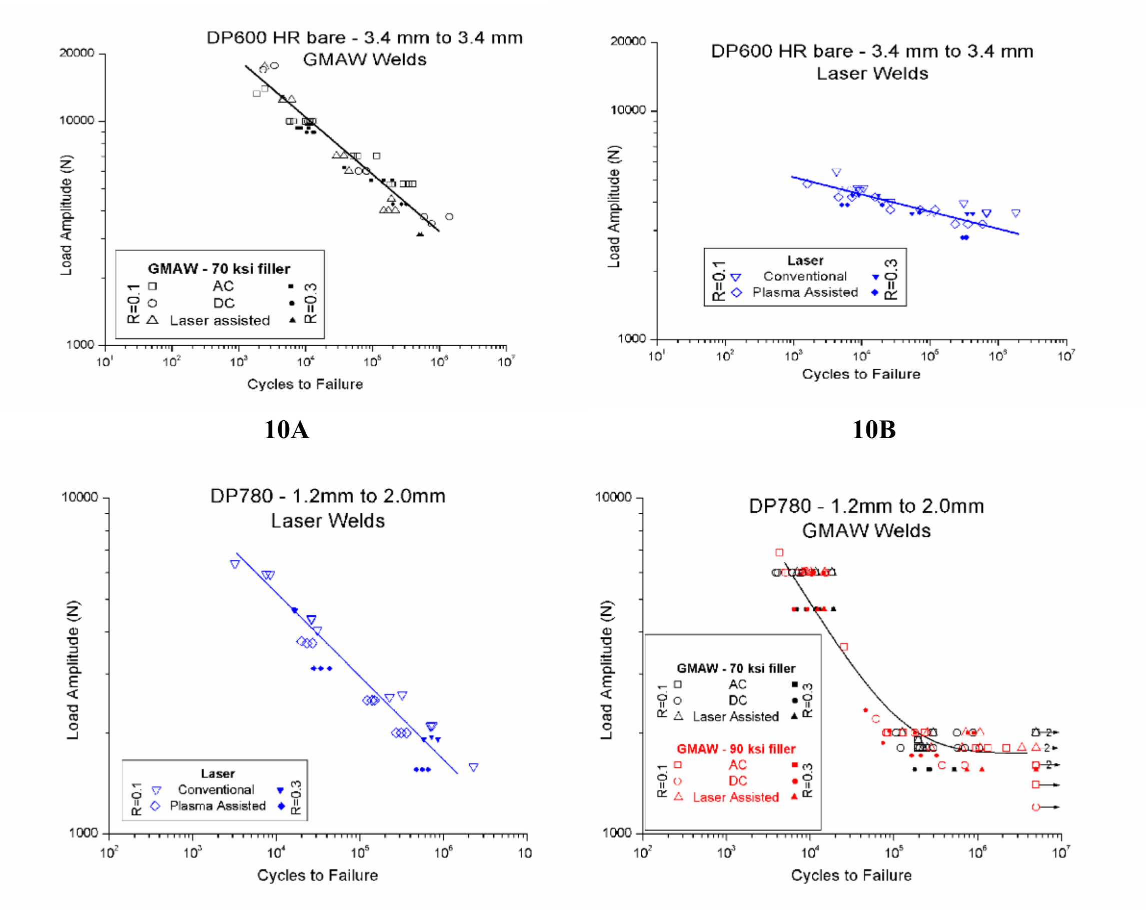

10A **10B**

10C **10D**

Figure 10. Fatigue performance evaluation of GMAW and laser welds in two advanced high strength steels, DP600 hot rolled, bare, and DP780 coated. Specimens for DP600 are 3.4 mm to 3.4 mm while the specimens for DP780 are 1.2 mm to 2.0 mm.

Presentations and Publications

1. "Sheet Steel Fatigue Group", Auto/Steel Partnership Program Review, Department of Energy, September 21, 2005.

2. "A/SP Sheet Steel Fatigue Committee", Joint Policy Board, Feb. 1, 2006.

3. J.J.F. Bonnen, Hari Agrawal, Mark A. Amaya, Raj Mohan Iyengar, Hong Tae Kang, A. K. Khosrovaneh, Todd M. Link, Hua Chu Shih, Matt Walp, Benda Yan, "Fatigue of Advanced High Strength Steel Spot Welds," 2006, Society of Automotive Engineers, SAE-2006-01-0978, pp. 19. *Republished in 2006 SAE Transactions.*

4. Kang, HongTae, "Evaluation of Spot Weld Fatigue Damage Parameters" 2006, Society of Automotive Engineers, SAE-2006-01-0978, pp. 19. *Republished in 2006 SAE Transactions.*

5. "Spot Welds, MIG Welds and their effect on the fatigue of AHSS steels," Mar. 10, 2006 (A/SP Frame group).

6. "Sheet Steel Fatigue Committee," A-S/P SPARC financial planning review, July 18, 2006.

7. "Spot Welds, MIG Welds and their effect on the fatigue of AHSS steels," Mar. 10, 2006 (Joining group).

8. "Fatigue of MIG Welds" AISI Wheel Task force meeting, Nov 18, 2005.

9. A/SP Team Review, Dec. 15, 2005.

10. "Fatigue of AHSS SpotWelds," 2nd Annual Ford AHSS Conference, Oct. 18, 2005.

11. J.J.F. Bonnen and R. Mohan-Iyengar, "Fatigue of Spot Welds in Low-Carbon, High-Strength Low-Alloy, and Advanced High-Strength Steels and Fatigue of Fusion Welds in Advanced High-Strength Steels," 2006 Proceedings of the International Automotive Body Congress (IABC 2006), pp 12, 2006.

12. H.-T. Kang, J. J. F. Bonnen, and R. Mohan Iyengar, "Sources of Variability in the Fatigue Strength of Spot Welded Specimens," Proceedings of Materials Science & Technology Conference, Detroit, September 2007.

13. J. J. F. Bonnen and R. Mohan Iyengar, "Fatigue Performance of Conventional and Advanced High-Strength Steel Spot Welds," presented at the special symposium marking the 20th Anniversary of A/SP, held as part of the Materials Science & Technology Conference, Detroit, September 2007.

D. Tribology (A/SP230*)

Project Manager: Pat V. Villano
Auto/Steel Partnership
2000 Town Center Drive, Suite 320
Southfield, Michigan 48075-1123
(248) 945-4780; fax: (248) 356-8511; e-mail: pvillano@a-sp.org

Project Chairperson: David Meuleman (disability leave)

Project Chairperson: Connie Yao (retired)

Acting Chairperson: Tareena Mulholland
General Motors Corporation
Manufacturing Engineering
30001 Van Dyke Avenue, Mail Code 480-210-Y25
Warren, Michigan 48090
(586) 575-5255; e-mail:tareena.mulholland@gm.com

Technology Area Development Manager: Joseph A. Carpenter
(202) 586-1022; fax: (202) 586-1600; e-mail: joseph.carpenter@ee.doe.gov

Field Project Officer: Aaron D. Yocum
(304) 285-4852; fax (304) 285-4403; e-mail: aaron.yocum@netl.doe.gov

Contractor: United States Automotive Materials Partnership (USAMP)
Contract No.: DE-FC05-02OR22910 through the National Energy Technology Laboratory

Objective

- The ability to fully realize the benefits of advanced high-strength steels depends upon the ability to aggressively form these steels into challenging parts. These steels have been shown to cause die failures in early implementations. This project is intended to improve the tribological understanding of the interaction among advanced high-strength steels (AHSSs), tooling, coatings, lubricants and the forming process so that the proper system can be selected to successfully manufacture automotive parts.
- Effective trimming of advanced high-strength steel parts has recently been noted as among the most challenging manufacturing operations for these materials particularly those steels with tensile strengths greater than 750 MPa. Accelerated wear of trim steels has lowered productivity and adversely affected part quality. There are many developments occurring in trim steel materials, but no effective method of screening the newly-available material is available.
- The work-hardening effects of advanced high-strength steel has also introduced excessive temperatures and wears on the forming and flanging operations. The challenge arises to determine what materials, surface treatments, lubrications, and die conditions are optimal for producing high quality, cost-effective parts.

---

*Denotes Project 230 of the Auto/Steel Partnership (A/SP), the automotive-focus arm of the American Iron and Steel Institute (see www.a-sp.org). The A/SP cofunds projects with DOE through a cooperative agreement between DOE and the United States Automotive Materials Partnership, one of the formal consortia of the United States Council for Automotive Research set up by Chrysler, Ford, and General Motors to conduct joint, precompetitive research and development (see www.uscar.org).

Approach

- Previously in this project, a continuous friction/die wear test had been developed for evaluating friction and wear during a long term (up to 100,000 strokes) simulation of the stamping process.
- This year's work was to extend the analysis of data already obtained, to fully extract information on heat generation during forming advanced high-strength steels, as well as, to further analyze the initiation and development of wear as it pertains to the metallurgy of the tooling material, tool coatings and sheet steel coating.
- Additional testing of specific form, flange, trim, and pierce steel materials/coatings will be conducted. However, as a result of delayed and unsatisfactory results from the previous methods of testing, a progressive die will be constructed and used to test several materials, coatings, angles, and clearances in form, flange, trim, and pierce functions in a production-type environment.

Accomplishments

- Completed Technical Paper—"Comparison of Friction Results Between Draw Bead Simulator & Twist Compressor Tester."
- Completed Technical Paper—"Effect of Process & Material Variables on Temperature Increase in Draw Bead Test."
- Completed Technical Paper—"Effect of Stroke Length and Penetration on Wear of Male Draw Beads."
- Completed design and construction of progressive die that tests 17 pierce, 12 flanging, 15 trimming, and 6 forming conditions.
- Completed 60,000 hits with dual phase (DP) 980 providing results for all operations.

Future Direction

- Further develop die to account for new materials and coatings in the completion of Phase 1 and Phase 2.
- Stamp 3.5 remaining coils of DP980 to complete Phase I of the Progressive Die Test with additional materials and coatings.
- Correlate results of progressive die test with production data as AHSS is implemented into production.
- Develop and begin Phase II of Progressive Die Test, vary current conditions, including findings from Phase I, and evaluate different grades of AHSS.

Introduction

Auto/Steel Partnership (A/SP) Tribology Team members designed a progressive die in which each operation is inserted in a way that the die can be designed to test a myriad of different conditions and materials. The team's interest is to determine the optimal die material and surface treatments for stamping AHSS.

Phase 1 Progressive Die Project

Phase 1 of the project has eleven stations of operation and two idle stations. Three of the piercing stations tested a range of pierce clearances. The trim and flange stations each tested seven different materials. Two-thirds of the DP980 bare sheet material has been stamped. While there is still ongoing work to complete Phase 1, the following conclusions are already apparent:

- There is a definitive clearance range from 5–15% where pierce is acceptable for part quality, burr height increases with clearance.
- The key-hole shaped pierce had a much larger burr than the other shaped pierce.
- The pre-strain from the bead accelerated trim steel wear significantly.
- Hardness of the trim steels directly impacted the failure mode of the insert.

- The bare materials in the flange operation failed quickly regardless of type of material.
- The low-temperature coating wore quickly in the flange operation, while the high-temperature coating proved superior.
- Higher trim angles result in a higher burr, and the "flange-out" pierce shape resulted in the largest burr.
- The coated flange steels ran at lower temperatures; however, flange steel temperature is not a good indicator of failure.
- Hardness of the flange steels has little impact on performance, whereas coating had high impact on performance.

The materials and coatings failed before we completed the stamping run. The team plans to complete Phase 1 utilizing the same operation design with additional materials and coatings.

When Phase 1 is complete, several parts and all die materials will be analyzed to determined exact mode of failure. At this time, the final report will be completed.

Publications/Presentations

1. One technical paper will be written from Phase 1 work and expected to be made available to various trade publications.

2. Phase 1 results are to be presented at the 2009 Great Designs in Steel Conference.

E. Advanced High-Strength Steel Stamping (A/SP050*)

Project Manager: Michael S. Bzdok
Auto/Steel Partnership
2000 Town Center, Suite 320
Southfield, Michigan 48075-1123
(248) 945-4778; fax: (248) 356-8511; e-mail: mbzdok@a-sp.org

Co-chair: James Fekete
General Motors Corporation
Body Manufacturing Engineering
30001 Van Dyke Avenue
Warren, Michigan 48090
(586) 201-9520; e-mail: jim.fekete@gm.com

Co-chair: Changqing Du
Chrysler LLC
800 Chrysler Drive
Auburn Hills, Michigan 48326
(248) 576-5197; fax: (248) 576-0230; e-mail: CD4@chrysler.com

Technology Area Development Manager: Joseph A. Carpenter
(202) 586-1022; fax: (202) 586-1600; e-mail: joseph.carpenter@ee.doe.gov

Field Project Officer: Aaron D. Yocum
(304) 285-4852; fax (304) 285-4403; e-mail: aaron.yocum@netl.doe.gov

Contractor: United States Automotive Materials Partnership (USAMP)
Contract No.: DE-FC05-95OR22363 through the National Energy Technology Laboratory

Objectives

- Determine how to accurately predict and control the amount of springback and other deviations from the desired stamping geometry for parts made from advanced high-strength steel (AHSS) prior to construction of production tooling.
- Develop part design and manufacturing process guidelines that can be recommended to automotive design and manufacturing engineers for the purpose of reducing springback and other part distortions.
- Investigate and analyze fractured materials for the purpose of understanding the fracture mechanism in terms of material properties and processing effects. Develop the ability to predict the onset of shear fracture in stamping processes.

Approach

- Predict AHSS stamping springback through finite-element analysis (FEA).

---

*Denotes Project 050 of the Auto/Steel Partnership (A/SP), the automotive-focus arm of the American Iron and Steel Institute (see www.a-sp.org). The A/SP cofunds projects with DOE through a cooperative agreement between DOE and the United States Automotive Materials Partnership, one of the formal consortia of the United States Council for Automotive Research set up by Chrysler, Ford, and General Motors to conduct joint, precompetitive research and development (see www.uscar.org).

- Control AHSS stamping springback by developing knowledge of part design geometries that affect flange springback and die processes that control springback.
- Develop predictive tools related to fracture in AHSS based upon an investigation and analysis of fractured material properties and microstructural characterization.

Accomplishments

- Modified tooling for stretch-forming processes of AHSS auto body structural components to neutralize the residual stresses that cause springback and sidewall curl. Predictable results have been shown for high-strength, low-alloy (HSLA) 350, DP600 MPa, DP780 MPa and DP980 MPa. Panel measurements and data analysis have been reported. The use of stiffening beads and other part shape modifications as well as control of key process variables are being recommended to product designers for control of twist, undercrown and springback based upon these results.
- Began a study to evaluate springback compensation technology developed in the DOE-supported "Die Face Engineering" project. A previously evaluated part (GM B-Pillar) was reevaluated, and numerical technology was used to develop a new die face which is expected to compensate for springback and lead to a dimensionally acceptable part.
- Completed five additional case studies of AHSS part developments by working through the original equipment manufacturers (OEMs). Applications guidelines studies were completed on roof rail reinforcement, three "B" pillar reinforcements, two "A" pillar reinforcements, and a rear rail. The volume "Advanced High-Strength Product and Process Applications Guidelines" was published, using the information developed from the case studies and other project activities.
- Made significant progress in an investigation of shear fracture of AHSS with the Edison Welding Institute, in cooperation with The Ohio State University (OSU), to perform analyses directed at understanding the basic characteristics of fractures at a microstructural level and predicting their onset.
- Completed an investigation of shear fracture in dual phase (DP) and transformation-induced plasticity (TRIP) steels at Wayne State University. The investigation included measuring the key material parameters needed to predict fracture; proposal of a new fracture criteria based on these material parameters; and preliminary guidelines to develop predictive tools and develop a standardized test for predicting failures in sheared edge stretching and breakage on a radius.
- Modified and tried out "15-Flange Die" for use in evaluating stretch-flanging capability of dual phase and other AHSS materials. Results were used in the Wayne State University study.
- Completed an evaluation of the mechanical properties of DP and TRIP steels in biaxial stretching through the OSU Center for Precision Forming. This forming mode allows data to be taken at higher strains than conventional tensile testing, resulting in more robust material models for forming and springback simulations.

Future Direction

- Additional material characterization work is required to evaluate material behavior at deformation levels beyond uniform elongation and close to failure. The team has identified mechanical testing with strain measurement accomplished with digital image correlation as a key method in this characterization. The team also recognizes that microstructural inhomogeneity has significant influence in the fracture performance of AHSS materials, and will be performing experiments to understand the effect of test direction as an additional step in understanding these phenomena.
- The B-Pillar springback compensation trials will be completed and the results analyzed for the purpose of evaluating the effectiveness of the technique.
- Additional applications guidelines case studies are being compiled.

Introduction

AHSS combining high-strength and superior formability compared to conventional high-strength steels are increasingly being used to deliver superior vehicle safety performance, while at the same time provide opportunities for mass reduction. AHSS have high initial work hardening rates as well as high tensile strengths. These characteristics, which make the material attractive to design engineers, also create challenges in the stamping and manufacturing processes; especially in terms of dimensional control and fracture prediction.

FEA has been widely used in automotive industry for vehicle designs and manufacturing feasibility. Over a period of 20 years, a high level of confidence has been achieved using FEA to predict splits and wrinkling in metal- forming processes. However, it remains a challenge to accurately predict springback, particularly for those parts with twists and sidewall curls. Numerous studies have been carried out to correlate computer prediction to experimental results. The material model, element formulation, friction and contact algorithm are important parameters affecting simulation accuracy. Other studies have also demonstrated the sensitivity of springback predictions to other numerical parameters, such as mesh size, number of through-thickness integration points, tooling travel speed, contact interface parameters, etc. During the last decade, FEA software developers and users have been investing much effort into the solution of springback prediction problems. A steady improvement has been seen in the prediction capability and methodology.

Prediction of splits using FEA has also been complicated with the emergence of shear fracture in AHSS stamping. Shear fractures are not predicted using conventional FEA analysis techniques, and this has resulted in significant issues during tryout of AHSS parts.

To address these issues, the A/SP initiated enabler projects, focusing on stamping experiments using production-intent tooling, with the results being compared to analyses using computer (FEA) models. To date, various classes of automotive parts have been studied, which were fabricated from AHSS with tensile strengths varying from 600 to 980 MPa. Stamping experiments included various forming process variables, including pad forces, blank holder forces and die configurations (drawing versus crash forming). Simulations were carried out using various numerical parameters (mass scaling, adaptive levels and mesh coarsening) in order to study their effects on the prediction accuracy. Experimental results were compared to the corresponding FEA simulations.

Discussion

Most experiments have been conducted with a multi-process research die with sub-die inserts (Figure 1) to produce various automotive structural components by a variety of processes. This die has the necessary higher holding pressures and controlled processes required for working the higher-strength materials. A programmable, hydraulic pressure cushion is the main component of this system that provides the means of stretch-forming the metal and controlling springback.

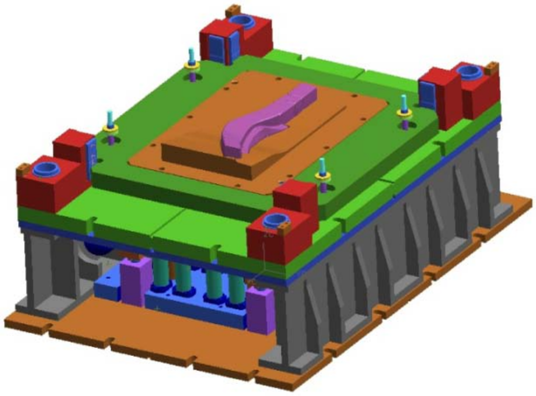

Figure 1. Lower half of multi-process die.

Sub-die inserts in the multi-process master shoe die enable stamping of underbody, cross-car and body side structural components with a variety of stamping processes.

The latest results of the experiments are described below.

Rear Longitudinal Rail Sub-Dies

Tryout utilized three different stamping processes: draw action, with part on post or part on binder; and form die with upper pad. Figure 2 shows examples of parts produced with these processes.

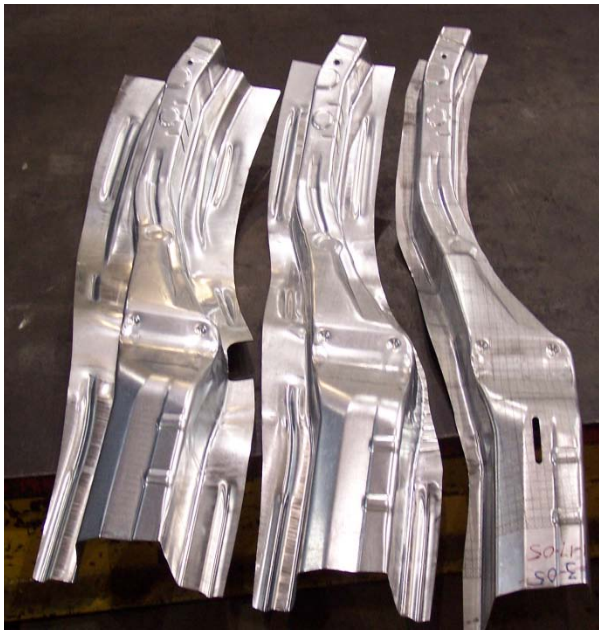

Figure 2. Rail stampings form three processes (from left to right: draw process– part on post; draw process– part on binder; form process).

Materials included 1.6 mm and 2.2 mm DP600 MPa steel and 1.6 mm DP780 MPa and DP980 MPa steel. Tryout resulted in identification of a forming process that lowered press forces and used material more efficiently, with springback comparable to the other processes. However, part dimensions were still outside acceptable ranges, so efforts continued with the higher strength grades to improve the springback control with a Four Break Bead, added to the forming process. Figure 3 shows a cross section of this die process.

This process feature was shown in previous work to be effective at controlling sidewall curl. The experiments were completed in this reporting period, with the following results:

- The amount of springback increases with the material strength;

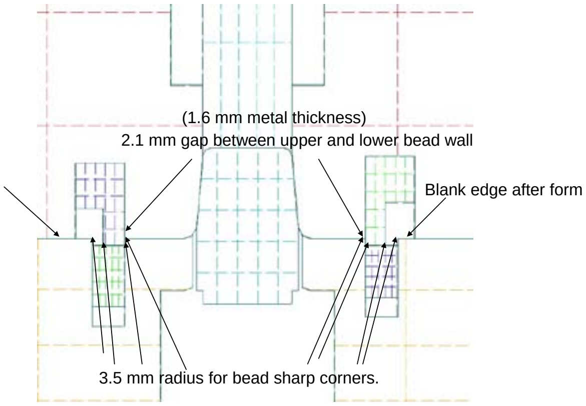
(1.6 mm metal thickness)
2.1 mm gap between upper and lower bead wall
Blank edge after form
3.5 mm radius for bead sharp corners.

Figure 3. Cross-section of four break-bead evaluated in this reporting period.

- Trimming increases the amount of springback;
- Four Break-Bead produces less springback than the crash form with developed blanks. However, the amount of springback after trimming is almost the same as that by crash form;
- Four Break-Bead produces more variations in springback than crash form;
- Four Break-Bead produces less twist than crash form;
- Four Break-Bead produces more side wall curl than crash form;
- Four Break-Bead produces less flange opening angle than crash form

LS-DYNA simulation results were compared to the experimental results. The following conclusions are obtained:

- Both the experimental and the simulation results showed that the draw form process produced more springback than the crash form process; and the amount of springback increased with the material strength.
- The FEA-predicted springback match to the experiments was seen to be dependent upon material strength. Reasonably good prediction accuracy was obtained for the DP600 parts.
- The correlation between the predicted and the experimental results for DP780 and DP980 parts is not as good as that for DP600 (Figure 4). Further study is needed to improve the predictability for higher strength materials.

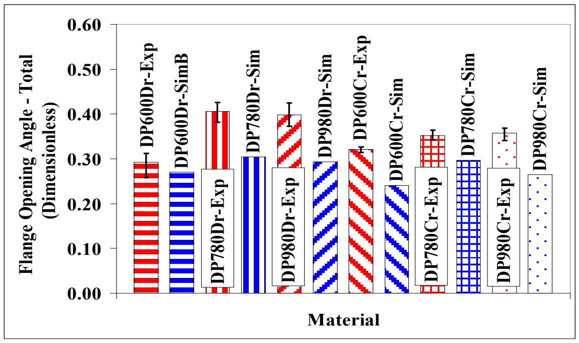

Figure 4. Correlation simulation vs experimental.

- Increasing mass scaling and reduced adaptive levels will deteriorate the prediction accuracy. Mesh coarsening prior to springback analysis does not greatly affect the prediction results.

Body Side Center Pillar Sub-Die

A sub-die for a Body Center Pillar was modified through tryout to optimize results (Figure 5). This part is crucial to the body side structure for meeting side impact requirements. It is also typically difficult to stamp in medium strength grades due to springback, twist and undercrown. The higher-strength grades increased the manufacturing difficulties.

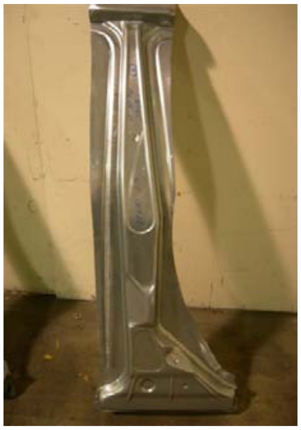

Figure 5. Body side center pillar.

During tryout, several features were added to the part to enable stamping in DP780 material. Changes were made to the product shape to take up excess metal and features were added to stiffen the part. Split- and fracture-free stampings were then made from both DP780 and DP980 material.

Parts have been scanned and dimensional analysis has been completed.

Phase two of the project is utilizing the dimensional evaluation of both untrimmed and trimmed parts. This information, FEA analysis, and computer-guided compensation were used to recut the die to achieve dimensional accuracy of the part. The recut die is complete and awaiting tryout upon receipt of appropriate steel material.

Viscous Bulge Mechanical Testing

Materials models for formability and springback simulation have weaknesses that compromise the quality of the results. One of the weaknesses is the limitations of data from tensile tests, since true stress-strain data can be easily extracted only at strains below the end of uniform elongation. In practical stamping processes, this level of effective strain is often exceeded. For this reason, the team contracted researchers at the OSU Center for Precision Forming to test a range of DP and TRIP steels using a viscous pressure bulge test, which allows data to be collected at significantly higher strains than can be achieved with tensile testing. This contract was successfully completed in this reporting period, and the data have been distributed to the team. An example is shown in Figure 6.

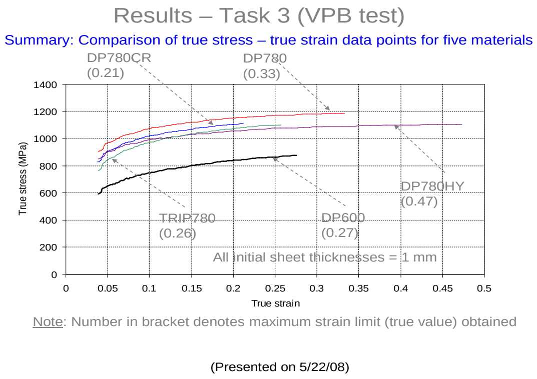

Figure 6. Results of viscous pressure bulge testing of DP and TRIP steels.

Shear Fracture Project

Beginning in 2007 the A/SP AHSS Stamping Team contracted with Edison Welding Institute (EWI), in association with OSU, to conduct a three year project for shear fracture characterization, Draw Bend Formability (DBF) testing and fracture criteria development of AHSS. Shear fracture has emerged as a common and unpredictable failure mechanism in production of AHSS parts. An example is shown in Figure 7.

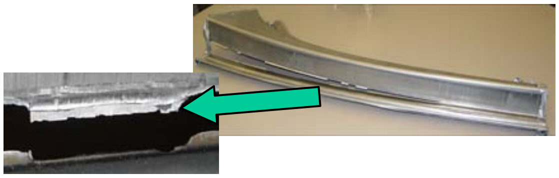

Figure 7. AHSS shear fracture phenomenon.

DBF testing to date has focused upon DP 590 and DP780 steel in 1.4 mm and 1.75 mm gauges. Work has also started developing constitutive equations for AHSS and finite-element simulation of AHSS deformation.

The results to date have indicated that the type of fracture (shear fracture vs conventional tensile-type failure) can be predicted based on knowledge of the material properties and test parameters (Figure 8). Further, the results have shown that the heat generated during the deformation of the sample has a significant influence on the hardening behavior of the material, and should be taken into account for the most accurate simulations.

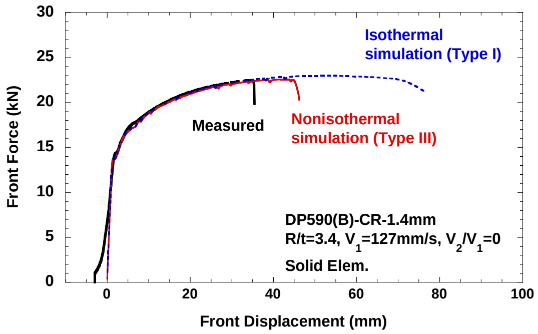

Figure 8. Comparison of predicted vs measured fracture behavior in a stretch-draw test.

Significant progress has also been made in characterizing microstructural damage that occurs during the stretch bending process. This information will be used in conjunction with microstructural-level FEA modeling to determine the relative influence of microstructural damage and thermal characteristics on the bending failures.

Flange Shear-Affected Zone Study

In October 2007 the A/SP AHSS Stamping Team contracted with Wayne State University in Detroit, Michigan to characterize the nature and extent of the shear-affected zone of shear-trimmed and subsequently flanged DP steel features (Figure 9).

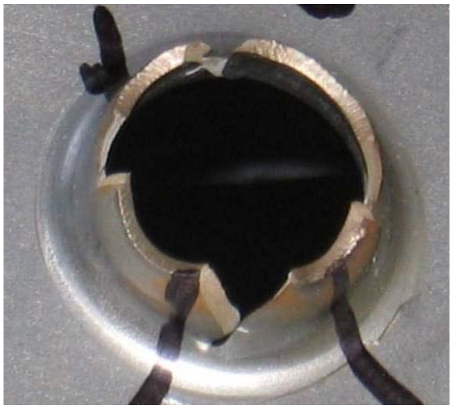

Figure 9. Example of performance of DP980 in flanging a 5 mm diameter hole.

This project was completed during this program period. The tasks of this project were two fold:
(a) experimentally characterize the shear-affected zone and material and edge microstructures for three DP steels: DP600, DP780 and DP980;
(b) perform computer simulation on flanging two specially designed parts made of three DP steels and with three flange lengths: 1 mm, 3 mm, and 5 mm.

The report describes the results of edge characterization of mechanically-pierced part edges, and makes a comparative study with samples containing laser-cut edges. A new technique, based on flow-line analysis commonly used in evaluation of deformation in forging processes, was used to calculate the strain in the pierced samples as a function of distance from the sheared surface.

Based on the experimental finding, a new computing technique was proposed that takes into account the non-uniform microstructure of materials. The model uses constituent properties as input, similar to that in microstructure-based micromechanics method, but the phase particles are modeled at the element level. The technique considers statistical features of the microstructure and the pierced edge characteristics are to be used as the input of FEA. Further work is necessary to fully develop this proposed technique.

AHSS Case Studies and Applications Guidelines

The work of this team was leveraged with evaluations of actual production parts. These detailed case studies include part designs, materials selections, stamping processes, analysis results, and lessons learned. Five case studies were completed this reporting period. They are available at http://www.a-sp.org/publications.htm.

In addition, this combined work was summarized and compiled into a volume entitled "Advanced High Strength Steel Applications Guidelines", which is also available as a download at the above website, or as a paperback book.

Summary and Conclusions

Evaluations of production parts and processes continued in this reporting period. The Four Break-Bead was again shown to have some positive effect on dimensional control. Further, FEA evaluation using current state-of-the-art techniques showed that though progress has been made, improvements were still required for robust dimensional prediction.

The team is in the process of evaluating the latest generation of FEA technology for springback prediction. The B-pillar die face has been recut based on FEA technology. The resulting tool is expected to deliver a dimensionally-correct part. The evaluation will be completed in the next reporting period.

Elements of the experimental work, combined with the results of the case studies, have been compiled into a volume entitled "Advanced High-Strength Product and Process Applications Guidelines."

Evaluation of shear fracture in bending and edge stretching are ongoing. Preliminary results show that fracture type can be predicted with knowledge of material and process variables. Microstructural damage occurs as a result of these processes, and its influence on fracture is currently under investigation. FEA modeling at the microstructural level is also being investigated to determine if it provides value in predicting these fractures.

Presentations and Publications

1. Ken D. Schmid, General Motors Corporation "Evaluation of DP780 and DP980 for B-Pillars," *Presented at the 2008 Great Designs in Steel Seminar, April 9, 2008, Livonia, Michigan.*
2. Changqing. Du, Chrysler LLC "Correlation of FEA Prediction and Experiments on Dual-Phase Steel Automotive Rails," *Presented at the 2008 Great Designs in Steel Seminar, April 9, 2008, Livonia, Michigan.*
3. "Advanced High-Strength Product and Process Applications Guidelines" manual prepared by the Auto/Steel Partnership Applications Guidelines Team, November, 2007.
4. The team held a one-day Shear Fracture Technical Progress Review on Sept. 10, 2008. All project contributors and some invited guests presented the status of their work to a group of researchers from the member companies of the Auto/Steel Partnership. The presentations can be made available.

F. Strain-Rate Characterization (A/SP190*)

Project Manager: Pat V. Villano
Auto/Steel Partnership
2000 Town Center Drive, Suite 320
Southfield, Michigan 48075-1123
(248) 945-4780; fax: (248) 356-8511; e-mail: pvillano@a-sp.org

Chairman: Kathy Wang
General Motors Corporation
2000 Centerpoint Parkway
Pontiac, Michigan 48341
(586)-986-1173; fax: (586) 986-8722; e-mail: kathy.wang@gm.com

Lead Scientist: Srdjan Simunovic
Oak Ridge National Laboratory
Oak Ridge, Tennessee 37831-6359
(865) 241-3863; fax: (865) 574-7463; e-mail: simunovics@ornl.gov

Technology Area Development Manager: Joseph A. Carpenter
(202) 586-1022; fax: (202) 586-1600; e-mail: joseph.carpenter@ee.doe.gov

Field Project Officer: Aaron D. Yocum
(304) 285-4852; fax (304) 285-4403; e-mail: aaron.yocum@netl.doe.gov

---

Contractor: United States Automotive Materials Partnership (USAMP)
Contract No.: DE-FC05-02OR22910 through the National Energy Technology Laboratory

---

Objectives

- Develop new experimental setups for characterization of crashworthiness and strain-rate sensitivity of both advanced high-strength steels (AHSS) and structural designs.
- Replicate impact conditions that occur in automotive impact by simpler and more manageable experiments in order to generate meaningful data for computer modeling.
- Initiate new, robust spot weld finite-element formulation procedures for modeling various modes of spot-weld failure as a function of impact, welding conditions and materials while maintaining the current computational efficiency.
- Establish an experimental database on the performance of resistance spot welds in AHSS components during impact.

Accomplishments

- Developed procedure for new crashworthiness characterization test based on parallel-plates buckling.
- Developed and conducted constant-velocity crash experiments on circular tubes.

---

*Denotes Project 190 of the Auto/Steel Partnership (A/SP), the automotive-focus arm of the American Iron and Steel Institute (see www.a-sp.org). The A/SP cofunds projects with DOE through a cooperative agreement between DOE and the United States Automotive Materials Partnership, one of the formal consortia of the United States Council for Automotive Research set up by Chrysler, Ford, and General Motors to conduct joint, precompetitive research and development (see www.uscar.org).

- Developed hydraulic tests for strain rate characterization of High Strength Steels (HSS).
- Developed web-based database for display and analysis of coupon, spot weld, and tube crush experiments
- Develop test method for investigation of strain-rate effects of spot welds.

Future Direction

- Develop experiments for characterizing fracture in HSS in forming and crash.
- Provide high-quality data for material and Finite-Element Modeling (FEM) development.
- Expand tests to other welding processes (weld bonding, friction stir spot welding, etc.).

Introduction

Crashworthiness characterization of AHSS requires testing of materials and structures under increased strain rates, large plastic strains, and large displacements that are characteristic of actual impact events. The AHSS characterization involves testing at several different length scales. The intrinsic material properties are investigated using the coupon-level specimens where the material is exposed to simple stress states that can be reduced to the equivalent stress and strain measures used in formulation of constitutive models. The coupon tests involve uniaxial tension and compression in plane-stress conditions. High-speed hydraulic equipment is used to impose constant velocity in order to determine material response to different loading rates. At a higher length scale, the characteristic plastic hinge mechanism responsible for crash energy absorption in AHSS structures is investigated using the double-plate test. This test has shown that the strain-rate sensitivity of AHSS in bending under out-of-plane compression exhibit trends that cannot be fully explained using the plate bending models derived from material behavior under uniaxial plane stress. At the component level, AHSS properties in tubular structures are investigated using specialized hydraulic equipment that allows constant crush speeds up to 8 m/s. In automotive design, the structural integrity of AHSS components is primarily provided by spot welds. The response of spot welds under different loading velocities and loading states have also been characterized in this project.

The above experiments provide high-quality data for development of material and structural FEM models for AHSS and thereby enable more accurate modeling and design of lightweight, crashworthy vehicles. The developed experiment technology is also directly relevant to other automotive materials as it provides a systematic approach to characterization and comparison of crashworthiness of new automotive materials.

Design of Experiments

The experiments conducted under this project have been compiled into interactive databases that are accessible over the World Wide Web. The portal page for the experiments is shown in Figure 1.

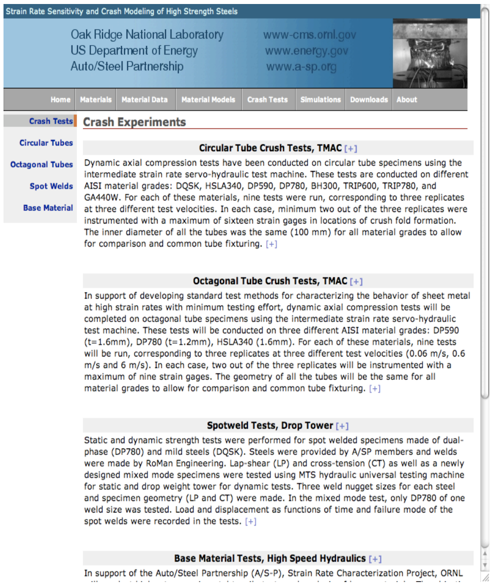

Crash Experiments

Circular Tube Crush Tests, TMAC [+]

Dynamic axial compression tests have been conducted on circular tube specimens using the intermediate strain rate servo-hydraulic test machine. These tests are conducted on different AISI material grades: DQSK, HSLA340, DP590, DP780, BH300, TRIP600, TRIP780, and GA440W. For each of these materials, nine tests were run, corresponding to three replicates at three different test velocities. In each case, minimum two out of the three replicates were instrumented with a maximum of sixteen strain gages in locations of crush fold formation. The inner diameter of all the tubes was the same (100 mm) for all material grades to allow for comparison and common tube fixturing. [+]

Octagonal Tube Crush Tests, TMAC [+]

In support of developing standard test methods for characterizing the behavior of sheet metal at high strain rates with minimum testing effort, dynamic axial compression tests will be completed on octagonal tube specimens using the intermediate strain rate servo-hydraulic test machine. These tests will be conducted on three different AISI material grades: DP590 (t=1.6mm), DP780 (t=1.2mm), HSLA340 (1.6mm). For each of these materials, nine tests will be run, corresponding to three replicates at three different test velocities (0.06 m/s, 0.6 m/s and 6 m/s). In each case, two out of the three replicates will be instrumented with a maximum of nine strain gages. The geometry of all the tubes will be the same for all material grades to allow for comparison and common tube fixturing. [+]

Spotweld Tests, Drop Tower [+]

Static and dynamic strength tests were performed for spot welded specimens made of dual-phase (DP780) and mild steels (DQSK). Steels were provided by A/SP members and welds were made by RoMan Engineering. Lap-shear (LP) and cross-tension (CT) as well as a newly designed mixed mode specimens were tested using MTS hydraulic universal testing machine for static and drop weight tower for dynamic tests. Three weld nugget sizes for each steel and specimen geometry (LP and CT) were made. In the mixed mode test, only DP780 of one weld size was tested. Load and displacement as functions of time and failure mode of the spot welds were recorded in the tests. [+]

Base Material Tests, High Speed Hydraulics [+]

In support of the Auto/Steel Partnership (A/S-P), Strain Rate Characterization Project, ORNL

Figure 1. Web portal for AHSS experiments.

The experimental data is integrated with the other project components and provides mechanisms for data analysis and collaboration between project participants.

Strain-Rate Characterization in Sub-Hopkinson Regime

In support of the Auto/Steel Partnership (A/SP), Strain-Rate Characterization Project, Oak Ridge National Laboratory researchers are conducting high-rate experimental tests and analysis of base material specimens in uniaxial tension configuration. The objective of the test program is to provide the necessary experimental data in support of the A/SP efforts to determine high-strain-rate mechanical properties of AHSS. The test program consists of testing tensile specimens under strain rates of quasi-static, 0.1/s, 1/s, 10/s, 100/s and maximum strain rates achievable in full open-loop configuration (1000/s) and the selected gage length. Among the unique features of the current approach is the ability to conduct tests across all speeds on the same apparatus and, thereby, eliminate variability associated with using different testing methods and actuators. The equipment allows for testing at speeds from quasi-static to 700 in/sec (18.5 m/s) over a range of 4 inches (100 mm) at maximum loads of 9000 lbf (40 KN). If an effective gage length for the chosen specimen is known, the equipment can run non-linear velocities in the drive file to achieve global strain control (engineering or true strain rate as desired). The test equipment is shown in Figure 2.

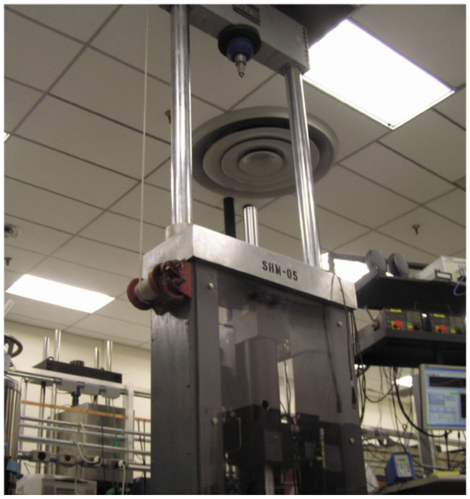

Figure 2. High-speed hydraulic tester. The test stage is elevated to allow for actuator acceleration to desired test speed.

The dynamic testing procedures from recent studies sponsored by International Iron and Steel Institute [1,2] and published literature [3,4] are followed and further enhanced using the new measurement techniques and synchronization. The multiple measurement methods of both forces and displacements allow for correlation of the results and verification of the different instrumentation techniques. Schematic representation of the test specimen and the measurement locations is shown in Figure 3.

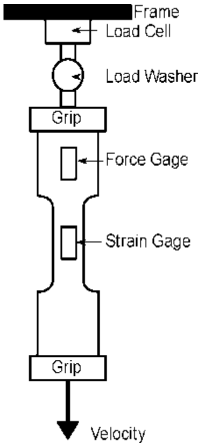

Figure 3. High strain-rate rate test setup.

The specimen geometry for dual phase 780 MPa (DP780) steel is shown in Figure 4.

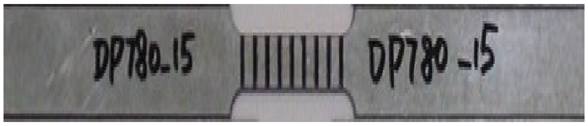

Figure 4. High strain-rate specimen geometry.

The horizontal lines in the gage area were added to allow for optical-measurement correlation with the data from actuator displacement and electrical resistance strain gage in the gage area. All the measurements are synchronized using the central trigger. High-speed video recording is used to provide detailed record of the test and to correlate optical measurement with the mechanical output data. An output of the program from tracing multiple markings in the high-speed movie developed for optical measurement is shown in Figure 5. The measurement is based on the variations in color intensity along the prescribed scan lines. The pixel location of the found gage marks is shown in the images for increasing displacement.

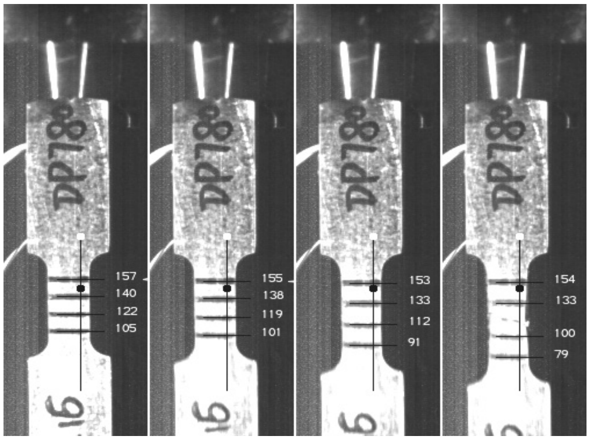
DP780
157
140
122
105
155
138
119
101
153
133
112
91
154
133
100
79

Figure 5. Optical strain measurement output for increasing strain. Horizontal black lines denote found gage mark based on color intensity. The test is conducted on DP780 material under 1000/s strain rate.

White numbers on the image denote vertical mark location in pixels. The distance between the lines can be used to determine uniformity of strain and the onset of localization. Figure 6 shows the output of the optical measurement and strain derived from the locations of the top (Line 1) and bottom (Line 4) marks.

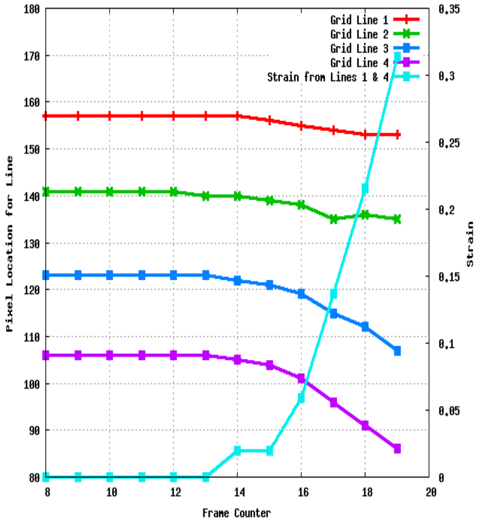

Figure 6. Analysis of the optical strain measurement output for increasing strain (Frame Counter). Divergence of the green (Line 2) and blue (Line 3) lines indicates onset of localization. Overall strain in the gage is calculated from the location of the top (Line 1) and bottom (Line 4) lines.

The multiple-measurement methods of both forces and displacements allow for correlation of the measurements, identification of test areas for further improvement, and verification of the method. All the measurements are synchronized using the central trigger. A Web-based database for the experiments has been created. The database is used to disseminate test results to the A/SP partners. A user can dynamically select and analyze tests results for different materials and strain rates. The main interface to the tests database is shown in Figure 7.

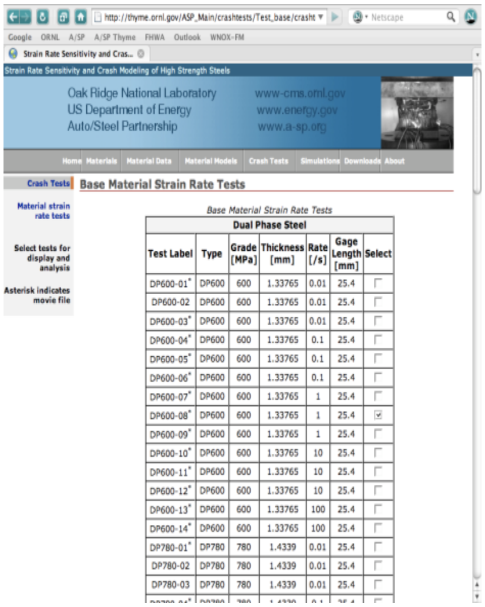
http://thyme.ornl.gov/ASP_Main/crashtests/Test_base/crasht
Netscape
Google
ORNL
A/SP
A/SP Thyme
FHWA
Outlook
WNOX-FM
Strain Rate Sensitivity and Cras...
Strain Rate Sensitivity and Crash Modeling of High Strength Steels
Oak Ridge National Laboratory
US Department of Energy
Auto/Steel Partnership
www-cms.ornl.gov
www.energy.gov
www.a-sp.org
Home
Materials
Material Data
Material Models
Crash Tests
Simulations
Downloads
About
Crash Tests
Material strain rate tests

Base Material Strain Rate Tests

Select tests for display and analysis

Asterisk indicates movie file

Base Material Strain Rate Tests

Dual Phase Steel						
Test Label	Type	Grade [MPa]	Thickness [mm]	Rate [/s]	Gage Length [mm]	Select
DP600-01*	DP600	600	1.33765	0.01	25.4	☐
DP600-02	DP600	600	1.33765	0.01	25.4	☐
DP600-03*	DP600	600	1.33765	0.01	25.4	☐
DP600-04*	DP600	600	1.33765	0.1	25.4	☐
DP600-05*	DP600	600	1.33765	0.1	25.4	☐
DP600-06*	DP600	600	1.33765	0.1	25.4	☐
DP600-07*	DP600	600	1.33765	1	25.4	☐
DP600-08*	DP600	600	1.33765	1	25.4	☑
DP600-09*	DP600	600	1.33765	1	25.4	☐
DP600-10*	DP600	600	1.33765	10	25.4	☐
DP600-11*	DP600	600	1.33765	10	25.4	☐
DP600-12*	DP600	600	1.33765	10	25.4	☐
DP600-13*	DP600	600	1.33765	100	25.4	☐
DP600-14*	DP600	600	1.33765	100	25.4	☐
DP780-01*	DP780	780	1.4339	0.01	25.4	☐
DP780-02	DP780	780	1.4339	0.01	25.4	☐
DP780-03	DP780	780	1.4339	0.01	25.4	☐

Figure 7. Web interface to the experimental data. Users select materials and proceed to the analysis phase.

The selected data is further analyzed and provided for download. It includes raw measurement data from multiple sources and high-speed video of the test. The stress-strain curves calculated from different sources for DP600 material are shown in Figure 8.

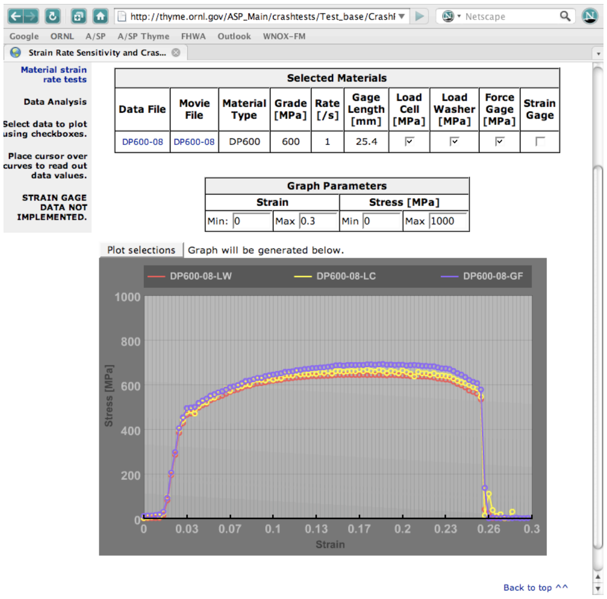
http://thyme.ornl.gov/ASP_Main/crashtests/Test_base/Crashl
Netscape
Google ORNL A/SP A/SP Thyme FHWA Outlook WNOX-FM
Strain Rate Sensitivity and Cras...
Material strain rate tests
Data Analysis
DP600-08-LW
DP600-08-LC
DP600-08-GF
1000
800
600
400
200
0
Stress [MPa]
0
0.03
0.07
0.1
0.13
0.17
0.2
0.23
0.26
0.3
Strain
Back to top ^^

Select data to plot using checkboxes.

Place cursor over curves to read out data values.

STRAIN GAGE DATA NOT IMPLEMENTED.

Selected Materials									
Data File	Movie File	Material Type	Grade [MPa]	Rate [/s]	Gage Length [mm]	Load Cell [MPa]	Load Washer [MPa]	Force Gage [MPa]	Strain Gage
DP600-08	DP600-08	DP600	600	1	25.4	☑	☑	☑	☐

Graph Parameters			
Strain		Stress [MPa]	
Min: 0	Max 0.3	Min 0	Max 1000

Plot selections

Graph will be generated below.

Figure 8. DP600 test at 1 /sec strain rate. The lower two lines (Red and yellow) denote measurement from load washer and force strain gage on specimen tab, respectively.

Conclusions

A new method for characterization of strain-rate sensitivity under automotive strain rates has been developed. This method uses multiple measurements of material response in a single testing apparatus. It enables the correlation of the measurements and identification of test areas for further improvement. The developed method allows for determination of material parameters to be used in computational modeling and design, and enabling of more-effective use of new materials and structures under impact loads.

Acknowledgments

Support from the Auto/Steel Partnership Strain Rate Characterization Team is acknowledged.

Future Work

Future work on the project will focus on the following.

1. Improvement of accuracy of strain and force measurements at strain rates larger than 100/s.
2. Development of integrated measurement system that automatically processes and correlates measurements.
3. Development of the specification for the testing of materials in the automotive strain rates regime.
4. Strain-rate sensitivity measurements for the new AHSS.
5. Development of new coupon-level crash characterization experiments for AHSS fracture under impact.

References

1. Recommendations for Dynamic Tensile Testing of Sheet Steels, International Iron and Steel Institute, 2005.
2. C. Wong, IISI-AutoCo Round-Robin Dynamic Tensile Testing Project, International Iron and Steel Institute, 2005.
3. D. Matlock, J. Speer, Constitutive Behavior of High Strength Multiphase Sheet Steels Under High Strain Rate Deformation, AISI/DOE Technology Roadmap Program, Report TRP 9904, 2005.
4. D.M. Bruce, “Dynamic Tensile Testing of Sheet Steels and Influence of Strain Rate on Strengthening Mechanisms in Sheet Steels”, Ph. D. Thesis # MT-SRC-003- 018, Colorado School of Mines, 2003.

G. Future Generation Passenger Compartment—Validation (A/SP241*)

Project Manager: Pat J. Villano
Auto/Steel Partnership
2000 Town Center Drive, Suite 320
Southfield, Michigan 48075-1123
(248) 945-4780; fax: (248) 356-8511; e-mail: pvillano@a-sp.org

Co-Chairman: Jody R. Shaw
Manager, Automotive Marketing
United States Steel Corporation
5850 New King Court
Troy, Michigan 48098-2608
(248) 267-2608; fax: (248) 267-2580; e-mail: jrshaw@uss.com

Co-Chairman: Joe Polewarczyk
General Motors Corporation
Body Systems & Closures
Engineering West
Mail Code 480-11-W13
30200 Mound Road
Warren, Michigan 48092-2025
(586) 986-2157: fax: (586) 986-8592; e-mail: joseph.m.polewarczyk@gm.com

Co-Chairman: Shawn Morgans
Ford Motor Company
Body Structure—Technical Leader
Product Development Center
20910 Oakwood Boulevard
Cube-2F-C11
Dearborn, Michigan 48121
(313)805-3596: fax:313-845-5634; e-mail: smorgans@ford.com

Technology Area Development Manager: Joseph A. Carpenter
(202) 586-1022; fax: (202) 586-1600; e-mail: joseph.carpenter@ee.doe.gov

Field Project Officer: Aaron D. Yocum
(304) 285-4852; fax (304) 285-4403; e-mail: aaron.yocum@netl.doe.gov

Contractor: United States Automotive Materials Partnership (USAMP)
Contract No.: DE-FC05-02OR22910 through the National Energy Technology Laboratory

Objective

- Validate the findings of the Future Generation Passenger Compartment (FGPC) Phase 1 project on a 5-passenger, 4-door, high production volume donor vehicle reducing passenger compartment mass by 25% or greater with cost parity relative to baseline while maintaining the structural performance in crash safety, stiffness and durability.

---

*Denotes Project 241 of the Auto/Steel Partnership (A/SP), the automotive-focus arm of the American Iron and Steel Institute (see www.a-sp.org). The A/SP cofunds projects with DOE through a cooperative agreement between DOE and the United States Automotive Materials Partnership, one of the formal consortia of the United States Council for Automotive Research set up by Chrysler, Ford, and General Motors to conduct joint, precompetitive research and development (see www.uscar.org).

- Mass Efficient Architecture for Roof Strength, (MEARS) project is the concept development of a large truck cab with no B-pillar that comprehends the increase from 1.5 to 2.5 times vehicle curb mass roof-strength criteria with weight parity.
- Comprehend manufacturing feasibility in advanced manufacturing.
- Comprehend opportunities and influence of mass compounding.

Approach

- Aggressive use of Advance High-Strength Steels (AHSS), advanced manufacturing and computer- aided topology, grade, gauge, and geometry optimization techniques.
- Comprehend secondary mass reduction of vehicle systems with empirical regression analysis of production vehicle data.
- Assemble production-intent vehicle structure and conduct crash testing.

Accomplishments

- Developed concepts for reducing sedan donor vehicle passenger compartment mass by 12% while maintaining baseline structural performance criteria, passenger requirements, and vehicle architecture.
- Developed three concepts for a truck cab with no B-pillar that satisfy Federal Motor Vehicle Safety Standard (FMVSS) 216 (3.0 times roof strength criteria) with minimal mass gains of 7.5 to 10.5 kg and $80 cost increase.
- Identified possible secondary mass reductions on the order of 1.5 times the primary mass savings in clean-sheet vehicle architectural executions due to mass compounding.

Future Direction

- Develop vehicle structure with radical architectural changes and mass compounding to achieve structural mass reductions up to 50%.

Introduction

The FGPC project will incorporate current propulsion systems and fuel-cell technologies into concept architectures. This project will reduce passenger compartment mass by 25% or greater with cost parity relative to FreedomCAR baseline while meeting the structural crash performance objectives in meeting Insurance Institute for Highway Safety (IIHS) tests and also in anticipation of future crash requirements for the FMVSS pole side- impact test and FMVSS 2.5x vehicle weight roof-strength test. Further, it will maintain performance in static and dynamic stiffness, durability and front and rear crash requirements and also comprehend passenger and component packaging constraints. The project addresses concept development and validation on a donated 5-passenger, 4-door sedan; concept development of a large truck cab with no B-pillar comprehending 2.5 times roof- strength criteria; and comprehends opportunities and influence of mass compounding.

Project Status

FGPC—Validation

This project was initiated in February 2007 using a current (OEM) production vehicle and applying the FGPC Phase 1 integrated solutions. This study will develop a new safety cage by benchmarking, developing and documenting proven integrated solutions that will balance the interaction of geometry, material, manufacturing and performance costs effectively.

The project has completed Task 1, which establishes the performance baseline for the donor vehicle and sets performance targets for the project. For Task 2, the initial investigations indicated that critical load paths identified in Phase 1 can be implemented in the donor vehicle. In addition, Task 2 shape-optimization work has been completed. Task 3 objectives were to perform design optimization of the final gauges and confirm that the final design met all performance objectives. This task has also been completed. Task 4 investigates impact of mass on vehicle performance in the side pole test. A study to investigate the sensitivity of seat alignment with the new cross-car load path and its impact on the side crash performance is currently underway. Also in progress is an investigation of the potential for additional mass savings with continuous joining methods such as laser welding and weld/bonding. Task 5 will establish a cost analysis against the baseline design. Task 6 will complete the engineering report and technology transfer of the findings.

Mass Efficient Architecture for Roof Strength (MEARS)

Passenger compartment concepts for large vehicles [trucks and sport utility vehicles (SUVs)], where the structure is driven by 2.5 times vehicle curb mass roof-strength criteria, were completed in 2007. The project focused on developing three different concepts: stamping-intensive (termed Concept 1), hydroforming-intensive (termed Concept 2), and stamped with composite structural inserts (termed Concept 3). All three concepts used AHSS steels.

Extensive optimization was carried out for each concept using HEEDS (optimization software tool).

In the stamping intensive design (Concept 1), structural changes including panel geometry, part thickness, and material grades were proposed. The major reinforcements in A-pillar, roof rail and C-pillar were proposed to be made from hot-stamped Boron steel. The inner parts of these sections were proposed to be of DP600 and DP800 steels. The body side outer material was not changed, but its thickness was increased. The most mass efficient design from several concepts was optimized as a final design for Concept 1.

In the hydroform-intensive design (Concept 2), the reinforcements in the A-Pillar, roof rail and C-Pillar were replaced with hydroform tubes made from DP780. Tubes were also investigated for the roof header and roof bow. A total of four concepts were proposed with different tube configurations, with the most mass-efficient design being optimized to obtain the final design for Concept 2.

In the stamped configuration with composite structural inserts (Concept 3), the thickness of major load-carrying members was reduced in the baseline model while materials were up-graded to AHSS to make the structure lighter and to take advantage of the stiffness provided by the lighter inserts. A total of four concepts was proposed with different types of inserts (i.e., steel-concepts 3A and 3B, Nylon-Concept 3B, and Beta foam-Concept 3C). Optimization was not carried out for these basic concept levels.

A comparative study of all concepts was done from the perspective of mass, cost, manufacturability, and reparability. The concept with the nylon inserts was selected as the final design. Further studies were carried out on the design to optimize the size of nylon inserts and the design of the sheet- metal parts. Formability studies were carried out on the major structural parts to ensure that there were no major issues.

Phase 2 has been approved and will focus on improving the modeling of the nylon inserts, adhesive materials, and validating the predictions with physical testing to validate the performance of the models.

Mass Compounding

Vehicle design engineers intuitively know that an unplanned mass increase in a component during vehicle design has a ripple effect throughout the vehicle; other components need to be resized increasing vehicle mass even more. The phrase *mass begets mass* describes this phenomenon. A more-encouraging view of this behavior considers a reduction in the mass of a component enabled by a new technology resulting in a greater mass reduction ripple effect throughout the vehicle. Published data on this effect are sparse and based on 1975-1981 model years. The purpose of the project was to update the data using contemporary vehicles.

The secondary mass change is the additional mass reduction resulting from primary mass reduction by the implementation of mass-reduction technology. When all subsystems can be resized, the secondary mass savings is from 0.8 to 1.5 kg/kg (1.25 kg/kg is the estimate for the *all* vehicle group). When the powertrain has been fixed and is not available for resizing, the secondary mass savings is from 0.4 to 0.5 kg/kg (0.5 kg/kg is the estimate for the all vehicle group).

The initial study is complete for D-segment sedans and SUV vehicles with the deliverable being a report and a calculator for estimating secondary mass savings.

The Project is currently extending the vehicle segments to include B and C class vehicles and is still in progress.

Conclusions

FGPC—Validation

The 2004 production donor vehicle baseline structure had aggressively used AHSS and was shown to be 6% lighter than a typical comparable 2004 vehicle. The final optimized design demonstrated a 39.8 kg mass reduction from the baseline, as summarized in Figure 1. This represents a 15% mass savings for the parts modified and a 12% mass savings for the full passenger compartment as compared to the baseline design, while meeting all structural performance objectives. The concept design is constrained by maintaining the existing architecture of the donor vehicle. The results were achieved by using more AHSS grades (thus increasing the average strength level of the vehicle structure), improving structural load paths (such as a cross car load path through the seat structure), and conducting shape optimization of the major structural components.

Additional findings will be made available with the completion of Tasks 4, 5 and 6.

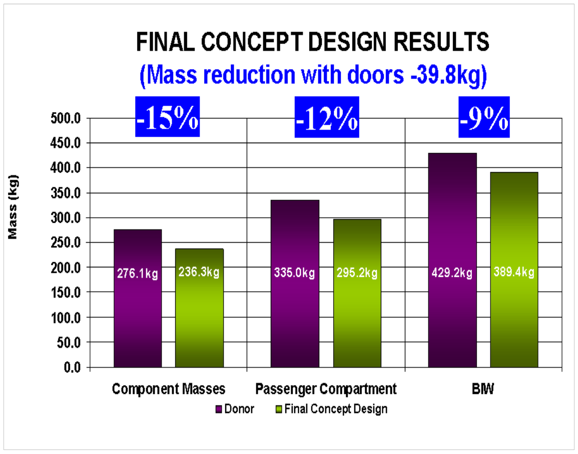

Figure 1. Final concept design results.

MEARS

The baseline design of the donor vehicle (large truck cab with no B-pillar) roof strength performance was improved from 1.5 times vehicle curb mass to 3.0 times vehicle curb mass with design optimization. Several concept design solutions were investigated and evaluated for mass, cost, manufacturability and reparability as shown in Table 1.

Table 1. Summary of concept design solutions.

S.No	Concept	Load Factor	Mass [kgs]	Cost	Rating				Weighted Rating
					Mass	Cost	Manufac turability	Repair	
	Weight Factor ------------------------->				4	3	2	1	
1	Stamping Intensive	3.06	17.6	$108	1	1	4	3	18
2	Hydroform intensive	3.00	10.5	$79	4	3	3	3	34
3 A1	Steel Inserts-Tube in C-Pillar	3.00	14.9	$79	2	3	3	4	27
3 A2	Steel Inserts-Stamped C-Pillar Rnf	3.06	13.8	$67	3	5	4	4	39
3. B	Nylon Inserts (Drop-in)	3.06	7.5	$80	5	3	4	2	39
3. C	BetaFoam (Injected)	2.95-3.82*	8.4	$78	5	3	2	2	35

Design 3B provides a 7.5 kg mass increase and $80 cost increase relative to the baseline donor vehicle design. The results were obtained with use of AHSS and hot-stamped boron steel, advance design optimization and use of nylon inserts to improve section stability.

Mass Compounding

When all subsystems can be resized, the secondary mass savings is from 0.8 to 1.5 kg/kg (1.25 kg/kg is the estimate for the *all* vehicle group). When the powertrain has been fixed and is not available for resizing, the secondary mass savings is from 0.4 to 0.5 kg/kg (0.5 kg/kg is the estimate for the all vehicle group).

The study indicates that optimized steel structure can meet the FreedomCAR mass reduction targets when mass compounding is considered. Realizing this objective requires additional technology development and is challenged by mass increases resulting from increased safety requirements, alternative powertrains and additional passenger amenities.

Presentations/Publications/Patents

There are no patents or publications associated with this project.

FGPC—Validation

This project is still being completed and final results being documented. No results have been formally communicated to date.

MEARS

This project is still being completed and final results being documented. No results have been formally communicated to date.

Mass Compounding

Phase 1 results of the study have been presented to engineers at automotive companies and steel partnerships and the USAMP Steering Committee and Multi-Material Vehicle Task Force.

Phase 2 of project is still being completed and final results are being documented. No results have been formally communicated to date.

H. Lightweight Rear Chassis Structure (A/SP601*)

Project Manager: Jim Cran
Auto/Steel Partnership
2000 Town Center, Suite 320
Southfield, MI 48075
(905) 385-8276; fax: (905) 383-3200; e-mail: jim.cran@sympatico.ca

Co-Chair: Jamal Alghanem, PhD
Chrysler LLC
800 Chrysler Drive—CIMS 484-01-09
Auburn Hills, MI 48326
(248) 576-0849; fax: (248) 576-2197; e-mail: ga5@chrysler.com

Co-Chair: Michael Gulas
ArcelorMittal USA
P.O. Box 2460
1330 Burlington St. E.
Hamilton, ON, Canada L8N 3J5
(905) 548-4719; fax: (905) 548-4250; e-mail: michael_gulas@arcelormittal.com

Technology Area Development Manager: Joseph A. Carpenter
(202) 586-1022; fax: (202) 586-1600; e-mail: joseph.carpenter@ee.doe.gov

Field Project Officer: Aaron D. Yocum
(304) 285-4852; fax: (304) 285-4403; email: aaron.yocum@netl.doe.gov

Contractor: United States Automotive Materials Partnership (USAMP)
Contract No.: DE-FC05-02OR22910 through the National Energy Technology Laboratory

Objectives

- Obtain a minimum mass reduction of 25% for a baseline passenger car rear chassis structure with no more than a 9% cost premium.
- Develop and document integrated solutions that balance the interaction of materials, manufacturing, and cost. The solutions will focus on high-volume production (200,000 plus vehicles per year).
- Demonstrate the successful use of advanced high-strength steel (AHSS) in a passenger car rear chassis structure.
- Address corrosion and durability issues associated with reduced-thickness AHSS.

Approach

- Phase 1: Material optimization. Through material substitution and minimal size and shape changes, the mass of the baseline chassis was reduced 15% noting limited reduction in stiffness. Prototypes have been fabricated and physically tested. The lessons learned are being used in Phase 2. Phase 1 completion is scheduled for February 2009.

---

*Denotes Project 601 of the Auto/Steel Partnership (A/SP), the automotive-focus arm of the American Iron and Steel Institute (AISI) (see www.a-sp.org). The A/SP cofunds projects with DOE through a cooperative agreement between DOE and the United States Automotive Materials Partnership, one of the formal consortia of the United States Council for Automotive Research set up by Chrysler, Ford, and General Motors to conduct joint, precompetitive research and development (see www.uscar.org).

- Phase 2: Design optimization. Through a clean-sheet redesign, the primary goal is to obtain a minimum mass reduction of 25% with no reduction in stiffness. A secondary goal is to obtain no more than a 9% cost premium. However, the cost goal may be relaxed to achieve mass reduction provided the design remains competitive in cost with any aluminum alternative. A Phase 2 final design has been prepared, and manufacturing feasibility and a cost analysis are underway. Phase 2 completion is scheduled for February 2009.
- Phase 3: Communications. The goal is to transfer the technology developed in the project to original equipment manufacturer (OEM) and Tier 1 chassis structure designers. Phase 3 completion is scheduled for April to June 2009.

Accomplishments

- Verified a fatigue methodology for validating the durability of the Phase 2 final design.
- Established a Phase 2 final design, which offers a 27% mass reduction.
- Completed a one-step forming analysis for all parts in the Phase 2 final design.
- Prepared a preliminary cost analysis for the Phase 2 final design.
- Determined the mass-compounding effect for a rear chassis associated with a 20% lighter vehicle.

Future Direction

- Conduct an incremental forming analysis for three parts in the Phase 2 final design.
- If required for manufacturing feasibility, modify the Phase 2 final design.
- Finalize the cost analysis for the final design.
- Evaluate the results from the 100 trailer test corrosion cycles.
- Prepare Final Reports for Phases 1 and 2.
- Transfer the technology through road shows to Auto/Steel Partnership (A/SP) member companies and key Tier 1 suppliers.

Introduction/Overview

Phase 1 is almost completed. Four of the five technology gaps have been addressed (AHSS Availability, AHSS Forming, AHSS Welding and Fatigue Resistance). Work on the remaining gap (Corrosion Resistance) will be completed by February 28, 2009.

By mutual agreement, due to changing the timing and scope of the project, Martinrea ceased contract work after completing the Phase 2 Preliminary Design in September of 2007. However, Martinrea graciously continued to support the project through in-kind work until December 2007. At that time, the team set a new direction, which meant that a Request for Quote (RFQ) was required to take the Phase 2 preliminary design to a Phase 2 final design. The new direction included a new baseline, the elimination of Phase 2 prototypes, and the addition of a fatigue analysis on the final design, a mass-compounding exercise and an extended project completion date.

In February 2008, Altair was awarded a contract to complete Phase 2 and conduct Phase 3. Altair reviewed the Martinrea Phase 2 Preliminary Design using the loads and stiffnesses associated with the new baseline (Figures 1 and 2). Altair concluded the preliminary design was solid. Optimization work led to a Phase 2 final design that is 27% lighter than the new baseline. However, modifications required to overcome

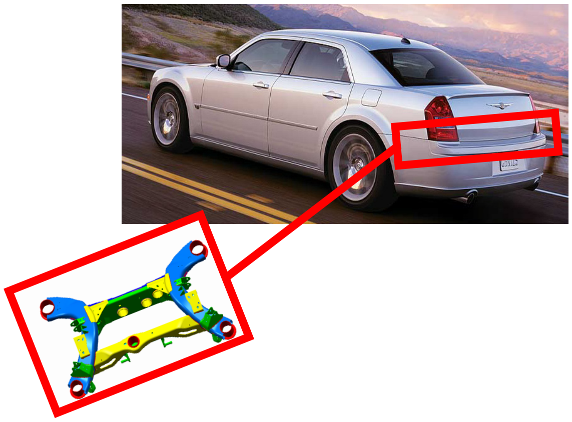

Figure 1. Donor vehicle and new baseline structure.

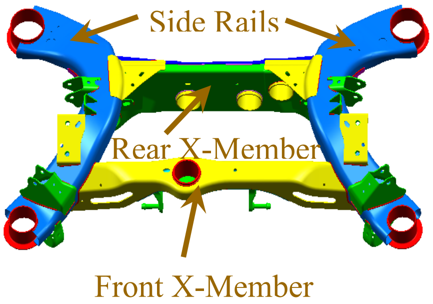
Side Rails
Rear X-Member
Front X-Member

Figure 2. Baseline structure detail.

stamping issues associated with three parts might reduce this mass saving.

Phase 1: Material Optimization

Ten prototypes were fabricated using DP590 and TRIP780 steels. The last two prototypes built (9 and 10) have a mass of 21.74 kg compared to the 25.81 kg mass of the baseline. Thus, a mass reduction of 15% was achieved. However, it should be noted that the prototype design was a material substitution exercise. Thus, the prototypes have a limited reduction in stiffness compared to the baseline. Computer-aided design (CAD) and finite-element analysis (FEA) models of the as-built prototypes were constructed.

The prototypes were allocated as follows: two for show pieces (Figure 3), one for modal testing (Figure 4), three for bracket fatigue testing (Figure 5), two for corrosion testing (Figure 6) and two (9 and 10 with gusset plates) for subsystem fatigue testing (Figure 7).

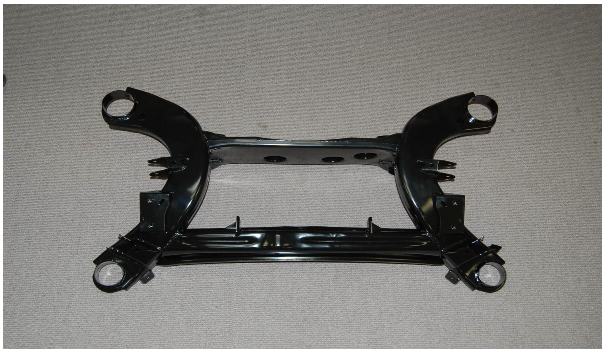

Figure 3. Phase 1 prototypes 1–8 without gusset plates.

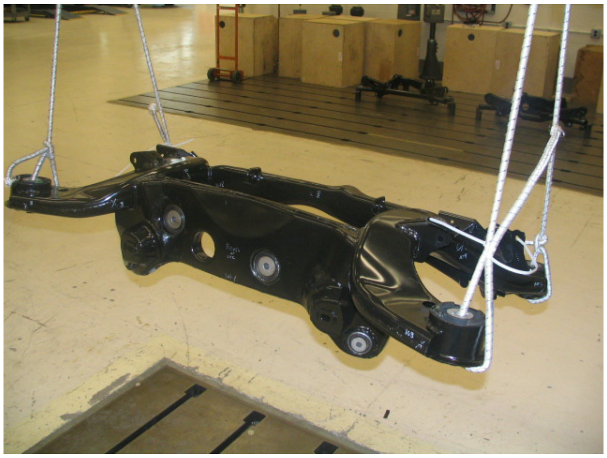

Figure 4. Modal test.

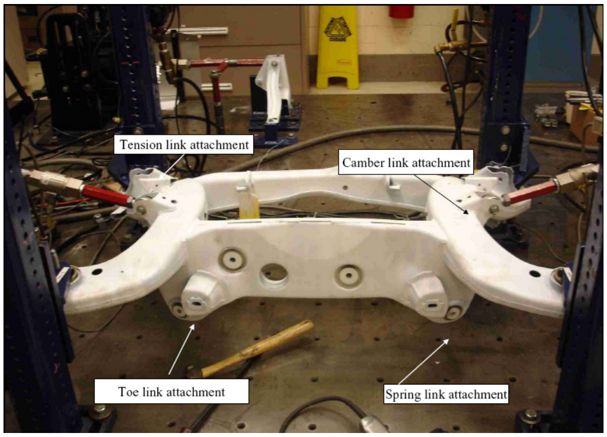
Tension link attachment
Camber link attachment
Toe link attachment
Spring link attachment

Figure 5. Bracket fatigue test.

Phase 1 completion is scheduled for February 2009.

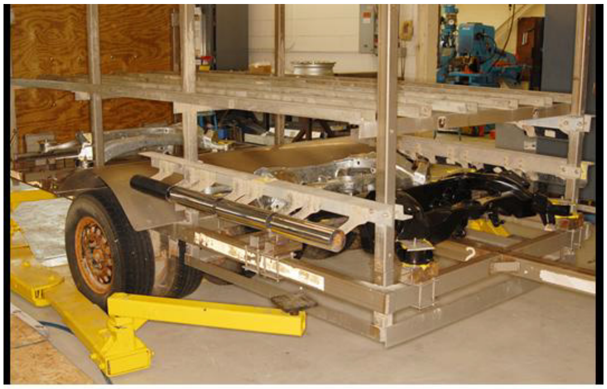

Figure 6. Corrosion trailer test.

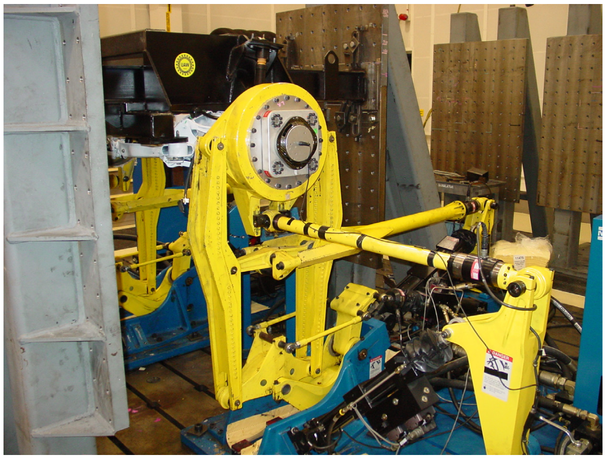

Figure 7. Subsystem fatigue test.

Phase 1 Technology Gap Analysis

Availability of AHSS

The team believes that the lack of a table showing the global availability of AHSS is hindering the use of AHSS for mass reduction in chassis structures. The team pursued the development of a global table but discovered that the steel producers, for commercial reasons, do not want the availability of their AHSS in the public domain. Thus, the team has reluctantly agreed that it is unable to address this technology gap.

Forming of AHSS

As discussed in the FY 2007 Annual Report, the team has concluded that commercially-available AHSS grades may be formed into satisfactory chassis structure parts. However, for dual phase steels, strain kicks off strain hardening even at room temperature. Thus, as much work as possible should be done during the first draw. Also, stampings need to be processed immediately from stage to stage.

Welding of AHSS

Heat-Affected Zone (HAZ) softening, which depends on steel chemistry, is more pronounced in higher strength steels. This softening reduces joint efficiency and must be taken into account when designing a chassis structure.

To address the softening issue, the team collaborated with A/SP's Joining Team (see report 5.A) to develop a Gas Metal Arc Welding *(GMAW) Weld Design Guideline for Chassis Structures*. The Joining Team finalized the Guideline in December 2007. It covers both conventional and AHSS steels.

Oak Ridge National Laboratory (ORNL) is developing a model to predict the effects of welding on AHSS microstructure. The model predicts softening in the HAZ. The Chassis Team is interacting with ORNL to ensure a simplified model. That is, a model suitable for inclusion into automotive FEA.

Corrosion Resistance

Downgaging with AHSS means thinner steel. In chassis structures, the thickness of the steel is used as the second line of defense against corrosion. Thus, there is a concern that thinner steel may cause corrosion problems.

The team's Corrosion Working Group has concluded that the performance of E-Coat over parts made from galvanized steel is a known technology for chassis applications. Hence, it can be used to protect thin AHSS chassis structure members (thickness less than 2.0 mm). However, the Group feels it is desirable to have an alternate corrosion protection method. Thus, it is evaluating the Electropoli hot-dip galvanizing method used in Europe to coat chassis structures after fabrication. Two baseline rear chassis structures and two Phase 1 prototypes have been coated with Electropoli in France. One baseline structure with E-coat, one baseline structure with Electropoli and one Phase 1 prototype with Electropoli were sectioned by Ford to evaluate coating coverage. The baseline structure with both E-coat and Electropoli had good coating coverage inside and out. However, the Phase 1 prototype with Electropoli had no coating on the inside corners. Insufficient holes to ensure good coverage or weld flux might be the reason.

One baseline structure with E-coat, one baseline structure with Electropoli and one Phase 1 prototype with Electropoli were subjected to 100 cycles of the General Motors corrosion trailer test. This test is an indicator of long term exterior cosmetic corrosion. It is also an indicator of interior/crevice corrosion; but, interior/crevice corrosion is accelerated to a much lower degree than exterior cosmetic corrosion.

Examination of the three chassis structures, sectioned after 100 cycles, showed that Electropoli offers more protection than E-coat. Pit depth measurements are being taken in order to establish the benefits of Electropoli.

Fatigue Resistance

Durability is a major criterion in chassis design. AHSS brings not only mass reduction but higher stresses, which may reduce fatigue resistance if not properly accommodated.

The team has addressed the fatigue issue with the A/SP Sheet Steel Fatigue Team (see report 5.C). There is ample evidence that the fatigue strength of sheet steel is proportional to tensile strength. Thus, even though design stresses are higher in AHSS, the higher tensile strength of AHSS results in higher fatigue strength. The end result is the fatigue strength of AHSS material is not an issue. There is little data on the fatigue strength of metal inert gas (MIG) welded joints made with AHSS. However, fatigue experts agree that the fatigue strength of all MIG welded joints depends on weld process and joint geometry. That is, the fatigue strength of MIG welded sheet steel joints is independent of steel grade. To verify this conclusion, the A/SP Fatigue Team has launched a test program using DP590, DP780, DP1000, and TRIP780 AHSS joined by MIG and laser welds. The program should be completed in 2009.

The team wished to develop an appropriate analytical method to evaluate the fatigue resistance of chassis structures and the Phase 2 final design. To this end, Altair evaluated the use of finite element (FE)-safe software with the Verity module and the use of FE-safe software with the British Standard (BS) 5400 module. Analytical results using these two methods were compared to the results from bracket fatigue tests on Phase 1 prototypes. Both methods predicted the fatigue crack locations. However, the Verity module gave a better prediction of fatigue life. The BS 5400 module, due to a built-in safety factor, gave an overly conservative fatigue life.

Analytical results using FE-safe and the Verity module were compared to results from subsystem fatigue testing conducted on Phase 1 prototype 9. The first crack in the analysis appeared at 1.9 lives compared to 1.4 lives in the test. There was no catastrophic failure in either the analysis or the test. For these reasons, the team concluded that the FE-safe and the Verity module may be used to validate the durability of the Phase 2 final design.

Phase 2: Design Optimization

Martinrea prepared a Phase 2 preliminary design in FY 2006, which had a 12% mass reduction compared to the new baseline. However, in order to properly incorporate the lessons learned from Phase 1 into Phase 2, work on Phase 2 was put on hold until February 2008. At that time, Altair commenced work to finalize the preliminary design. Its first activity was to evaluate the preliminary design using the loads associated with the new baseline. The preliminary design is superior to the baseline from the maximum stress point of view. Further, it has a stiffer response than the baseline for virtually all of the load cases. The team concluded it was not necessary to match the baseline stiffness in all directions. The team identified the stiffnesses to be matched. Also, the team decided that the lesser of a 10x bushing rate and the actual baseline bushing rate should be used in the redesign.

Altair explored numerous alternatives in order to increase the 12% mass reduction of the Phase 2 preliminary design. In fact, over 20 gage optimizations were prepared in order to evaluate material selection, the use of patches and the use of tailored blanks. The team detected that an inefficient bracket was adding unnecessary mass to the chassis structure. Altair optimized this bracket. The end result of all this activity is the Phase 2 final design (Figures 8 and 9). The mass of the Phase 2 final design is 18.83 kg compared to 25.81 kg for the baseline. Thus, a mass reduction of 27% was achieved while meeting all stress and stiffness targets. Using the correlated fatigue methodology (see *Phase 1 Technology Gap Analysis—Fatigue Resistance*), Altair compared the fatigue resistance of the Phase 2 final design to the fatigue resistance of the new baseline chassis structure. The fatigue life of the Phase 2 final design is as good as or better than the fatigue life of the baseline.

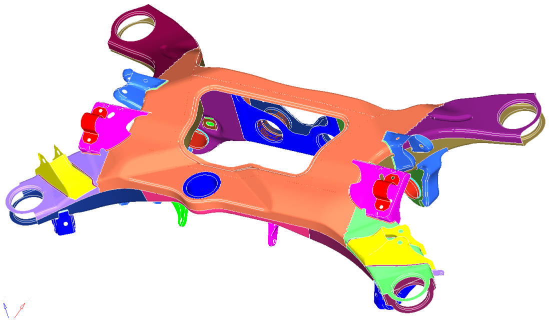

Figure 8. Phase 2 final design.

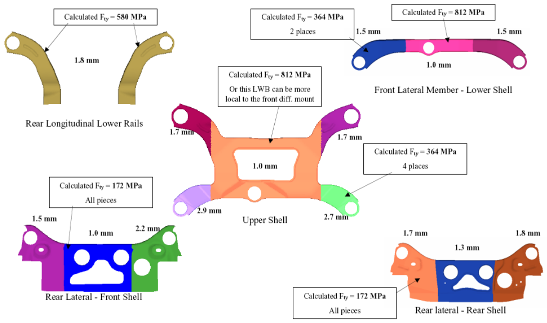
Calculated F_{ty} = 580 MPa
1.8 mm
Rear Longitudinal Lower Rails
Calculated F_{ty} = 364 MPa
2 places
Calculated F_{ty} = 812 MPa
1.5 mm
1.5 mm
1.0 mm
Front Lateral Member - Lower Shell
Calculated F_{ty} = 812 MPa
Or this LWB can be more local to the front diff. mount
1.7 mm
1.7 mm
1.0 mm
Calculated F_{ty} = 364 MPa
4 places
2.9 mm
Upper Shell
2.7 mm
Calculated F_{ty} = 172 MPa
All pieces
1.5 mm
1.0 mm
2.2 mm
Rear Lateral - Front Shell
1.7 mm
1.3 mm
1.8 mm
Calculated F_{ty} = 172 MPa
All pieces
Rear lateral - Rear Shell

Figure 9. Exploded view of Phase 2 final design.

A one-step forming analysis was used to check the manufacturability of all parts in the Phase 2 final design. It disclosed that there are forming issues with three of the parts. The team has agreed to extend the Altair contract to allow Altair to conduct an incremental forming analysis for the three parts. If necessary, the Phase 2 design will be modified to overcome the stamping issues associated with the three parts. Any modifications might reduce the 27% mass saving associated with the present Phase 2 final design.

The Massachusetts Institute of Technology (MIT) Cost Model has been used to establish a greenfield site cost for the baseline chassis structure and the Phase 2 final design chassis structure. The costs will be finalized after the stamping issues associated with the three parts are resolved.

Phase 2 completion is scheduled for February 2009.

Mass Compounding

To determine the mass compounding effect for a rear chassis structure, the Phase 2 design was modified through gage optimization to suit a vehicle, similar in size to the baseline, but having a 20% lower gross vehicle weight. The team assumed that a 20% reduction in gross vehicle weight results in 20% lower stiffness targets. Thus, the gage optimization was conducted using 20% higher deflection constraints. Stresses were not checked because the design is stiffness driven. Stresses only affect the choice of steel grades. A 20% reduction in gross vehicle weight results in an 8% mass reduction of the rear chassis structure.

Phase 3—Communications

Phase 3 communications activity is scheduled for January–March 2009.

Conclusions

The technology gaps that prevent mass reduction in chassis structures through the use of AHSS have been addressed. The team is confident that the project objectives will be accomplished and the results will facilitate the use of AHSS by chassis engineers to achieve mass reduction.

Presentations/Publications/Patents

To date, no presentations or publications have been placed into the public domain.

I. Characterization of Thermomechanical Behaviors of Advanced High-Strength Steels (AHSS): Formability, Weldability, and Performance Evaluations of AHSS Parts for Automotive Structures

Principal Investigator: Mohammad A. Khaleel
Pacific Northwest National Laboratory
P.O. Box 999, Richland, WA 99352
(509) 375-2438; fax: (509) 375-4392; e-mail: moe.khaleel@pnl.gov

Technology Area Development Manager: Joseph A. Carpenter
(202) 586-1022; fax: (202) 586-1600; e-mail: joseph.carpenter@ee.doe.gov

Field Technical Monitor: Mark T. Smith
(509) 375-4478; fax: (509) 375-4448; e-mail: mark.smith@pnl.gov

Contractor: Pacific Northwest National Laboratory
Contract No.: DE-AC06-76RL01830

Objective

- Investigate the formability of advanced high-strength steels (AHSS) with emphases on loading temperature, loading paths and secondary deformation effects on part residual strength and microstructure.
- Develop a fundamental understanding of transformation kinetics of AHSS steels by analyzing the crystallographic and morphological features of the phase transformations subject to different thermal and mechanical loading paths from forming and welding.
- Provide performance data and constitutive models for formed AHSS parts.
- Investigate the weldability of AHSS under various welding processes and parameter conditions applicable to auto-production environment.
- Generate weld performance data including static strength, formability, impact strength and fatigue life as function of welding processes and parameters.
- Investigate welding techniques for improved AHSS weld performance and benchmark the performance against the current welding practices for roll- and hydro-formed AHSS frame and underbody structure applications.
- Develop design guidelines on AHSS to assist rapid structure design and prototyping.

Approach

- Investigate formability and weldability of AHSS. This task includes forming under complex loading paths (uniaxial and biaxial); quantification of formability and weldability for various grades of AHSS based on their chemistries and corresponding thermal-mechanical process.
- Investigate the interdependency of manufacturing processes: both weldability of a formed part and formability of a welded part.
- Develop transformation kinetics model and macroscopic constitutive relationships for AHSS (dual phase [DP], transformation-induced plasticity [TRIP] and complex phase [CP]).
- Systematically evaluate the effects of various welding process and process parameters on the microstructure and weld property. Welding processes include gas metal arc, laser, hybrid laser-arc, and resistance spot. Metallurgical and process models will be used to analyze the microstructure evolution. The properties will be

measured as a function of geometry, composition, process and process parameters. A performance evaluation procedure will be developed that allows for quantifying the performance improvement, weight and cost savings associated with use of AHSS.

- Evaluate structural performance evaluation of formed and welded parts made of AHSS. This task will provide the automotive design engineers with accurate material performance data for design verification of AHSS structural parts.

Accomplishments

- Completed micromechanics-based failure analysis and stress versus strain predictions for DP800/DP980.
- Completed quantifying individual phase stress and strain partition in TRIP800 in transverse direction.
- Completed micromechanics-based failure analysis and failure mode prediction modeling for TRIP800.
- Completed examining effects of martensite mechanical properties on failure mode and ductility of DP800/DP980.
- Completed examining effects of martensite volume fraction on the failure of DP steels.
- Completed examining potential sources for shear fracture of DP steels during stamping process using microstructure-based representative volume element (RVE).
- Completed preliminary fracture toughness prediction of TRIP800 using microstructure-based RVE.
- Started preliminary studies on three grades of twinning induced plasticity (TWIP) steels and a nano-precipitate-strengthened steel (NPSS).
- Performed advanced photon source tests in an attempt to quantify the evolution of micro-twin volume fraction during deformation of TWIP steels, data analyses underway.

Future Direction

- Complete the micromechanics based cyclic and fracture toughness modeling of TRIP800.
- Complete preliminary evaluations of three TWIP steel grades with various manganese compositions.
- Complete microstructure and mechanical property characterizations of NPSS.

Introduction

This project is a collaborative effort between the Department of Energy, Pacific Northwest National Laboratory (PNNL), Oak Ridge National Laboratory and the United States (U.S.) Automotive Materials Partnership of the U.S. Council for Automotive Research. The work began in October 2005.

Because of their excellent strength and formability combinations, advanced high-strength steels (AHSS) are being used in vehicle body structures to reduce vehicle weight and improve crash performance. Currently, technical barriers hindering wider applications of AHSS in the domestic auto industry are as follows:

- The fundamental behaviors of AHSS parts subject to different thermal and mechanical loading paths (forming and welding) are not fully understood and quantified.
- The constitutive behaviors for the formed parts are not available to computer-aided engineers for rapid prototyping.
- Welding-induced complex microstructures and the effects of different welding processes and welding parameters on weld performance are not well understood.

To address these issues, PNNL's role in this project includes investigating the formability of AHSS with emphases on loading temperature, loading paths and secondary deformation effects on part residual strength and microstructure. The project also develops a fundamental understanding of transformation kinetics of AHSS steels by analyzing the crystallographic and morphological features of the phase transformations subject to different thermal and mechanical loading paths from forming. The goal is to provide the automotive design engineers with accurate material performance data and constitutive models for design evaluations and verification of AHSS structural parts.

Approach

Prediction of Failure Modes and Ductility for DP980 Using Plastic Strain Localization

Ductile failure of metals is often treated as the result of void nucleation, growth and coalescence. Throughout this study, ductile failure of dual-phase steels is predicted in the form of plastic strain localization resulting from the incompatible deformation between the harder martensite phase and the softer ferrite matrix.

Failure modes and ultimate ductility of DP980 steels are analyzed using finite element analyses (ABAQUS) based on the actual steel micro-structure. Figure 1 shows an actual micro-structure of DP980 obtained using scanning electron microscopy (SEM) and the corresponding finite-element model used for the representative volume element (RVE) in this study. For the finite element analysis, the mechanical properties of the constituent phases (ferrite and martensite) are determined by the *in-situ* synchrotron-based high energy X-ray diffraction (HEXRD) technique together with the RVE prediction for the uniaxial tension. The *in situ* experiments were performed at the 11-ID-C beamline of Advanced Photon Source (APS) at Argonne National Laboratory.

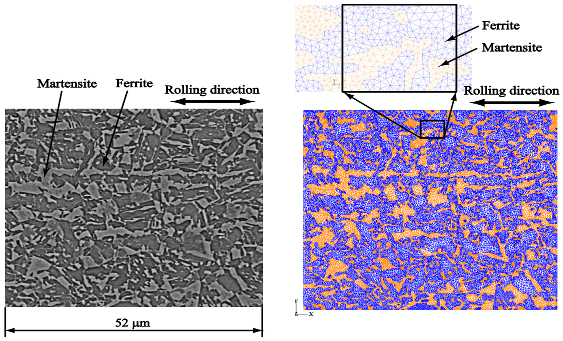

(a) **(b)**

Figure 1. (a) An actual microstructure of DP980; (b) the corresponding finite element model used for the RVE of DP980 ($V_{f,M}$=38%). ($V_{f,M}$ = *Volume* fraction of martensite).

Under different loading conditions, different failure modes and ultimate ductility are predicted in the form of plastic strain localization. It is found that the local failure mode and ultimate ductility of dual-phase steels are closely related to the stress state in the material. Under plane-stress condition with free lateral boundary (Figure 2, Region A), one dominant shear band develops and leads to final failure of the material. However, if the lateral boundary is constrained (Figure 2, Region B), splitting failure perpendicular to the loading direction is predicted with much reduced ductility. On the other hand, under plane-strain loading condition (Figure 2, Region C), commonly-observed necking phenomenon is predicted that leads to the final failure of the material. Figure 3 shows three different failure modes predicted in the RVE under the different loading conditions corresponding to the three regions shown in Figure 2. These predictions are in reasonably good agreement with experimental observations shown in Figure 4.

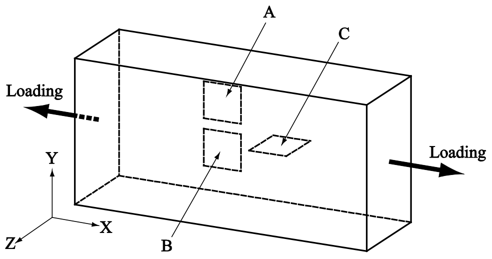

Figure 2. Three different locations of a sheet specimen under tension.

The methodology developed in this study can be used as a tool in studying the effects of the various factors on the ductile failure mechanisms of dual-phase (DP) steels.

Martensite Mechanical Property Effects on DP980 Failure Mode and Ductility

In this section, the effects of the mechanical properties of the martensite phase on the failure mode and ductility of DP980 under uniaxial tension are investigated using the microstructure-

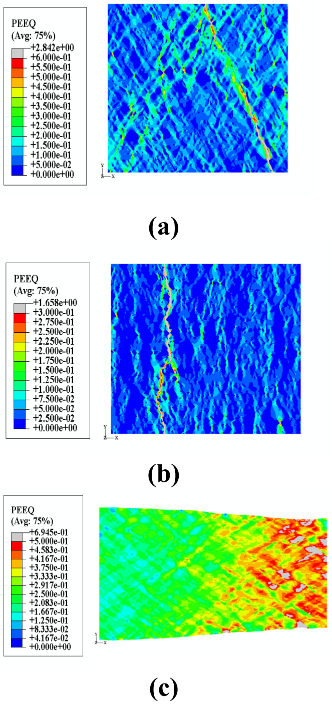
PEEQ
(Avg: 75%)
+2.842e+00
+6.000e-01
+5.500e-01
+5.000e-01
+4.500e-01
+4.000e-01
+3.500e-01
+3.000e-01
+2.500e-01
+2.000e-01
+1.500e-01
+1.000e-01
+5.000e-02
+0.000e+00
(a)
PEEQ
(Avg: 75%)
+1.658e+00
+3.000e-01
+2.750e-01
+2.500e-01
+2.250e-01
+2.000e-01
+1.750e-01
+1.500e-01
+1.250e-01
+1.000e-01
+7.500e-02
+5.000e-02
+2.500e-02
+0.000e+00
(b)
PEEQ
(Avg: 75%)
+6.945e-01
+5.000e-01
+4.583e-01
+4.167e-01
+3.750e-01
+3.333e-01
+2.917e-01
+2.500e-01
+2.083e-01
+1.667e-01
+1.250e-01
+8.333e-02
+4.167e-02
+0.000e+00
(c)

Figure 3. Different failure modes in the RVE for the three Figure 2 locations. Engineering strains for (a), (b), and (c) are 12.5%, 3.6% and 30.2%, respectively.

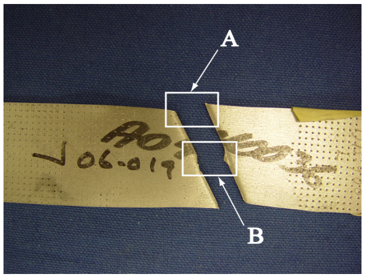

Figure 4. A failed DP980 sheet specimen.

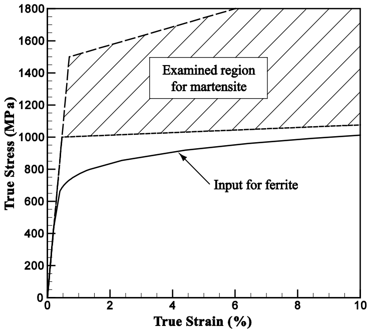

Figure 5. Examined region for the mechanical properties of the martensite phase to investigate its effects on the RVE macroscopic response.

based modeling methodology presented in the previous section. The reference mechanical properties of the constituent phases in DP980 are the same as those obtained in the previous section. Computations are then conducted on the RVE in Figure 1. Various reasonable combinations of initial yield strength ($\sigma_{y,M}$) and linear hardening rate (K_M) for the martensite phase are considered for this purpose. Figure 5 shows the input stress-strain curve for the ferrite phase and the examined region for the mechanical properties of the martensite phase in this investigation. Figure 6 shows an example of the effects of the mechanical properties of the martensite phase on the macroscopic response of the RVE. The computations show that, as the strength of the martensite phase increase, the ultimate tensile strength (UTS) of DP980 steels increases but UTS strain and failure strain decrease.

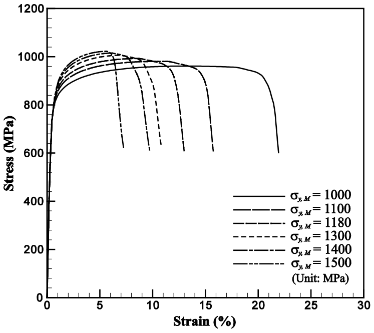

Figure 6. Effects of the initial yield strength of the martensite with K_M=1740 megapascals (MPa) on the macroscopic response of the RVE.

The computations also show that shear-dominant failure modes usually develop for DP980 with lower martensite strengths, whereas split failure modes typically develop for DP980 with higher martensite strengths. These trends are well presented in Table 1, which shows a clear diagonal band separating the shear and split modes. Figure 7 shows the predicted different failure modes in the RVE for different mechanical

Table 1. Predicted failure modes in the RVE of DP980 under tensile loading for different mechanical properties of the martensite phase. (PS=pure shear failure, SD=shear dominant failure, SSC=split and shear combined failure, S=split failure)

K_M / $\sigma_{y,M}$	800	1740	2800	3800	4800	5800
1000	PS	SD1	SD1	SD2	SD3	SSC1
1100	SD1	SD1	SD2	SD3	SSC1	SSC3
1180	SD1	SD2	SD3	SD3	SSC3	S
1300	SD2	SD3	SD3	S	S	S
1400	SD2	SD3	S	S	S	S
1500	SSC2	S	S	S	S	S

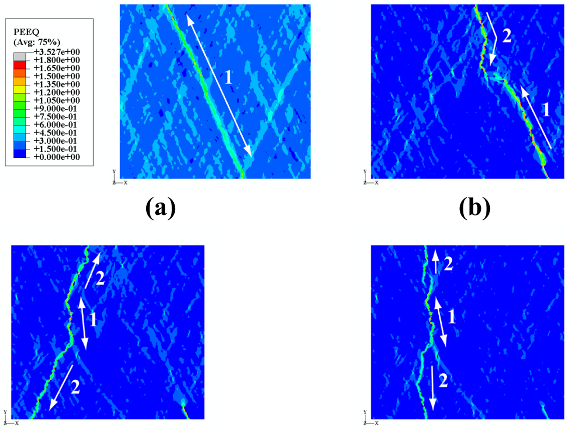

(a) (b)

(c) (d)

Figure 7. Different failure modes in the RVE depending on the mechanical properties of the martensite phase: (a) PS, (b) SD3, (c) SSC1, and (d) S.

properties of the martensite phase. The information based on these investigations can be used as a quantitative design guideline for DP steels.

Effects of Martensite Volume Fraction on Failure of DP Steels

For the DP steels with lower martensite volume fractions, ultimate failure can be dominated by the ductility of the ferrite phase through the conventional void nucleation, growth and coalescence process. There may be some range of martensite volume fraction where the failure of DP steels may depend on the inhomogeneity among the various constituent phases, rather than on the ductility of the individual constituent.

The approximate range of martensite volume fraction controlled by initial phase inhomogeneity is determined in this section. For this purpose, various micromechanics-based finite-element models are generated based on the actual microstructures of DP and TRIP steels. Figure 8 shows two examples of the various finite-element models with different martensite volume fractions, used in this investigation. The mechanical properties for the ferrite and martensite phases are the same as those determined for the DP980 in the previous section.

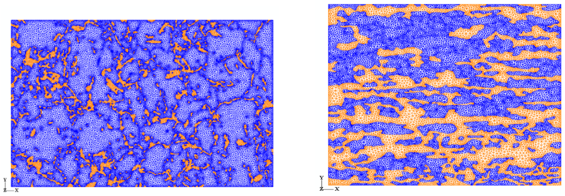

(a) (b)

Figure 8. Finite-element models based on different microstructures of DP and TRIP steels. $V_{f,M}$ percentage in the models are (a) 14 and (b) 44.

First, the influence of ductility of the constituent phases on the overall ductility of DP steels was examined. Figure 9 shows the failure strains (ultimate ductility) as function of martensite volume fraction for different input strain ranges of the ferrite phase. Similar trends are observed when varying the input strain ranges of martensite. The results in Figure 9 indicate that the phase inhomogeneity dominant region appears to be with

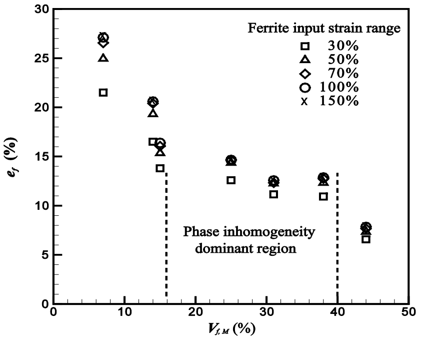

Figure 9. Ultimate ductility as function of martensite volume fraction for different input strain ranges of ferrite.

the martensite volume fraction between 15% and 40% since in this region, the failure strains of DP steels shows no dependence on the ductility of the constituent phases.

Additionally, the effects of voids on the overall ductility of single phase (SP) and DP steels were examined. Figures 10 and 11, respectively, show the engineering stress-strain curves and failure modes of selected RVEs with and without voids for the cases of SP and DP steels. Based on these figures, it seems that voids do not have noticeable influence on the failure strain and/or mode of DP steels when the martensite volume fraction in DP steels is larger than about 15%, which is similar to the effects of ductility of the constituent phases. This is also because the phase inhomogeneity becomes a dominant factor for the failure of RVE (rather than voids) in this range of martensite volume fraction. Therefore, based on actual micro-structures of DP steels, the methodology can be applied to DP steels with the martensite volume fraction within the phase inhomogeneity region in tailoring the DP steel design without serious consideration of the ductility of the constituent phases.

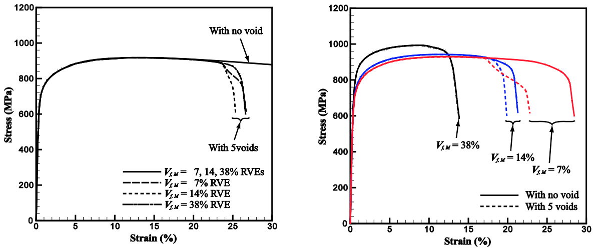

(a) (b)

Figure 10. Engineering stress-strain curves based on three different RVEs with and without voids: (a) single- and (b) dual-phase materials.

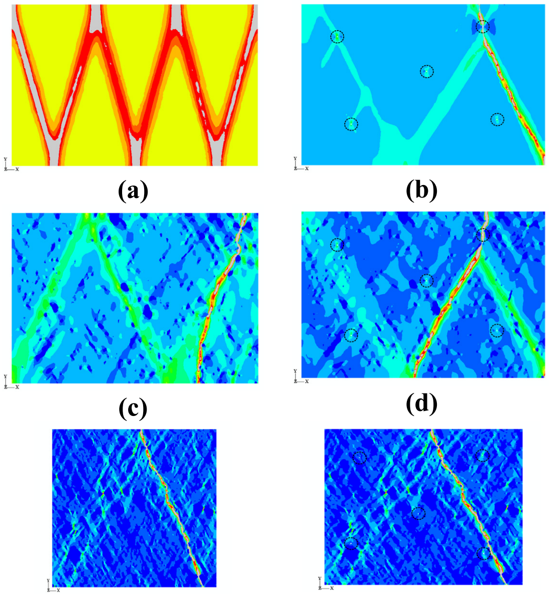

(a) (b)

(c) (d)

(e) (f)

Figure 11. Failure modes of RVEs: (a) SP w/o voids, (b) SP with 5 voids, (c) DP ($V_{f,M}$=7%) w/o voids, (d) DP ($V_{f,M}$=7%) with 5 voids, (e) DP ($V_{f,M}$=38%) w/o voids, and (f) DP ($V_{f,M}$=38%) with 5 voids. Dotted circles represent the void positions.

Simulation of Shear Fracture in Stamping Process of DP Steels

DP steels appear to exhibit shear fracture during stamping of a variety parts that are not normally experienced with conventional drawing quality steel and high-strength low-alloy (HSLA) steel. Figure 12 shows DP980 steel sheets after a stamping process. Note that the sheet in Figure 12(b) is fractured by shear. Figure 13 shows the corresponding micro-structures of the two DP980 steel sheets. Note that the DP980 in Figure 13(a) has an evenly distributed microstructure whereas that in Figure 13(b) has a banded structure.

In this section, the possibility of using the developed micromechanics models to simulate the tendency for shear fracture in DP steels and understand the fundamentals of the driving forces for the observed shear fracture during stamping

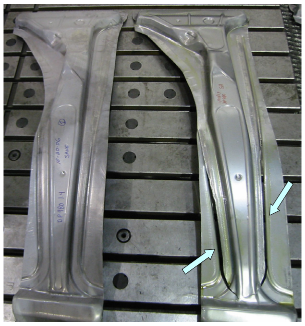

(a) (b)

Figure 12. Fractured B-pillar, made of DP 980, during stamping process: (a) Type A and (b) Type B.

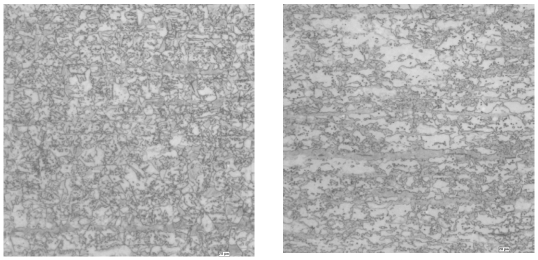

(a) (b)

Figure 13. Microstructures of (a) Type A and (b) Type B. RVE in Figure 8(b) was used, which is developed based on the actual microstructure in Figure 13(b). The input stress-strain curves for the ferrite and martensite phases are newly calibrated within the reasonable variation range from the mechanical properties of the DP980 determined in the previous sections.

was examined. For this purpose, Figure 14 shows the distributions of equivalent plastic strain under uniaxial tension based on the plane-strain elements (CPE3) at engineering-strain level of 32%. From the figure, the predicted failure mode seems to be a shear failure mode under plane-strain state. In order to simulate the shear fracture during stamping process, an indentation to the RVE was applied in addition to a tension. Figure 15 shows the distribution of equivalent plastic strain in the homogeneous material and DP980 under tension and indentation. For homogeneous material, the strain distribution shape is symmetric with respect to the center line and, therefore, a shear fracture is hard to be predicted. However, for DP980, high strain-localization area is developing from under the contact and propagating in the inclined downward direction, which may lead to a shear fracture. This is naturally due to the combined effects of contact and tension. The strain distributions shown in Figure 15(b) may explain the shear fracture which usually occurs near the corner area during stamping process as shown in Figure 12(b). This type of shear strain localization seems to be originated mainly from the microstructures and/or its uniformity in DP steels. More detailed investigation may be needed on the effect of morphology on the overall behavior and failure behavior of DP steels.

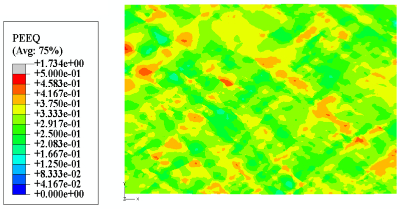

Figure 14. Distribution of equivalent plastic strain in DP 980 of type B under tension, based on the RVE in Figure 8(d).

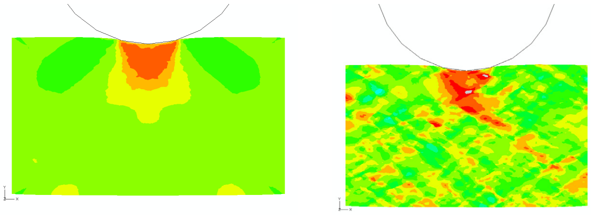

(a) (b)

Figure 15. Distribution of equivalent plastic strain under tension and indentation for (a) homogeneous material and (b) DP980 of type B.

Prediction of Failure Mode and Ductility for TRIP800 Based on Micromechanical Model with Consideration of Phase Transformation

In this section, a micromechanical finite-element model is developed based on an actual microstructure of TRIP800 steel to capture the complex deformation behavior of TRIP steels. A transformation yield function considering the stress-state effect is employed to model the martensite transformation kinetics.

Figure 16 shows an actual microstructure of TRIP800 obtained from SEM and the corresponding finite-element model used for the RVE in this study. Here, the RVE is composed of three different phases as shown in Figure 16 with the initial volume fraction of 15% of austenite. The mechanical properties of the constituent phases of TRIP800 steel and the fitting parameters describing the martensite transformation kinetics are determined using the synchrotron-based *in-situ* HEXRD experiments performed under a uniaxial tensile deformation together with the RVE prediction of the evolution of the volume fraction of austenite phase under different loading

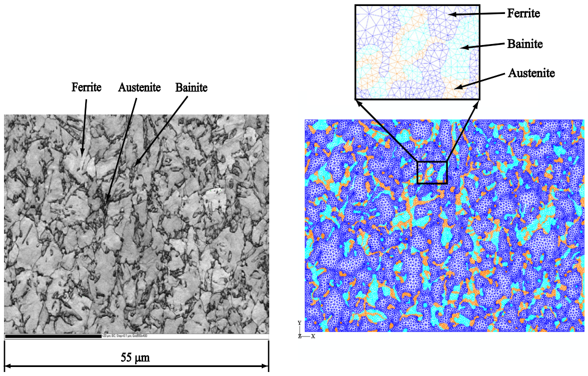

(a) **(b)**

Figure 16. (a) An actual microstructure of TRIP800 and (b) the corresponding finite element model used for the RVE.

conditions. Figure 17 compares the RVE prediction and test results for uniaxial tension based on the determined material parameters, which shows a good agreement with each other.

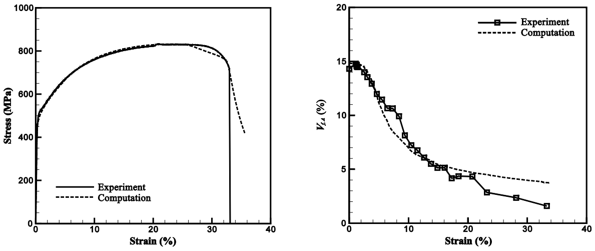

(a) **(b)**

Figure 17. Macroscopic responses of the RVE under uniaxial tension based on the fitted input stress-strain curves for the four constituent phases: (a) engineering stress-strain curves and (b) volume fractions of austenite phase as function of applied strain.

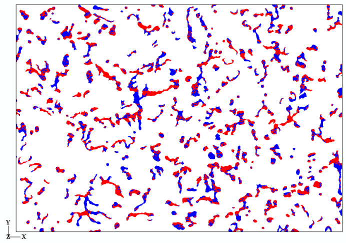

Figure 18. Martensite distribution in the RVE under uniaxial tension at strain of 10.6%. (Black: austenite; Grey: martensite; White: ferrite and bainite).

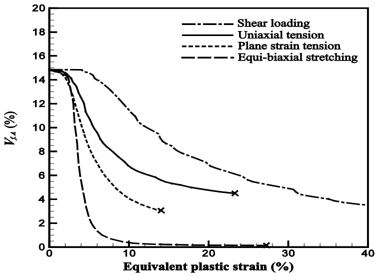

Figure 19. Volume fractions of austenite phase as functions of the macroscopic equivalent plastic strain of the RVE under different loading conditions.

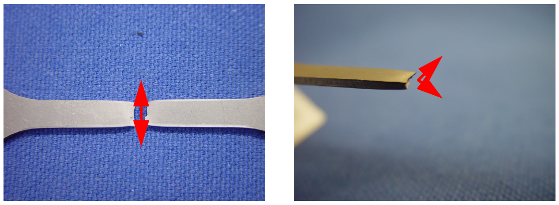

(a) **(b)**

Figure 20. A failed TRIP 800 specimen under uniaxial tension: (a) plane-stress state and (b) plane-strain state.

Figure 18 shows a martensite distribution in the RVE under uniaxial tension. The ability of the current model to predict the martensite distribution in the RVE is helpful to obtain information on the better morphology in TRIP steels under different loading conditions. Figure 19 shows the volume fractions of austenite phase as functions of the macroscopic equivalent plastic strain of the RVE under different loading conditions. This figure indicates that the phase transformation and the failure of the RVE depend on the overall stress triaxiality in the RVE, which shows the similar trends reported in other experimental researches. Figures 20 and 21 show a failed TRIP800 sheet specimen and the predicted failure modes in the RVE under plane stress and plane strain states, respectively. In Figure 21, the predicted failure under plane stress state is rather vertical failure mode whereas the predicted failure under plane strain state seems to lead to the shear failure mode, which correlates well with the experimental observations in Figure 20. The methodology adopted in this investigation may be a first step in predicting optimum processing parameters in TRIP steel productions.

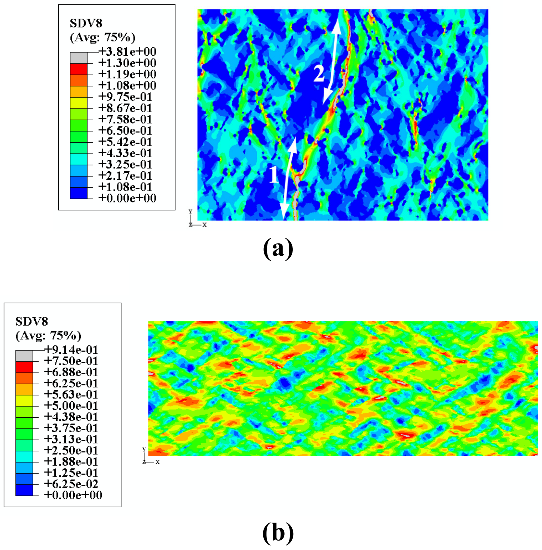

Figure 21. Different failure modes in the RVE: (a) plane-stress state and (b) plane-strain state.

Prediction of Crack Growth and Fracture Toughness of TRIP800

In this section, the fracture toughness of TRIP steels is investigated using both experiments and micromechanics-based finite-element analysis. Uniaxial tensile tests on TRIP800 notched sheet specimens were first conducted in order to determine the fracture resistance curve. The micromechanics-based finite-element model of TRIP800, shown in Figure 22, was then employed to predict the crack initiation and propagation and determine the resistance curve at the microstructure level.

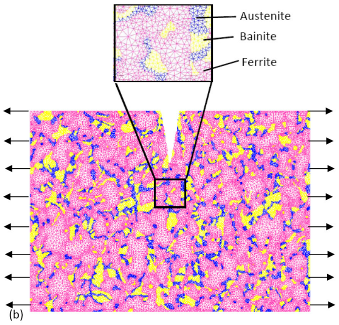

Figure 22. Finite-element model used for the RVE.

The same mechanical properties for the constituent phases and the same fitting parameters for the transformation kinetics, introduced for TRIP800 steel in the previous sections, were adopted for this simulation. A strain-based failure criterion is also adopted to model the damage and crack growth in the RVE and the levels of strain-to-failure for each phase are calibrated in order to fit the overall behavior of the RVE with the experimental data.

Figure 23 shows the comparisons of experiments and simulations for stress-strain curves and resistance curves. As shown in this figure, the predicted results based on the RVE are generally in good agreement with those of experiments despite some over-constrained boundary conditions on the RVE. Figure 24 shows the distribution of the martensite phase in the RVE under uniaxial tension at different engineering strain levels. As the crack tip advances, more area of the retained-austenite phase transforms to the martensite phase as shown in the figure. This freshly-formed martensite has high strength and thus increases the fracture resistance of TRIP steels. Figure 25 shows the predicted crack-propagation path in the microstructure. The predicted crack-propagation path is not straight, and it tends to be along the grain boundaries between ferrite-bainite and ferrite-martensite, consistent with most experimental observations for multiphase materials. Future work in this area includes the implementation of some mesh-insensitive techniques (i.e., energy-based failure criterion or strain gradient plasticity theory).

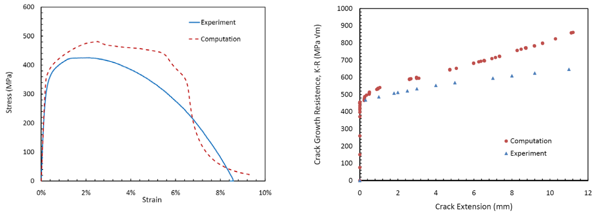

(a) (b)

Figure 23. Comparison of experiments and simulations: (a) engineering stress-strain curves and (b) resistance curves.

Preliminary Studies on Twinning-Induced Plasticity (TWIP) and Nano-precipitate Strengthened (NPSS) Steels

In this section, results based on preliminary TWIP and NPSS steel studies are discussed. The goal is

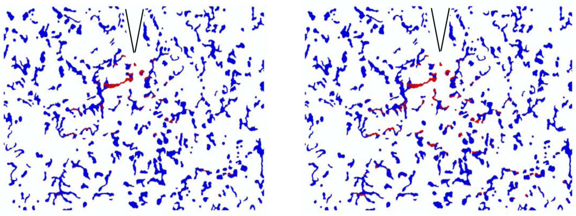

(a) (b)

Figure 24. Martensite distributions in the RVE under uniaxial tension at the strains of (a) 3% and (b) 5%. (Black: austenite; Grey: martensite; White: ferrite and bainite).

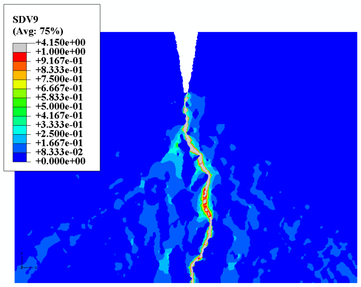

Figure 25. Predicted crack growth: distributions of equivalent plastic strain in the RVE.

to explore the possible directions for development of third-generation AHSS.

Three different grades of TWIP steels and a NPSS were covered in this preliminary investigation. Tables 2 and 3 and Figure 26 show the chemical compositions and the engineering stress-strain curves of two TWIP steels and the NPSS, respectively. Note that the Mn content in TWIP Steels B is considerably lower than 27–30%, which is typically observed in second-generation AHSS. The results in Figure 26(a) show that TWIP Steel B with lower Mn content has much higher ductility and almost equivalent UTS as TWIP Steel A with higher Mn content. These preliminary results indicate a possible direction for the development of third-generation AHSS: cost-effective low Mn TWIP steel. The examined NPSS also demonstrates good combinations of UTS and ductility due to the presence of nano-precipitates. To understand the basic attributes of these steels, various experimental approaches are still planned and underway, including the interrupted tensile test, dynamic tensile test and SEM/TEM analyses. Molecular Dynamics (MD) simulation is also considered for NPSS to get more fundamental understanding of the nanoparticles strengthening mechanisms.

Table 2. Chemical composition of two different TWIP Steels, A and B.

	C	*Mn*	*P*	*S*	*Si*	*Cr*
A	0.05	22.47	0.007	<0.001	1.90	<0.01
B	0.52	17.53	0.007	0.008	0.98	<0.01
	Ni	*Mo*	*Cu*	*Co*	*Nb*	*Ti*
A	<0.01	0.11	0.02	<0.01	0.02	0.01
B	<0.01	0.05	0.02	<0.01	0.01	0.01

Table 3. Chemical composition of NPSS.

C	Mn	P	S	Si	Cr	Ni
0.04	1.25	0.012	0.001	0.06	0.03	<0.01
Mo	Cu	Ti	V	Al	Co	Nb
0.18	0.01	0.08	0.015	0.048	0.006	0.011

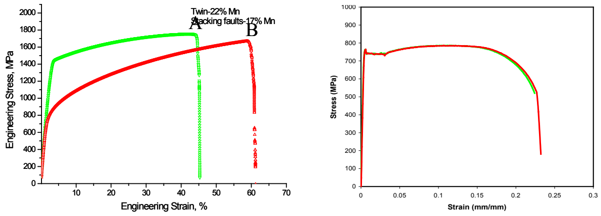

(a) (b)

Figure 26. Stress-strain curves for (a) two different TWIP steels and (b) NPSS.

Presentations/Publications/Patents

1. K. S. Choi, W. N. Liu, X. Sun, and M. A. Khaleel. 2008a. "Influence of Martensite Mechanical Properties in Failure Mode and Ductility of Dual Phase Steels." To appear in *Metallurgical and Materials Transactions A*.
2. ---. 2008b. "Micromechanics-Based Constitutive Modeling of TRIP Steel–Prediction of Ductility and Failure Modes." Submitted for publication in *Journal of the Mechanics and Physics of Solids*.
3. K. S. Choi, W. N. Liu, X. Sun, M. A. Khaleel, Y. Ren, and Y. D. Wang. 2008. "Advanced Micromechanical Model for TRIP Steels with Application of In-Situ High-Energy X-ray

Diffraction Method." *Metallurgical and Materials Transactions A* 39:3089-3096.

4. K. S. Choi, A. Soulami, W. N. Liu, X. Sun, and M. A. Khaleel. 2009. "Applicability of Micro-mechanics Model Based on Actual Micro-structure for Failure Prediction in DP Steels." SAE Technical Paper 09M-0176. To be presented in SAE 2009 World Congress, April 20–23, Detroit, MI.
5. A. Soulami, K. S. Choi, W. N. Liu, X. Sun, and M. A. Khaleel. 2009. "Characterization of the Fracture Toughness of TRIP 800 Sheet Steels Using Microstructure-Based Finite Element Analysis." SAE Technical Paper 09M-0174. To be presented in SAE 2009 World Congress, April 20–23, Detroit, MI.
6. X. Sun, K. S. Choi, W. N. Liu, and M. A. Khaleel. 2008. "Predicting failure modes and ductility of dual phase steels using plastic strain localization." *International Journal of Plasticity*, doi:10.1016/j.ijplas.2008.12.012.

J. Characterization of Thermomechanical Behavior of Advanced High-Strength Steels (AHSSs): Task 2—Weldability and Performance Evaluations of AHSS Parts for Automotive Structures

Principal Investigator: Zhili Feng
Oak Ridge National Laboratory
P. O. Box 2008, Oak Ridge, TN 37831-6095
(865) 576-3797; fax: (865) 574-4928; e-mail: fengz@ornl.gov

Participants:
Wan C. Woo, Eliot D. Specht, and Stan A. David
Oak Ridge National Laboratory
John Chiang
Ford Motor Company
Cindy Jiang
AET Integration, Inc.
Min Kuo
ArcelorMittal Steel

Technology Area Development Manager: Joseph A. Carpenter
(202) 586-1022; fax: (202) 586-1600; e-mail: joseph.carpenter@ee.doe.gov

Field Technical Monitor: C. David Warren
(865) 574-9693; fax: (865) 574-6098; e-mail: warrencd@ornl.gov

Contractor: Oak Ridge National Laboratory (ORNL)
Contract No.: DE-AC05-00OR22725

Objective

- Develop fundamental understanding and predictive capability to quantify the effects of welding and service loading on the structural performance of welded AHSS auto-body parts.
- Investigate welding techniques and practices to improve structural performance of AHSS welded auto-body components.
- Establish design guidelines and computer-aided engineering (CAE) methodology to assist rapid structure design validation and prototyping for vehicle weight reduction and safety enhancement through knowledge-based selection and use of AHSSs.

Approach

- Develop fundamental understanding of phase transformations in AHSSs during welding through thermodynamic analysis, advanced microstructure characterization, and in situ neutron and synchrotron phase transformation measurement.
- Develop integrated thermal-mechanical-metallurgical predictive models to predict the microstructure and mechanical property gradients in the weld region that potentially govern the performance of welded AHSS parts.
- Conduct comparative welding experiments on various AHSSs to develop the correlations between the joint properties, welding process conditions, and steel chemistry.

- Characterize and rank the factors controlling the weld geometry, weld microstructures, and weld joint performance.
- Investigate welding techniques for improved AHSS weld performance and benchmark them against the current welding practices.
- Generate weld performance data including static strength, impact strength, and fatigue life as a function of welding processes/parameters and steel chemistry.
- Develop design guidelines and CAE methodology for AHSSs to assist rapid structure design and prototyping.

Accomplishments

- Identified the fundamental metallurgical mechanisms causing the complex microstructure variations and the heat-affected zone (HAZ) softening phenomenon of current-generation AHSS welds.
- Developed an integrated thermal-mechanical-metallurgical welding process model capable of simulating the microstructural changes and the softening in the HAZ of AHSS welds. The initial version of the integrated model is being licensed and transferred to the auto and steel industry.
- Developed the correlation between the static structural performance and the microstructural changes of AHSS welds. A practical design parameter—joint efficiency—was introduced to quantify the effect of welding on the strength of AHSS welds.
- Revealed the influence of HAZ softening on the impact strength of AHSS joints.
- Demonstrated considerable fatigue-life improvement by refining welding conditions (within industry's acceptable welding practices).
- Developed a weld fatigue-life prediction model relating the fatigue life of a weld joint to weld geometry and local weld properties.
- Applied in situ neutron and synchrotron diffraction experiments to understand the phase changes during welding of AHSSs and the stress partitioning among different phases in transformation-induced plasticity (TRIP) steel.
- Developed close interactions with the industry including different Auto/Steel Partnership (A/SP) technical committees and the auto and steel companies to exchange research progress, to collaborate on related research projects, and to transfer and commercialize the technology developed in this project.

Future Direction

- Continue to investigate key factors controlling weld joint performance under static, fatigue, and impact loading conditions.
- Further investigate weld-joint performance under impact/crash loading conditions.
- Investigate the structural performance of AHSS weld joints under complex loading conditions (component level behavior).
- Continue to investigate welding techniques and practices to improve weld performance.
- Complete CAE analysis methodology to assist rapid design and prototyping of AHSS structures.
- Support the third generation AHSS initiative (see reports 5.K–5.T), focusing on new steel alloying and design concepts to avoid/minimize welding-induced thermal instability and microscopic deformation behavior of the new steels.

Introduction

This report describes an ORNL-Pacific Northwest National Laboratory (PNNL; see report 5.I) collaborative research project on characterization of thermomechanical behavior of AHSSs. This joint project aims at developing fundamental understanding and predictive modeling capability to quantify the effects of auto-body manufacturing processes (forming, welding, paint baking, etc.) and in-service conditions on the performance of auto-body structures made of AHSSs. ORNL's research (designated as Task 2 in this project) focuses on welding AHSSs and the influence of welding parameters on the structural performance of weld joints.

The specific relation of Task 2 to the mission of the DOE Lightweighting Materials efforts and the needs of the automotive industry for accelerated use of AHSSs for body structure lightweighting has been given in previous annual reports and will not be repeated here.

Task 2 has a technical steering committee with representatives from Chrysler, Ford, General Motors (GM), A/SP technical committees, and steel companies.

Since initiation of the project in fiscal year (FY) 2006, considerable progress has been made toward obtaining a basic understanding of microstructural changes and their influence on the structural performance (static, fatigue, and impact) of AHSS welds and potential practical welding techniques/methods to effectively use AHSSs in auto-body structures. The progress has been summarized in the previous DOE project reports, review meeting presentations, and publications and presentations [1–4]. Following are highlights of previous research findings.

- The static tensile strength of the lap-weld joint made by the gas metal arc welding process (GMAW) increases as the base-metal steel strength increases. However, the joint efficiency (the ratio of weld strength to the base-metal strength) is influenced by the HAZ softening in the AHSS weld. Ultra-AHSSs such as martensitic and boron steels have the most noticeable HAZ softening and therefore lower joint efficiency. The lower grade AHSSs without HAZ softening exhibit high joint efficiency. Nevertheless, AHSS welds typically exhibit considerably higher absolute static strength than mild-steel welds.
- The HAZ softening phenomenon is inherently associated with the thermal instability of the hardened phases (such as martensite or bainite) subjected to welding heat, the existence of the intercritical temperature range in Fe-C alloy, and the allotropic phase transformation and solution strengthening used in the current AHSS steelmaking practice.
- Microstructural changes in the weld region of AHSS welds and the degree of HAZ softening have been quantified in an integrated thermal-mechanical-metallurgical weld process model. The initial version of this model has been licensed and transferred to several industry collaborators of the project.
- The HAZ softening does not appear to be a major factor affecting the fatigue life of GMAW joints. However, AHSS welds do not exhibit improved fatigue life over the mild-steel welds. New and/or improved welding practices specific for weld fatigue-life enhancement are required to realize the potential of using AHSSs to "down-gauge" (and thus "lightweight") the steels in a vehicle.
- It is feasible to improve the weld fatigue life of AHSS by manipulating welding process conditions. It has been demonstrated that, by adjusting the welding parameters (within the process window acceptable to the auto industry), the weld geometry profile can be improved to reduce the stress concentration at the fatigue crack initiation site. This has resulted in drastic improvement of weld fatigue life, especially at the high-cycle fatigue regime.

FY 2008's research and development (R&D) efforts focused on the following major activities.

Predictive Models for Fatigue Life of AHSS GMAW Lap Joints

The predictive model for weld fatigue life of AHSSs initially developed in FY 2007 has been further extended to cover a wide range of loading conditions and grades of steels. We also improved prediction of weld fatigue life in the fatigue crack propagation part of the model. More detailed description of the fatigue-life model is given in citation [5] in the project presentations list at the end of this report.

Our fatigue prediction model uses the notch strain approach for crack initiation and the Paris law for fatigue crack propagation. The total fatigue life (N_t) consists of the crack initiation part (N_i) and the subsequent cracking propagation (to failure) part (N_p):

$$\mathrm{N_t} = \mathrm{N_i} + \mathrm{N_p} \quad . \qquad (1)$$

The notch strain approach was based on the Coffin-Manson-Morrow equation [1–3]:

$$\frac{\Delta\varepsilon}{2} = \frac{(\sigma_f' - \sigma_m)}{E}(2N_i)^b + \varepsilon_f'(2N_i)^c\,(N_i \le N_E) \quad .(2)$$

The fatigue initiation life $\mathrm{N_i}$ was solved iteratively using the solution scheme proposed by Darcis et al. [4]. The stress concentration factor used in the fatigue initiation was determined using the finite-element method.

The crack-propagation equation developed by Paris and Erdogan [5] was used to describe the relationship between the fatigue crack propagation rate, *da/dN*, and the stress intensity factor range, *ΔK*:

$$\frac{da}{dN} = C(\Delta K)^m(\Delta K_{th} << \Delta K << K_{IC}, R = 0) \quad . \qquad (3)$$

The crack-propagation life, N_p, is obtained by integration of Eq. (3) with crack-depth-dependent *ΔK* values calculated by finite-element method over the entire crack-propagation range:

$$N_p = \int_{a_i}^{a_f} \frac{da}{C(\Delta K)^m} \quad . \qquad (4)$$

The model developed in this project relates the weld fatigue life to the three major governing factors: (1) the stress state, including the weld residual stress; (2) the local stress concentration due to weld geometry and discontinuity; and (3) the local material strength, which is a function of the microstructure in the weld region. Therefore, our fatigue-life prediction model is capable of including the experimentally observed effect of weld geometry and the local microstructure and material strength gradients of the weld region on the fatigue life of welded joints.

The fatigue crack life prediction model has been evaluated against the experimental testing data for nine steels and two different weld geometries. The comparison and evaluation are summarized in Figure 1 for three different characteristic loading regimes (low-stress, high-cycle; medium-stress, medium-cycle; and high-stress, low-cycle) of nine steels.

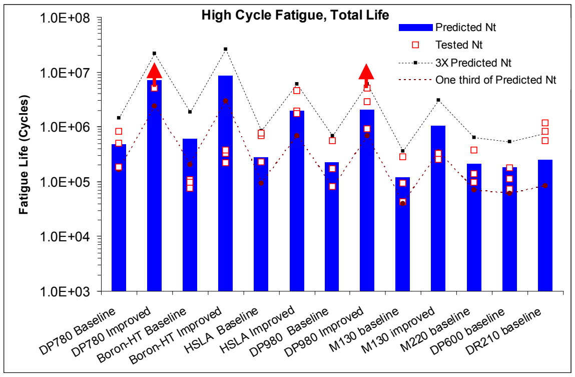

(a) low-stress, high-cycle fatigue

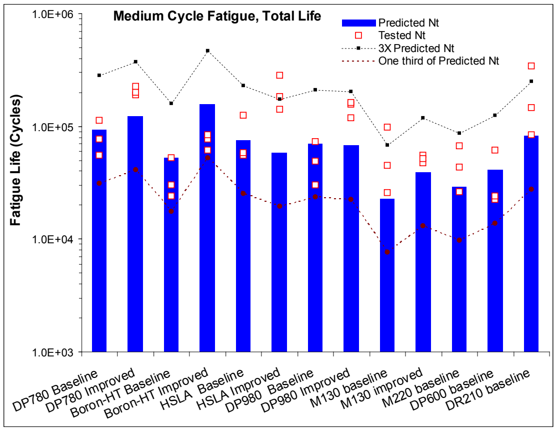

(b) medium-stress, medium-cycle fatigue

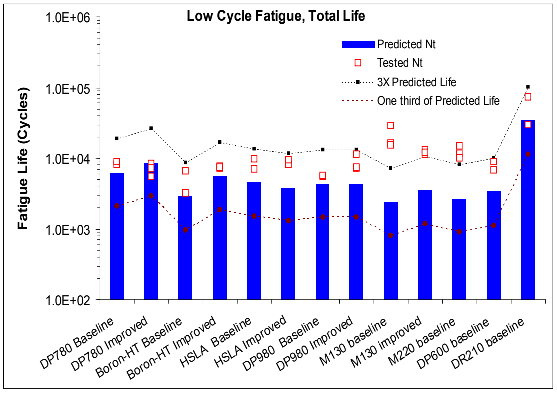

(c) high-stress, low-cycle fatigue

Figure 1. Comparison between predicted total fatigue lives and the experimental results for GMAW lap joints [Arrow in (a) represents test runout].

Overall, the model reasonably predicts the experimentally observed influences of steel grade (local mechanical property in the weld and HAZ) and the weld geometry for the steel grades investigated. With a few exceptions (e.g., hardened boron steel under high-cycle fatigue), the experimental data fall within a narrow band bounded by the 3× and 1/3× lines of the predicted data in the figure. The discrepancies between the model prediction and the testing results are on the same order as the scatter of the testing data. The few exceptions where the discrepancies are significant appeared to be related to the dramatic material property change in the weld region in boron steel. Further improvement in the prediction model is being developed.

Impact Testing of AHSS Weld Joints

Preliminary impact tensile testing was conducted in FY 2008 to investigate the effects of weld microstructure changes on the tensile strength of AHSS welds under loading rates relevant to auto-body crash conditions. The tests were performed using ORNL’s hydraulic high-strain-rate test machine. A high-speed camera was used to record the dynamic deformation and failure processes during the test. Strain gages were attached on selected specimens to record the dynamic load changes during high-strain-rate testing.

Three types of steel (DP 780, hardened boron steel, and DP 210) were tested under three loading rates (5, 15, 25 mph). A lap-shear tensile coupon with reduced cross section was used (Figure 2). DR 210, a mild steel with nominal static tensile strength of 350 MPa, did not exhibit noticeable HAZ softening. It was used for reference in the remaining tests. For both AHSSs (DP 780 and boron steel), all specimens failed in the softened HAZ region under all loading rates. On the other hand, all DR 210 welds failed in the base-metal region of the specimen, as shown in Figure 3.

Our preliminary study indicated that, similar to the behavior observed during static testing, the impact strength of AHSS welds is generally higher than that of mild steels. However, the HAZ softening phenomenon will play an important role in determining the level of strength reduction (compared to the base metal strength) of AHSS welds.

In-depth study of the impact behavior of AHSS welds is planned in FY 2009.

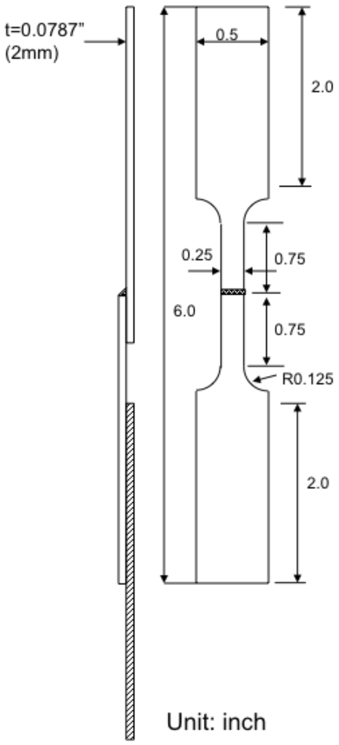

Figure 2. Dimensions of lap-shear tensile specimen used in impact testing of GMAW joint.

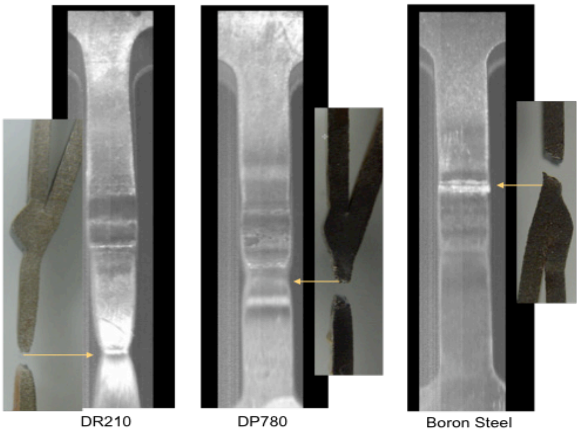

Figure 3. Failure location of GMAW joints during impact tensile testing. The effect of HAZ softening on localized deformation failure is evident in both DP 780 and boron steel.

In Situ Phase-Transformation Study Using High-Energy X-Ray Synchrotron Source

The high-energy X-ray synchrotron source at the Advanced Photon Source of Argonne National Laboratory was used to study the kinetics of phase transformations of current generation AHSSs under the rapid heating and cooling conditions associated with welding. Four types of steels were included in the study. They were boron steel, DP 980, TRIP 700, and DR 210.

A miniature electric-resistance-heating device built specifically for this study was used to provide Joule heating to the steel sample during the in situ experiment. The heating rate was closed-loop controlled during the experiment. The experimental principles and setup are shown in Figure 4.

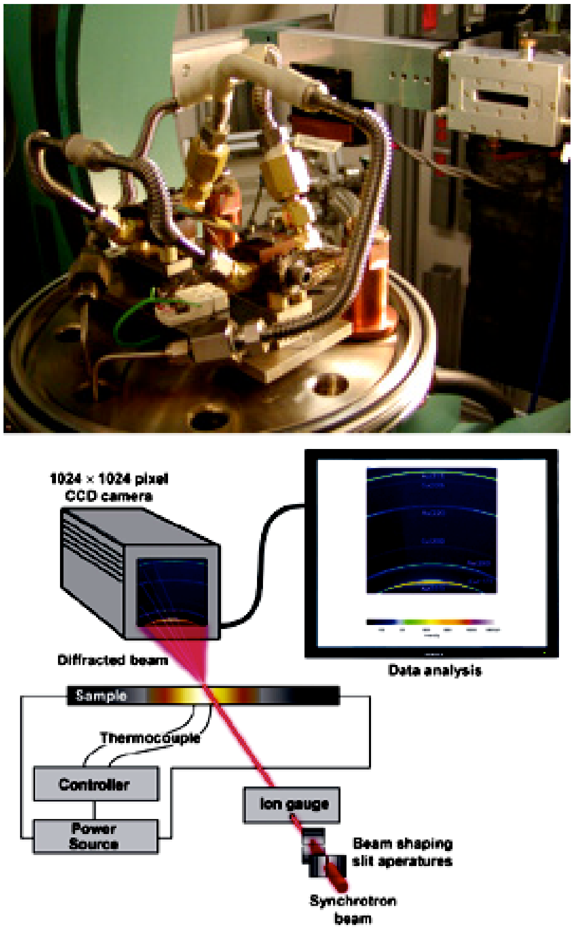

Figure 4. In situ synchrotron X-ray diffraction experiment to study phase transformation kinetics of AHSSs.

The in situ synchrotron diffraction measurements focused on elucidating the phase transformation kinetics during heating in the intercritical temperature range (i.e., between the A_1 and A_3 temperatures of the Fe-C phase diagram) and its impact on the phase transformation during cooling, as the intercritical temperature region is most critical to the HAZ softening observed in the current generation of AHSSs.

The heating rates varied from 3ºC to 150ºC per second during the in situ synchrotron diffraction experiments. The measurement data are still being analyzed, but preliminary results suggest a noticeable dependency of phase-transformation kinetics on the heating rate. In addition, aluminum-bearing TRIP steel showed very different phase-transformation behavior than the other two AHSSs.

Additional neutron and synchrotron experiments are planned in FY 2009. We expect to report the detailed findings of this work in the FY 2009 progress report.

Interactions with the Auto and Steel Industry

The weldability task (Task 2) has received strong industry support from the start of the project. We have maintained active interactions with the auto and steel industry through the technical steering committee and various A/SP committees. Such interactions have been mutually beneficial to the project and to the industry. We were invited to attend meetings of A/SP's Joining Technologies Team (see report 5.A), Sheet Steel Fatigue Committee (see report 5.C), and Lightweight Chassis Structures Team (see report 5.H) to exchange research results. We were also invited to Chrysler, Ford, and GM to discuss our research progress and learn more about the needs of the industry. Several collaborative efforts have come out of these interactions. For example, the A/SP Joining Technologies Team has used the joint efficiency index to characterize the static joint strength of a much wider range of steels, gage thickness, and other welding processes. The Sheet Steel Fatigue Committee is interested in incorporating our findings on fatigue-life improvement into their studies. The integrated weld model, weld fatigue-life prediction model, and weld fatigue improvement techniques developed in this project have been licensed and transferred to several automotive and steel companies for their internal R&D applications. A/SP's joining and lightweight chassis design committees are looking into the feasibility of incorporating our weld microstructure model in some of their CAE design and research activities. We plan to maintain the strong interactions with the industry in this program.

Plan for FY 2009

The R&D activities in FY 2009 will be built on the progress of the program, focusing on completing the following tasks.

1. **Welding and mechanical performance testing of AHSS weld joints.** Continue to study the effects of microstructural changes in the weld region on the dynamic (crash) behavior of AHSSs. Techniques to further improve the weld fatigue life will be investigated.
2. **Microstructural Characterization.** Conduct in situ neutron and/or high-energy X-ray (synchrotron) diffraction measurements to better understand the phase transformation behavior of AHSSs.
3. **Strengthening Mechanisms and Phase Stability in Third Generation AHSSs.** Explore new steel design and alloying approaches to mitigate the detrimental effects of welding on the current generation of AHSSs. A close collaboration with universities is anticipated.
4. **Weld Process and Performance Model.** Complete development of the integrated thermal-mechanical-metallurgical welding process and performance model with emphasis on integrating damage-mechanics-based failure prediction under dynamic-loading conditions.

Presentations/Publications/Patents

1. Z. Feng et al., "A New Perspective on Fatigue Performance of Advanced High-Strength Steels (AHSS) GMAW Joints" *Sheet Metal Welding Conference XIII* (Livonia, Michigan, American Welding Society, 2008).
2. Z. Feng. et al., "Fatigue Performance of Advanced High-Strength Steels (AHSS) GMAW Lap Fillet Welds," *8th International Symposium of The Japan Welding Society*, Kyoto, Japan, 2008.
3. S. Cheng et al., "Probing the Characteristic Deformation Behaviors of Transformation-Induced Plasticity Steels," *Metallurgical and Materials Transactions A*, **39A**(8), pp. 3105–3112 (2008).
4. Z. Feng et al., "Weldability and Performance of Advanced High-Strength Steels (AHSS) in Automotive Structure," (invited) SAE World Congress (Society of Automotive Engineers, Detroit, 2007).
5. Z. Feng, et al., "Weldability and Performance of GMAW Joints of Advanced High Strength Steels," *Great Designs in Steel 2007* (American Iron and Steel Institute, Livonia, Michigan, 2007).
6. Z. Feng et al., "Fatigue Performance of Advanced High-Strength Steels (AHSS) GMAW Joints," paper 09M-0256, *SAE 2009 World Congress,* Detroit, April 20–23, 2009 (to be presented).

Acknowledgements

We would like to acknowledge the following individuals and A/SP committees who contributed to this project.

Chrysler: W. Marttila
Ford: J. Chiang, P. Geck
GM: S. Gayden, J. Bohr, C. Chen
Mittal Steel: M. Kuo
US Steel: M. F. Shi
Severstal N. A.: R. M. Iyengar, Y.-W. Wang
AK Steel: T. Montroy
Dofasco: W. Bernert
OTC: P. Mosquera

A/SP Joining Technologies Team
A/SP Sheet Steel Fatigue Committee
A/SP Lightweight Chassis Structure Team

References

1. J. D. Morrow, “Cyclic plastic strain energy and fatigue of metals,” *ASTM STP 378* (American Society for Testing and Materials, Philadelphia, 1965), pp. 45–87.
2. L. F. Coffin, “A study of the effects of cyclic thermal stresses on a ductile metal,” *Transactions ASME*, **76**, pp. 931–950 (1954).
3. S. S. Manson, “Fatigue-a complex subject-some simple approximations,” *Experimental Mechanics*, **5**, pp. 193–226 (1965).
4. P. Darcis, T. Lassen, and N. Recho, “Fatigue behavior of welded joints part 2: physical modeling of the fatigue process,” *Welding Journal*, **112**, pp. 19s–26s (2006).
5. P. C. Paris and F. Erdogan, “A critical analysis of crack propagation law,” *Trans. ASME, J. Basic Eng.*, **85**, pp. 528–539 (1963).

K. Fundamental Study of the Relationship of Austenite-Ferrite Transformation to Austenite Retention in Carbon Steels

Principal Investigator: Michael L. Santella
Oak Ridge National Laboratory
P.O. Box 2008, Oak Ridge, TN 37831-6096
(865) 574-4805; fax: (865) 574-4928; e-mail: santellaml@ornl.gov

Technology Area Development Manager: Joseph A. Carpenter
(202) 586-1022; fax: (202) 586-1600; e-mail: joseph.carpenter@ee.doe.gov

Field Technical Monitor: C. David Warren
(865) 574-9693; fax: (865) 574-6098; e-mail: warrencd@ornl.gov

---

Contractor: Oak Ridge National Laboratory (ORNL)
Contract No.: DE-AC05-00OR22725

Objective

- Support the development of the Generation (Gen) III advanced high-strength steels (AHSSs) through fundamental studies of the ferrite-austenite phase transformation during steel finishing operations and its relationship to stabilizing and retaining austenite in finished microstructures.
- Characterize in situ the austenite-ferrite phase transformation behavior of carbon steels under the rapid heating/cooling conditions that typify modern sheet steel production.
- Determine the extent to which retained austenite can be increased in commercial and experimental low-carbon (<0.2 wt %) steels.

Approach

- The majority of the experimental part of this work will be done using the DOE Office of Science, Advanced Photon Source (APS) to provide synchrotron radiation for high-speed diffraction. Diffraction patterns can be collected at rates of one every second, possibly even higher. Capabilities exist for integrating diffraction with rapid heating/cooling cycles. Control of temperatures and heating/cooling rates are sufficient for replicating most of the processing steps used to produce existing AHSS. Analysis of the diffraction data can determine volume fractions of the ferrite and austenite phases, their lattice parameters, and how they vary under dynamic temperature/time conditions.

Accomplishments

- Held discussions about potential collaborations with several universities with National Science Foundation (NSF) funding to support development of Gen III AHSSs.
- Prepared and submitted a proposal for access to the APS. It received a high score in the proposal review process, but due to the overall level of demand, it was rejected for access in the October–December 2008 time frame.
- Secured an allocation of beam time from APS as part of a standing allocation available to ORNL.
- Prepared specimens for the first round of experiments in November 2008.
- Contacted beam-line scientists at APS for input on future proposal submissions.

Future Direction

- Revise and resubmit the proposal for access to APS, incorporating input from APS scientists. (Note: In the mean time, an allocation of beam time has been secured from a standing allocation available to ORNL.)
- Continue to seek university partners for collaboration.

Introduction

Project Background

Metals comprise about 80% of all the materials used for light vehicle construction and, by a wide margin, the largest fraction of the metals are steels [1, 2]. Steels represent about 62% of average vehicle weight. Of the various steel mill products used for auto construction, about 70% of the total, or 839 kg of the 1,970 kg average light vehicle weight, is supplied as flat-rolled carbon steel for chassis parts and body panels. The dominance of carbon steels, in terms of total vehicle weight, results from a variety of factors. The metallurgy of carbon steels creates broad boundaries for manipulating important properties such as strength and ductility, as indicated in Figure 1. Carbon steels are relatively inexpensive and they have excellent potential for recycling (e.g., the recycle rate for automotive steels is about 100% [3]).

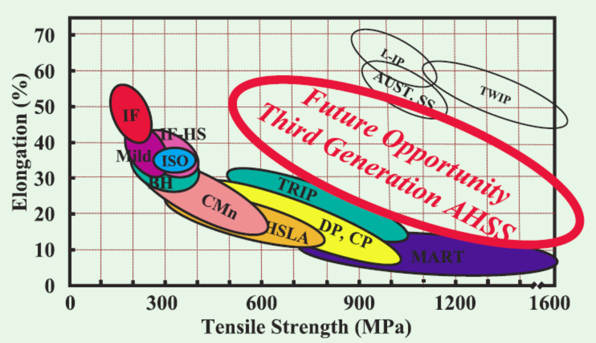

Figure 1. General variation of tensile elongation with strength showing how these properties characteristically balance in various grades of steel (*Source:* Steel Recycling Institute Website [3]).

The traditional sheet steels used for chassis and body constructions are the so-called "mild" steels. The alloying and processing of mild steels are relatively simple, and their microstructures consist principally of ferrite (the equilibrium iron phase at room temperature that has a body-centered cubic crystal structure) and iron carbide (cementite, Fe_3C). Examples of mild steel grades are the interstitial-free, bake-hardenable, and solid-solution-strengthened steels.

The combined interests of improving crash worthiness and reducing vehicle weights were at least partially responsible for the development of the first generation (Gen I) of AHSSs. Included in this group are the dual-phase (DP), complex-phase, martensitic, and transformation-induced plasticity (TRIP) steels. Metallurgically, a characteristic of this group is the development of properties, in part, from more specialized processing that results in the retention of various amounts of nonequilibrium ferrite constituents such as martensite and bainite or metastable phases such as retained austenite (an equilibrium form of iron that is stable above about 700°C and has a face-centered cubic crystal structure). As Figure 1 shows, remarkable strength levels can be developed in the Gen I AHSSs. However, these strength levels are obtained at the expense of reduced ductility and increased alloying. The more limited ductilities complicate forming operations. Increased alloying increases materials cost and complicates other essential processing operations such as welding.

The need to maintain high ductilities while simultaneously developing high strength led to development of the second generation (Gen II) of AHSSs, indicated on the upper right region of Figure 1. The Gen II AHSSs are much more highly alloyed to either completely stabilize the austenite phase or to retain much higher fractions of metastable austenite than in Gen I AHSSs. For example, steels containing 25–30 wt % of manganese are austenitic and capable of developing very high strengths and ductilities. Some of their ductility derives from a metallurgical mechanism known as twinning, which is the source of the term, twinning-induced plasticity (TWIP). Based on raw materials costs, TWIP steels are cheaper than standard austenitic stainless steels, but they are much more expensive than ferrite-based carbon steels. There are concerns about whether they can be produced reliably with the existing primary steelmaking infrastructure. Also, their responses to fabrication processes like forming and welding are virtually unknown.

What is now desired is a third generation (Gen III) of AHSSs that borrows from the Gen I and Gen II steels to achieve intermediate strengths and ductilities, as indicated in Figure 1, but at costs that would make acceptance for automotive construction feasible. Controlling cost will likely require that Gen III AHSSs be no more than modestly alloyed compared to Gen I AHSSs and capable of being produced within existing steel mill infrastructures. This project was initiated in late 2008 to address those desires.

Approach

Developing the Gen II AHSSs required developing completely new alloys that, in a commercial sense, did not exist at the time. In terms of their properties this was successful, as illustrated in Figure 1. In terms of costs and processing, however, this approach appears to have been unrealistic. Consequently, a more productive approach to identifying Gen III steels is to emphasize better understanding of processing in existing Gen I-type steels (e.g., DP 600, DP 780) and to supplement this with work on experimental steels having chemical compositions specifically modified to promote retained austenite. Emphasizing development based on Gen I-type steels is also likely to ensure that acceptable forming and welding properties will be maintained.

There are two temperature ranges where improved understanding is crucial to achieving these goals. One is the so-called intercritical temperature range. This is the range from about 700–850°C where, depending on chemical composition, the ferrite and austenite phases coexist at equilibrium. The time and temperature of intercritical annealing during sheet production controls both the relative fractions and chemical compositions of ferrite and austenite in the microstructure. These properties, combined with cooling rate, will determine how the austenite behaves during subsequent cooling. In other words, these factors determine whether austenite transforms to martensite, bainite, or ferrite and whether any austenite is retained in the microstructure. The second critical range is from about 200–500°C where austenite can be maintained in a metastable condition due to the partitioning of alloying elements like carbon, manganese, and silicon. As is well known, retaining austenite can markedly improve ductility at high strength through the TRIP effect.

Because of their commercial significance, there is considerable practical knowledge about how steels behave in these temperature ranges. However, there is a lack of scientific underpinnings that limits progress on improving properties to the limits of experience. Better fundamental understanding of austenite-ferrite transformations will enable a more scientific approach to improving properties through novel processing that can be achieved with existing infrastructure.

Technical Challenges

1. Making direct, in situ observations of the time dependence of austenite-ferrite transformation behavior at elevated temperatures, during rapid heating/cooling, and during low-temperature treatments designed to maximize retained austenite.
2. Measuring partitioning of carbon between austenite and ferrite during processing.
3. Understanding effects of critical alloying elements such as carbon, manganese, and silicon on transformation behavior and retention of austenite.

The technical activities of this task are complementary to and will be coordinated with those of NSF-funded Gen III AHSS projects at universities (see reports 5.L–5.T).

Materials and Experimental Details

Initial work will be done using two uncoated high-strength steels: the DP steel DP 780 (ArcelorMittal) and a hot-stamp boron steel (HSBS) sourced from a Swedish supplier, the parent of U.S. HardTech. The analyzed compositions of the steels are as follows.

- DP 780 (wt %): Fe-0.11C-1.93Mn-0.24Si
- HSBS (wt %): Fe-0.20C-1.26Mn-0.27Si-0.22Cr-0.002B

Specimens with dimensions of 5 mm × 1.25 mm × 110 mm were machined from sheets of both steels. The surfaces of these strips were ground by machining to remove oxides.

The thermal cycles shown in Figure 2 will be used for the initial experiments. We will heat specimens through these conditions while simultaneously collecting X-ray diffraction spectra at the rate of about 1/s. The data will be analyzed to measure the relative fractions of ferrite and austenite phases. The lattice parameters of these phases will also be determined and analyzed for possible relationships to chemical compositions.

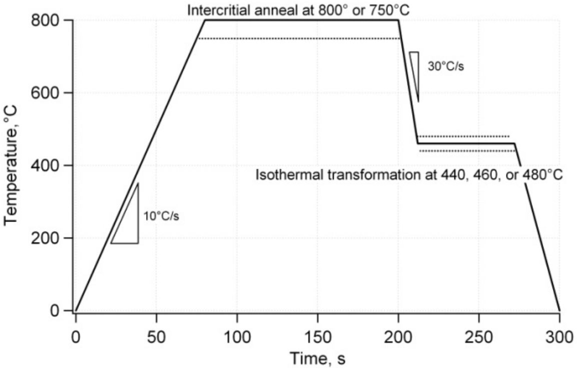

Figure 2. Schematic representation of thermal cycles used for initial diffraction experiments.

Conclusions

Because this was a start-up activity during the second-half of FY 2008, we do not have any conclusions to report at this time.

Presentations/Publications/Patents

None

References

1. Richard A. Schultz, "Metallic Material Trends for North American Light Vehicles," *Great Designs in Steel* seminar presentation, 2007; available: American Iron and Steel Institute website (http://www.autosteel.org/AM/Template.cfm?Section=GDIS&CONTENTID=24666&TEMPLATE=/CM/HTMLDisplay.cfm).
2. John Schnatterly, "Steel Content in North American Vehicles," *Great Designs in Steel* seminar presentation, 2007; available: American Iron and Steel Institute website (http://www.autosteel.org/AM/Template.cfm?Section=GDIS&CONTENTID=24666&TEMPLATE=/CM/HTMLDisplay.cfm).
3. Steel Recycling Institute Website (www.recycle-steel.org).

L. National Science Foundation Funding for the Development of Third Generation Advanced High-Strength Steels (A/SP 280*)

Project Manager: Roger A. Heimbuch
Auto/Steel Partnership
2000 Town Center Drive, Suite 320
Southfield, Michigan 48075-1123
(248) 945-4770; fax: (248) 356-8511; e-mail: rheimbuch@a-sp.org

Chairman: Ronald Krupitzer
American Iron and Steel Institute
2000 Town Center Drive, Suite 320
Southfield, Michigan 48075-1123
(248)-945-4761; fax : (248) 352-1740; e-mail: krupitzerr@autosteel.org

Technology Area Development Manager: Joseph A. Carpenter
(202) 586-1022; fax: (202) 586-1600; e-mail: joseph.carpenter@ee.doe.gov

Field Project Officer: Aaron D. Yocum
(304) 285-4852; fax: (304) 285-4403; e-mail: aaron.yocum@netl.doe.gov

Contractor: United States Automotive Materials Partnership (USAMP)
Contract No.: DE-FC05-02OR22910 through the National Energy Technology Laboratory

Objectives

- Conduct the fundamental research required to develop a third generation advanced high-strength steel (AHSS) that is higher in strength and more formable than currently available commercial grades of AHSS with the potential of being more cost-effective than stainless steels and twinning-induced plasticity (TWIP) steels.

Approach

- Conduct fundamental steel research at universities that can lead to the development of a cost-effective family of third generation AHSS that can be applied for mass reduction in the auto body.
- Utilized National Science Foundation (NSF) processes to manage the research.
- Provide a portion of the funding (25%), through this project, for fundamental research required to develop a third generation AHSS.
- Additional funding will be provided directly by DOE (25%) and the NSF (50%).

Accomplishments

- NSF AHSS Workshop held October 22–23, 2006, Arlington, Virginia.

---

*Denotes project 280 of the Auto/Steel Partnership (A/SP), the automotive-focus arm of the American Iron and Steel Institute (see www.a-sp.org). The A/SP cofunds projects with DOE through a cooperative agreement between DOE and the United States Automotive Materials Partnership, one of the formal consortia of the United States Council for Automotive Research set up by Chrysler, Ford, and General Motors to conduct joint, precompetitive research and development (see www.uscar.org).

- NSF AHSS Proposal Panel Review held April 10–11, 2007, Arlington, Virginia. Eight proposals, from 30 submitted, were selected for funding, using the NSF process, and a budget allocation prepared by NSF. The research projects will be carried out over 3 years.
- NSF will notify the appropriate principal investigators (PIs) and universities of their grants and track and document the research projects following NSF standard practices.
- An NSF/DOE Steel Research Program Review was held April 10, 2008. Participants included the university professors that are conducting the NSF research; DOE national laboratory researchers working on steel research; Canada Centre for Mineral & Energy Technology (CANMET) steel researchers; and personnel from NSF, DOE, and Auto/Steel Partnership (A/SP) member companies.
- An industry-based steering committee has been formed.

Future Direction

- The industry-based steering committee will work to provide the requested additional support to the researchers.
- A web-based site will be developed for researchers to store and share information.
- An annual review of the NSF/DOE Steel Research Program will be held in spring 2009.

Introduction

One of the tasks of the A/SP241 Future Generation Passenger Compartment Project (see report 5.G) was to run the structural optimization codes with unrestricted strength limitations to define the upper strength bound for auto body steel for optimized mass reduction. Several areas of the body were found that would benefit from higher strength.

An additional 5% to 8% mass reduction is possible in those areas of the vehicle. Based on the specific areas of the body, estimates were made of the forming characteristic needed to make those types of parts. A window of opportunity was defined ranging from 600 MPa/40% elongation to 1,600 MPa/20% elongation for a cost-effective third generation AHSS family. It was recognized fundamental steel research would be required to develop steels in that property range. A collaborative effort by NSF, DOE, American Iron and Steel Institute (AISI), and A/SP has been put together to fund eight university research proposals, using the NSF processes, to fund the supporting fundamental research to develop steels with the desired properties.

Objective

The objective of this project is to provide a portion of the funding (25%) for the fundamental research required to develop a cost-effective family of third generation AHSS that can ultimately be applied for mass reduction in the auto body. Additional funding will be provided directly by DOE (25%) and NSF (50%). The research will be done utilizing the processes of the NSF. If the research is successful, it will provide the basis for the commercial development of cost-effective third generation AHSS by the A/SP steel members.

Project Status

An NSF AHSS Workshop was held October 22–23, 2006, in Arlington Virginia. As a result of that workshop, the NSF requested proposals for basic research to support the development of a family of third generation AHSS. An NSF AHSS Proposal Panel Review was held April 10–11, 2007, in Arlington, Virginia. Eight proposals, from 30 submitted, were selected for funding, using the NSF process, and a budget allocation was prepared by NSF. The research projects will be carried out over 3 years starting the academic year 2007–2008. The following table shows the PIs, institutions, and titles.

University	Professor	Topic
Carnegie Mellon University	Warren Garrison	AHSS through microstructure and mechanical properties
Case Western Reserve University	Gary Michal	AHSS through C partitioning
Colorado School of Mines (CSM), Ohio State University (OSU)	David Matlock (CSM) and Robert Wagoner (OSU)	Collaborative GOALI Project Formability and Springback of AHSS
Drexel University	Surya Kalidindi	FEM using crystal plasticity simulation modeling tools
OSU	Ju Li	Multi-scale modeling of deformation for design of AHSS
Texas A&M University	Abu Al-Rub Rashid	AHSS through particle size and interface effects
University of Missouri-Rolla	David C. Van Aken	AHSS through nano-acicular duplex microstructures
Wayne State University	Susil K. Putatunda	High strength high toughness bainitic steel

An industry-based steering committee has been formed with members from A/SP member companies. They include representatives from steel research centers, mills, and automotive applications centers and advanced materials representatives from the automotive companies. The steering committee will help coordinate additional support for the NSF researchers and become the technology transfer interface for the research back into industry.

An NSF/DOE Steel Research Program Review was held April 10, 2008, in Southfield, MI in conjunction with AISI's Great Designs in Steel (GDIS) event April 9, 2008. GDIS provided the steel researchers the opportunity to see the need for a third generation AHSS. Overviews of each of the NSF sponsored research programs were presented. In addition, related research being conducted at Pacific Northwest National Laboratory, Oak Ridge National Laboratory, and Canada's CANMET Laboratory was reviewed. Eleven representatives from the steel industry; seven representatives from the automotive industry; and staff from A/SP, AISI, NSF, and DOE participated. There was active discussion during the reviews among the participants. Opportunities for future interactions among the attendees, areas needing additional support, and gaps in the research were identified and are being addressed.

The researchers requested a web-based system where information could be stored and shared. A system was developed and became available in May 2008.

Conclusions

NSF has initiated the research contracts with the eight selected Universities. Reporting of the research will follow the normal processes of NSF.

Future Work

The industry-based steering committee will work to provide the additional support requested by the researchers**.** A second annual progress review of third generation AHSS research is being planned for spring 2009. The intent is to share progress, identify gaps in the research program, and identify areas where additional support would be valuable. A web site debuted in May 2008 to store and share data among the researchers.

Acknowledgments

The support and guidance of Drs. Mary Lynn Realff and Joyceleyn Harrison of NSF, Dr. Joseph Carpenter of DOE, and Ronald Krupitzer of AISI in developing and implementing this research initiative are greatly appreciated.

References

1. The NSF Report "Advanced High Strength Steel Workshop Oct.22–23, 2006, Arlington, Virginia" by Professor Robert Wagoner, Department of Material Science and Engineering, The Ohio State University, Columbus, Ohio.

M. A Multiresolution Analysis of the Particle Size and Interface Effects on the Strength and Ductility of Advanced High-Strength Steels

Principal Investigator: Rashid K. Abu Al-Rub
Texas A&M University
3136 TAMU, College Station, TX 77843-3136
(979) 862-6603; fax (979) 845-6554, e-mail: rabualrub@civil.tamu.edu

Technology Area Development Manager: Joseph A. Carpenter
(202) 586-1022; fax: (202) 586-1600; e-mail: joseph.carpenter@ee.doe.gov

Field Project Officer: Aaron D. Yocum
(304) 285-4852; fax: (304) 285-4403; e-mail: aaron.yocum@netl.doe.gov

---

Contractor: Texas Engineering Experiment Station
National Science Foundation Contract No.: CMMI 0728032, jointly funded by NSF and DOE

Objective

- Identification of the role of dispersed micro- and nano- particles (inclusions) on enhancing the yield strength, ultimate strength, and ductility of advanced high strength steels (AHSSs) reinforced with inclusions at decreasing microstructural length scales.
- Development of a multiresolution (multiscale) computational framework that can be used effectively in the design of AHSS with superior strength and ductility.

Approach

- Development of a robust, multiresolution theoretical framework for the multiscale modeling of inelastic-deformation processes of evolving multiphase AHSS.
- Development of a non-local strain gradient theory coupled with the developed multiresolution analysis.
- Implementation of the developed theoretical models in a multiscale hierarchal computational framework.
- Conduct of a parametric study of the effect of microstructural features (e.g., particle size, interfacial properties, particle volume fractions and distribution) on the strength and ductility of AHSS.

Accomplishments

- A theoretical model based on nonlocal strain gradient plasticity has been developed and successfully validated. This model can be used in predicting the increase in yield strength and strain-hardening rates of AHSS with decreasing the particle (inclusion) size and by increasing the stiffness of these second-phase particles.
- It is found that there is an optimum combination between hard and soft particles that can be dispersed within the matrix of AHSS to achieve a simultaneous increase in both strength and ductility.

Future Direction

- Incorporate micro-damage nucleation and growth laws that can simulate micro and nano crack evolution within the matrix material of AHSS and at internal interfaces of second-phase materials and particles.
- Incorporate phase-transformation laws that can be used to explain additional strengthening besides the strengthening due to dispersed particles.

- Implement the proposed multiresolution framework and conduct a parametric study of the effect of microstructural features on the strength and ductility of AHSS.

Introduction

With the introduction of stronger safety legislation and increased dependence on foreign oil, auto manufacturers must respond with higher car-body stiffness for safety and lower body weight for fuel efficiency. The fields of materials development, engineering, and manufacturing are working together to achieve autobody weight reduction with improved crash characteristics [1]. For that reason, the use of advanced high-strength steels (AHSS) [steels with tensile strength ≥ 500 MPa and tensile elongation ≤ 20% in car bodywork has spread in recent years [2]. The American Iron and Steel Institute (AISI) is forecasting a dramatic increase in the use of AHSS in the automotive industry. As shown in Figure 1, the second generation of AHSS offers superior combinations of strength (performance) and ductility (formability) over the other types of steels. This is attributed to their elevated strain hardening capacity as a result of a lower yield strength/ultimate tensile strength ratio. Therefore, the main advantage of these types of steels is a higher impact resistance, which allows reducing the weight of the bodywork components by using thinner metallic sheets. However, the cost of the second generation AHSS is prohibitive for widespread adoption because of costly alloy content (e.g., nickel or manganese). The to-be-developed third generation AHSS are envisioned as affordable alternatives to second generation AHSS, but will trade some mechanical properties, still being much more effective than current and first generation AHSS.

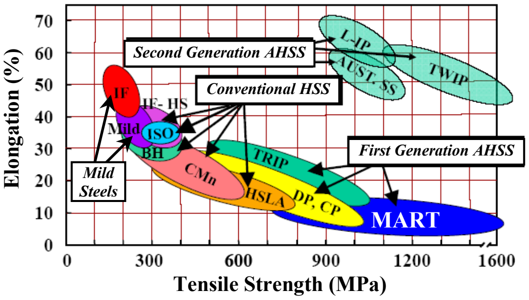

Figure 1. Comparison between different grades of steels for strength and ductility [3].

Work-hardening is one of the primary reasons for the enhanced strength and ductility of AHSS over other types of steels. Work-hardening can be enhanced by second phase particles (inclusions) of different sizes at distinct length scales. The main objective of this study is the development at different nested length scales (i.e., multiresolution) a fundamental understanding of the particle size and interface effects on the strengthening (strain hardening) and micro-damage (strain softening) mechanisms that lead to drastic increase/decrease in the strength and ductility of AHSS. This will ultimately lead to design of modern AHSS with desirable micro/nanostructures and optimized properties through alloy component/phase selection. Therefore, the AHSS that we are interested in display strong particle size and interface effects. It is well known that conventional steels contain soft iron matrix and hard inclusions. For the AHSS that will be the core of this study, the iron matrix comprised of martensite and austenite that is designed to be transformable into body-centered-cubic (BCC) martensite, which is a desirable hard substance. The inclusions, which are distributed in a non-homogeneous manner, are divided into two groups (see Figure 2): the primary particles with diameters around several microns and the secondary particles in the range of 1 to 0.1 microns. It is argued until now that the secondary particles increase the strength by strain-hardening mechanisms whereas primary particles lower the fracture toughness by strain- softening mechanisms. Therefore, by optimizing the volume fractions, sizes, shapes, interfacial strength, and distribution of these constituents, one may be able to increase the strength and ductility of AHSS simultaneously.

Approach

Theoretical modeling and multiscale computational simulations are necessary for the design of new generations of AHSS. Therefore, it is imperative to develop a constitutive model and a multiscale framework that can be used

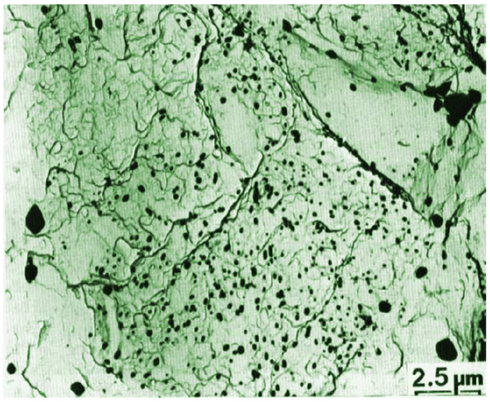

Figure 2. A TEM micrograph of the microstructure of an AHSS showing the different levels of dispersed small particles [4].

successfully in incorporating the strengthening effects due to the reduction in particle (inclusion) size and the effects of the interfacial hardening by incorporating the particle-matrix interfacial mechanical properties (e.g., interfacial strength and hardening). Unfortunately, the classical continuum plasticity theories (e.g., von Mises or Drucker-Prager) are unable to predict the influence of particle size due to the absence of a microstructural length scale parameter in their constitutive equations [4]. Therefore, within a classical continuum mechanical framework, the mechanical properties of multiphase materials only depend on the volume fraction of particles while the particle size is not accounted for. However, the mechanical properties of lightweight advanced materials, with a typical distance D between particles and particle size d, depend on how these geometrical parameters interfere with other characteristic distances such as the mean-free path of dislocations. Reducing the size of particles, while keeping the volume fraction constant, significantly improves the material macroscopic mechanical properties.

Since the increase in strength with decreasing scale can be related to proportional increase in the plastic strain gradients that evolve at the particle-matrix interfaces due to dislocation pileups (see Figure 3), the gradient plasticity theory has been successful in addressing the size effect problem [5]. This success stems from the incorporation of a microstructural length scale parameter through functional dependencies on the plastic strain gradient of nonlocal media [5]. The gradient-dependent theory abandons the assumption that the stress at a given point is uniquely determined by the history of strain at this point only. It takes into account possible interactions with other material points in the vicinity of that point.

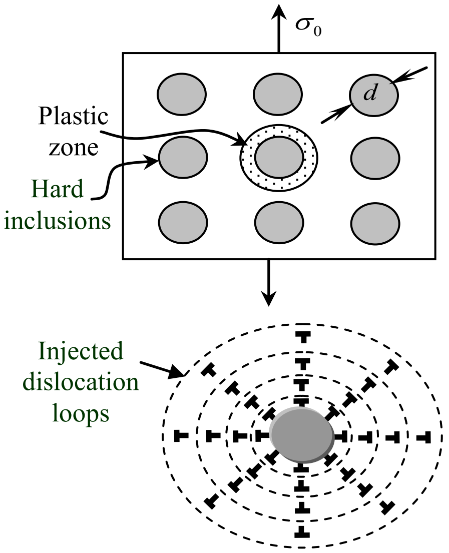

Figure 3. Plastic strain gradients are caused by evolution of geometrically necessary dislocations (GNDs) around spherical inclusions of size d under uniaxial loading.

As an initial effort, in order to include the size effect of dispersed particles within the AHSS matrix, a higher-order gradient plasticity theory have been developed and validated. This nonlocal theory takes into account the plastic strain gradient (i.e., heterogeneous distribution of plasticity) around the second-phase inclusions (see Figure 3). Also, the interfacial mechanical properties of the particle-matrix interface (e.g., interfacial yield strength and interfacial hardening) are explicitly incorporated in the formulated theory. Depending on the interfacial properties, the effect of hard, stiff, or soft inclusions are incorporated.

Also, in this theory, two plasticity yield conditions are formulated, one for the bulk (i.e., the matrix) and one for particle-matrix interface and grain boundaries. Therefore, two length scale parameters are incorporated. The bulk length scale parameter, ℓ, is related to the average spacing between dislocations within the matrix material; whereas, the interfacial length scale, ℓ_I, is related to the boundary layer thickness at the particle-matrix interface. Both length scales can be identified from nanoindentation tests.

Results

The formulated nonlocal strain gradient plasticity theory has been implemented in the commercial finite-element program ABAQUS through its user material subroutine UMAT and used to demonstrate the ability of the model in predicting particle size effects on the strength of AHSS. The direct and simple numerical implementation method for gradient-dependent theories as presented in [6] has been utilized for calculating the plastic strain gradients.

Figure 4 shows that strain gradient plasticity is successful in predicting the inclusion size effect for a constant volume fraction unlike the classical plasticity theory. Moreover, Figure 5 shows mesh dependent results when simulating strain localization due to particle debonding when using the classical theory of plasticity which can be largely corrected when using the proposed strain gradient plasticity theory.

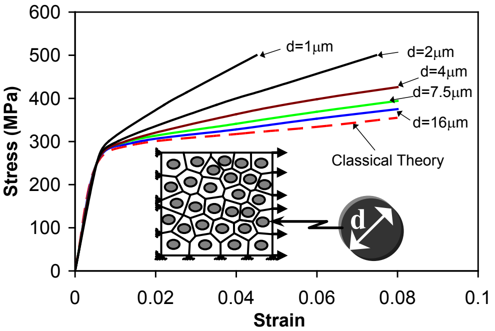

Figure 4. Finite-element computational comparisons between the predictions from strain gradient plasticity theory and the classical plasticity theory for inclusion size effect on strain hardening at a constant volume fraction.

Moreover, it is shown that the proposed nonlocal strain gradient plasticity theory can predict the increase in the initial yield strength (i.e., onset of plasticity) characterized by the ratio of the average yield strength of AHSS σ_Y to the matrix size-independent yield strength σ_y as shown in Figure 6. This increase in the initial yield strength is shown for different particle sizes d (characterized by the ratio ℓ/d where ℓ is the material length scale) and for different particle-matrix interfacial strengths (characterized by the ratio ℓ_I/ℓ, where ℓ_I is the interfacial length scale parameter). As ℓ_I/ℓ increases, the hardness of the particle increases. Similarly, Figure 7 shows the particle size effect on the strain hardening rate characterized by the normalized ratio of the hardening tangent modulus E^T to the Young's modulus E. It can be seen that as the particle size decreases or as the particle hardness increases, the strain hardening rate increases. In other words, the smaller the particle size and the larger the particle hardness, the larger the ultimate strength. However, it is noteworthy that the above

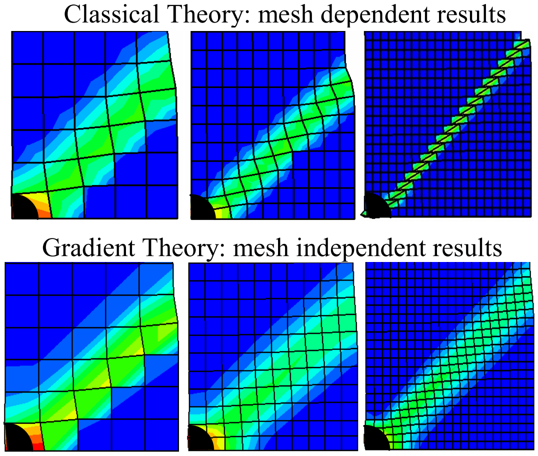
Classical Theory: mesh dependent results
Gradient Theory: mesh independent results

Figure 5. Finite element computational comparisons between the predictions from strain gradient plasticity theory and the classical plasticity theory for strain localization induced particle debonding.

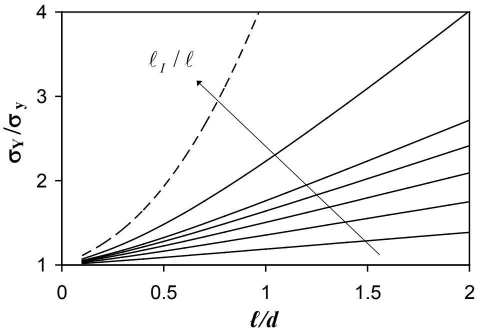

Figure 6. Normalized macroscopic yield strength of AHSS σ_Y versus particle size d for different particle-matrix interfacial strength increases. The dashed line is for a rigid particle.

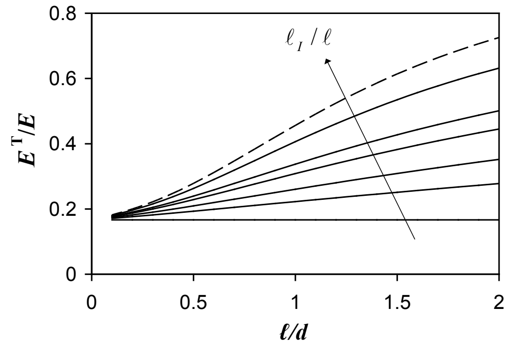

Figure 7. Normalized macroscopic hardening modulus of AHSS E^T versus particle size d for different particle-matrix interfacial strength increases. The dashed line is for a rigid particle.

conclusions and observations are valid only in the case wherein the particle debonding and fracture effects are not considered. These effects will be incorporated in the subsequent development of the current study.

Conclusions

It is concluded that a nonlocal strain gradient plasticity theory can be used to qualitatively predict the particle size effect in AHSS reinforced with particles (inclusions) at decreasing microstructural length scales. These particles can range in size from few hundreds of nanometers to few microns.

It is shown that as the particle size decreases or particle hardness increases both the onset of plasticity (yield strength) and strain hardening rate (or ultimate strength) increases. This is a crucial conclusion for the design of AHSS with improved yield and ultimate strengths. However, these conclusions are only valid in the case wherein both debonding and fracture of particles are not considered. Future extensions of the current study will consider damage evolution in the matrix, particle, and particle debonding which are very important to validate the aforementioned conclusions and for assessment of the effect of particle size and hardness on the ductility of AHSS.

Moreover, future work will be concerned with incorporating the formulated nonlocal strain gradient plasticity theory in a multiscale hierarchal computational framework ranging from the nano scale to the macro scale. This is important to study the effect of each scale on the other and how the microstructural changes within each scale affect the overall macroscopic strength and ductility of AHSS or low-density materials. Furthermore, phase transformation of austenite to the hard phase martensite will also be incorporated into the proposed multiscale framework. One of the important aspects of this study that will be investigated thoroughly is the calibration, validation, and verification of the proposed theoretical models and computational tools. The proposed frameworks will be validated and verified against available experimental results for specific material systems or microstructures.

Presentations

1. Abu Al-Rub, R. K. “Non-local Strain Gradient Plasticity and Damage: A Multiresolution Framework for Bridging the Material Length Scales,” Computational Sciences & Mathematics Division, Pacific Northwest National Laboratory (PNNL), Richland, Washington, September 4, 2008.
2. Abu Al-Rub, R. K., “Nonlocal Gradient-dependent Plasticity and Damage: An Approach for Bridging the Material Length Scales,” Symposium of Predictive Science and Technology of Mechanics and Materials, Center for Advanced Vehicular Systems (CAVS), Mississippi State University, June 24, 2008.
3. Abu Al-Rub, R. K., “AHSS through Particle and Interface Effects,” NSF/DOE Steel Research Program Review, Auto/Steel Partnership Offices, Southfield, MI, April 10, 2008.
4. Abu Al-Rub, R. K., “On the Higher-Order Nonlocal Gradient-Dependent Theory and its Non-classical Microscopic Boundary Conditions,” In. 2008 ASME International Mechanical Engineering Congress and Exposition, Session on Nonlocal Methods and Length-Scale Effects, Boston, Massachusetts, November 2–6, 2008.
5. Abu Al-Rub, R. K., “Interfacial Gradient Plasticity Governs Scale-Dependent Yield Strength and Strain Hardening Rates at

Decreasing Microstructural Length Scales," In. 2008 ASME International Mechanical Engineering Congress and Exposition, Session on Multiscale Constitutive Modeling, Boston, Massachusetts, November 2–6, 2008.

6. Abu Al-Rub, R. K., "Multiresolution Modeling of Size and Interfacial Effects in Metal Matrix Composites with Dispersed Particles at Decreasing Microstructural Length Scales," In. 2008 ASME International Mechanical Engineering Congress and Exposition, Session on Mechanics of Composites with Coupled Mechanical and Nonmechanical Behaviors, Boston, Massachusetts, November 2–6, 2008.
7. Abu Al-Rub, R. K., "Prediction of Nanoindentation Size Effect from Conical or Pyramidal Indentation," In. 2008 ASME International Mechanical Engineering Congress and Exposition, Session on Modeling and Experiments in Nanoindentation, Boston, Massachusetts, November 2–6, 2008.
8. Abu Al-Rub, R. K., and Kim, S.-M., "Nonlocal Framework for Simulating the Micromechanics of Localized Damage and Fracture in Metals at High-Speed Impact," In. 2008 ASME International Mechanical Engineering Congress and Exposition, Symposium Honoring John W. Hutchinson, Boston, Massachusetts, November 2–6, 2008.
9. Abu Al-Rub, R. K., Voyiadjis, G. Z., Bammann, D. J., and Aifantis, E. C., "On the Higher-Order Gradient Plasticity Theory and its Non-classical Boundary Conditions," In. 45th Annual Technical Meeting of the Society of Engineering Science (SES), Symposium on Plasticity and Damage Size Effects at the Micron and Nano Length Scales, Champaign, Illinois, October 12–15, 2008.
10. Abu Al-Rub, R. K., "Prediction of Micro and Nano Indentation Size Effects from Pyramidal and Spherical Indentation," In. 45th Annual Technical Meeting of the Society of Engineering Science (SES), Symposium on Plasticity and Damage Size Effects at the Micron and Nano Length Scales, Champaign, Illinois, October 12–15, 2008.
11. Abu Al-Rub, R. K., "Interfacial Gradient Plasticity Governs Scale-Dependent Yield Strength and Strain Hardening Rates at Decreasing Microstructural Length Scales," In. 45th Annual Technical Meeting of the Society of Engineering Science (SES), Session in Honor of Professor Subra Suresh, Champaign, Illinois, October 12–15, 2008.
12. Abu Al-Rub, R. K., "Multi-scale Prediction of Micro and Nano Indentation Size Effect," In: First American Academy of Mechanics Conference, Session on Multi-scale Modeling and Simulation of Nano Structured Materials, New Orleans, Louisiana, June 17–20, 2008.
13. Abu Al-Rub, R. K., "Prediction of Size Effects at the Micron and Submicron Length Scales," In: First American Academy of Mechanics Conference, Session on Modeling Inelastic Deformation at Varying Length Scales, New Orleans, Louisiana, June 17–20, 2008.
14. Abu Al-Rub, R. K., "Surface/Interfacial Effects on Size Dependent Strength of Micro/Nano Systems," In. 49th AIAA/ASME/ASCE/AHS/ASC Structures, Structural Dynamics and Materials Conference, AIAA 2008, Session on Multiscale Material Analysis, Schaumburg, Illinois, April 7–10, 2008.

Publications

1. Abu Al-Rub, R. K., "Modeling the interfacial effect on the yield strength and flow stress of thin metal films on substrates," Mechanics Research Communications, Vol. 35, No. 1-2, pp. 65–72, 2008.
2. Abu Al-Rub, R. K., "Interfacial gradient plasticity governs scale-dependent yield strength and strain hardening rates in micro/nano structured metals," International Journal of Plasticity, Vol. 24, No. 8, pp. 1277–1306, 2008.
3. Abu Al-Rub, R. K., Voyiadjis, G. Z., and Aifantis, E. C. "On the thermodynamics of higher-order gradient plasticity for size-effects at the micron and submicron length scales," International Journal of Materials and Product

Technology, Vol. 34, Nos. 1/2, pp. 172–187, 2009.

4. Abu Al-Rub, R. K., "Surface/interfacial effects on size dependent strength of micro/nano systems," In. Collection of Technical Papers AIAA/ASME/ASCE/AHS/ASC Structures, Structural Dynamics and Materials Conference, AIAA 2008-1946 (5 pages).

References

1. Marsh, M., 2000. "Development of autobody sheet materials for crash performance," In: Proc. of Conf. Materials and Structures for Energy Absorption, IMech, London, May 9, 2000, 55–64.
2. Baker, M. A., 2004. Proceedings of the International Conference on Advanced High Strength Sheet Steels for Automotive Applications. Association for Iron and Steel Technology, Warrendale, PA, USA.
3. Wagoner, R. H., and Smith, G. R., 2006. Advanced High-Strength Steels (AHSS) Workshop. October 22–23, 2006, Arlington, Virginia, USA.
4. Abu Al-Rub, R. K., 2008. "Interfacial gradient plasticity governs scale-dependent yield strength and strain hardening rates in micro/nano structured metals," International Journal of Plasticity, 24, 1277–1306.
5. Voyiadjis, G. Z., and Abu Al-Rub, R. K., 2009. Nonlocal Continuum Damage and Plasticity: Theory and Computation. World Scientific Publishing Co Pte Ltd., UK.
6. Abu Al-Rub, R. K., and Voyiadjis, G. Z., 2005. A direct finite element implementation of the gradient plasticity theory. Int. J. Numer. Meth. Engng. 63, 603–629.

N. Study of the Effects of Microstructure on the Mechanical Properties and Failure Mechanisms of Advanced High-Strength Steels

Warren M. Garrison Jr., Anthony Rollett, Sridhar Seetharaman
Carnegie Mellon University
5000 Forbes Avenue
Pittsburgh, PA 15213
(412) 268-3593; fax: (925) 268-7596; e-mail: wmg@andrew.cmu.edu

Technology Area Development Manager: Joseph A. Carpenter
(202) 586-1022; fax: (202) 586-1600; e-mail: joseph.carpenter@ee.doe.gov

Field Project Officer: Aaron D. Yocum
(304) 285-4852; fax: (304) 285-4403; e-mail: aaron.yocum@netl.doe.gov

---

Contractor: Carnegie Mellon University, Pittsburgh, Pennsylvania
National Science Foundation (NSF) Award CMMI 0726949, jointly funded by NSF and DOE

Objectives

- To understand the effect of complex, multiphase microstructures on the mechanical behavior and formability of advanced high-strength sheet steels.
- To investigate the effect of void nucleation resistance at inclusion particles on the mechanical behavior and formability of high-strength sheet steels.

Approach

- Develop microstructures consisting of lower bainite mixed with 0%, 25%, and 50% ferrite and assess the mechanical behavior and formability of these microstructures.
- Develop microstructures consisting of martensite mixed with 0%, 25%, and 50% ferrite and assess the mechanical properties and formability of these microstructures and compare the behavior of these martensite structures with those of the lower-bainite structures.
- Prepare heats of steel which are identical except for the sulfide type with one sulfide type having low resistance to void nucleation and the other sulfide type being resistant to void nucleation. Sulfide particles which have a low resistance to void nucleation are achieved by gettering the sulfur as particles of manganese sulfide. Sulfide particles which are very resistant to void nucleation are achieved by gettering the sulfur as particles of titanium carbo-sulfide.

Accomplishments

- Defined four steel compositions to be used in investigating mixtures of lower bainite and ferrite and mixtures of martensite and ferrite on mechanical behavior and formability.
- Defined two steel compositions to be used to assess void nucleation resistance of inclusions on mechanical behavior and formability.
- Melted the six heats corresponding to the six selected compositions and processed some of each composition to one-half-inch-thick plate. This was done at US Steel research facilities in Pittsburgh.
- Investigated the effect of solution treatment temperature on the amount of ferrite, hardness, and Charpy impact energy for the four compositions used to explore effects of mixed microstructures on mechanical behavior and formability.

- Obtained Charpy impact toughness and tensile properties of the two compositions to be used to assess the effect of void nucleation resistance on formability of sheet steels.

Future Directions

- Decide on heat treatments to be used to obtain the mixed microstructures.
- Prepare sheet material which have the desired mixed microstructures and begin to carry out studies of formability.
- Prepare sheet material from the two heats which represent inclusions resistant to void nucleation and inclusions not resistant to void nucleation and begin to carry out studies of formability.

Introduction

The purpose of this work is to examine the effects of heat treatment and composition on the microstructure and mechanical properties of high-strength steels with the ultimate goal of producing microstructures which would have ultimate tensile strengths of at least 1,200 megapascals (MPa) and which would be suitable for use in automotive applications, especially for steel sheet to be used in forming operations.

There are several factors to consider in assessing the formability of steel. The first is that the work-hardening capacity and characteristics be sufficient to ensure formability in the sense that strain localization and/or local thinning do not take place in the forming process; thus, the strains which can be tolerated prior to local thinning increase with work-hardening rate [1]. The uniform strain is often taken as measure of this characteristic, thus high uniform strains are desired in steels which are intended for applications in which they must be formed. The second is that the material has sufficient ductility that fracture does not take place during the forming operation. The latter characteristic is important because it has been found that as the strength levels of steels for forming applications are increased, there is a tendency for fracture to take place before the forming operation is complete, at least for some forming operations [2–7]. Thus, not only are the work-hardening characteristics important, in that the work-hardening rates should be high and remain high even at large strains, but that resistance to fracture should also be high. Thus, in assessing sheet materials for forming using a tensile test, one would want both high uniform strains and high true strains to fracture. That is, the behavior of the material after necking is also of importance. Coupled with the requirements for high formability there are interests in steels of higher strength in order to reduce weight and the ability of the structures produced of these materials to absorb energy under impact conditions [8].

Our approach is strongly influenced by two papers concerning Transformation Induced Plasticity (TRIP) [2-5, 9-15] steels developed for steel sheet applications. These TRIP steels contain several microstructure features, including ferrite, bainite, martensite, and retained austenite which, through control of composition and heat treatment, is mechanically stable. In the TRIP steels developed for sheet applications, it is believed that the carefully controlled transformation of the retained austenite to a high-carbon martensite during deformation is critical to achieving high rates of work hardening and high uniform strains, which are important to good formability.

The first paper is a note by Bhadeshia [16] which was inspired by a paper by Jacques et al. [17]. Jacques et al. found that one could obtain excellent uniform elongations in multiphase steels which did not contain silicon or aluminum to promote the existence of mechanically stable retained austenite which is free from carbide formation. Badheshia suggested, based on these results, that the 8 to 15 volume % retained austenite commonly found in TRIP steels contributed about 2% to a total uniform elongation of say 25%. Badheshia suggested that the high work-hardening rates in the multiphase steels typical of TRIP steels might be instead due to a mixture of soft and hard phases. In his discussion, Badheshia suggested that the high work- hardening rates might be associated with initial deformation of the ferrite which would not work harden at a high rate but, at some point, the as-quenched martensite in the microstructure would start to deform and the high work-hardening rate of the as-quenched martensite is what determines the high work-hardening rate of the structure and the high uniform elongations. (The high work-hardening rate of as-quenched martensite is related to not only the distribution of the carbon [18] in the martensite but also, we believe, to the amount of retained austenite in the as-quenched martensite).

The second paper is one by Lee et al. [19] in which void generation in multiphase steels was investigated. They found that voids are generated during plastic deformation not only at inclusions and carbide particles but at interfaces between strong and weak microstructural elements; for example, voids could be generated at interfaces between ferrite and martensite. The rate at which voids are formed during deformation can have important consequences in terms of tensile ductility and possibly on formability. The slower the rate at which voids are generated the greater the chance that tensile ductility can be improved. The rate of void generation will be influenced by the rate at which the volume fraction of voids increases and by the strain at which voids is nucleated. The goals would be to minimize the volume fraction of voids at each point of the deformation process and to make void nucleation as difficult as possible.

As a consequence of these observations, we view the proposed work to be primarily an examination of the effects of complex, multiphase microstructures on strength, work-hardening behavior, and ductility or toughness. In the end, of course, the objective would be to examine the formability of such steels, particularly in applications where ductility as measured by, for example, the true strain to fracture in a tensile test or toughness, are important. The microstructure to be examined will be essentially dual phase steels, which we can control through heat treatment and composition, the amounts of ferrite and martensite, and the amount of retained austenite, and TRIP steels. Thus, we would be examining the effects of mixtures of ferrite and martensite or of ferrite and bainite on mechanical behavior. In both systems we have the possibility of introducing different amounts of retained austenite. In this work, we will adhere to one melt practice and aim to maintain constant inclusion types and inclusion volume fractions. We also propose a separate study of the effect of inclusion resistance to void nucleation on formability.

Statement of Objectives

The primary objective of this work is to understand the effects of complex, multi-phase microstructures on the mechanical properties of such steels. To be specific, we are assessing the effect of ferrite in combination with either a martenstic structure or with a bainitic microstructure on mechanical properties. And, we will be comparing the properties of bainitic structures and martensitic structures at the same amounts of ferrite. Furthermore, at each ferrite level the bainitic and martensitic structures should have very similar strength levels. The mechanical properties of interest will be the tensile properties, including strength, work-hardening behavior, the associated uniform strain, and the tensile ductility, which is taken as the true strain to fracture. An important issue is the strain to fracture after reaching the uniform strain. Also, the toughness of the microstructures will be assessed and formability assessed, primarily for forming operations in which ductility and or toughness appears to be an issue. This work will be done using materials which should have the same inclusion characteristics.

In addition, we will explore the effect of the void-nucleation resistance of inclusions on tensile properties and toughness of a low-alloy martensitic steel and assess the effect of inclusion void-nucleation resistance on formability.

Proposed Compositions

We will employ the compositions given in Table 1. The first four compositions will be used in the development of complex microstructures and the assessment of the mechanical properties and void-generating characteristics of these microstructures and the effects of void generation and the fine-scale microstructure on tensile ductility, toughness, and formability. The last two

Table 1. Compositions of proposed heats in weight percent.

Alloy	C	Mn	Ni	Al	Si	Cr	Mo	Ti
MP1	0.2	4.0	–	–	–	–	–	–
MP2	0.2	4.0	–	1.5	–	–	–	–
MP3	0.2	4.0	–	–	1.5	–	–	–
MP4	0.2	4.0	–	–	3.0	–	–	–
M1	0.15	0.5	3	–	2.0	1	0.25	–
M2	0.15	–	3	–	2.0	1	0.25	0.04

compositions are for the assessment of martensitic steels to be used to study the influence of inclusion void-nucleation resistance on formability.

First, we will discuss the heats labeled MP for multiphase. We have pushed the carbon from a more typical 0.15 wt. % primarily to increase the potential strength level and to reduce the martensite-start temperature. The manganese is added to make sure that we can completely austenitize the samples. The manganese is also critical to hardenability. Use of Thermo-Calc indicates that the alpha and gamma two-phase region will be sufficiently large that we will be able to achieve the desired levels of ferrite. The aluminum and silicon are there to delay to higher tempering temperatures the decomposition of retained austenite in martensite on tempering and to repress the precipitation of carbides in the bainite laths and in the austenite during isothermal heat treatments to form bainite. The latter reason is why they are added to low-alloy TRIP steels. Aluminum is preferred to silicon by manufacturers of these steels because silicon promotes the formation of a scale which makes galvanizing difficult. Heat treatments planned for these four compositions to obtain multiphase microstructures will be discussed in the next section.

The last two heats will be given quenched and tempered heat treatments (tempering at 200°C), so that the microstructure will be tempered martensite. The silicon is added to promote higher strength and to promote retained austenite on air-cooling from the austenitizing temperature. The sulfide particles in the first martensitic heat will be small, closely spaced particles of manganese sulphide (MnS). The sulfide particles in the second martensitic heat will be small, closely spaced particles of titanium carbo-sulfide. We have found in highly alloyed steels such as HY180 [20] and AF1410 [21] and in high-strength, low-alloy steels that gettering sulfur as titanium carbo-sulfide can substantially improve fracture toughness because the particles of titanium carbo-sulfide are much more resistant to void nucleation than the particles of MnS. These two martensitic steels will be used to investigate the effect of inclusion resistance to void nucleation on ductility, toughness, and formability. We have previously investigated this composition and have achieved excellent levels of toughness at a carbon content of 0.35 wt. % [22].

Proposed Heat Treatments and Microstructures

Multiphase Microstructures

Current low-alloy TRIP steels are heat treated and processed by hot rolling to obtain a microstructure of pro-eutectoid ferrite and pearlite. They are then cold rolled with the main purpose of the cold reduction to form sheet but the cold rolling does provide the stored energy for the re-crystallization of ferrite in the next step. They are then held in the α-γ two-phase field to form a mixture of about 50% ferrite and 50% austenite. The carbon content of the ferrite is quite low whereas the carbon content of the austenite is on the order of 0.3 wt. %. The material given the inter-critical anneal is then quenched to a reaction temperature during which low-carbon bainite forms, and the remaining austenite is continuously enriched in carbon reaching carbon contents of about 1.3 wt. %. The material is then quenched to room temperature so that the microstructure consists of ferrite, some form of bainite, martensite formed from some of the high- carbon austenite on quenching from the reaction temperature to room temperature and some regions of retained austenite. The martensite would be primarily plate martensite and would itself contain some retained austenite. The austenite could exist as retained austenite associated with the martensite, as finely distributed austenite associated with the bainite and perhaps as large pools of retained austenite not associated with either the martensite or the bainite. The retained austenite would have a high carbon content, and this high carbon content would make it resistant to transforming to martensite during straining. Presumably, the more finely distributed retained austenite associated with the martensite and the bainite would have its mechanical stability further enhanced due to mechanical constraint. It is believed that this mechanically stable austenite is what gives rise to the high work-hardening capacity of these TRIP steels as the retained austenite would continuously transform to untempered plate martensite with increasing strain. However, as Bhadeshia has pointed out, the large volume fraction of the ferrite may be critical to achieving the high work hardening rates and a high uniform strain [16].

Using the four compositions designated for the formation of multiphase microstructures, we plan, broadly speaking, two different types of heat treatments. We will describe these heat treatments and the types of microstructures we expect to see.

Obtaining Mixed Microstructures Consisting of Martensite and Ferrite

Here, it is proposed to obtain microstructures containing ferrite and martensite. The first microstructure will consist of martensite which will be formed by directly quenching to room temperature from a temperature at which the alloy is completely austenitic. The next microstructure will be obtained by using an inter-critical anneal to form 25% ferrite and 75% austenite. This structure will then be quenched to room temperature, and the final microstructure would consist of 25% ferrite and 75% martensite. The third heat treatment would be to form 50% ferrite and 50% austenite in the inter-critical anneal. On quenching to room temperature, the structure would consist of 50% ferrite and 50% martensite. In all cases the martensite would be expected to be lath martensite and with inter-lath films of retained austenite. However, the martensite carbon content will be only about 0.2 wt. % in the wholly martensitic structure. It would be higher for the microstructure obtained by quenching the material held at the first inter-critical anneal in which 25% ferrite would be formed. The martensite formed on quenching the material held at the inter-critical anneal designed to form 50% ferrite would be about 0.4 wt. %. Thus, the three martensites would differ significantly in strength and in the amount of inter-lath retained austenite. The microstructures could be altered by tempering the as-quenched structures at 200°C. This would have the effect of increasing the yield strength of the martensite and lowering its ultimate tensile strength. The mechanical stability of the retained austenite in the martensite would be substantially increased by this tempering treatment. The tempered martensite should have considerably higher ductility and toughness than the as-quenched martensite. The strength of the martensite in the final microstructure would be high indeed, approaching a hardness of 550 Vickers.

We will outline in the next section how we will obtain microstructures containing 0, 25, and 50% ferrite and 100, 75, and 50% bainite. The bainite formed in the three microstructures will have strength levels comparable to those of the martensite formed at 0, 25, and 50% ferrite. Thus, differences in the ductility of the bainitic and martensitic structures for a given amount of ferrite will not be influenced by strength but by details of the microstructure. We can vary the amount of retained austenite in the ferrite-martensite structures by slowing the cooling rate from the austenitizing or inter-critical annealing temperatures (this will increase the amount of retained austenite), by refrigeration of retained austenite to reduce the amount of retained austenite or by using heat treatments to stabilize the retained austenite to increase the amount of retained austenite.

Obtaining Mixtures of Bainite and Ferrite

Here, we will use three basic heat treatments. In the first, the material will be austenitized and then quenched to a series of reaction temperature in which bainite would be formed. There would be no ferrite. In the second, the material would be given an inter-critical anneal to form 25% ferrite, and then samples would be quenched to a series of isothermal hold temperatures in which bainite would be formed. In the third set of experiments, the material would be given an inter-critical anneal in which the ferrite formed would be 50% and then the material would be quenched to a range of isothermal- transformation temperatures in which bainite would be formed. At each isothermal reaction temperature, the effect of isothermal hold time on the microstructure will be evaluated. From what we understand of bainite formation, during the isothermal holds it is expected that the bainite formed would be carbide free and the carbon content of the retained austenite would reach levels approaching 1.3 wt. %, at least with the addition of silicon or aluminum. On quenching from the isothermal hold temperature, we would expect to have a microstructure consisting of low-carbon bainite laths, films of retained austenite interspersed through the bainite laths, pools of high-carbon retained austenite, and some plate martensite, which is formed from the high-carbon austenite on quenching from the isothermal hold temperature [23–27]. The plate martensite formed from this high-carbon austenite would, of course, contain retained austenite. The possibility of carbide precipitation cannot be excluded either in the bainite laths or associated with the retained austenite. However, the aluminum and silicon additions are believed to stabilize the structure with respect to cementite formation. These microstructures could also be tempered. For example, it might be interesting to temper at 200°C in order to increase the mechanical stability of the austenite, at least the austenite within the bainite laths and the martensite.

Whether or not such tempering would improve the mechanical stability of the austenite in pools in the microstructure is not known. We note that it has been reported that the quench rate from these isothermal holds can significantly increase the amount of total retained austenite in the structure. Thus, retained austenite could be varied by varying the cooling rate from the reaction temperature. Miihkinen and Edmonds [23–25] found that refrigeration in liquid nitrogen had no effect on the amount of retained austenite in their bainitic microstructures.

The Effect of Inclusion Void- Nucleation Resistance on Formability

The two martensitic steels will be heat treated in the following manner. They will be austenitized at 900°C for one hour, oil- quenched to room temperature, and tempered at one hour at 200°C. The microstructures will consist of lath martensite and a small amount of inter-lath retained austenite. The microstructures of the two steels will differ in that the titanium-modified steel will contain some small titanium carbides which might have an effect on prior austenite grain size and a different type of sulfide. In the titanium-modified heat, the sulfides will be titanium carbo-sulfides and in the other heat the sulfides will be MnS. Our expectation is that the titanium-modified heat will have a substantially higher true strain to fracture and a substantially higher toughness as the particles of titanium carbo-sulfide are much more resistant to void nucleation than the particles of MnS. We intend to compare the formability of the two heats. Primarily we will be interested in forming operations where ductile fracture has precluded use of other high-strength sheet steels. However, we have found in previous studies of the deformation and forming of sheet steels that voids at inclusions were nucleated well before reaching the forming limit and the extent of void growth was considerable before the forming limit was reached, as defined by a strain at which local thinning of the sheet was observed. There are theoretical studies in support of the idea that void generation can influence formability by hastening the onset of local thinning [28–30], and we will use these materials to test this idea in more conventional forming operations.

Results

We have accomplished the following. First, we have melted heats of the six desired compositions. Second, we have begun processing these materials into one-half-inch plate and into sheet. Third, we have begun to establish the heat treatment for the compositions MP1, MP2, MP3, and MP4 to obtain the desired mixtures of ferrite and martensite and the desired mixtures of ferrite and bainite in each of these four compositions. Fourth, we have heat treated Charpy impact specimens and tensile specimens for the two heats of the compositions M1 and M2 which are to be used in the assessment of void-nucleation resistance of inclusions on the formability of steel sheet.

Melting and Composition of Heats

The heats having the composition of MP1, MP2, MP3, MP4, M1, and M2 have been prepared in the following by vacuum induction melting using aluminum additions to deoxidize the heats. The compositions of the six heats are given in Table 2.

Table 2. Compositions of experimental heats in weight percent.

Alloy	C	Mn	Ni	Cr	Mo	Ti	Al	Si	P	S	O_2	N_2
MP1	0.188	3.84	<0.002	0.01	0.002	<0.002	0.021	0.015	0.005	0.0037	0.0021	0.0041
MP2	0.183	3.73	<0.002	0.01	0.021	<0.002	1.437	0.021	0.005	0.0024	0.0033	0.0041
MP3	0.197	4.22	<0.002	0.011	0.003	<0.002	0.030	1.461	0.005	0.0031	0.0013	0.0056
MP4	0.205	4.27	<0.002	0.010	0.003	0.002	0.033	2.837	0.004	0.0025	0.0027	0.0055
M1	0.180	0.49	3.013	0.983	0.244	<0.002	0.031	1.979	0.003	0.0027	0.0015	0.0018
M2	0.158	0.007	2.927	0.971	0.248	0.038	0.025	1.945	0.002	0.0034	0.0013	0.0014

Processing to Plate and Sheet

From each of material, we wanted 1.27 cm thick flat plate as well as sheet material with a thickness of 0.1397cm.

The ingots after melting were 12.7 cm × 27.9 cm × 45.72 cm. Each ingot was hot rolled from a thickness of 12.7 cm to a thickness of 2.54 cm using a reheat temperature of 1,250°C and a finishing temperature of 870°C. They were then air- cooled to room temperature. Each of the slabs thus produced were cut into four 30.5 cm lengths. One of these four slabs was rolled from a thickness of 2.54 cm to a thickness of 1.27 cm using three passes and a reheat temperature of 1,100°C and a finishing temperature of 920°C. The finished plates were then air-cooled to room temperature. This resulted in the 1.27-cm- thick plate to be used in initial studies.

To prepare sheet material, two of the slabs of a thickness of 2.54 cm were further hot rolled to a thickness of 0.457 cm. This was done in five passes using a reheat temperature of 1,250°C and a finishing temperature of 920°C. The strip thus produced was water-spray cooled to 650°C, placed in a furnace set at 600°C, and then furnace-cooled to room temperature. Beginning with the two strips of a thickness of 0.457 cm, the sheet material is being produced by two different routes. The two different routes are used to obtain two different surfaces. The two different routes are termed Process A and Process B. In process A, one of the hot- rolled strips is sheared into five pieces each having a length of 25.4 cm and a thickness of 0.457 cm. Two of these pieces were sent to the machine shop and surface ground to a thickness of 0.3175 cm. Then, after the surface grinding they were cold rolled from 0.3175 cm to a thickness of 0.1397 cm. This results in two sheets of a thickness of 0.1397 cm and a width of 27.94 cm and a length of 50.8 cm. In process B a hot-rolled strip of a thickness of 0.457 cm is sheared into five pieces of a length of 25.4 cm and a thickness of 0.457 cm. Then, two of these pieces are grit blasted and pickled to remove scale. Then the pieces are cold rolled from the thickness of 0.457 cm to a thickness of 0.201 cm. This will result in two sheets of a thickness of 0.201 cm and a width of 27.94 cm and a length of 50.8 cm. Thus, the sheet produced by process B is thicker and it would be possible to grind surfaces of pieces of this sheet which have been heat treated and still arrive at a final thickness of 0.1397 cm.

Determining Solution Treatment Temperatures for Compositions Used to Produce Multiphase Microstructures

For the compositions MP1, MP2, MP3, and MP4, we want to obtain structures which are 100% martensite, 25% ferrite and 75% martensite, and 50% ferrite and 50% martensite, and we also want microstructures which are 100% bainite, 25% ferrite and 75% bainite, and 50% ferrite and 50% bainite. Thus, we need to determine for each of the four compositions the temperatures at which we have 25% ferrite and 75% austenite and 50% ferrite and 50% austenite. To do this we began with using Thermo-Calc to determine the phase diagrams relevant to our compositions.

Based on these phase diagrams, we have selected a number of temperatures spaced 20°C apart for each of the four alloys and have held samples at these temperatures for one hour and then oil-quenched. The austenite which was present at a given temperature will transform to martensite on quenching, and the ferrite present at that temperature will remain ferrite on quenching. Thus by determining the volume fractions of ferrite and martensite in a quenched sample, we can determine the volume fractions of austenite and of ferrite present at the temperature of interest prior to quenching.

For the alloy MP1, the temperatures selected were 900°C, 800°C, 780°C, 760°C, 740°C, 720°C, 700°C, 680°C, and 660°C. For the alloy MP3, which contains 1.5 wt. % silicon, the same temperatures were selected. For the alloy MP4, which contains 3 wt. % silicon, the temperatures selected were 900°C, 800°C, 780°C, 760°C, 740°C, 720°C, and 700°C. The temperatures selected for the composition MP2, which contains 1.5 wt. % aluminum, were 1,000°C, 950°C, 900°C, 880°C, 860°C, 840°C, 820°C, 800°C, 780°C, 760°C, and 740°C. Samples from each temperature selected for each alloy are now being mounted for metallography. From these specimens we will obtain a plot of the amount of ferrite as a function of temperature for each of the four alloys, and we can then decide on the solution treating temperatures which result in 25% ferrite and 50% ferrite for each of the four alloys. In addition, we have mounted samples of the hot-rolled plate for each of the compositions to determine the initial microstructure for each of the alloys.

We have also prepared Charpy impact specimens for each of the selected temperatures for each of the four alloys which were tempered at 200°C for one hour From these we have obtained the Charpy impact energy and hardness for each alloy as a function of solution treating temperature, at least for the ferrite-martensite mixed microstructures.

The hardness levels for all four heats were about 72 Rockwell-A at higher solution treating temperatures. The hardness of the alloy containing 1.5 wt. % aluminum begins to decrease with decreasing solution treatment temperature for solution treatment temperatures less than 800°C. This decrease begins at 780°C for the alloy containing 3 wt. % silicon and begins at a solution treating temperature of 740°C for the alloy with 1.5 wt. % silicon and for the alloy containing no aluminum or silicon. The Charpy impact values also change with solution treating temperature. At high hardness levels the Charpy impact energy of the alloy containing 1.5 wt. % silicon is the highest of the four alloys and is about 70 J. However, this Charpy impact energy is less than those of the two high-nickel steels being used to assess the effect of inclusion void nucleation resistance on formability.

Once we have established the appropriate solution treating temperatures for the four alloys, we will be able to heat treat test specimens which contain 100% martensite, 25% ferrite and 75% martensite, and 50% ferrite and 50% martensite. However, before we can produce the structures which are bainitic, 25% ferrite and 75% bainite and 50% ferrite and 50% bainite, we will need to determine for each solution treatment temperature for the four alloys the martensite-start temperature, and this will be done by dilatometry.

Mechanical Properties of Alloys to be Used to Investigate Effect of Inclusion Void-Nucleation Resistance on Formability

Charpy impact and tensile specimens have been tested for the two alloys M1 and M2. The sulfides in M1 are manganese sulfides, and the sulfides in M2 are titanium carbo-sulfides. The heat treatment was austenitizing at 900°C, oil quenching and then tempering at 200°C. The yield strengths and ultimate tensile strengths for the two heats were about 1,100 MPa and 1,400 MPa, respectively. The tensile percent reduction-in-areas were 64.2% for the heat in which the sulfur was gettered as MnS and 66.2% for the heat in which the sulfur was gettered as titanium carbo-sulfide particles. The Charpy impact energies were 124 J for the heat in which the sulfur was gettered as MnS and 113 J for the heat in which the sulfur was gettered as titanium carbo-sulfide.

References

1. W. F. Hosford and R. M. Caddell. *Metal Forming: Mechanics and Metallurgy*, Prentice-Hall, Englewood Cliffs, N.J., 1983, p. 299.
2. K. Sumimoto, J. Sakaguchi, T. Iida, and T. Kashima, Stetch-flangeability of High-strength TRIP Type Bainitic Sheet Steel, ISIJ international, Vol. 40, 2000, 920.

3. K. Sumimoto, A. Kanda, R. Kikuchi, S. Hasimoto, T. Kashima, and S. Ikeda, Ductility and Formability of Newly Developed High Strength Low Alloy TRIP-aided Sheet Steels with Annealed Martensite Matrix, ISIJ international, Vol. 42, 2002, 910.
4. K. Sugimoyo, B. Yu, Y. Mukai, and S. Ikeda, Microstructure and Formability of Aluminum Bearing TRIP-Aided Steels with Annealed Martensite Matrix, ISIJ international, Vol. 45, 2005, 1194.
5. K. Yamazaki. M. Oka, H. Yasuda, Y. Mizuyama, and H. Tsuchiya, Recent Advances in Ultrahigh-Strength Sheet Steels for Automotive Structural Use, Nippon Steel Technical Report No. 64, January 1995, 37.
6. Y. J. Park, A. P. Coldren, and J. W. Morrow, Effect of Martensite Bands and Elongated Manganese Sulfide Inclusions on the Formability of Dual-Phase Steels, Proceedings on the Conference on the *Fundamentals of Dual Phase Steels*, held at Chicago, 1981, p. 485.
7. Nishimoto, Y. Hosoya, and K. Nakaoka, Relation Between Hole Expansion Formability and Metallurgical Factors in Dual-Phase Steel Sheets, Proceedings on the Conference on the *Fundamentals of Dual Phase Steels*, held at Chicago, 1981, p. 447.
8. C. D. Horvath and J. R. Fekete, Opportunities and Challenges for Increased Usage of Advanced High Strength Steels in Automotive Applications, International Conference on Advanced High Strength Sheet Steels for Automotive Applications Proceedings, Winter Park, Colorado, 2004, p. 3.
9. J. Van Slycken, P. Verleysen, J. Degrieck, L. Samek, and B.C. De Cooman, High-Strain-Rate Behavior of Low-Alloy Multiphase Aluminum and Silicon Based Transformation Induced Plasticity Steels, Metall. and Mat. Transactions A, Vol. 37A, 2006, 1527.
10. S. Traint, A. Pichler, K. Hauzenberger, P. Stiaszny, and E. Werner, Influence of Silicon, Aluminum Phosphorus and Copper on the Phase Transformations of Low Alloyed TRIP Steels, Steel Research, Vol. 73, 2002, 259.
11. T. Lung, J. Drillet, A. Couturier, and C. Olier, Detailed Study of the Transformation Mechanisms in Ferrous TRIP Aided Steels, Steel Research, Vol. 73, 2002, 218.
12. H. Matsuda, F. Kitano, K. Hasegawa, T. Urabe, and Y. Hosoya, Metallurgy of Continuously Annealed High Strength TRIP Steel Sheet, Steel Research, Vol. 73, 2002, 211.
13. B. Ehrhardt, T. Gerber, and T.W. Schaumann, Approaches to Microstructural Design of TRIP and TRIP Aided Cold Rolled High Strength Steels, International Conference on Advanced High Strength Sheet Steels for Automotive Applications Proceedings, Winter Park, Colorado, 2004, p. 39.
14. K. Sugimoto, S. Hashimoto, and S. Ikeda, Ultra High Strength Low Alloy TRIP-Aided Sheet Steels With Bainitic Ferrite Matrix, International Conference on Advanced High Strength Sheet Steels for Automotive Applications Proceedings, Winter Park, Colorado, 2004, p. 63.
15. Y. R. Cho, S. K. Kim, H. N. Han, Y. S. Jin, and J. H. Jung, Development of Hot Rolled High Strength TRIP Steel With a Tensile Strength of 780MPa Grade, International Conference on Advanced High Strength Sheet Steels for Automotive Applications Proceedings, Winter Park, Colorado, 2004, p. 71.
16. H.K.D.H. Bhadeshia, TRIP-Assisted Steels. ISIJ international, Vol. 42, 2002, 1059.
17. P. J. Jacques, E. Girault, Ph. Harlet, and F. Delannay, The Developments of Cold-rolled TRIP-assisted Multiphase Steels. Low Silicon-assisted Multiphase Steels, ISIJ international, Vol. 41, 2001, 1061.
18. M. Saeglitz and G. Krauss, Deformation, Fracture, and Mechanical Properties of Low-Temperature-Tempered Martensite in SAE 43xx Steels, Metall. and Mat. Transactions A, Vol. 28A, 1997, 377.

19. S. B. Lee, J. G. Speer, and D. K. Matlock, The Influence of Phase Distributions and Interfaces on Fracture and formability of High Strength Sheet Steels, International Conference on Advanced High Strength Sheet Steels for Automotive Applications Proceedings, Winter Park, Colorado, 2004, p. 383.
20. J. L. Maloney and W. M. Garrison Jr., The Effect of Sulfide Type on the Fracture Behavior of HY180 Steel, Acta Materialia, Vol. 53, 2005. 533.
21. L. E. Iorio and W. M. Garrison Jr., The Effects of Titanium Additions on AF1410 Ultra-high Strength Steel. Metallurgical and Materials Transactions A, Vol. 37A, 2006, 1165.
22. W. M. Garrison, Jr., The Effect of Silicon and Nickel Additions on the Inclusion Spacing and Fracture Toughness of a 0.4 Carbon Low Alloy Steel, Metall. Trans. A, Vol. 17A, 1986, 669.
23. V.T.T. Miihkinen and D. V. Edmonds, Microstructural Examination of Two Experimental High Strength Bainitic Low-Alloy Steels Containing Silicon, Mat. Sci. and Eng., Vol. 3, 1987, 422.
24. V.T.T. Miihkinen and D. V. Edmonds, Tensile Deformation of Two Experimental High Strength Bainitic Low-Alloy Steels Containing Silicon, Mat. Sci. and Eng., Vol. 3, 1987, 432.
25. V.T.T. Miihkinen and D. V. Edmonds, Fracture Toughness of Two Experimental High Strength Bainitic Low-Alloy Steels Containing Silicon, Mat. Sci. and Eng., Vol. 3, 1987, 441.
26. H.K.D.H. Bhadeshia and D. V. Edmonds, Bainite in Silicon Steels: New Composition-Property Approach, Part 1, Metal Science, Vol. 17, 1983, 411.
27. H.K.D.H. Bhadeshia and D. V. Edmonds, Bainite in Silicon Steels: New Composition-Property Approach, Part 2, Metal Science, Vol. 17, 1983, 420.
28. Z. Narciniak and K. Kuczynski, Limit Strains in the Processes of Stretch-Forming Sheet Metal, Int. J. Mech. Sci. Vol. 9, 1967, 609.
29. J. H. Schmitt and J.M. Jalinier, Damage in Sheet Metal Forming-I. Physical Behavior, Acta Metall., Vol. 30, 1982, 1789.
30. J. H. Schmitt and J. M. Jalinier, Damage in Sheet Metal Forming-II. Plastic Instability, Acta Metall., Vol. 30, 1982, 1799.

O. Development of Novel Finite-Element Simulation Tools that Implement Crystal-Plasticity Constitutive Theories Using an Efficient Spectral Framework

Principal Investigator: Surya R. Kalidindi
Drexel University
Department of Materials Science and Engineering, Philadelphia, PA 19104
(215) 895-1311; fax: same; e-mail: skalidin@coe.drexel.edu

Technology Area Development Manager: Joseph A. Carpenter
(202) 586-1022; fax: (202) 586-1600; e-mail: joseph.carpenter@ee.doe.gov

Field Project Officer: Aaron D. Yocum
(304) 285-4852; fax: (304) 285-4403; e-mail: aaron.yocum@netl.doe.gov

---

Contractor: Drexel University
National Science Foundation (NSF) Award CMMI 0727931, jointly funded by NSF and DOE

Objective

- Develop spectral crystal-plasticity-based, finite-element tools for simulating deformation-processing operations and final mechanical performance of advanced high-strength steel (AHSS) components. A salient feature of these tools is that they can be executed with computational times that are comparable to the tools currently used by the industry, which largely employ phenomenological material models.
- Systematically introduce the inherent complexities of the physics of plastic deformation at multiple length scales in the spectral crystal-plasticity framework. The goal is to start with crystallographic slip and then proceed to deformation twinning. From the perspective of length scales, the goal is to start with grain-scale deformation and then proceed to incorporating explicitly the mechanics of dislocation networks.
- Develop computationally-efficient spectral approaches for higher-order homogenization theories that utilize local spatial correlations for a rigorous quantification of the interactions at the lower length scales in the material.
- Critical validation of the tools and methodologies developed in this work by comparisons with experiments and numerical predictions obtained by other approaches.

Approach

- Capture solutions at the lower length scales in an efficient spectral database. Although building the database requires substantial effort, it is a one-time activity. Once an appropriate database is built, all subsequent computations requiring solutions at the lower length scales can be accomplished with minimal computational effort and resources.
- Explore the use of discrete Fourier transforms (DFTs) for building such databases, as they offer tremendous computational efficiency.

Accomplishments

- Demonstrated that it is possible to speed up the crystal-plasticity calculations in cubic metals that deform by crystallographic slip by two orders of magnitude using a compact database of DFTs. Observed that a relatively small number of dominant transforms adequately captured the dependence of the stresses, the lattice spins, and the strain hardening in individual crystals on their lattice orientation and the applied-deformation mode.

- The feasibility of the basic concepts underlying the spectral approaches for capturing higher-order structure-to-structure evolution linkages at the lower length scales has been demonstrated by taking a specific example in dislocation dynamics. In particular, it was demonstrated that the dislocation dynamics solutions from a previously-developed code at the Indian Institute of Science (Bangalore, India) can be captured efficiently in a spectral database. This database is now capable of providing solutions that are equivalent to the original formulation for a very broad set of initial conditions and strain rates, but with significantly-reduced computational effort. The main advantage of our approach is that it is now feasible to explore a rigorous multiscale simulation involving multiple length scales with very reasonable computational resources.

Future Direction

- Incorporate the spectral crystal-plasticity tools developed for cubic metals deforming by crystallographic slip in a finite-element code used in simulating metal-forming operations. In particular, we will focus our efforts on FORGE3 and ABAQUS.
- Extend the spectral linkages to incorporate deformation twinning and details of dislocation networks and their evolution during plastic deformation.
- Extend the spectral linkages to include grain-scale interactions using a framework newly developed by our research group.

Introduction

Crystal-plasticity theories [1–6] are used extensively in understanding and predicting the evolution of the underlying microstructure (mainly texture-related aspects) and the concomitant anisotropic stress-strain response in polycrystalline metals subjected to finite plastic strains. Such physics-based constitutive theories are highly desirable for conducting more accurate simulations of various metal manufacturing/fabrication processes, since they provide better understanding and predictions of the material behavior [7–9]. The main deterrent in the more widespread use of these theories (in place of the highly simplified phenomenological isotropic plasticity theories typically used) is the fact that the implementation of the crystal-plasticity theories in a finite-element modeling framework demands substantial computational resources and highly- specialized expertise.

In recent work [10, 11], we have identified that the crystal-plasticity solutions for face-centered cubic (fcc) polycrystals experiencing rigid-viscoplastic deformations can be organized efficiently as a set of functions that describe the dependence of the stresses, the lattice rotations, and the total slip rates in individual crystalline regions on their lattice orientation and the imposed velocity gradient tensor (quantifying the deformation mode) on those regions. The domain of these functions was defined to be the product space comprising all possible crystal orientations and all possible isochoric deformation modes.

In this work, we have explored the representation of all of the functions capturing the crystal-plasticity solutions in their complete respective domains using DFTs. The most remarkable discovery in this new direction was the recognition that only a limited number of the dominant DFTs were adequate to recover the functions of interest on their entire respective domains. This new approach was found to be able to speed up the crystal-plasticity computations by about two orders of magnitude compared to the traditional approaches used in crystal plasticity computations. A particularly attractive feature of this new approach is that it provides the user with tremendous flexibility in making trade-offs between accuracy and computational speed. In other words, the new spectral database described here will allow the user to perform a large number of very quick simulations at a lower than desired accuracy, identify the specific ones that appear to produce promising results, and redo these much more accurately (at a higher computational cost).

The above approach has been applied here initially to rigid-plastic Taylor-type (full constraints) model calculations for fcc polycrystals with equal hardening of all slip systems, where it is assumed that all constituent crystals experience the same deformation history. Development of higher-order models requires a more sophisticated approach that partitions the imposed deformation on the polycrystal to each of the constituent grains while taking into account the details of its neighborhood. With the goal of extending the spectral crystal plasticity framework to include details at lower length scales as well as higher-order interactions, we have a novel spectral approach in this work. This new approach and its potential for facilitating physics-based, multiscale models will be discussed in this report.

Spectral Crystal Plasticity Framework

The crystal-plasticity computations typically demand significant computational resources because of the low value of strain-rate sensitivity parameter denoted by *m* in the rate-dependent crystal-plasticity formulations [1] (which makes the resulting system of algebraic equations numerically extremely stiff). Moreover, the same computations are likely to be repeated several times in simulations performed by the conventional approach because the results of computations in any one time step are immediately forgotten when the computations advance to the next time step. In the spectral crystal-plasticity approach [10, 11], we have established efficient spectral representations for the essential functions capturing the solutions to the traditional crystal-plasticity theory. In other words, we have established the functions $\sigma'_{ij}(g,\mathbf{L})$, $W^*_{ij}(g,\mathbf{L})$, and $\sum_{\alpha}\left|\dot{\gamma}^{\alpha}\right|(g,\mathbf{L})$, where g is the crystal lattice orientation and L is the applied velocity gradient tensor. In any given time step in the simulation of the deformation process, these functions are then used to compute all of the needed microscale and macroscale field quantities that would be typically computed by the traditional crystal-plasticity approach.

In the approach developed here, the functions mentioned above are stored as their DFTs. It is typically observed that only a small fraction of the DFTs are numerically significant compared to the others. The numbers of numerically-significant DFTs (henceforth referred to as dominant DFTs) varied for the different field variables. In particular, it was noted that by retaining only about 500 dominant transforms for the stress tensor, the spin tensor and the total shearing rate, the average error was well below 5%.

In order to demonstrate the validity of the new DFT-based spectral approach developed in this work, we simulated plane strain compression on polycrystalline face-centered cubic (fcc) metals to a true strain of $\varepsilon = -1.0$ along the compression axis. The polycrystal was assumed to possess a random initial texture that was captured by a set of 1000 discrete crystal orientations. We computed the deformed textures and the anisotropic stress-strain curves using the Taylor-type model, both by the traditional approach and the new DFT spectral approach based on the dominant transforms described here. The predicted textures from the traditional approach are compared against those obtained from the DFT method using a minimal set of dominant transforms (134 for stress, 255 for lattice spin, and 182 for shearing rate) in Figure 1(a), while the corresponding predictions of the stress-strain responses are shown in Figure 1(b).

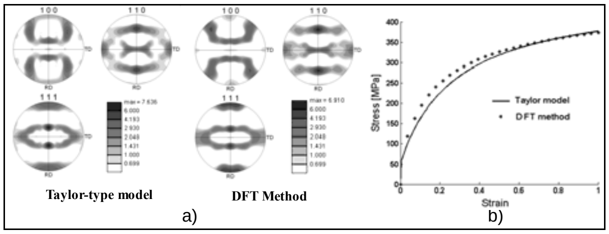

Figure 1. Comparison of the predictions from the DFT-spectral method using a minimal set of dominant transforms against the corresponding predictions from the conventional Taylor-type model for plane strain compression of oxygen-free high-conductivity (OFHC) copper: (a) pole figures, and (b) stress-strain curves.

Another calculation was performed using more of the dominant DFTs (500 for stress and shearing rate and 3000 for lattice spin) and its comparison with predictions from the traditional approach is presented in Figure 2 (note the slight improvement in the accuracy of the spectral approach between Figure 1 and Figure 2). It is seen that the DFT method described here accurately reproduced all of the features of the Taylor-type model predictions. This simulation took 108 seconds on a regular Pentium 4 desktop personal computer

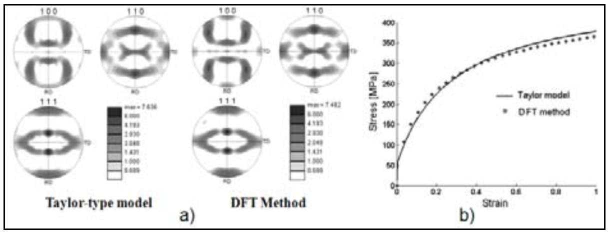

Figure 2. Comparison of the predictions from the DFT-spectral method, using more dominant transforms against the corresponding predictions from the conventional Taylor-type model for plane strain compression of OFHC copper: (a) pole figures, and (b) stress-strain curves.

using the conventional crystal-plasticity algorithms and only 0.7 seconds using the minimal set of the dominant DFTs, and 2.3 seconds using the larger number of dominant DFTs. This establishes that the spectral approach developed in this work has the potential to accelerate the computations by about two orders of magnitude.

Higher-Order Spectral Linkages

There have been several notable accomplishments in the development and validation of physics-based numerical models (e.g., atomistic simulations, finite- element models, phase-field models) for exploring structure-property-processing relationships at various length scales of interest in a given material system. It is now possible to incorporate very complex physics in these models that accurately accounts for the anisotropy inherent to the local behavior at any selected length scale. However, there is a critical need to couple these simulations over several length scales to predict macroscale performance characteristics, which tantamounts to executing sophisticated numerical models within other sophisticated numerical models in a hierarchical manner. Currently no computationally- efficient algorithms to accomplish a robust and accurate scale-transition exist.

As a specific example to demonstrate the potential of spectral approaches, we have studied the phenomenon of the Portevin-Le Chátelier (PLC) effect. This problem is of major interest to automobile manufacturers. The PLC effect is characterized by a stress-strain curve that exhibits repeated yield drops that are dependent on strain rate and temperature along with undesirable deformation bands on the surface of panel. The PLC effect is a plastic instability that is caused by dynamic strain aging (DSA), i.e., the interaction of mobile dislocations with diffusing solute atoms. During plastic deformation, mobile dislocations become arrested at solute atoms. When a sufficient stress is applied, the arrested dislocations become mobilized again until they encounter another obstacle. The remobilization of the dislocations occurs on a very fast time scale resulting in the drops in the stress-strain curve, resulting in the PLC effect.

A well-established model proposed by Ananthakrishna et al. [12] simulates the spatio-temporal details of the PLC effect. The model captures the cooperative behavior of the dislocations for the different band types while capturing the slow and fast time scales associated with the phenomenon. The governing set of differential equations in this model describe the kinetics of the evolution of the mobile dislocation densities (ρ_m), the immobile dislocation densities (ρ_{im}), the Cottrell-type dislocation densities (ρ_c), and the effective stress (ϕ). These equations can be expressed as:

$$\frac{\partial \rho_m(x,t)}{\partial t} = -b_o\rho_m - \rho_m\rho_{im} + \rho_{im} - a\rho_m + \phi_{eff}^m \rho_m + \frac{D}{\rho_{im}} \frac{\partial^2 \left(\phi_{eff}^m(x)\rho_m(x)\right)}{\partial x^2}$$

$$\frac{\partial \rho_{im}(x,t)}{\partial t} = b_o\left(b_o\rho_m^2 - \rho_m\rho_{im} - \rho_{im} + a\rho_c\right)$$

$$\frac{\partial \rho_c(x,t)}{\partial t} = c\left(\rho_m - \rho_c\right)$$

$$\frac{\partial \phi(t)}{\partial t} = d\left(\dot{\varepsilon} - \frac{1}{L}\int_0^L \phi_{eff}^m(x)\rho_m(x)\,dx\right)$$

$$\phi_{eff}^m(x) = \left(\phi - h\,\rho_m^{1/2}\right)^m$$

where a, b_o, c, d, D, and h are parameters that are empirically fit to experimental observations. Varying the value of the imposed strain rate, $\dot{\varepsilon}$, results in three different types of bands that are experimentally verified. A stiff differential solver is required to solve this equation.

Casting the interactions between each of the dislocation densities and their spatial variations will dramatically improve the computational efficiency of solving these equations. For this purpose, we seek spectral linkages that can be expressed as:

$$\Im[\dot{\rho}_m] = \sum_{H}\sum_{K} A_k^h M_k^h(\rho_m, \rho_{im}, \rho_c)$$

$$\Im[\dot{\rho}_{im}] = \sum_{H}\sum_{K} B_k^h M_k^h(\rho_m, \rho_{im}, \rho_c)$$

$$\Im[\dot{\rho}_c] = \sum_{H}\sum_{K} \Gamma_k^h M_k^h(\rho_m, \rho_{im}, \rho_c)$$

where A, B, and Γ are the spectral influence coefficients, and $\Im[\;]$ denotes the DFT operation. M describes the DFT of the microstructure function that captures the dislocation densities discretized into H bins (h enumerates these bins).

After the database of coefficients is built, the instantaneous changes in dislocation densities can be reasonably well predicted using these computationally-efficient linkages as shown in Figure 3. Figure 4 shows the evolution of the mobile dislocations using the Euler Forward method in conjunction with spectral influence coefficients.

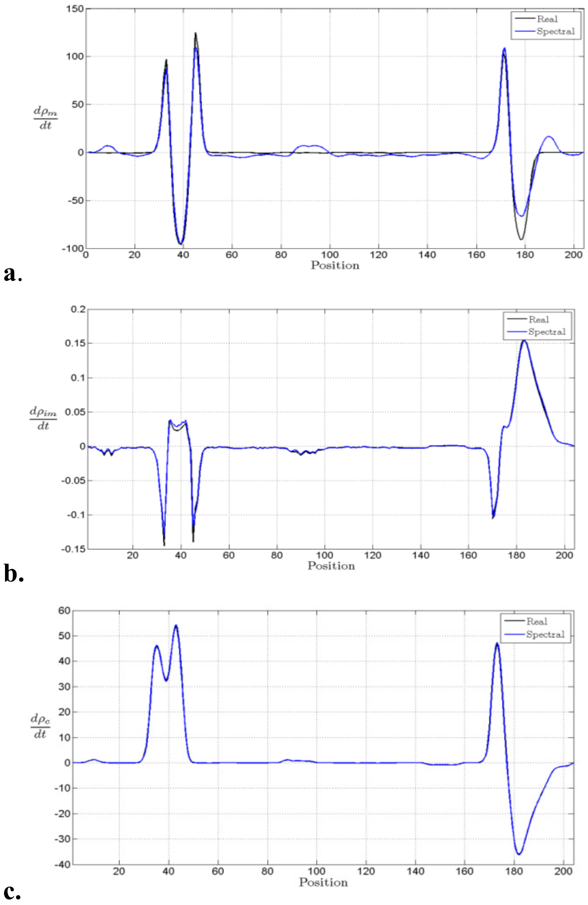

Figure 3. A comparison between the predictions from solving the dynamical system of equations and those from the spectral methods at an intermediate time step in the evolution. a. Mobile, b. Immobile, and c. Cottrell-type components.

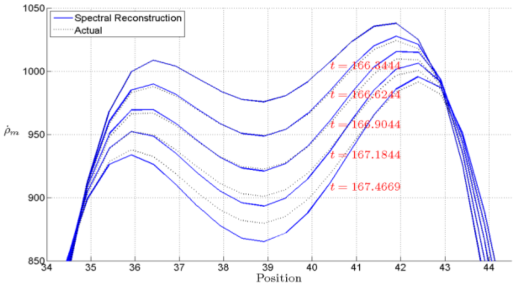

Figure 4. Comparison of the predictions for the temporal evolution of the mobile dislocations from actually solving the governing equations and those predicted by the spectral database coefficients.

Conclusions

It has been demonstrated that it is possible to speed up the crystal-plasticity calculations by two orders of magnitude in fcc metals using a compact database of DFTs. It was seen that a limited set of dominant transforms adequately captured the dependence of the stresses, the lattice spins, and the strain hardening in individual crystals as a function of their lattice orientation and the applied-deformation mode. A computationally-efficient spectral interpolation scheme was devised and implemented to recover values of these functions for any selected combination of crystal orientation and deformation mode using only the dominant DFTs. The case studies conducted thus far revealed tremendous savings in the computational time and provide a significant incentive for incorporation into the finite- element simulations of bulk deformation-processing operations.

It has also been demonstrated that spectral approaches can be used to capture the complex interactions that occur in a higher-order composite system. In particular, it was demonstrated that it is possible to capture the complex physics of the dynamics of dislocation systems controlling the PLC effect in a suitable spectral database. The broad range of strain rates and the complex description of the microstructural states involved in this problem provide unambiguous testament to the potential of the spectral approaches in multiscale materials modeling.

Publications

1. M. Knezevic, H. F. Al-Harbi, S. R. Kalidindi, "Crystal Plasticity Simulations Using Discrete Fourier Transforms," submitted to Acta Materialia (2008).

References

1. R. J. Asaro and A. Needleman, Acta Metallurgica et Materialia 33 (1985) 923–953.
2. C. A. Bronkhorst, S. R. Kalidindi, and L. Anand, Philosophical Transactions of the Royal Society of London Series A-Mathematical Physical and Engineering Sciences 341 (1992) 443–477.
3. S. R. Kalidindi, C. A. Bronkhorst, and L. Anand, Journal of the Mechanics and Physics of Solids 40 (1992) 537–569.
4. L. Delannay, S. R. Kalidindi, and P. Van Houtte, Materials Science and Engineering A 336 (2002) 233–244.
5. P. Van Houtte, L. Delannay, and S. R. Kalidindi, International Journal of Plasticity 18 (2002) 359–377.
6. B. S. R. Kalidindi and R. Doherty, Proceedings of the Royal Society of London: Mathematical, Physical and Engineering Sciences. (2004).
7. D. Raabe, Z. Zhao, and F. Roters, Steel Research 72 (2001) 421–426.
8. D. Raabe, Y. Wang, and F. Roters, Computational Materials Science 34 (2005) 221–234.
9. W. F. Hosford and R. M. Caddell, Metal forming mechanics and metallurgy, Prentice-Hall, Inc, 1993.
10. S. R. Kalidindi, H. K. Duvvuru, and M. Knezevic, Acta Materialia 54 (2006) 1795–1804.
11. M. Knezevic, S. R. Kalidindi, and D. Fullwood, International Journal of Plasticity 24 (2008) 1264–1276.
12. G. Ananthakrishna and M. S. Bharathi, Physical Review E 70, 02611.

P. Advanced High-Strength Steel through Paraequilibrium Carbon Partitioning and Austenite Stabilization

Principal Investigator: Gary M. Michal
Case Western Reserve University
Department of Materials Science and Engineering
Cleveland, OH 44106
(216) 368-5070; fax: (216) 368-3209; e-mail: gmm3@case.edu

Co-Principal Investigator: Arthur H. Heuer
Case Western Reserve University
Department of Materials Science and Engineering
Cleveland, OH 44106
(216) 368-3869; fax: (216) 368-3209; e-mail: ahh@case.edu

Technology Area Development Manager: Joseph A. Carpenter
(202) 586-1022; fax: (202) 586-1600; e-mail: joseph.carpenter@ee.doe.gov

Field Project Officer: Aaron D. Yocum
(304) 285-4852; fax: (304) 285-4403; e-mail: aaron.yocum@netl.doe.gov

Contractor: Case Western Reserve University
National Science Foundation (NSF) Contract No.: CMMI 0727583, jointly funded by NSF and DOE

Objective

- The development of a third generation of advanced high-strength steel (AHSS) possessing:
  - strength and ductility combinations exceeding those of ferritic first-generation AHSS.
  - the ability to be manufactured much more economically than austenitic second-generation AHSS.
- Establish a steel chemistry that fulfills the three transformational characteristics required to achieve a double-stabilization thermal-processing scheme:
  - the steel can be completely austenitized at 900°C.
  - the hardenability of the steel is great enough that the bainite transformation can be avoided during a liquid-metal quench to 450°C.
  - carbide formation is suppressed during aging somewhere in the range of 300 to 500°C during which carbon will partition from the martensite phase to the austenite phase.

Approach

- The strength/ductility goal of a third-generation AHSS can be achieved by employing a microstructure comprised of martensite and a significant volume fraction of austenite.
- The austenite must have sufficient stability such that it transforms to martensite only at progressively higher levels of strain, so that the work-hardening rate of the steel concurrently increases in a continuous fashion.
- A high volume fraction of austenite must be obtained within the constraints of:
  - a carbon content low enough that weldability is not severely compromised.
  - the alloy levels in the steel do not greatly increase its price.
  - the processing route for the steel is consistent with current sheet-steel commercial production practice.
- Use of a double-stabilization thermal-processing scheme to increase the amount of austenite:
  - the steel will be held for a brief time at approximately 450°C for its first stabilization.

  - the second stabilization will be an aging of the steel at a temperature at which carbides will not form while carbon partitions from the martensite phase to the austenite phase.

Accomplishments

- A thermal-processing facility was constructed based upon four crucible furnaces that will maintain the four key temperatures associated with a double-stabilization thermal-processing scheme:
  - austenitization in a molten salt bath at 900°C.
  - the initial quench temperature of approximately 450°C using liquid tin.
  - the final quench temperature of 20 to 200°C using oil or Wood's metal.
  - the aging temperature of 300 to 500°C during which carbon partitioning from martensite to austenite occurs and comprises the second stabilization.
- Interstitial solid solution models for ferrite and austenite phases were constructed using the compound energy (CALPHAD) formalism to:
  - determine austenitization temperatures for various candidate alloy chemistries.
  - compare predictions of the models with those made by standard Thermo-Calc software.
- Four laboratory induction air melted heats of steel have been processed at AK Steel Corporation—Research:
  - carbon contents vary from 0.092 to 0.29 wt. %.
  - the heats were boron treated to increase their hardenability.
  - manganese contents vary from 2.0 to 4.1 wt. %.
  - the alloy levels for silicon and aluminum were nominally 2 wt. %. and 1.5 wt. %., respectively.
- Final processing of the laboratory heats was a cold reduction of 67% to a final thickness of 1.02 mm (0.040 inch).

Future Direction

- Perform austenitization thermal cycles with the initial series of cold-rolled steels:
  - followed by an immediate rapid quench to room temperature.
  - determine the volume fraction of austenite that was present at 900°C.
- Carry out two-step austenitization followed by a liquid-metal quench to 450°C thermal cycles:
  - finish with a rapid quench to room temperature.
  - determine if bainite formed during the liquid metal quench.
- Do complete double-stabilization thermal-processing procedures using the most promising alloy chemistries.
- Determine the amount of retained austenite present in thermally-processed samples using an x-ray technique.
- Prepare thin foil samples and conduct transmission electron microscopy (TEM) analyses of the retained austenite contained in select samples.

Introduction

Efforts are aimed at the development of a third generation of advanced high-strength steel (AHSS) with strength and ductility combinations exceeding those of ferritic first-generation AHSS and can be manufactured much more economically than austenitic second-generation AHSS. The strength/ductility goal of a third-generation AHSS can be achieved employing a microstructure comprised of martensite and a significant volume fraction of austenite. The austenite must have sufficient stability to transform to martensite only at progressively higher levels of strain, so that the work-hardening rate concurrently increases in a continuous fashion. The key to a viable third-generation AHSS is obtaining a high volume fraction of such austenite within the constraints of a carbon content low enough to not severely compromise weldability, alloy levels that do not greatly increase the cost of the steel, and a processing route consistent with current sheet steel production practice.

Initial activities on the project have proceeded along two parallel routes. One undertaking has been the design and construction of a thermal-processing facility. Such a facility will enable a steel strip to track the rapid temperature changes associated with a double-stabilization thermal cycle. The second effort has pursued the design and production of the first series of candidate heats of steel. The steels were designed with the aid of CALPHAD-based interstitial solid-solution models for the ferrite and austenite phases. The initial group of three steel chemistries already has been produced by AK Steel Corporation—Research.

Thermal Processing Requirements

The core design requirement for the thermal-processing facility was to be able to achieve the thermal cycle illustrated in Figure 1.

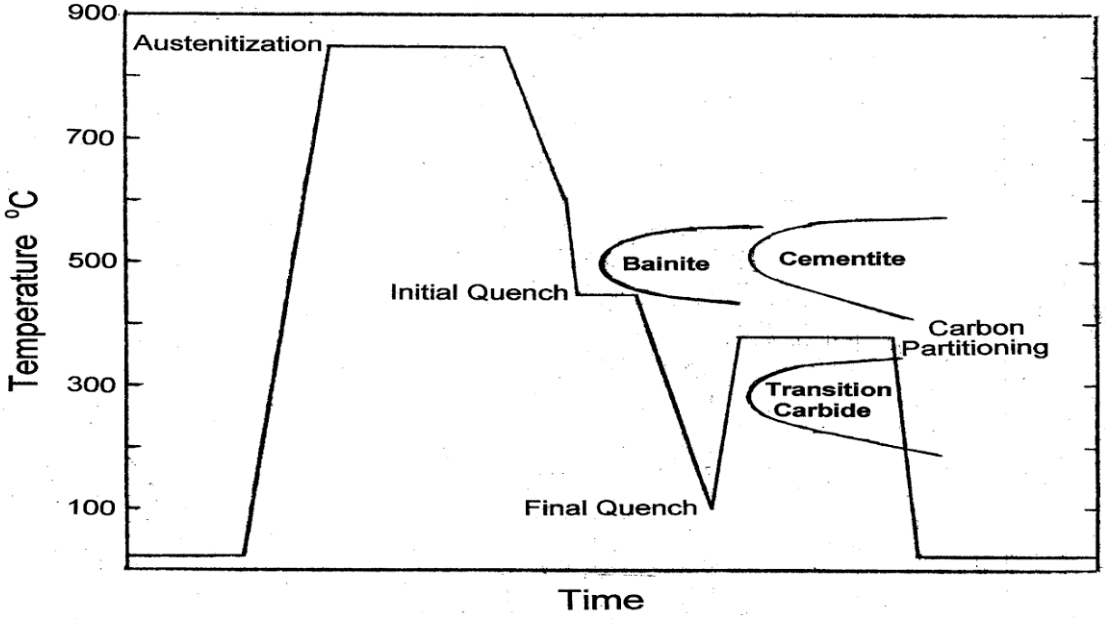

Figure 1. A schematic representation of a double stabilization thermal cycle.

The thermal cycle contains four brief isothermal holds corresponding to (1) austenitization, (2) initial quench and stabilization, (3) final quench, and (4) carbon partitioning for final stabilization. The hold times at the four relevant temperatures are anticipated to vary from as little as two seconds to several minutes. The demand for rapid temperature changes associated with movement from one isothermal hold to another prompted the use of liquid media to establish the isothermal hold temperatures. For austenitization the temperature will be in the range of 800 to 900°C, and the chosen medium will be a neutral salt. For the initial quench and the carbon partitioning, the temperature will be in the range of 300 to 500°C and the medium will be liquid tin. For the final quench, the temperature will be in the range of 20 to 200°C, and the medium will be oil.

Four crucible furnaces were purchased to establish the core of the thermal-processing facility. Funding for the furnaces was obtained through a grant from the Ohio Department of Development. The austenitization furnace is equipped with a high-alumina cylindrical crucible 190 mm (7.5 inch) deep with an inside diameter of 102 mm (4 inch). The other three furnaces contain KIMAX cylindrical crucibles 184 mm (7.25 inch) deep with an inside diameter of 83 mm (3.25 inch). Each furnace has a primary control thermocouple and a second over-temperature control thermocouple. A third thermocouple is inserted directly into the liquid media in each crucible. These latter four thermocouples and a set of two thermocouples constructed with very fine chromel-alumel wires for an extremely fast response time will all be read with an eight-place analog-to-digital board with output to a laptop computer for data display and storage. The set of fast-response thermocouples will be embedded in the test samples. The thermal-processing facility comprised of furnaces, crucibles, liquid media, and control and analysis thermal couples has been assembled and is now operational. The facility is currently undergoing a series of tests to assess it performance characteristics.

Modeling

Interstitial-solid-solution models for ferrite and austenite phases were constructed using the compound energy (CALPHAD) formalism. The free energy of both phases defined with the conventional method of one mole of formula units was transformed to a one-mole-of-atoms basis to allow examination of molar free-energy diagrams as a function of temperature. The anticipated austenitization times will be less than 60 seconds. The brief time will limit partitioning of the substitutional alloying elements during austenitization. As such, the thermodynamic modeling evaluated the molar free energies of the ferrite and austenite phases under paraequilibrium conditions.

Candidate Steels Chemistry

The chemical compositions of candidate steels were strongly influenced by the requirements of the double-stabilization thermal cycle. To maintain a completely austenitic microstructure during cooling to the initial quench temperature, the steel must have sufficient hardenability to avoid the formation of bainite as shown schematically in Figure 1. To enhance hardenability, boron was chosen as an alloying element in all of the candidate steels. In order to reliably achieve boron levels of 0.001 to 0.003 wt. %, titanium also must be added to the steel to prevent the formation of BN. Manganese increases the hardenability of steel. Conventional steel-making practices limit the manganese content to a maximum of 2 wt. %. That level of manganese provides substantial hardenability and was chosen as a baseline value for the candidate steels. A manganese content of 4 wt. %. was chosen for a more highly-alloyed heat. To suppress the formation of carbides during the carbon-partitioning isothermal hold, the candidate steels must contain ample concentrations of silicon or aluminum. The decision was made to make a combined addition of silicon and aluminum to the candidate steels at concentrations commonly used for electrical steel grades. The chosen alloying levels for the silicon and aluminum were nominally 2 wt. % and 1.5 wt. %, respectively.

Carbon is the alloying element that has by far the greatest potency with respect to increasing the stability of the austenite phase and the strength of the martensite phase. Carbon also is a very low-cost alloying element. The primary restraint to having high carbon contents in candidate alloys is provided by a loss of weldability. To maintain good spot-welding performance, sheet steels typically have less than 0.1 wt. % carbon. Other forms of welding steel can tolerate carbon contents several times that value. The decision was made to have nominally 0.3 wt. % carbon in the most highly-alloyed candidate steel and half that level of carbon in the baseline candidate steel. As carbon partitions from martensite to austenite, the austenite's resistance to transformation to martensite increases and the strength of the martensite decreases. To bolster the strength of the martensite phase, the decision was made to nominally add 0.5 wt. % chromium to the highly-alloyed candidate steel. As an example of the effect of chromium, the tensile strength of martensite containing 0.02 wt. % carbon has been shown to increase from 525 to 625 MPa due to an increase in its chromium content from essentially zero to 0.5 wt. %. [1]

A total of three candidate steel chemistries were selected for initial preparation and evaluation. The chemical compositions of these first three candidate alloys are listed in Table 1.

Production of Laboratory Heat of Steel

AK Steel Corporation-Research has produced four laboratory induction air-melted heats of steel using high purity materials. Each heat yielded one 14 Kg (30 lb) ingot 9.5 × 9.5 × 19 cm (3.75 × 3.75 × 7.5 inch) in size. One heat of the baseline (A) and one heat of the intermediate (B) alloy chemistries were melted. Two heats of the highly-alloyed (C) chemistry were melted. To prevent excessive

Table 1. Proposed chemical compositions (in weight percent) for the initial candidate steels.

Alloy	C	Mn	Si	Al	S	P	B	Cr
A	0.13/0.17	1.95/2.05	2.0/2.30	1.50/1.70	0.015 max	0.010 max	0.001/0.003	0.12 max.
B	0.18/0.22	1.95/2.05	2.0/2.30	1.50/1.70	0.015 max	0.010 max	0.001/0.003	0.12 max.
C	0.28/0.32	3.90/4.10	2.0/2.30	1.50/1.70	0.015 max	0.010 max	0.001/0.003	0.45/0.55

oxidation and losses during melting, the liquid steel surface was shrouded with argon.

After solidification was complete, the ingots were removed from their molds and their hot tops were sawn off and discarded. A 13 mm (0.5 inch) thick slice was sectioned from the top of each ingot and submitted for chemical analysis. The measured chemical compositions are listed in Table 2. The ingots were then machined so that their faces were made parallel. The ingots were reheated to 1,205°C (2,200°F) for three hours in a nitrogen-enriched atmosphere, then hot rolled in five passes to produce billets 25 mm (1 inch) thick. After this initial hot rolling, the temperature of the billets was still above 900°C (1,650°F). The billets were subsequently air-cooled to room temperature.

Table 2. Ingot analysis of the chemical compositions (in weight percent) of the initial candidate steels.

Heat	C	Mn	P	S	Si	Ni	Cr	Cu	Mo	N	Nb	V	Ti	Al	B
3	0.12	2.18	<0.002	0.0011	2.14	0.002	<0.002	<0.002	<0.002	0.0039	<0.002	0.002	0.003	1.47	0.0028
4	0.29	4.16	0.002	0.0014	2.16	0.003	0.48	<0.002	<0.002	0.0068	<0.002	<0.002	0.002	1.57	0.0036
5	0.28	1.96	0.002	0.0008	2.07	0.004	0.014	<0.002	<0.002	0.0027	<0.002	0.002	0.002	1.48	0.0024
6	0.32	4.0	0.002	0.0012	2.1	0.003	0.49	<0.002	<0.002	0.0045	<0.002	0.002	0.023	1.52	0.0018

The billets were sectioned to a length of 18 cm (7.1 inch) to ensure that after hot rolling the steel strips would fit inside of the 152 cm (60 inch) deep furnace used for coiling simulations. The billets were reheated to 1,250°C (2,275°F) in a nitrogen-enriched atmosphere, then hot rolled in five passes to a thickness of 3 mm (0.12 inch). The finishing temperature prior to the last pass was maintained near 900°C (1,650°F), excluding the two hot bands from heat #3. The hot bands from heat #3 cobbled during the last rolling pass resulting in their finishing temperature being below 815°C (1,500°F). All of the hot bands were subsequently placed inside of a coiling simulation furnace set at 593°C (1,100°F) and cooled at a rate of 28°C (50°F) per hour to room temperature. The hot bands were then descaled by shot blasting.

The two hot bands from each of the heats #3 and #5 (hot bands 3A, 3B, 5A, and 5B) were sectioned into 14 cm (5.5 inch) long pieces which were cold-reduced 67% to a final thickness of 1.02 mm (0.040 inch) using a laboratory cold mill. One hot band from each of the highly alloyed chemistry heats (hot bands 4B and 6B) was sectioned into 14 cm (5.5 inch) long and 2.5 cm (1 inch) wide pieces. The highly-alloyed steel was sectioned into narrow pieces to decrease rolling loads. However, attempts to cold reduce these pieces of hot band in their as-hot-rolled and "coiled" condition resulted in edge cracks and fracture of the samples. To circumvent this problem, the pieces of hot band were given an additional thermal treatment at 704°C (1,300°F) for 40 minutes then air-cooled to room temperature. After this annealing, the edges of the pieces were ground flat. Cold reductions of 67% to a final thickness of 1.02 mm (0.040 inch) using a laboratory cold mill were then readily achieved. One hot band from each of the highly-alloyed chemistry heats (hot bands 4A and 6A) has been retained for evaluation and possible alternative processing to a cold-rolled thickness.

Results

Chemical compositions obtained from cold-rolled samples derived from all six hot bands are listed in Table 3. Comparison of the chemical compositions measured in the samples obtained from the original four ingots to those from the final cold-rolled samples reveals a consistent loss of approximately 0.03 wt. % carbon due to reheating and hot working of the steels. For the ingot samples boron was analyzed by acid dilution followed by inductively-coupled plasma (ICP) spectroscopy. High levels of manganese in the steels caused interference with the determination of the boron signal and yielded values significantly higher than the actual boron levels. For the cold-rolled samples, a more time-consuming and accurate extraction and back-extraction followed by ICP analysis procedure was employed. The final boron contents fell within the range of 0.001 to 0.002 wt. %. Table 3 shows that the manganese, silicon, aluminum, and chromium contents of the cold-rolled samples essentially met the proposed concentration levels as listed in Table 1. Only heat #6 had an extra titanium addition to prevent the boron from combining with nitrogen.

Table 3. Chemical compositions (in weight percent) of cold reduced samples of the initial candidate steels.

Hot Band	**C**	**Mn**	**P**	**S**	**Si**	**Ni**	**Cr**	**Cu**	**Mo**	**N**	**Nb**	**V**	**Ti**	**Al**	**B**
3A	**0.10**	**2.16**	<0.002	0.0008	**2.15**	0.004	**<0.002**	<0.002	<0.002	0.0049	<0.002	0.002	**0.003**	**1.48**	**0.0018**
3B	**0.092**	**2.17**	<0.002	0.0008	**2.17**	0.002	**<0.002**	<0.002	<0.002	0.0046	<0.002	0.002	**0.003**	**1.48**	**0.0016**
4B	**0.26**	**4.12**	0.002	0.0008	**2.12**	0.002	**0.47**	<0.002	<0.002	0.0080	<0.002	0.002	**0.002**	**1.58**	**0.0014**
5A	**0.25**	**1.95**	0.002	0.0007	**2.08**	0.002	**0.013**	<0.002	<0.002	0.0055	<0.002	0.002	**0.002**	**1.46**	**0.0016**
5B	**0.25**	**1.95**	0.002	0.0008	**2.06**	0.003	**0.014**	<0.002	<0.002	0.0039	<0.002	0.002	**0.002**	**1.44**	**0.0015**
6B	**0.29**	**3.99**	0.002	0.0008	**2.12**	0.002	**0.48**	<0.002	<0.002	0.0047	<0.002	0.002	**0.022**	**1.50**	**0.0011**

The baseline chemistry "A" carbon level was supposed to be realized in heat #3. The carbon contents attained in the cold-rolled samples from hot bands 3A and 3B are only two-thirds of the aim value of 0.15 wt. %. Initial CALPHAD-based solution-thermodynamic modeling predicts that the low carbon content of the 3A and 3B steels will prevent them from achieving complete austenitization at any temperature. The intermediate chemistry "B" carbon level was supposed to be realized in heat #5. The carbon contents attained in the cold-rolled samples from hot bands 5A and 5B are 0.05 wt. % above the aim values of 0.20 wt. %. The additional carbon will enable these steels to achieve complete austenitization at lower temperatures than initially anticipated. The highly alloyed chemistry "C" carbon level was supposed to be realized in heats #4 and #6. Only the cold-rolled samples from the hot band 6B have essentially the aim carbon concentration value of 0.30 wt. %. Preliminary examination of the microstructure produced in the hot band 6B found that the steel possesses a high degree of hardenability based upon the presence of a substantial volume fraction of bainite/martensite/retained austenite constituent.

The sum total of the cropping, machining, sectioning, and descaling applied to the original 13.6-Kg (30-lb) ingots resulted in a yield of the final cold-rolled steel of about 24%, i.e., 3.2 Kg (7 lb). Each hot band produced approximately 0.2 m^2 (310 $inch^2$) of cold-rolled steel 1.02 mm (0.040 inch) thick. That amount of steel will provide an ample number of test coupons to enable exploration of an extensive range of time/temperature parameters associated with double-stabilization thermal cycles.

Conclusions

Initial modeling results indicate that substantial carbon and manganese contents will be required in steels that are to be fully austenitized that have silicon and aluminum concentrations of nominally 2 wt. % and 1.5 wt. %, respectively. There is a distinct tradeoff between the competing goals of lowering the carbon content for enhanced weldability and raising the aluminum and silicon levels to suppress carbide formation and promote carbon partitioning.

Presentations

1. G. M. Michal, "AHSS through Paraequilibrium Carbon Partitioning and Austenite Stabilization," Special seminar at AK Steel Corporation—Research, Middletown, Ohio, August 30, 2007.
2. G. M. Michal and A. H. Heuer, "Increasing the Austenite Content of AHSS by Dual Stabilization Processing," MS&T'07 Conference and Exhibition, Detroit, Michigan, September 17, 2007.
3. G. M. Michal, "AHSS through Carbon Partitioning," NSF/DOE Steel Research Program Review, Southfield, Michigan, April 10, 2008.
4. G. M. Michal and A.H. Heuer, "Use of Dual Stabilization Thermal Processing to Increase the Austenite Content of AHSS," MS&T '08 Conference and Exhibition, Pittsburgh, Pennsylvania, October 6, 2008.

Reference

1. E. G. Bain and H. W. Paxton, "Alloying Elements in Steel," ASM, Metals Park, OH, 1966, P. 126.

Q. Development of a High-Strength, High-Toughness Bainitic Steel

Principal Investigator: Susil K. Putatunda
Chemical Engineering and Material Science, Wayne State University, Detroit, MI- 48202
(313) 577-3808; fax: (313) 577-3810; e-mail: sputa@eng.wayne.edu

Technology Area Development Manager: Joseph A. Carpenter
(202) 586-1022; fax: (202) 586-1600; e-mail: joseph.carpenter@ee.doe.gov

Field Project Officer: Aaron D. Yocum
(304) 285-4852; fax: (304) 285-4403; e-mail: aaron.yocum@netl.doe.gov

---

Contractor: Wayne State University
National Science Foundation (NSF) Contract No.: CMMI 0727004, jointly funded by NSF and DOE

Objective

- The primary objective of this investigation was to develop a new bainitic steel with simultaneous high yield strength, ductility, and fracture toughness by applying the novel concept of an adiabatic deformation and two-step austempering process.
- The secondary objective was to examine the influence of austempering temperature on the microstructure and mechanical and physical properties of this new steel.

Approach

- In the preliminary investigation under a seed grant, a new low-alloy steel has been designed and austempered by single-step austempering process. The alloy steel has been designed such that its M_s (martensite start) temperature is below 315°C, because 315°C is the general position of the boundary line between upper and lower bainite. The steel with the following composition has been designed for this investigation: C=0.50%, Si=2.0%, Cr=1.0%, Mn=0.60% and Mo=0.20% and Cu = 0.50%, with S and P as low as possible. The M_s temperature of such steels can be expressed as $M_s = 1000 - (650 \times \%\ C) - (70 \times \%\ Mn) - (35 \times \%Ni) - (70 \times \%\ Cr)$.
- The calculated M_s temperature of the steel was 296°C. Inclusion of high silicon helped in the prevention of cementite formation during the transformation to upper bainite. The addition of chromium helped in reducing graphitization and improving hardenability. This also depressed the M_s temperature. The carbon content has been selected as 0.50% because we need sufficient carbon to depress the M_s temperature and inhibit pearlite formation during austempering. Carbon also helped to depress the upper to lower bainite boundary transition line. This allowed us to initially quench the steel to a lower austempering temperature and thus achieve refinement of bainitic ferrite-austenite structure. Addition of a small amount of molybdenum helped to attain higher hardenability. We added copper, recognizing the fact that while it is not normally a very desirable element in commercial steel because of the formation of pearlite phase, it can improve corrosion resistance. We show that even with copper added, we did not find evidence for any pearlite phase formation in this steel during the austempering.

Accomplishments

- A new low-alloy, medium-carbon steel with high silicon content has been developed.
- By austempering this steel in the temperature range of 260°C–400°C, considerable strength, toughness, and ductility were produced in the steel.

- After austempering this steel in the temperature range of 315°C–400°C, a mixed microstructure consisting of bainitic ferrite and austenite was obtained in this steel. However, presence of some martensite was also observed.
- Exceptionally high fracture toughness of 116 MPa√m was obtained in this steel after austempering at 315°C.
- The steel had relatively large magnetization compared to traditional low-alloy steels.
- This steel is an inexpensive alternate to maraging steel in applications requiring very high fracture toughness.
- This steel has high ductility and very good strength and toughness. Therefore, it can be used in automotive components to reduce weight and increase fuel efficiency.

Future Directions

- In the future, we propose to apply adiabatic deformation and a novel concept of two-step austempering in this steel. Applying adiabatic deformation and two-step austempering will result in an extremely fine-scale microstructure (nano-scale region) and very high carbon in the austenite. Further, higher density of nucleation at the same growth rate will cause the austempering reaction (stage 1) to occur very fast; i.e., the end point of reaction one will be achieved quickly. The purpose of step austempering is to momentarily force the material into the lower bainitic region to increase nucleation, and we intend to raise the temperature of transformation into the upper bainitic region to grow the ferrite austenite structure. In our opinion, single-step austempering will not produce as fine a structure as the two-step austempering. When we do the initial quench to a temperature just above the M_s temperature of the steel, we expect to be in the region below the bainitic nose of the IT diagram. Therefore, we do not expect a significant amount of lower bainite to be formed in the material.
- Thus, the overall new process will include the following steps:
  - Heat up the material to an initial austenitizing temperature (T_1) (i.e., just below and above A1)
  - Enclose in an insulated chamber with heated rolls maintained at the same temperature.
  - Adiabatically deform it by rolling to a final temperature (T_2) (i.e., about 871°C)
  - This will be followed by two-step austempering, i.e., immediate quenching to first austempering temperature T_3 in a salt bath (above $M_{s\ t}$emperature) and then raising the temperature of the salt bath to the final austempering temperature (T_4) and holding and finally air cooling .
- This processing will result in a steel with very fine-scale ausferritic microstructure (nano-scale region) and will also result in exceptional combination of mechanical and physical properties.

Introduction

The primary focus of this investigation was to create a high-strength, high-toughness bainitic steel. This was achieved by austempering medium-carbon low-alloy steel with high silicon content.

Steels with bainitic structure have several advantages including high strength, high toughness, and high ductility. In conventional steels, the fracture toughness generally decreases as yield strength increases. On the other hand, the fracture toughness will be high when the yield strength is low. Thus the combination of high strength and high fracture toughness cannot easily be obtained in most conventional steels. In this investigation, new bainitic steel with simultaneous high yield strength and high fracture toughness was developed. This novel steel was synthesized using the concepts of austempered ductile cast iron (ADI) technology.

Austempered Ductile Cast Iron

ADI has emerged as a major engineering material in recent years because of its excellent properties, such as high strength with good ductility [1–3], good wear resistance [4], good fatigue properties [5–9], and good fracture toughness [10]. It is widely used in manufacturing components as diverse as gears [11], crankshafts [12], locomotive wheels [13], connecting rods, brake shoes, etc. ADI has other advantages, such as low production cost arising from its good castability, excellent machinability resulting in consequently longer tool life, and shorter heat-treatment processing cycles.

ADI is an alloyed and heat-treated nodular cast iron. It has a unique acicular matrix structure [14] that consists of high carbon austenite (γ_{HC}) and ferrite (α) with dispersed graphite nodules. This unique microstructure, the product of the austempering process, provides the excellent mechanical and physical properties of ADI. The chemical composition of ADI is similar to that of conventional ductile cast iron [15]. However, some alloying elements, such as nickel, copper and molybdenum, are usually added to increase its heat treatability, i.e., to delay austenite decomposition to pearlite and ferrite upon cooling. Proper austempering heat treatment will avoid [16] the formation of unwanted microstructural constituents such as martensite, carbides, and pearlite.

ADI Processing

The development of ADI involves a two-stage process. The first step is the melting and casting of alloyed nodular (ductile) cast iron. This is followed by heat treatment. The casting is heated and held in the austenitizing temperature range of 815°C -927°C for one to two hours. At this stage, the structure becomes fully austenitic (γ). After austenitizing, the alloy is quenched in a molten-salt bath and cooled to an austempering temperature range between 260°C and 400°C. The casting is maintained at this temperature range for about two to four hours and then air- cooled to room temperature.

During austempering, ADI goes through a two-stage phase-transformation process [15–18]. In the first stage, the austenite (γ) decomposes into ferrite (α) and high carbon austenite (γ_{HC}):

$$\gamma \rightarrow \alpha + \gamma_{HC} \qquad (1)$$

If the casting is held at the austempering temperature for too long, a second reaction takes place [15–18], during which the high-carbon austenite γ_{HC} can further decompose into ferrite and carbide:

$$\gamma_{HC} \rightarrow \alpha + \varepsilon \qquad (2)$$

In this case, the structure will contain ε carbide, which makes the material brittle. Therefore, this reaction must be avoided. The best combination of mechanical properties (tensile strength and ductility) is obtained in ADI after the completion of the first reaction but before the onset of the second reaction. This time period between the completion of the first reaction and the onset of the second reaction is termed the "process window." This process window can be enlarged by addition of alloying elements such as nickel, molybdenum and copper. Proper austempering produces a unique bainitic structure that consists of high-carbon or transformed austenite (γ_{HC}) and acicular ferrite with dispersed graphite nodules.

The exact morphology of the ferrite phase and the relative amounts of ferrite and austenite determine [19–22] the mechanical properties of ADI and can be controlled by austempering temperature and time. For example, when ADI is austempered at a lower temperature (e.g., 260°C), it has a very high yield strength. On the other hand, when it is austempered at higher temperature (e.g., 385°C), it has a lower yield strength. This higher yield strength (for ADI processed at lower temperatures) is due to the presence of fine ferrite and austenite in the matrix [15–18]. On the other hand, at higher austempering temperature, ferrite and austenite become feathery or coarse and this causes a decrease [19] in the yield strength of ADI. This higher yield strength at lower austempering temperature develops from a smaller grain size and a lattice mismatch effect [15–18].

The term austempered ductile iron therefore describes a family of materials whose properties can be varied over a wide range by the correct choice of heat-treatment variables (temperature and time) and chemical composition. Austempered ductile irons can have tensile strengths up to 260 Ksi (1600 MPa) with 1 percent elongation and high hardness (in excess of 60 R_c) for applications in which wear resistance is of primary importance. Materials of lower hardness having tensile strengths of [120–170 Ksi (800 to 1200 MPa)] and elongation up to 14% can also be produced when higher ductility is required.

Another interesting possibility exists with ADI. Generally, in almost all materials, fracture toughness decreases as yield strength increases and vice versa. However, ADI is an exception. This investigator [20–21] and others [23–25] have observed that fracture toughness is higher in ADI when its yield strength is also high. Thus, it is possible to produce simultaneous high yield strength and high fracture toughness in ADI, something that cannot be obtained in most other materials.

Austempering Reaction in ADI

During austempering of nodular or ductile cast iron, acicular ferrite grows from austenite by a nucleation and growth [2, 16, 26–28] process. While the ferrite phase grows, the remaining austenite becomes enriched with carbon. When ADI is austempered at lower temperatures (i.e., in the lower-bainitic region), it develops a microstructure that consists of acicular ferrite with precipitated carbide [16, 26] and retained austenite. This is similar to a lower-bainitic structure in steel. However, when ADI is austempered in the upper-bainitic region, it produces a microstructure that consists of carbide-free ferrite and austenite [16, 26]. Due to the high silicon content, the formation of cementite phase, which is normally associated with the bainitic reaction in steel, is suppressed in ADI. Consequently, the remaining austenite continues to be enriched with carbon as the reaction proceeds. As the austenite becomes enriched with carbon, the growth of bainitic ferrite platelets is inhibited [17] and the reaction is arrested. Depending upon the transformation temperature and time, it can contain large amounts [26] (up to 50%) of austenite. Presence of this high-carbon austenite (γ_{HC}) increases the work-hardening rate [25–28] of ADI. This, in turn, contributes to the good fatigue strength and fracture toughness in ADI.

Austempering Reaction in Steel

When steel is austempered at temperatures below the nose of the time-temperature-transformation (TTT) curve, a structure is produced in which ferrite and iron carbide are not lamellar. This transformation product is called bainite. Bainite in steel has a needle-like (acicular) microstructure. Whereas pearlite is nucleated by iron carbide [29, 30] and is accompanied by the subsequent formation of ferrite, bainite is nucleated by ferrite and followed by the precipitation of iron carbide. This process leads to the dispersion of iron carbide in a ferrite matrix. With a lower transformation temperature, the distribution of carbide is finer and the ferrite needles are thinner [29–32]. This product is called lower bainite. The transformation product at relatively higher temperatures consists of lath- or plate- shaped ferrite units arranged in packets and interlath carbide precipitates. This product is called upper bainite [35]. In steel, lower bainite produces higher yield strength but lower toughness. While the austempering reaction in ADI is a two-step reaction process, it is a one-step reaction process [29–32] in the case of steel. During austempering in steel, austenite directly decomposes into acicular ferrite and carbide (bainite). Austempering of steel offers the advantages of increased ductility, reduced distortion, and a short overall time cycle to harden thoroughly. Generally, upper-bainitic temperatures are above 316°C (600°F) in the case of steels and cast iron. Temperatures between 232°C (450°F) to 316°C (600°F) are the lower-bainitic temperature range.

However, when steels contain sufficient silicon or aluminum (exceeding 2.0%) and are austempered in the upper-bainitic temperature range, a unique microstructure similar to ADI develops. The carbon that is partitioned into residual austenite does not precipitate but remains stable to ambient temperature. The microstructure obtained consists of fine plates of bainitic ferrite separated by a carbon-enriched region of austenite. The potential advantages of this mixed microstructure can be listed as follows:

- Cementite is responsible for initiating fracture in high-strength steels. Its absence is expected to make the microstructure more resistant to cleavage failure and void formation.
- The bainitic ferrite is almost free of carbon, which substantially strengthens the ferrite [42].
- The microstructure derives its strength from the fine grain size of the ferrite plates, which

are less than 1 micrometer (µm) in thickness. It is the thickness of these plates, which determines the mean free-slip distance, so that the effective grain size is less than a µm. This cannot be achieved by any other commercially-viable process. Grain refinement is the only method available for simultaneously improving the strength and toughness of steels.

- The ductile films of austenite, which are intimately dispersed between the plates of ferrite, have a crack-blunting effect. They further add to toughness by increasing the work of fracture as the austenite is induced to transform to martensite under the influence of the stress field of a propagating crack. This is the transformation-induced plasticity (TRIP) effect.
- The diffusion of hydrogen in austenite is slower than in ferrite. The presence of austenite can therefore improve the stress-corrosion resistance.
- Steels with the bainitic ferrite and austenite microstructure can be obtained without the use of expensive alloying elements. All that is required is that the silicon or aluminum concentration should be large enough to suppress the cementite formation.

In spite of these appealing features, the microstructure does not always give the expected good combination of strength and toughness. This is because the relatively large, blocky regions of austenite between the sheaves of bainite readily transform into high-carbon martensite under the influence of stress. This untempered, hard, and coarse martensite regions severely embrittle the steel. Therefore, we argue that if the austenitic and ferrite can be made in very fine-grained structure and austenite sufficiently enriched with carbon so that its M_s temperature is sufficiently depressed [39–41], then the strength and other mechanical properties will increase significantly.

A novel concept of adiabatic deformation and two step austempering process has been conceived by this investigation to produce extremely fine-scale microstructure consisting of ferrite and austenite. This is expected to produce an exceptional combination of strength, ductility, and fracture toughness in this steel.

Results

This investigator was awarded a seed grant to establish the proof-of-principle for this project. With this seed grant, we melted and cast a medium-carbon, low-alloy steel with high silicon content of the following composition (C-0.5%, Si-2%, Mn-0.4%, Ni-1%, Cr-0.8% and Mo-0.3%). After hot rolling and annealing, the steel was austenitized at 926°C for 2 hours and then austempered at several temperatures between 260°C and 398°C. Figure 1 shows the typical microstructure of the steel after austempering at 371°C .This microstructure shows a fine-scale ausferritic structure, i.e., a mixture of ferrite and high-carbon austenite. X-ray diffraction confirmed the microstructure consisting of ferrite and high-carbon austenite. Table 1 below reports the mechanical properties of the steel including the fracture toughness .We obtained exceptionally high strength (1336 MPa) and high fracture toughness (116 MPa√m, comparable to maraging steel) in this material after austempering at 315°C. The ductility of the material is also significantly high (11.5% elongation). We also processed a few samples by adiabatic deformation and single-step austempering and this resulted in an extremely fine-scale microstructure. Thus, we have already established the proof-of-principle for this project. We now propose to apply the novel concept of adiabatic deformation and two-step austempering in this steel to produce an extremely fine (nearly nano crystalline) microstructure with austenite and ferrite together with a very high carbon content in the austenite. We expect to have properties significantly higher than maraging steels. As

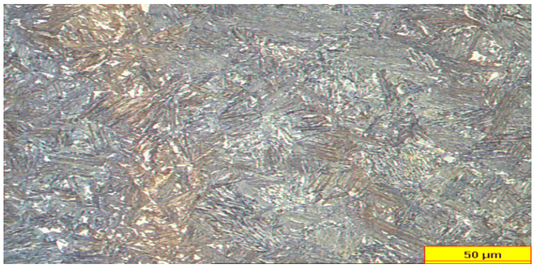

Figure 1. Microstructure of the steel after austempering at 700°F.

Table 1. Mechanical Properties of Steels Investigated in Initial Proof-of-Concept Project

Austempering Temp (°C)	Yield Strength (MPa)	Ultimate Tensile Strength (Mpa)	Ductility (% elongation)	Fracture Toughness (MPa√m)
As-cast	507	882	16.8	42.8
260	1423	1779	10.1	84.5
315	1336	1653	11.5	116.2
343	1244	1381	12.7	96.3
371	1103	1408	14.9	75.8
398	864	1384	18.5	62.6

mentioned earlier, such high-strength, high-toughness steel will have major applications in defense, automotive and other manufacturing industries because it will result in significant weight savings. Another potential application of this steel will be in armored plates and combat tanks. This steel will have extremely high fracture toughness, impact resistance, and ballistic mass efficiency (BME). Moreover, they will have major applications in automotive components, reducing weight and improving fuel economy and reducing pollution.

Once this steel of the above-mentioned composition has been developed, we will concentrate on developing other ausferritic steels with lower carbon content and different alloying composition using the same basic principle; i.e., designed with a lower M_s temperature and processed by adiabatic deformation and two-step austempering.

Conclusions

A new low-alloy, medium-carbon steel with high silicon content has been developed. By austempering this steel in the temperature range of 260°C–400°C, considerable strength and ductility were produced in the sample. After austempering this steel in the temperature range of 315°C–400°C, a mixed microstructure consisting of bainitic ferrite and austenite was obtained in this steel. The steel had properties comparable to maraging steel. Adiabatic deformation produced very fine-scale ferrite and austenite.

Presentations/Publications/Patents

1. Two papers were presented at M.S and T conferences in October 2007 and October 2008.
2. One paper has been accepted for publication in Materials Science and Engineering A.
3. One patent application has been filed with U.S. Government.

References

1. J. Dodd, “High Strength, High Ductility Ductile Irons,” Modern Casting, Vol. 68, No. 5, pp. 60–66 (1978).
2. R. B. Gundlach and J. F. Janowak, “Development of a Ductile Iron for Commercial Austempering,” AFS Transaction, Vol. 94, pp. 377–388 (1983).
3. R. A. Harding and G.N.J. Gilbert, “Why the Properties of Ductile Irons Should Interest Engineers,” British Foundryman, Vol. 79, pp. 489–496 (1986).
4. I. Schmidt and A. Schuchert, “Unlubricated Wear of Austempered Ductile Cast Iron,” Zeitschriftjbr Metalkunde, Vol. 78, pp. 871–875 (1987).
5. M. Johansson, “Austenitic Bainitic Ductile Iron,” AFS Transaction, Vol. 85, pp. l 17122 (1977).
6. S. K. Putatunda et. al., “Influence of Microstructure on High Cycle Fatigue Behavior of Austempered Ductile Cast Iron,” Materials Characterization, Vol. 30, pp. 22l-234 (1993).
7. P. Shanmugam, P. P. Rao, K. R. Udupa, and N. Venkataraman, “Effect of Microstructure on the Fatigue Strength of an Austempered Ductile Iron,” J of Materials Science, Vol. 29, pp. 4933–4940 (1994).
8. L. Bartosiewicz, S. Duraiswamy, A. Sengupta, and S. K. Putatunda, “Near Threshold Fatigue

Crack Growth behavior of Austempered Ductile Cast Iron," Morris Fine Symposium, TMS, Detroit, pp. 135–138 (1991).

9. L. Bartosiewicz, A. R. Krause, A. Sengupta, and S. K. Putatunda, "Relationship between Fatigue Threshold and Fatigue Strength in Austempered Ductile Cast Iron." International Symposium for Testing and Failure Analysis, ISTFA, ASM Vol. 16. pp. 323–336 (1990).
10. G. Wilkinson and C. Grupke, "Design Consideration and Product Applications of Casting," 2nd International Conference on Ductile Iron, Ann Arbor, Michigan. pp. 349–358, (March 1986).
11. J. Panasiewicz, C. Grupke, and J. Huth, "Chrysler's Experience with Austempered Ductile Iron," World Conference on Austempered Ductile Iron, Bloomingdale, IL, pp. 176–194 (March, 1991).
12. K. Okazaki, H. Asai, M. Tokuyoshi, H. Kusonoki, and H. Sakahara, Proceeding World Conference on Austempered Ductile Iron, Bloomingdale, IL, pp. 288–299 March, 1991.
13. B. V. Kovacs, "Austempered Ductile Iron, Facts and Fiction," Modern Casting, Vol. 36, pp. 38–41, (1990).
14. T. Shiokara, "On the Austempered Ductile Cast Iron, Their Mechanical properties and Some Practical Applications," 59th Japan Ductile Cast Iron, Association conference, Tokyo, Japan, pp. 138–150 (1978).
15. J. F. Janowak and P. A. Norton, "A Guide to Mechanical Properties Possible by Austempering, 1 Spercent Ni, 0.3 percent Mo Iron," AFS Transaction, Vol. 88. pp. 123–135, (1985).
16. R. B. Gundlach and J. F. Janowak, "Austempered Ductile Irons Combine Strength with Toughness and Ductility," Metal Progress, Vol. 12, pp. 231–236 (1985).
17. J. F. Janowak, R. B. Gundlach, G. T. Eldis, and K. Rohrting, "Technical Advances in Cast Iron Metallurgy," AFS International Cast Metal Journal, Vol. 6, pp. 28–42 (1982).
18. D. J. Moore, T. B. Noun, and K. B. Rundman, "The Relationship between Microstructure and Tensile Properties in Austempered Ductile Cast Iron," AFS Transaction, Vol. 87, pp. 165–174, (1987).
19. L. Bartosiewicz, A. R. Krause, B. V. Kovacs, and S.K. Putatunda, "Fatigue Crack Growth Behavior of Austempered Ductile Cast Iron," AFS Transaction, Vol. 92, pp. 135–142, (1992).
20. S. K. Putatunda and I. Singh, "Fracture Toughness of Unalloyed Austempered Ductile Cast Iron," Journal of Testing and Evaluation, Vol. 23, No. 5, pp. 325–332, (September 1995).
21. S. K. Putatunda, I. Singh, and L. Bartosiewicz, "Influence of Chromium on Mechanical Properties of Austempered Ductile Cast Iron," Journal of Materials Engineering and Performance, Vol. 4, No. 1, pp. 90–101, (Feb.1995).
22. I. Singh, "Fatigue and Fracture behavior of ADI," Ph. D. Thesis, Wayne State University, June 1996, Advisor S.K. Putatunda.
23. J. L. Doong and C. Chen, "Fracture Toughness of Bainitic-Nodular Cast Iron," Fatigue Fracture of Engineering Material and Structure, Vol. 12, pp. 155–165 (1989).
24. E. Dorazil and M. Holzman, "Fracture Behavior of Austempered Ductile Iron," Proceeding World Conference on Austempered Ductile Iron, Bloomingdale, IL, March, 1991, pp. 32–66.
25. M. Grech, P. Bowen, and J. M. Young, "Effect of Austempering Temperature on the Fracture Toughness and Tensile Properties of an ADI alloyed with Copper and Nickel," Proc. World Conference on Austempered Ductile Iron Bloomingdale, IL, March, 1991, pp. 338–374.
26. D. J. Moore, T. N. Rouns, and K. B. Rundman, "The Effect of Heat Treatment, Mechanical Deformation and Alloying Elements on Rate of Bainitic Formation in Austempered Ductile Cast Iron," J of Heat Treating, Vol. 4, No. 1, June 1985, pp. 7–24.

27. S. K. Putatunda and P. P. Rao, “Influence of Microstructure on Fracture Toughness of Austempered Ductlie Cast Iron,” Metallurgical and Materials Transaction, Vol. 28A. No. 7, pp. 1457–1470, July 1997.
28. S. K. Putatunda, R. Gupta, and P. P. Rao, “Influence of Austempering time and temperature on Fracture Toughness of Austempered Ductile Iron,” Microstructural Sciences, ASM International, Vol. 24, pp. 103–110, (1996).
29. R. E. Reed Hill, “Physical Metallurgy Principles 2nd Edition, D. Van Nostrand Company New York, 1973.
30. D. A. Porter and K. E. Easterling, “Phase Transformations in Metals and alloys,” Chapman and Hall, 2nd Edition, 1992.
31. P. G. Shewmon, “Phase Transformations in Metals,” McGraw Hill, 1986.
32. W. F. Smith, “Structure and Properties of Engineering Alloys,” McGraw Hill (1981).
33. B.P.J. SandVik, “Bainitic Transformation in High Silicon Steel,” Metallurgical Transactions, Vol. A13, pp. 777–787, 1982.
34. H.D.K.H. Bhadeshia, “Bainite in Steels,” Second Edition, The University Press, Cambridge, IOM communication Ltd., London, pp 373–375, 2001.
35. J. Aranzabal et al., “Influence of Heat Treatment on the Microstructure of an Austempered Ductile Iron,” Materials Science and Technology, Vol. 20, pp. 36–46, 1994.
36. S. K. Putatunda, “Development of a High Carbon and High Silicon Steel,” Journal of Materials Processing and Technology, pp. 335–358, August 2001.
37. S. K. Putatunda, “Fracture Toughness of a High Carbon and High Silicon Steel,” Materials Science and Engineering, Vol. A297, pp. 31–43, January 2001.
38. H.K.D.H Bhadeshia et al., “Very Strong Low Temperature Bainite,” Material Science and Technology, Vol. 18, pp 279 – 284, March 2002.
39. S. K. Putatunda and P. P. Rao, “Comparative Study of Fracture Toughness of Austempered Ductile Iron with Upper and Lower Ausferritic Microstructure,” Materials Science and Technology, Vol. 14, pp 1257–1263, December, 1998.
40. P. P. Rao and S. K. Putatunda, “Investigations on Fracture Toughness of Austempered Ductile Iron Alloyed with Chromium,” Materials Science and Engineering, Vol. A346, pp. 254–265, 2003.
41. P. P. Rao and S. K. Putatunda, “Dependence of Fracture Toughness of Austempered Ductile Cast Iron on Austempering Temperature,” Metallurgical and Materials Transaction, Vol. 29A, pp. 3005–3016, December 1998.
42. S. Yazdani and A. Firouzi, “Influence of Heat Treatment on Fatigue Behavior of a Cu-Ni Alloyed Austempered Ductile Iron,” Material Science Forum, Vols. 426–432, pp. 925–930, 2003.
43. K. L. Harynen, D. J. Moore, and K. B. Rundman, “Tensile Properties and Microstructure of a Clean Austempered Ductile Iron,” AFS Transaction, Vol. 98, pp. 471, 1990.
44. A.S.H. Ali, K. I. Uzlov, N. Darwish, and R. Elliot, “Austempering of a Low Manganese Ductile Iron, Part 4 Relationship between Mechanical Properties and Microstructure,” Materials Science and Technology, Vol. 70, pp. 35–48, 1994.
45. S. K. Putatunda and P. Gadicherla, “Influence of Austenitizing Temperature on Fracture Toughness of a Low Manganese Austempered Ductile Cast Iron, “Materials Science and Engineering, Vol. A268, pp. 15–31, August 1999.
46. S. K. Putatunda, “Development of Austempered Ductile Cast Iron (ADI) with Simultaneous High Yield Strength and Fracture Toughness by a Novel Two-step Austempering Process,” Materials Science and Engineering, Vol. A 315, pp. 70–80, September (2001).

47. ASTM E-8, “Standard Test Method for Tensile Testing of Metallic Materials,” Annual Book of ASTM Standards, ASTM Philadelphia, Vol. 03.01, pp. 506–536, 1992.
48. C. S. Roberts, “Effect of Carbon Content on Lattice Parameter of Austenite,” Transaction TMS-AIME, Vol. 230, pp. 373, 1964.
49. B. D. Cullity, “Elements of X-Ray Diffraction,” Addison-Wesley, Reading, MA. 1974, pp. 411–412.
50. ASTM E-399, “Standard Test Method for Plane Strain Fracture Toughness testing of Metallic Materials,” Annual Book of ASTM Standard, PA, Vol. 3.01, p.745, (1992).

R. Development of Nano-Acicular Duplex Steels

Principal Investigator: David C. Van Aken
Missouri University of Science and Technology
Materials Science and Engineering, 1400 N. Bishop, Rolla, MO 65409-0340
(573) 341-4717; fax: (573) 341-6934; e-mail: dcva@mst.edu

Co-Principal Investigator: Julia E. Medvedeva
Missouri University of Science and Technology
Physics, 1315 N. Pine St., Rolla, MO 65409-0640
(573) 341-4789; fax: (573) 341-4715; e-mail: juliaem@mst.edu

Co-Principal Investigator: Von L. Richards
Missouri University of Science and Technology
Materials Science and Engineering, 1400 N. Bishop, Rolla, MO 65409-0340
(573) 341-4730; fax: (573) 341-6934; e-mail: vonlr@mst.edu

Technology Area Development Manager: Joseph A. Carpenter
(202) 586-1022; fax: (202) 586-1600; e-mail: joseph.carpenter@ee.doe.gov

Field Project Officer: Aaron D. Yocum
(304) 285-4852; fax: (304) 285-4403; e-mail: aaron.yocum@netl.doe.gov

---

Contractor: Missouri University of Science and Technology
National Science Foundation (NSF) Contract No.: MMI 0726888, jointly funded by NSF and DOE

Objective

- Develop a third-generation advanced high-strength steel (AHSS) that is both lighter and stronger than current automotive steels. The new steel is to be stronger than first-generation AHSS that is based upon ferritic microstructures and less expensive than the high-manganese (Mn), austenitic grades that are second- generation AHSS.
- Improve automotive crashworthiness by producing a microstructure that is similar to acicular $\alpha+\beta$ titanium (Ti) alloys that have high fracture toughness. The new steel will be a duplex microstructure of acicular ferrite and austenite.
- Develop a physics-based understanding of phase stability with respect to alloying. Use first-principles calculations to determine appropriate alloy additions to strengthen the austenitic phase. This knowledge can then be used in the formulation of steel alloys to produce nano-scale, acicular ferrite microstructures.
- Develop an acoustic-emission facility for studying bainitic phase transformation.

Approach

- To address the questions related to the structural, electronic, and magnetic properties of steels, we have performed a thorough density-functional investigation of the electronic structure, magnetic properties, and stability for α (body-centered cubic, bcc) and γ (face-centered cubic, fcc) iron (Fe) phases, their solid solutions with interstitial carbon and substitutional manganese, as well as for cementite with $2p$ and $3p$ impurities. A projector augmented wave (PAW) method was implemented in the Vienna *ab initio* simulation package within the generalized gradient approximation (GGA). We considered the octahedral interstitial sites for carbon (C) which are the most preferable in both bcc and fcc Fe phases, and the nearest substitutional positions of manganese. In cementite, to determine the most energetically-preferable location of the $2p$ or $3p$ impurity (nitrogen, N; oxygen, O; boron, B; or silicon, Si; aluminum, Al; sulfur, S; phosphorous, P), we compared the formation energies of either carbon or iron substitution by the impurity. For all the structures investigated, we optimized the lattice parameters and the internal positions of all atoms in the supercells via the atomic force and the total-energy minimization.

- The solution enthalpy is calculated as ΔH_s = E(Fe32C)-E(Fe32)-E(C) for carbon and ΔH_s = E(Fe31MnC)-E(Fe32C)+E(Fe)-E(Mn) for manganese, where supercells were taken with the same magnetic states and E(C), E(Fe) and E(Mn) are the total energies of carbon as graphite, iron and α-Mn, respectively.
- Steelmaking will be performed at Missouri University of Science and Technology with the aim of producing steel microstructures similar to the acicular α+β titanium alloys, which have high fracture toughness. Of particular interest will be alloys containing manganese, aluminum, and silicon, where the addition of aluminum and silicon promotes the formation of bainitic ferrite, but discourages the formation of cementite. Aluminum has the added benefit of lowering the overall density of the steel. Initial steel heats will be used to verify the thermochemical database for Fe-Mn-Al-Si-C steel compositions using FactSage (a free-energy minimization modeling program). Alloy and phase-composition studies will then be performed to narrow the range in steel compositions explored.

Accomplishments

- A charge-density distribution plot for the (110) plane reveals the formation of a Mn-C-Fe (180°) defect structure. Other Mn positions result in higher total energy by ~50-230 millielectron volt (meV). Previously-reported Mn-C complexes based on a solid-mechanics model place the carbon atom in the next nearest octahedral position relative to the Mn atom.
- The phase stability and physical properties of Fe_3C can be varied within a wide range by substitutional or interstitial additions of appropriate elements. We found that ΔH is negative only for cementite with boron addition $Fe_3C_{0.75}B_{0.25}$, i.e., boron stabilizes orthorhombic cementite and prevents the graphitization (dissociation of metastable cementite with the formation of bcc Fe and graphite).
- Three types of steels have been produced at Missouri University S&T: 5%Mn steel with nitrogen, a hard, bainitic steel with composition Fe-2.1Mn-4Co-1.2Si-0.6C-0.2Mo, and a lightweight steel with composition Fe-13Mn-4Al-1Si-0.1C. Steel compositions are reported in weight percent. Transformation in the 5% Mn steel was too sluggish to be practical in steelmaking practice. Microstructures similar to acicular α+β titanium alloys were produced in the Fe-2.1Mn-4Co-1.2Si-0.6C-0.2Mo steel by austempering 3 days at 300°C. The high cost of cobalt and the sluggish transformation kinetics also make this steel impractical for automotive steels. The Fe-13Mn-4Al-1Si-0.1C steel appears promising. The addition of aluminum and silicon reduced the density by 5-7% and slow cooling the steel from 1000°C produced a microstructure of degenerate Widmanstätten ferrite and retained austenite.

Future Direction

- Ferrite and austenite Fe-Mn-N alloys. We will perform comparative investigations of the electronic structure, magnetic properties, and stability of α- and γ-Fe with interstitial nitrogen and substitution manganese. The main goal is to determine the ground states of the Fe-N, and Fe-Mn-N phases with small manganese and nitrogen concentration and to understand how these impurities affect the lattice parameters, local crystal structure, magnetic interactions and phase stability. The results will be compared to those obtained for Fe-Mn-C alloys.
- Austenite Fe-Mn-(C,N)-(Al,Si) alloys. We will study the distribution of the light impurities (N, C) with respect to the substitutional 3*d* (Mn) or 3*p* (Al, Si) atoms, as well as the distribution of the latter two with respect to each other.
- Phase-stability maps will be constructed to determine a composition near the Fe-13Mn-4Al-1Si-0.1C steel that produces a fully-austenitic microstructure at hot-rolling temperatures. First, a chemical analysis will be performed on regions in the experimental Fe-13Mn-4Al-1Si-0.1C steel that are austenitic. FactSage will be used to determine vertical sections of the phase diagram near the measured composition of the austenite to formulate new steel compositions.

- Three to four experimental heats will be produced based upon compositions derived from the thermodynamic studies. These steels will be hot rolled to produce sheet product and metallurgically characterized.
- Mechanical-property tests will be conducted on the derivative steel compositions. Both static tensile tests and instrumented impact testing will be performed.
- The role of displacive relaxation and strength in the transformation of the parent phase will be examined using acoustic emission. Initial studies will examine the melting of indium inclusions embedded in aluminum. Inclusions that are embedded within crystalline grains are known to require superheating prior to melting, since the melting is inhibited by the additional pressure produced by the matrix confining the volume expansion. Acoustic-emission studies of the bainitic reaction will be conducted using the Fe-2.1Mn-4Co-1.2Si-0.6C-0.2Mo steel produced at Missouri University S&T.

Introduction

Recent developments in steels have resulted in first-generation advanced high-strength steels (AHSSs) with ferritic microstructures and second-generation high-strength steels with austenitic microstructures. The research performed here is to develop steels with duplex ferrite and austenite microstructures that will be analogous to acicular microstructures developed in $\alpha+\beta$ titanium which have high fracture toughness (see Figure 1).

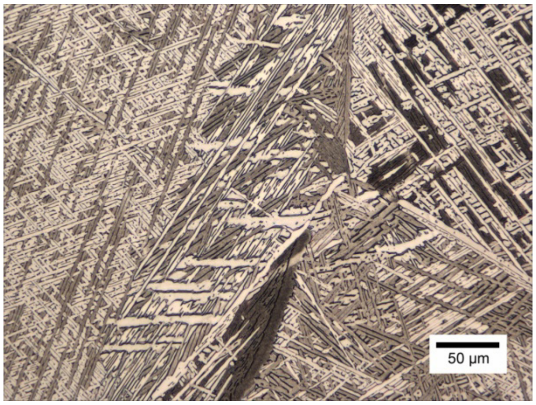

Figure 1. A titanium $\alpha+\beta$ microstructure of acicular α plates with retained β developed for high toughness.

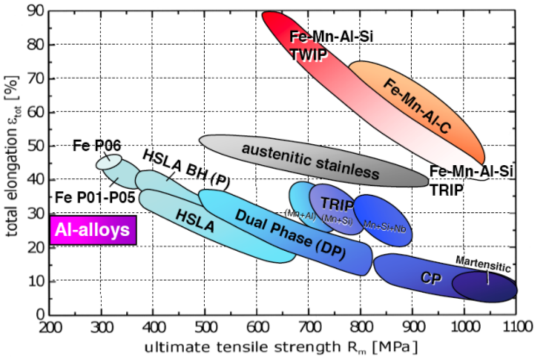

Figure 2. Property distribution plot for first- and second-generation AHSS.

These new steels will have strengths greater than first-generation advanced high-strength steels, but cost less than the ultra-high- manganese second-generation twinning-induced plasticity (TWIP) and transformation-induced plasticity (TRIP) steels (see Figure 2). These new third-generation steels will have nanometer-size acicular ferrite microstructures with metastable austenite, which results in steels both high in strength and toughness. These steels are expected to maintain steel as the preeminent high-strength structural material in designing low-weight automobiles with exceptional crashworthiness.

The complex structural and magnetic properties of iron (Fe) make it a challenge to determine the effect of impurities on the microstructure of steel, as well as its electronic structure, which is critical for the fundamental understanding of the observed macroscopic properties.

A physics-based approach to alloy design is being pursued to understand the role of Mn in the defect formation with interstitial atoms. Systematic calculations of the electronic structure and lattice distortions are being performed using the highly-precise, first-principles, full-potential linearized augmented plane wave (FLAPW) method with the structure-optimization capabilities. This allows us to calculate the dependence of the lattice parameters on carbon and nitrogen concentrations for austenite and ferrite. Similar calculations will be performed for the transition metal additions including manganese (Mn), chromium (Cr), and molybdenum (Mo). The interaction between solutes and interstitials is the most important part of our investigations. The total- and formation - energy calculations allow us to analyze the possibility of clustering and the effect of solutes on the diffusion of interstitial impurities (C, N, and B).

As distinct from the Fe and Fe-Mn phases, less-theoretical studies exist for the Fe-C and Fe-Mn-C alloys. The structural and magnetic properties of fcc Fe-C and Fe-Mn-C alloys were suggested to differ from those in pure fcc Fe. The observed anomalies in magnetic susceptibility indicate the occurrence of inhomogeneous ferromagnetic and spin-glass-like regions in the Fe-Mn-C alloys. Recent *ab initio* calculations show that interstitial carbon favors local ferromagnetic coupling, but the results for the ground state (both magnetic and crystal structure) are inconclusive. This calls for in-depth, accurate investigations of Fe, Fe-C and Fe-C-Mn systems.

Besides ferrite and austenite, carbon steels and white cast iron contain iron carbide, Fe_3C (cementite), which may substantially affect the resulting mechanical properties. The Fe-C phase diagram exhibits complex interplay of many factors including carbon concentration, temperature, treatment processes (solidification), etc. To shed light on the microscopic role of impurities in electronic and magnetic properties of cementite and its stability, we have studied Fe_3C doped with 2*p* (N, O, B) and 3*p* (Si, Al, S, P).

Theoretical Modeling of Ferrite and Austenite with Manganese: Crystal Structure, Local Distortions and Magnetic Instability

Using an *ab initio* density-functional approach, we performed calculations of α-Fe (bcc) and γ-Fe (fcc), Fe-C, Fe-Mn, and Fe-Mn-C phases (with carbon and/or manganese content of 3 atomic (at.) % in order to determine the ground states in α-Fe and γ-Fe with small manganese and carbon concentration and to understand how these impurities affect: (1) the lattice parameters, (2) local crystal structure, (3) magnetic interactions, and (4) thermodynamic stability. All α-Fe, Fe-C and Fe-Mn-C phases were found to exhibit ferromagnetic (FM) ground states and carbon in octahedral interstitial sites, which leads to tetragonal distortion. Manganese had little effect on the local and bulk crystal parameters. For Fe-Mn-C, we obtained only one stable state where manganese has ferromagnetic coupling with iron. On the other hand, two stable configurations with opposite magnetic moments of manganese (1.05 and -1.90 μ_B) differibg in energy by only 3 meV, were found for bcc Fe-Mn alloy. Thus, we demonstrate that carbon stabilizes the ferromagnetic Fe-Mn coupling in the Fe-Mn-C alloys (Figure 3).

For γ- Fe, Fe-C and Fe-Mn-C phases, the calculations were performed with fixed cubic or tetragonal symmetry for nonmagnetic (NM), FM, single-layer antiferromagnetic (AFM1), and double-layer antiferromagnetic (AFMD) states. Our results reveal that the AFMD state (which is a good collinear approximation for spiral magnetism) is the most stable in all γ- Fe, Fe-C and Fe-Mn-C phases. For every magnetic phase, the tetragonal equilibrium structure was found to have larger volume and larger magnetic moment and is lower in energy by 27–45 meV than the corresponding cubic phase, in agreement with the $c/a>1$ tetragonality of all magnetic fcc Fe states.

We predict that among two FM γ- Fe states, the tetragonal equilibrium high-spin (HS) state (FM/HS) has much lower energy, whereas the low-spin (LS) state is the most unfavorable magnetic state. Hence, the anti-Invar transition involves AFMD and FM/HS states, but not the low-spin FM state. Analyzing the α- γ transition, we show that the total energy difference between the ground magnetic states of α and γ phases corresponds to the experimentally-observed temperature, while the energy difference between the nonmagnetic phases is more than three times larger and has an opposite sign, pointing out the crucial role of magnetism in this transition.

Local tetragonal distortions around interstitial carbon strongly depend on the magnetic state, being the largest in the tetragonal FM state and much smaller in the antiferromagnetic states. We predict the frustration of ideal magnetic order for the AFM1 state in the interstitial Fe-C alloy, where the region of the Fe atoms with the opposite

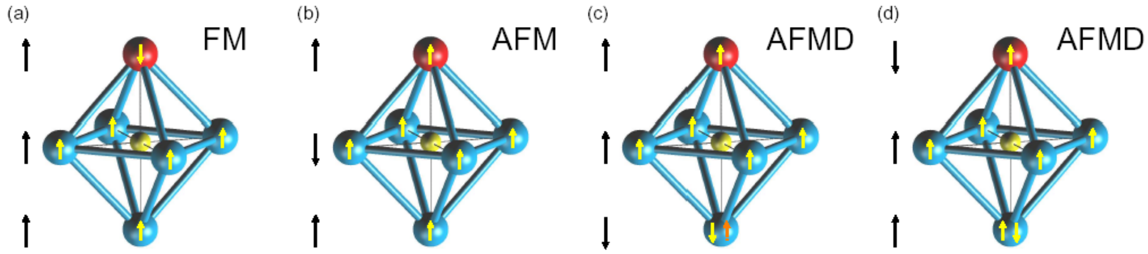

Figure 3. Local magnetic coupling of the Fe (blue) and Mn (red) atoms, which are nearest to the interstitial carbon (yellow). Black arrows at left show bulk magnetic ordering. In the double-layer configuration (AFMD), Mn and C may belong to the layers of the same (c) or opposite (d) spin. These configurations differ by only a few meV in total energy.

intra-layer coupling arises locally near the octahedral site of carbon. So, we demonstrate that carbon favors short-range ferromagnetism in γ-Fe. For the AFMD structure, we find two, nearly-degenerate, stable AFMD states which correspond to the cases where either five or all six nearest Fe atoms have ferromagnetically aligned spins. It is a competition between the intra-layer and inter-layer FM coupling that results in spin flip of the magnetic moments (–2.0/1.9 μ_B) at the Fe atoms near carbon. Thus, we show that carbon introduces FM coupling of the nearest Fe atoms and leads to magnetic instability.

For fcc Fe-Mn-C alloy, we find that manganese is antiferromagnetically coupled with the host iron atoms in FM state, but shows the ferromagnetic intra-layer coupling in both antiferromagnetic ground states. Further, the moments of planar Fe atoms may be either antiferro- or ferromagnetically coupled with the moments of the other Fe atoms in the layers to which they belong to for the ground antiferromagnetic or AFMD states, respectively. In the first case, the moments of all six nearest Fe atoms are ferromagnetically coupled. This behavior in local magnetic ordering is similar to that found in the Fe-C alloy.

Thus, we find that the nearest manganese and iron atoms may be FM or antiferromagnetic coupled with the host iron in the fcc Fe-Mn-C alloy and the energies for spin flip are very small, which should result in magnetic instability of both manganese and iron. Furthermore, for cubic structures, we show that the short-range ferromagnetism of the nearest iron atoms is compensated by the appearance of antiferromagnetic order of the iron atoms in the neighbor layers.

These results provide an understanding of the origin for the observed spin-glass behavior in Fe-Mn-C.

Finally, we estimated the solution enthalpy ΔH for carbon and manganese in α-Fe and γ- Fe. For the bcc FM Fe-3%C alloy, we found positive solution enthalpy of +0.79 electron volt (eV) for carbon in octahedral sites that is in good agreement with experimental value 0.6-0.8 eV. The positive solution enthalpy corresponds to low carbon solubility in bcc Fe. For fcc Fe-3%C, we obtained ΔH to be +0.02, -0.05 eV, -0.06 and -0.07 eV for NM, FM, AFM1 and AFMD states, respectively. The negative solution enthalpy was obtained for magnetic states and this result demonstrates the crucial role of magnetism in the solubility of interstitial impurities.

For manganese, the solution enthalpy is +0.39 eV for bcc FM Fe-Mn-C, and –0.29, –0.37 and –0.40 eV for fcc FM, AFM1 and AFMD Fe-Mn-C states, respectively. Thus, manganese and carbon destabilize α-Fe, but give a strong stabilizing effect in γ-Fe. This fact explains the shift of the α-γ phase transition to lower temperatures caused by manganese in austenite.

Electronic Structure, Stability and Magnetic Properties of Fe_3C (Cementite) with 2*p* and 3*p* Impurities.

Cementite as a bulk compound in the Fe-C system is metastable with respect to α-Fe and graphite at all temperatures, and this graphitization process plays an important role for iron alloys with high carbon content e.g., cast irons. Alloying impurities may dissolve in Fe and (or) in Fe_3C and may favor or prevent the graphitization. The phase stability and physical properties of Fe_3C can be varied within a wide range by substitutional or interstitial additions of appropriate elements. Here, we study the electronic structure, enthalpy of formation and magnetic properties of cementite Fe_3C doped with 2*p* (N, O, B) and 3*p* (Si, Al, S, P) impurities. We predict that all 2*p* elements, phosphorus and sulfur replace carbon and have a small effect on the values of the magnetic moments of the nearest iron atoms, while aluminum and silicon substitute for iron in special positions and reduce the iron magnetic moments as well as the total magnetization.

All 2*p* and 3*p* impurities have a small effect on the location of the Fermi level, which is in the region of almost-filled Fe3*d*↑ states and local minimum of partially-occupied Fe3*d*↓ states, similar to the undoped cementite and γ-Fe. The main changes occur near the bottom of the hybrid band, and we find that the total density of states increases for all 2*p* and 3*p* impurities except for oxygen (Table 1). All impurities mainly contribute in the spin-up density of states $N^{\uparrow}(E_F)^{imp}$, while $N^{\downarrow}(E_F)^{imp}$ remains much lower.

Each impurity (except for oxygen) substituted for carbon has a small negative magnetic moment and slightly changes the magnetic moments at the nearest iron atoms in special (Fe_s) and general (Fe_g) positions (Figure 4). The total magnetization is also little affected. The impurities, which substitute for iron (Al, Si) have antiferromagnetic coupling with iron, but they essentially decrease the magnetic moments of the nearest iron atoms and magnetization (Table 1).

The positive formation energy $\Delta H = 0.06$ eV/atom was obtained for the unalloyed cementite. The experimental finding (0.05–0.07 eV/atom) also gave the positive value testifying that Fe_3C is a metastable bulk compound. To estimate the effect of 2*p* and 3*p* impurities on the stability of cementite, we analyzed the enthalpy of formation energies ΔH, which were calculated as the difference of total energies Fe_3C-X, where impurity X was substituted in the preferable site, iron, carbon, and impurity in their ground states.

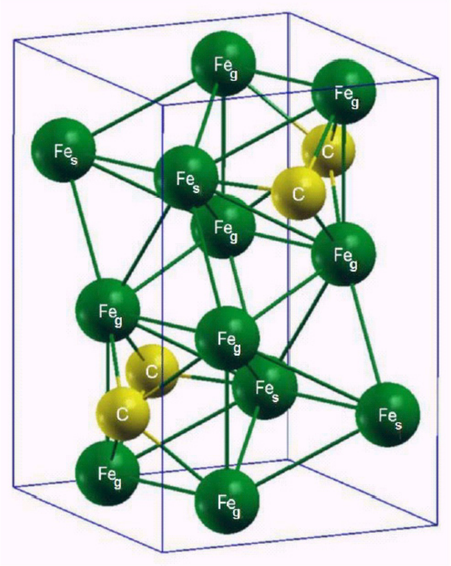

Figure 4. Unit cell of cementite showing general (Fe_g) and special (Fe_s) lattice positions.

We found that ΔH is negative only for cementite with boron addition $Fe_3C_{0.75}B_{0.25}$, i.e., boron stabilizes orthorhombic cementite and prevents the graphitization (dissociation of metastable cementite with the formation of bcc Fe and graphite).

A small stabilizing effect was obtained for nitrogen, while oxygen and sulfur slightly destabilize cementite. Aluminum and especially silicon lead to strong destabilization of cementite, which explains their effects on the promoting of graphitization. Thus, our results reveal that among 2*p* and 3*p* impurities, only aluminum and silicon may completely suppress the formation of cementite.

Production of Third-Generation High-Strength Steels

Development of a third-generation AHSS based upon a nano-acicular duplex microstructure will require new strategies in alloy chemistry to produce nano-scale microstructures in continuously-cooled wrought steel products. The important issues in developing nano-acicular duplex steels of high strength are
(1) understanding the fundamental alloy effects in Fe-X-C and Fe-X-N systems, (2) predicting physical properties of these alloys, (3) eliminating

Table 1. Total density of states at the Fermi level $N^{\uparrow}(E_F)$ and $N^{\downarrow}(E_F)$ and the contribution of impurity states ($N^{\uparrow}(E_F)$ and $N^{\uparrow}(E_F)^{imp}$ (states/eV*f.u.); the averaged local magnetic moment (m, in μ_B), the total magnetization (M, in μ_B) and the formation energy ΔH (eV/f.u.) for cementite with 2*p* and 3*p* impurities.

	$Fe_3C_{0.75}B_{0.25}$	Fe_3C	$Fe_3C_{0.75}N_{0.25}$	$Fe_3C_{0.75}O_{0.25}$
$N^{\uparrow}(E_F)$	1.24	1.19	1.26	0.78
$N^{\downarrow}(E_F)$	1.83	1.78	1.92	1.54
$N^{\uparrow}(E_F)^{imp}$	0.011	0.012	0.036	0.029
$N^{\downarrow}(E_F)^{imp}$	0.004	0.005	0.009	0.012
$m(X)\ \mu_B$	–0.14	–0.12	–0.06	0.14
$m(Fe_s)\ \mu_B$	2.10	1.96	1.98	2.19
$m(Fe_g)\ \mu_B$	1.89	1.86	1.88	2.09
M, μ_B	1.90	1.85	1.89	2.05
ΔH, eV	–0.06	0.22	0.18	0.33
	$Fe_{2.75}Al_{0.25}C$	$Fe_{2.75}Si_{0.25}C$	$Fe_3C_{0.75}P_{0.25}$	$Fe_3C_{0.75}S_{0.25}$
$N^{\uparrow}(E_F)$	1.44	1.27	1.06	1.08
$N^{\downarrow}(E_F)$	1.94	2.02	2.19	2.31
$N^{\uparrow}(E_F)^{imp}$	0.006	0.014	0.013	0.022
$N^{\downarrow}(E_F)^{imp}$	0.002	0.003	0.004	0.005
$m(X)$, μ_B	–0.04	–0.04	–0.08	–0.03
$m(Fe_s)\ \mu_B$	1.34	1.33	2.02	2.08
$m(Fe_g)$	1.70	1.48	1.87	1.89
M, μ_B	1.55	1.54	1.88	1.90
ΔH, eV	0.65	1.29	0.21	0.29

precipitation of ferrite along prior austenite grain boundaries, (4) inoculating the steel to produce intragranular precipitation of the acicular ferrite, (5) controlling the ferrite subunit width during transformation to produce nanometer scale microstructures, and (6) reducing silicon levels to produce steel of better surface finish.

The starting point for many high-strength bainitic alloys is Fe-2Si-2Mn-C, which has sufficient hardenability to reach the bainite start temperature, which avoids allotriomorphic ferrite and pearlite microstructures. The bainite start temperature is largely controlled by the carbon content and decreases with increasing carbon content. Manganese is the next most effective alloy addition with respect to reducing the bainite start temperature and the program of study is examining steel chemistries with higher Mn contents than the first-generation AHSS, ferritic alloys, but substantially less Mn than that used in the second-generation AHSS, austenitic alloys. We expect to utilize manganese in the range of 2 to 14 weight % (wt %) for the nano-acicular duplex steels. The total interstitial content will be reduced to 0.10 wt % to maintain a high chemical driving force for the formation of ferrite. Additions of aluminum, rather than cobalt, will be employed to encourage transformation to ferrite upon continuous cooling. Aluminum has the added benefit of lowering the steel density and as shown in the theoretical studies of this report, aluminum destabilizes the cementite. Thus, the addition of aluminum may lower the required amount of silicon to inhibit cementite formation and encourage incomplete transformation, i.e., retention of austenite.

Missouri University S&T has a strong and active steelmaking program. We have the ability to cast up to 200 pounds of steel of a single chemistry. Steelmaking was performed by melting high-purity charge materials under argon using a coreless induction furnace (see Figure 5). Active oxygen is measured in the ladle using a Hereaus Electronite oxygen probe. Steels are deoxidized by measured additions of aluminum or titanium and subsequently cast into no-bake sand molds. Molds

Figure 5. Photograph of casting steel in the Missouri University S&T foundry.

were designed to produce sound slabs for hot rolling.

An initial study was performed to examine Fe-5Mn-1.5Si-0.35C-0.3Mo steel alloyed with and without nitrogen. The first heat was divided into two casts: the base composition and the base steel modified by the addition of nitrided ferromanganese. Each of these steels was deoxidized with either aluminum or a combination of aluminum and titanium. When both aluminum and titanium were used, the initial addition of aluminum was insufficient to fully deoxidize the melt and deoxidation was finished with titanium. The expectation was that the initial Al_2O_3 formed would act as a nucleation site for Ti_2O_3, which then serves as an inoculant for acicular ferrite.

We discovered very quickly that these nitrided manganese steels were very resistant to bainitic transformation. Indeed, annealed specimens that were furnace cooled had microstructures that were fully martensitic. Figure 6 shows an example of the steel austempered 7 days at 400°C, which was partially transformed. The figure shows that degenerate Widmanstätten ferrite nucleated on TiN particles. The scale of the ferrite width could be measured in microns and the steel composition was deemed unworkable for automotive steel.

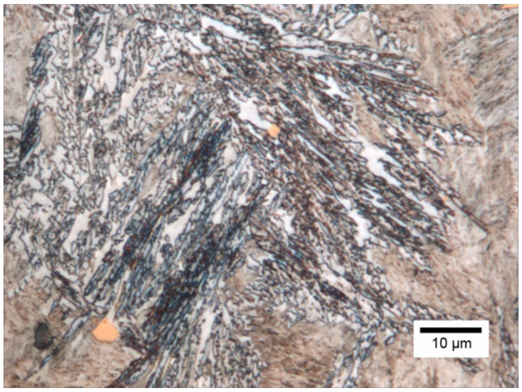

Figure 6. Austempered microstructure of steel alloy with composition Fe-5.01Mn-1.34Si-0.29Mo-0.075Al-0.80Ti-0.029N. Nital etch.

A traditional, hard bainitic steel was cast to study nanometer-scaled ferritic microstructures. The steel composition was Fe-0.63C-3.99Co-2.1Mn-1.35Si-0.34Cr-0.21Mo-0.61Al. The steel was austenitized at 920°C and isothermally transformed at 300°C to produce a classic "basket-weave" microstructure (see Figure 7). This microstructure compares favorably with the $\alpha+\beta$ titanium alloys developed for high fracture toughness. The scale of the bainitic ferrite was measured by x-ray diffraction to be 10–20 nanometers (nm). The retained austenite was also determined to be less than 10%.

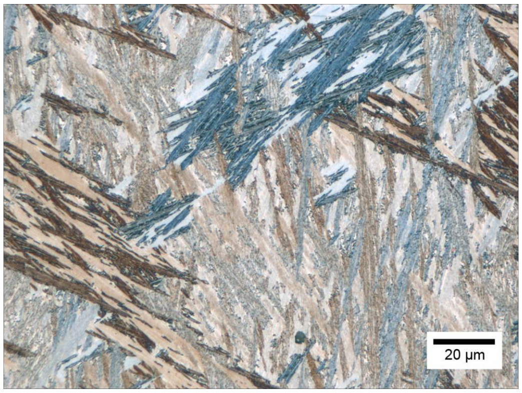

Figure 7. A basket-weave microstructure produced by austempering a Fe-0.63C-3.99Co-2.1Mn-1.35Si-0.34Cr-0.21Mo-0.61Al steel at 300°C for 3 days. Nital etch and imaged with cross-polarized light and ¼ wavelength filter.

The high cost of cobalt makes the hard bainitic type steel impractical for automotive applications. However, we will use this steel in our acoustic-emission studies of bainitic transformation. There are three definitions of bainite currently in use. The surface-relief theory states that a displacive transformation produces a surface-relief distortion and that this transformation occurs at velocities fast enough to produce acoustic emissions. Thus far, these emissions have only been observed in continuously-cooled steels. We are building a facility to measure the emissions during isothermal transformation and will study this phenomenon. It is also possible that these emissions are a displacive relaxation in the parent phase and these relaxations occur as a dynamic strain-aging effect with sudden dislocation multiplication. Understanding this reaction will be fundamental in the design of new steels.

Aluminum is the only other addition to steel that is known to increase bainitic transformation kinetics. Aluminum has the added benefit of reducing the density of steel. Aluminum has a lower mass and produces lattice dilatation; both contribute to reducing the density. Manganese will also reduce the density, but to a lesser degree. A new steel was formulated with the following nominal composition: Fe-13Mn-4Al-1Si-0.1C. The steel was produced at Missouri University S&T. These high-manganese compositions require wet chemical analysis and this information was not available at the time of this report. The density of the cast steel was measured to be 7.2 g/cm^3 and this would be approximately a 7% decrease in density relative to typical automotive steels. This low density is similar to that of TWIP steels. The cast microstructure was a combination of ferrite and austenite. When slowly cooled from an elevated temperature, the austenite transformed producing a degenerate Widmanstätten ferrite (see Figure 8). Degenerate structures are produced by sympathetic nucleation of small subunits of ferrite and are often associated with the phenomenon of incomplete transformation.

FactSage, a free-energy minimization modeling program, was used to predict the equilibrium phase stabilities of this alloy system. The simulation is shown in Figure 9. There was good agreement between the observed and calculated ferrite and austenite content. Based on these results, we will use FactSage to determine appropriate alloy content to produce steel that can be fully austenitized at typical hot-working temperatures. This composition will also be measured directly from the austenitic regions of our cast steel.

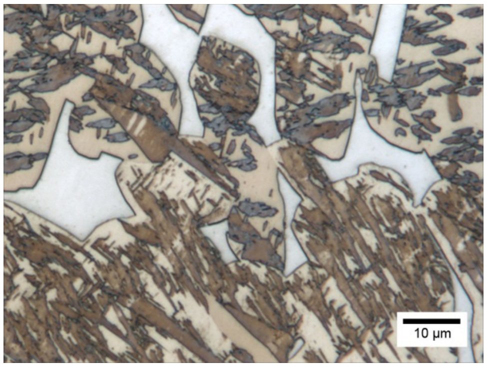

Figure 8. Microstructure of Fe-13Mn-4Al-1Si-0.1C alloy that was heated to 1000ºC then slowly cooled to ambient temperature. Interdendritic ferrite appears as the light contrast feature and degenerated Widmanstätten ferrite appears as the darkest contrast feature. Etched with 10% $Na_2S_2O_5$.

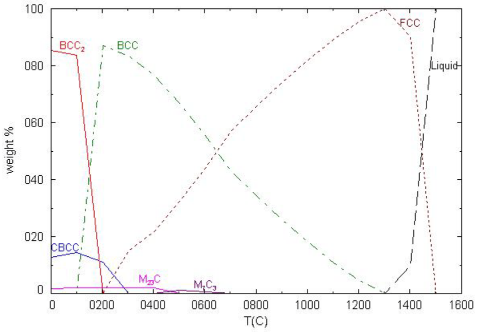

Figure 9. FactSage predictions of phase composition as a function of temperature for the Fe-13Mn-4Al-1Si-0.1C alloy. A duplex mixture of ferrite and austenite is predicted at typical hot working temperatures between 900 and 1100°C.

The transformed austenite shown in Figure 8 has many of the qualities desired for a third-generation advanced high-strength steel: a basket-weave microstructure of ferrite plates in a matrix of retained austenite. Future experiments on this steel will examine hot working of the steel, grain-size control, controlled cooling, microstructural characterization, and mechanical properties.

Presentations/Publications/Patents

1. M. C. McGrath, D. C. Van Aken, J. Medvedeva, S. N. Lekakh, and V. L. Richards. “Advanced High Strength Steels (AHSS) with Duplex Ferrite and Austenite Microstructures,” MS&T 08 Conference and Exhibition, Pittsburgh, PA October 5–9, 2008.

S. Sheet Formability and Springback of Advanced High-Strength Steels—CSM

Principal Investigator: David K. Matlock
Advanced Steel Processing and Products Research Center
Department of Metallurgical and Materials Engineering
Colorado School of Mines
Golden, CO 80401
(303) 273-3775; fax: (303) 273-3016; e-mail: dmatlock@mines.edu

Co-Principal Investigator: John G. Speer
Advanced Steel Processing and Products Research Center
Department of Metallurgical and Materials Engineering
Colorado School of Mines
Golden, CO 80401
(303) 273-3897; fax: (303) 273-3016; e-mail: djspeer@mines.edu

Co-Principal Investigator: James G. Schroth
General Motors
R & D Center
30500 Mound Road
M/C 480-106-212
Warren, MI 48090-9055
(586) 986-0977; fax: (586) 986-9204; e-mail: james.g.schroth@gm.com

Principal Investigator: Robert H. Wagoner
Department of Materials Science and Engineering
The Ohio State University
2041 College Road
Columbus OH 43210
(614) 292-2079; fax: (614) 292-6530; e-mail: wagoner.2@osu.edu

Technology Area Development Manager: Joseph A. Carpenter
(202) 586-1022; fax: (202) 586-1600; e-mail: joseph.carpenter@ee.doe.gov

Field Project Officer: Aaron D. Yocum
(304) 285-4852; fax: (304) 285-4403; e-mail: aaron.yocum@netl.doe.gov

Contractor: Colorado School of Mines (CSM)
National Science Foundation (NSF) Award CMMI 0729114, jointly funded by NSF and DOE

Objective

- Identify new processing routes and microstructures which lead to economical steels with properties characteristic of third-generation advanced high-strength steel (AHSS).
- Experimentally and theoretically evaluate properties of new AHSS materials.

Approach

- Utilize theoretical predictions developed by the authors and others to predict ideal microstructures that lead to potential strength/ductility combinations characteristic of the third-generation AHSS.

- Evaluate and develop novel laboratory processing methods to produce materials with controlled variations in phase volume fractions, distributions, and properties.
- Produce sample material for use in this project as well as in the companion springback study at the Ohio State University, a partner with CSM through the NSF GOALI program.
- Experimentally evaluate the mechanical properties, including formability, of the experimental steels.
- Compare experimentally-measured properties to predictions of the theoretical models.
- For materials which appear promising based on laboratory data, assess potential paths to process materials on a larger scale.

Accomplishments

- Supported Senior Design Project at the CSM. The project entitled “Design Concepts to Produce the Next Generation of Advanced High Strength Sheet Steels,” was completed during the spring semester, 2008.
- Successfully recruited a PhD graduate student, Mr. Paul Gibbs.
- Research plan was reviewed in March 2008 with the sponsors of the Advanced Steel Processing and Products Research Center at the CSM.
- Initial materials for evaluation have been received and initial heat-treat experiments have begun.

Future Direction

- Identify and obtain additional materials for analysis.
- Evaluate the microstructures and properties of heat-treated manganese (Mn) steels.
- Evaluate the mechanical properties of austenitic stainless steels with controlled volume fractions of deformation-induced martensite.
- Initiate discussions about the applicability of including duplex stainless steels in the study.
- Assess predictions of theoretical models for the deformation behavior of multi-constituent steels and compare to predictions based on simplified composite model.
- Support a senior design project at CSM for the spring semester of 2009.

Introduction

This project is in the early stages of development and has concentrated on literature review and analysis of the composite models on which the original research proposal was based. The project was budgeted for 3 years, and DOE/NSF funded the project over 4 years. The PhD graduate student, Mr. Paul J. Gibbs, initiated his graduate studies in August 2008, after completing his BS in Metallurgical and Materials Engineering at CSM in May 2008. In this report, the background for the project is highlighted, along with the materials and processing approaches that have been identified for the first phase of the research program.

Background

Recently, significant interest has been expressed by steel-producing and steel-using industries for development of the next generation of advanced high-strength steels (AHSSs) sheet to meet the demanding requirements for strength, formability, toughness, cost, etc [1–3]. To produce the new AHSS sheet steels, unique processing schemes will be required. It is anticipated that these will be initially based on modifications to routes currently employed to produce dual phase (DP) and transformation-induced plasticity (TRIP) steels. To produce materials with the desired final properties, several microstructural features must be simultaneously and independently controlled. These include: number of constituents (e.g., phases) and constituent volume fractions, sizes, and distributions, along with the mechanical properties (e.g., strength and strain-hardening behavior) of the individual constituents.

A methodology to assess effects of microstructural variables in new AHSS grades has been demonstrated [2, 3] based on the composite model approach of Mileiko [4]. Figure 1 compares predicted effects of systematic microstructural variations, obtained by increasing the martensite volume fraction (up to 70 pct), in hypothetical, two-component composite materials of ferrite plus martensite or stable austenite plus martensite [2, 3]. These predictions are superimposed on a strength-ductility map often used to compare sheet-steel properties [1] and identify property bands associated with first- and second-generation AHSS. For these calculations, specific properties for each phase were assumed based on literature data and predictions utilized a composite model for two ductile constituents assuming iso-strain [2]. Figure 1 shows that the properties of a wide variety of sheet-steel families, including the first-generation AHSS steels, are reasonably predicted with a two-component system based on ferritic steels and that steels in the third-generation band may be modeled by various combinations of martensite with stable austenite. Similar calculations based on metastable austenite have shown that the resulting composite properties depend sensitively on austenite stability against deformation-induced transformation to martensite [3].

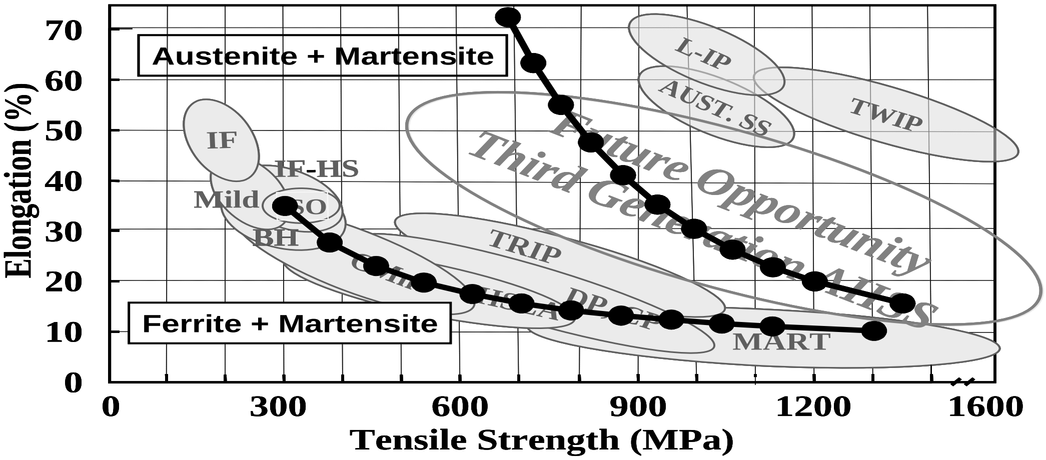

Figure 1. Predicted [2, 3] strength/ductility combinations for two hypothetical steel families with systematically-varied martensite volume fractions with property bands for various classes of conventional and AHSS steels [1]. Predictions shown are for composites consisting of ferrite + martensite or stable austenite + martensite.

The analysis summarized in Figure 1 successfully predicted strength-ductility properties for existing ferritic-based steels from low-strength interstitial free (IF) to high-strength martensitic steels. While predictions from the composite analyses provide insight into microstructural combinations required for the new AHSS, the simplifying assumptions (each constituent was assumed to deform independently and iso-strain was assumed) embedded in the composite model [4] and consideration of actual deformation behavior of and interactions between constituents will be required to predict optimal microstructures. Nonetheless, it appears clear that the third generation of AHSS will consist of complex microstructural combinations, with significant use of both high-strength constituents (e.g., martensite, bainite, ultrafine-grained ferrite, etc.) and high-ductility constituents with significant strain-hardening capacity (e.g., austenite with controlled stability against deformation-induced transformation to martensite) [2, 3]. The methodology has been applied, as illustrated in the following sections, to predict properties of steels of interest here.

Predictions of AHSS Microstructures and Properties

The predictions presented in Figure 1 depend on variations in the mechanical properties of the individual constituents used in the model. Figure 2 presents one example which shows the significance of increasing the strength of the stable austenite from 640 MPa used in Figure 1 to 850 MPa with a corresponding decrease in uniform strain from 0.6 to 0.4. These property changes are consistent with a mechanism such as temper rolling or refinement of the austenite grain size. For Figure 2, the volume fraction of martensite was varied from 0 to 0.7, and the martensite properties were assumed constant. An increase in austenite strength with a corresponding *decrease* in the true uniform strain, is shown to lead to an *increase* in ductility of the composite at a given strength level. The observation that increasing the strength of one phase leads to a ductility increase is interesting, counterintuitive, and illustrates the importance of phase interactions on the overall properties of multi-phase steels.

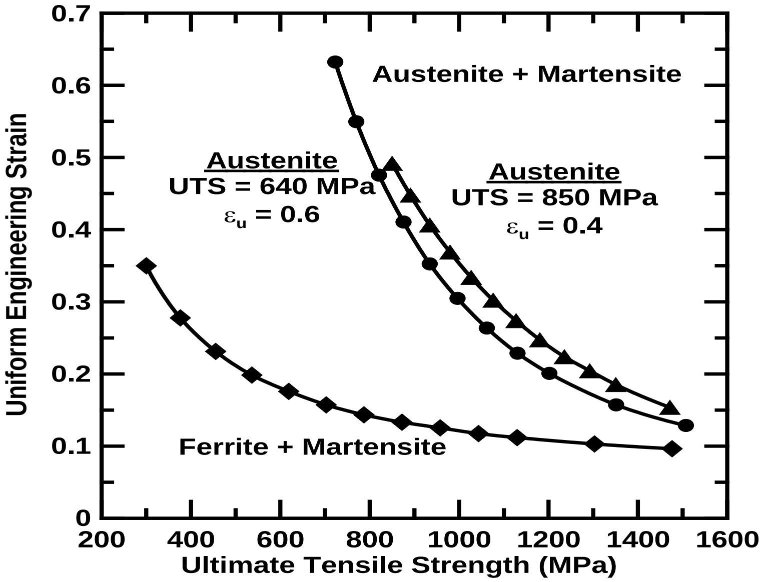

Figure 2. Influence of austenite properties on the predicted strength/ductility combinations shown in Figure 1 obtained by applying Mileiko's analysis [4]. The effect of increasing the austenite ultimate tensile strength (UTS) to 850 MPa with a corresponding decrease in ductility are shown. For each material, the ferrite + martensite data used in the calculations are UTS and true uniform strain, ε_u. The specific data used are: ferrite UTS = 300 MPa, ε_u = 0.3 [5, 6]; stable austenite, UTS = 640 MPa, ε_u = 0.6 [7]; and martensite, UTS = 2000 MPa, ε_u = 0.08 [5, 6].

The importance of metastable austenite transformation to martensite with strain and variations in austenite stability have been evaluated with predictions based on the Mileiko model for steels with hypothetical microstructures containing up to 85% austenite [2, 3]. Following the composite modeling approach used to generate Figures 1 and 2, the results with metastable austenite highlight the importance of controlling the austenite stability. Specifically, low austenite stability leads to rapid (with strain) austenite transformation to martensite resulting in properties similar to dual phase steels while relatively high austenite stability delays martensite formation, improving work hardening at high strains leading to suppression of necking and higher ductilities. These predictions suggest that the next generation of AHSS may consist of complex microstructural combinations, with significant contents of high-strength phases, which could be martensite as considered here, bainite, or ultrafine-grained or cold-worked ferrite, and highly-ductile phases with significant capacity for strain-hardening phases (e.g., austenite). Once a desirable combination of properties and microstructure is identified, then novel techniques must be identified to produce microstructural constituents with the necessary deformation response.

Evaluation of Methodologies to Produce Third-Generation AHSS

Recently, there has been considerable research interest in cold-rolled steels annealed at temperatures greater than A_3 or at an intercritical temperature and then rapidly cooled to a temperature below the martensite-start temperature, M_s, but above the martensite-finish temperature, M_F. This sequence is akin to a modified martempering process as employed in quenched and tempered steels, but is designed to modify the microstructure rather than the thermal stresses. After cooling, the material is held at the quench temperature (QT) or is reheated slightly and held for a specified time prior to cooling to room temperature. Materials produced by this interrupted quenching process have been referred to by a variety of terms including “quenching and partitioning (Q&P)” [8, 9], “TRIP-dual” [10], “TRIP aided bainitic ferrite (TBF)” [11], “isothermal quench and tempering (IQ+T)” [12], and “quenching, partitioning, and tempering (Q-P-T)” [13]. For the discussion that follows, steels from these studies are referred to as “Q&P” steels, although Q&P processing usually implies quenching temperatures meaningfully below the martensite-start temperature (M_s). On quenching, the amount of initial martensite that forms depends on the M_s for the austenite present during annealing, and the difference between the M_s and QT. Subsequent changes in the microstructure on isothermal holding prior to cooling to room temperature depend on alloy content, temperature, and holding time.

To illustrate the potential for the Q&P process to produce AHSS materials of interest, Streicher et al. evaluated the heat-treating response of a 0.19C, 1.59Mn, 1.63Si (wt %) alloy processed with Q&P temperature-time histories as well as thermal histories designed to simulate more conventionally heat-treated Q&T and austempered TRIP steels [9, 14]. Figure 3 correlates ultimate tensile strengths with total elongations for one-step and two-step Q&P materials annealed from both above and below the A_{c3}, with similar data on dual phase, TRIP, and martensitic steels. In addition to steels processed by Streicher et al., Figure 3 also includes data from the literature [9, 14]. The Q&P materials included samples with austenite volume fractions up to 16 pct. The dual phase steels included here were of relatively high strength, owing to the effects of relatively high martensite fractions.

The data in Figure 3 show that strength/ductility combinations characteristic of the third generation of AHSS were obtained, indicating that Q&P processing may be a viable route to producing new steel grades. Clearly, the data obtained to date are promising, but significantly more work is required to optimize Q&P processing and design alloys and process histories compatible with current and future production constraints.

Recently, two studies designed to extend current production technologies to higher strength-ductility regimes have been shown to produce materials with properties in the third-generation AHSS property band in Figure 1. Wakita et al. [15], in their study on thermomechanically-controlled processing (TMCP), evaluated ultrafine TRIP-aided multi-phase microstructures in a 0.19C, 1.96Si, 2.01Mn (wt pct) low-carbon steel. They found that heavy deformation at low austenite rolling temperatures led to the formation of 2 micrometer (µm) ferrite, a high volume fraction of retained austenite (on the order of 25 pct), and a modification of the retained-austenite morphology from film-like to granular. The resulting ultra-fine TRIP microstructure exhibited a tensile strength of 1080 MPa and total elongation of 26.9 pct. The high ductilities were attributed to austenite which was partially stabilized by the ultrafine microstructure and only transformed at higher strains, leading to high work-hardening rates which suppressed necking.

In comparison to the work of Wakita et al.[15], Merwin [16, 17] evaluated the effects of processing on the TRIP behavior of a series of 0.1 wt pct C steels with Mn contents in the range of 5.2 to 7.1 wt pct. Data were obtained for material in the as-hot-rolled and in the cold-rolled

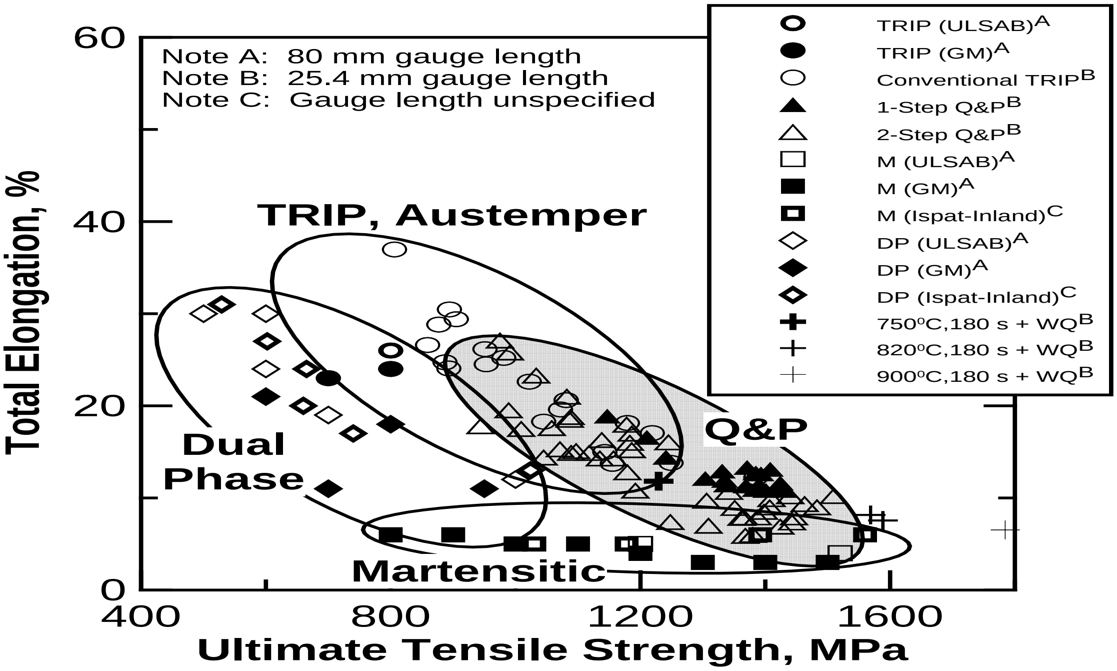

Figure 3. Total elongation vs. ultimate tensile strength for sheet steels processed with microstructures characteristic of TRIP, dual phase (DP), martensitic, Q&P materials. References for the individual data are summarized elsewhere [9, 14].

and annealed conditions. In the as-hot-rolled condition, all microstructures were martensite (i.e., the alloys were fully hardenable even at the coil cooling rates applicable to conventional hot-strip mill processing). Cold rolling and annealing of the initially martensitic structure resulted in very fine ferrite-austenite microstructures, with the amount of austenite dependent on the annealing temperatures and times chosen to simulate hot and cold spots in batch annealing. In the cold-rolled and annealed samples, retained austenite contents up to approximately 38 pct were observed. Tensile data were obtained and Figure 4 correlates UTS and total elongation values for cold-rolled and annealed materials with the desired property band for third-generation AHSS steels. Also shown is the result from the thermomechanical processing study of Wakita et al. [15]. Data for samples from Merwin [16, 17] and the data of Wakita et al. [15] that plot within the desired property band correspond to samples with high volume fractions of retained austenite. This comparison indicates that development of the next generation of steels may be possible with controlled Mn additions along with controlled thermomechanical processing to produce ultrafine-grained ferrite for strength and high volume fractions of retained austenite for ductility.

Additional processing routes have been identified based on recent results on new AHSS products published in the proceedings of the International Conference on New Developments in Advanced High Strength Sheet Steels, held in Orlando, Florida, on June 15–18, 2008 [18]. These include modifications to traditional DP, TRIP, and martensitic steel processing, and further analysis of these to produce property combinations of interest are underway.

Status of Current Research Activities

Several alloying and processing approaches that have been identified to assess the predictability of the composite model that has been developed and to assess microstructural combinations that lead to strength-ductility combinations characteristic of the third generation of AHSS currently under study. Following the work of Merwin [16, 17], a processing methodology to increase austenite stability via Mn partitioning is currently being evaluated at CSM. Hot- and cold-rolled materials

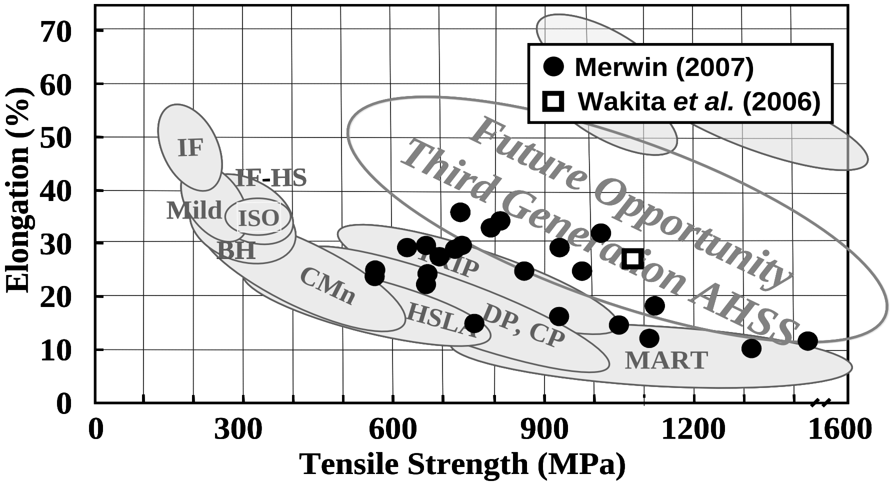

Figure 4. A comparison of tensile strength and tensile elongation data for thermomechanically controlled processed, Mn-modified, low-carbon steels with fine microstructures, some with significant amounts of retained austenite compared to the opportunity band for third-generation AHSS. Data shown from Wakita et al. [15] and Merwin [16, 17].

have been obtained from US Steel Corporation from the same heats used by Merwin.

Metastable austenitic stainless steels, prestrained a constant amount at various temperatures below room temperature to produce a series of samples with different initial martensite volume fractions, are being used to directly evaluate the predictability of the composite modeling. Specifically, tensile tests on these materials at and above room temperature provide data on materials with different austenite stabilities (the austenite stability against deformation-induced transformation increases with test temperature). Initial data on metastable austenitic stainless steels were obtained as part of the spring 2008 senior design project at the CSM. A follow-up senior design project is being planned for 2009. Initial evaluation of duplex stainless steels as an “ideal material” to assess deformation fundamentals in two-constituent materials has also been completed.

Conclusions

The composite methodology based on iso-strain deformation, while simplistic, can be used to predict the effects of microstructural, property, and testing variables including grain size; second-phase volume fraction, size and distribution; imposed strain rate; strain-hardening behavior of the martensite; etc. Potential approaches to develop new steels with microstructures that produce mechanical properties characteristic of the third generation of AHSS have been identified. The importance of combining an understanding of fundamental deformation mechanisms with predictions based on appropriate composite models to describe the deformation behavior of multiphase materials has been illustrated. From these analyses, it is predicted that the third generation of AHSS will require significant amounts of a high-strength constituent (e.g., martensite or ultrafine-grained ferrite) and significant amounts of austenite. Furthermore, the austenite must be designed with controlled deformation-induced transformation behavior to modify the work-hardening response. While the required microstructures are complex, alloying and processing approaches, particularly involving Q&P processing or Mn-modified low-carbon steels, might be used to produce the desired microstructures. It is also clear that significant research is still required to design alloying and processing methodologies to optimize third-generation AHSS material properties.

Presentations/Publications/Patents

1. David K. Matlock (Speaker) and John G. Speer, “Third Generation of AHSS: Microstructure Design Concepts,” presented at Materials and Textures in Steels

(MATS2008), Jamshedpur, India, February 6, 2008 (invited presentation).

2. David K. Matlock, “Collaborative Proposal: GOALI: AHSS: Sheet Formability and Springback of Advanced High Strength Steels—An NSF/DOE Funded Program,” Presented at the Advanced Steel Processing and Products Research Center Semi-Annual Review Meeting, Golden, CO, March 18, 2008.
3. David K. Matlock, “Summary: International Conference on New Developments in Advanced High Strength Sheet Steels,” Conference Closing Keynote Lecture, Orlando, Florida, June 18, 2008.
4. David K. Matlock, “Advanced High Strength Sheet Steels: Microstructures, Properties, and Formability,” 20th Posco Conference on Iron and Steel Technology, Postech University, Pohang, Korea, August, 27, 2008, keynote lecture.
5. Paul J. Gibbs, “Development of the Third Generation of Advanced High Strength Sheet Steels,” Presented at the Advanced Steel Processing and Products Research Center Semi-Annual Review Meeting, Golden, CO, September 23, 2008.
6. David K. Matlock, “Advanced High Strength Sheet Steels: Microstructures, Properties, and Formability,” invited lecture to the Saudi ASM Chapter; meeting held at the SABIC Technology Center in Jubail, Saudi Arabia on November 9, 2008.
7. D. K. Matlock and J. G. Speer, “Third Generation of AHSS: Microstructure Design Concepts,” *Proceedings International Conference on Microstructure and Texture in Steels*, ed. by A. Haldar, Springer-Verlag, London, 2008, in press.
8. D. K. Matlock and J. G. Speer, “Processing Opportunities for New Advanced High Strength Sheet Steels,” *Proceedings of the 2nd International Conference on Thermo-Mechanical Simulation and Processing of Steels*, ed. by S. K. Chaudhuri, B. K. Jha, S. Srikant, P. K. Maini, A. Deva, and R. Datta, Allied Publishers Ltd., New Dehli, India, 2008, pp. 169–179.

References

1. “Third Generation Advanced High Strength Steel (AHSS),” Research and Development Solicitation, AISI, Washington, D.C., 2006.
2. D. K. Matlock and J. G. Speer, *Proceedings of the 3rd International Conference on Structural Steels*, ed. by H. C. Lee, The Korean Institute of Metals and Materials, Seoul, Korea, 2006, pp. 774–781.
3. D. K. Matlock and J. G. Speer, *Proceedings International Conference on Microstructure and Texture in Steels*, ed. by A. Haldar, Springer-Verlag, London, 2008, in press.
4. S. T. Mileiko, *J. of Mat. Sci.*, vol. 4, 1969, pp. 974–977.
5. R. G. Davies, *Metall. Trans. A*, vol. 9A, 1978, pp. 451–455.
6. R. G. Davies, *Metall. Trans. A*, vol. 9A, 1978, pp. 41–52.
7. G. Frommeyer, U. Brüx, and P. Neumann, *ISIJ Int.*, vol. 43, no. 3, 2003, pp. 438–446.
8. J. G. Speer, A. M. Streicher, D. K. Matlock, F. Rizzo, and G. Krauss, *Austenite Formation and Decomposition*, ed. by E.B. Damm and M. J. Merwin, TMS, Warrendale, PA, 2003, pp. 505–522.
9. A. M. Streicher, J. G. Speer, D. K. Matlock, and B.C. De Cooman, *International Conference on Advanced High Strength Sheet Steels for Automotive Applications Proceedings*, edited by J. G. Speer, AIST, Warrendale, PA, 2004, pp. 51–62.
10. H. J. Jun and N. Fonstein, in *Proceedings, International Conference on New Developments in Advanced High-Strength Sheet Steels*, ed. by J. G. Speer, B. Nelson, and R. Pradhan, AIST, Warrendale, PA, 2008, pp. 155–168.
11. J. W. Jin, S. H. Byun, S. B. Lee, S. I. Kim, C.S. Oh, N.K. and K.M. Cho, in *Proceedings, International Conference on New Developments in Advanced High-Strength Sheet Steels*, ed. by J. G. Speer, B. Nelson, and R. Pradhan, AIST, Warrendale, PA, 2008, pp. 169–178.

12. S. Cobo, C. Colin, and S. Allain, *Proceedings, New Developments on Metallurgy and Applications of High Strength Steels*, edited by Teresa Perez, published by Tenaris, Ternium, and Argentina Association of Materials, Buenos Aires, Argentina, 2008, Paper #65.
13. T. Y. Hsu and Z. Xu, *Mat. Sci. Forum*, vols. 561–565, 2007, pp. 2283–2286.
14. A. Clarke, Ph.D Thesis, *Carbon Partitioning Into Austenite From Martensite In A Silicon-Containing High Strength Sheet Steel*, Colorado School of Mines, Golden, CO, 2006.
15. M. Wakita, Y. Adachi, and Y. Tomota, *Materials Science Forum*, vols., 539–543, 2007, pp. 4351–4536.
16. M. J. Merwin, SAE Technical Paper #2007-01-0336, SAE, Warrendale, PA, 2007.
17. M. J. Merwin, *Proceedings of Steel Properties and Applications Conference*, edited by L. C. Oldham, AIST, Warrendale, PA, 2007, pp. 1017–1038.
18. J. G. Speer, B. Nelson, and R. Pradhan, editors, *Proceedings, International Conference on New Developments in Advanced High-Strength Sheet Steels*, AIST, Warrendale, PA, 2008.

T. Sheet Formability and Springback of Advanced High-Strength Steels—OSU

Principal Investigator: Robert H. Wagoner
Distinguished Professor of Engineering, George R. Smith Chair, and Professor, Department of Materials Science and Engineering, Ohio State University
484 Watts Hall, 2041 N. College Rd, Columbus, OH 43210
(614) 292-2079; fax: (614) 292-6530; e-mail: wagoner.2@osu.edu

Co-Principal Investigator: James G. Schroth
General Motors R & D Center, 30500 Mound Road, M/C 480-106-212, Warren, MI 48090-9055
(586) 986-0977; fax: (586) 986-9204; e-mail: james.g.schroth@gm.com

Principal Investigator: Partner University: David K. Matlock
Advanced Steel Processing and Products Research Center
Department of Metallurgical and Materials Engineering, Colorado School of Mines
Golden, CO 80401
(303) 273-3775; fax: (303) 273-3016; e-mail: dmatlock@mines.edu

Technology Area Development Manager: Joseph A. Carpenter
(202) 586-1022; fax: (202) 586-1600; e-mail: joseph.carpenter@ee.doe.gov

Field Project Officer: Aaron D. Yocum
(304) 285-4852; fax: (304) 285-4403; e-mail: aaron.yocum@netl.doe.gov

---

Contractor: The Ohio State University Research Foundation
National Science Foundation Award CMMI-0727641, jointly funded by NSF and DOE

Objectives

- Process Development: formability and springback of existing and new advanced high- strength steels (AHSSs)
- Material Development: identification of new processing routes and microstructures upon which to base a 3rd generation of AHSS
- Educational Program: attraction of promising and diverse students to related technical areas at both undergraduate and graduate levels

Approach

- Measure strain hardening in complex paths
- Devise advanced constitutive equations, implement in finite-element (FE) model
- Measure springback
- Simulate springback
- Simulate draw-bend tests

Accomplishments

- Three characteristics are found in reverse loading tests: Bauschinger effect, transient behavior near re-yielding domain, and permanent softening
- Two-path tests show complicated but systematic directional-hardening behaviors

- Developed a novel one-dimensional (1-D) constitutive equation which can predict post-uniform behavior well based on total elongation.
- Developed a thermomechanical FE model and used it with 1-D constitutive law to predict AHSS failure without damage mechanics.
- Developed three-dimensional (3-D) constitutive equations which have good agreement with tension/compression (T/C), compression/tension (C/T) test.
- As the back-force increases, the springback angle can drop quickly with increasing material strength. This behavior is pronounced at low bend radius (R) to thickness (t) (R/t) ratios.
- Anticlastic curvature and curl radius have direct implication on the springback angle in the draw-bend specimen.
- Constructed a new formability test for a draw-bend test and identified the importance of thermal effect.

Future Direction

- Develop 1-D constitutive equation for transformation-induced plasticity (TRIP) steels
- Compare constitutive equation with balanced biaxial bulge test at elevated temperatures
- Simulate springback with 3-D constitutive equations
- Springback test of AHSS at various roller sizes

Introduction

There is a growing need to conserve energy, reduce environmental impact, and increase energy for the performance of transportation vehicles. Based on the requirement of the marketplace, advanced high-strength steels (AHSS) are produced and provide outstanding mechanical properties in strength and ductility. Among the fundamental technical questions which need to be addressed before AH SS are widely used, sheet formability and springback are the most crucial ones. In this report, springback and formability are investigated and experiments and simulations are applied to the AHSS.

Springback Objective

"Springback" is the elastically driven recovery after forming material into a useful shape and releasing the forming force. The inability to accurately predict springback is a major cost factor in industry. To provide enough knowledge and tools to obtain reliable, precise prediction of springback, the following steps are taken for AHSS.

1. Conduct T/C, C/T, two-path, and biaxial-bulge tests.
2. Devise accurate constitutive equations.
3. Conduct draw-bend springback tests.
4. Develop simulations of springback.

Measure Strain Hardening for Complex Paths

Tension/Compression and Compression/Tension Tests

Springback is sensitive to transient hardening and stabilized T/C and C/T tests are necessary for accurate springback prediction. The laboratory equipment (Figure 1) developed by OSU is used to obtain accurate experimental results. T/C and C/T tests are applied to three grades of dual phase (DP) steels and one grade of transformation-induced plasticity (TRIP) steels: DP590, DP780, DP980, and TRIP780. Figure 2 shows the results of C/T tests with different compression strain compared with the monotonic tension test for DP590. From the experimental results, three characteristics are found: (a) Bauschinger effect, (b) transient behavior near re-yielding domain, and (c) permanent softening. Taking into account the behavior of Figure 2 in the simulations of springback will massively reduce error.

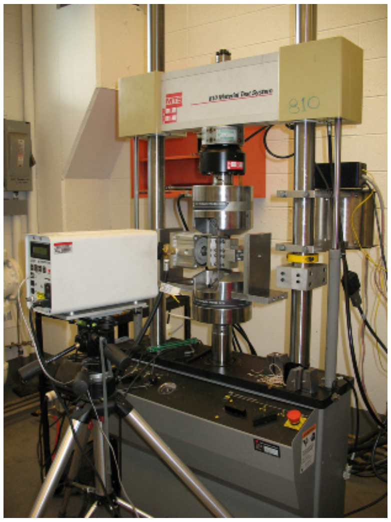

Figure 1. T/C and C/T test device developed by OSU.

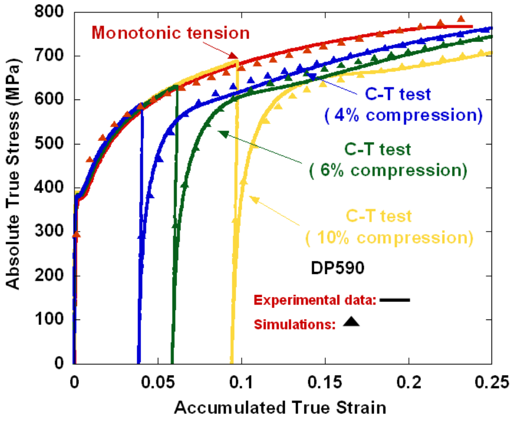

Figure 2. C/T tests and monotonic tension test compared with 3-D constitutive equations (DP590).

Two-Path Tensile Tests

Non-proportional loading results are important for devising precise 3-D constitutive equations for the AHSS. During two-path tensile tests for DP980, the specimens are preloaded along the rolling direction (RD) followed by different loading paths (RD, transverse direction (TD), and 45-degree direction). The different material- hardening behaviors are observed in Figure 3. It shows that the directional-hardening behaviors are complicated but systematic.

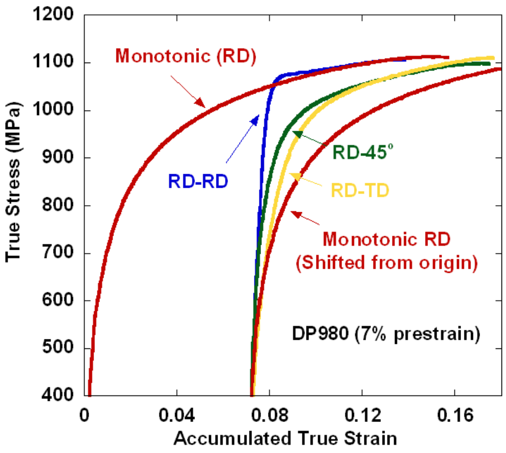

Figure 3. Two-path tensile tests compared with monotonic tension (DP980).

Balanced Biaxial Bulge Tests

Balanced biaxial bulge tests are conducted in cooperation with the Alcoa Research and Development (R&D) Center. In-plane membrane stress, σ_b and the magnitude of thickness strain, ε_b are transformed to effective stress and strain using '79 Hill's criterion and measured normal anisotropy value, $\overline{r}$. The results of biaxial bulge tests for DP590, DP780, and DP980 are shown in Figure 4.

Constitutive Equations

1-D Constitutive Equation

A new empirical work-hardening constitutive model for DP steels, Holloman/Voce (H/V) model, is proposed as three multiplicative functions, Eq. (1). Each function represents the effects of strain hardening, strain rate, and temperature, respectively. This model differs from other models in that the strain hardening is a function of strain and temperature.

$$\sigma = \sigma(\varepsilon, \dot{\varepsilon}, T) = f(\varepsilon, T) \cdot g(\dot{\varepsilon}) \cdot h(T) \qquad (1)$$

Coefficients of the constitutive equation are found by fitting Eq. (1) to tensile-test results at various conditions: various temperatures and speeds.

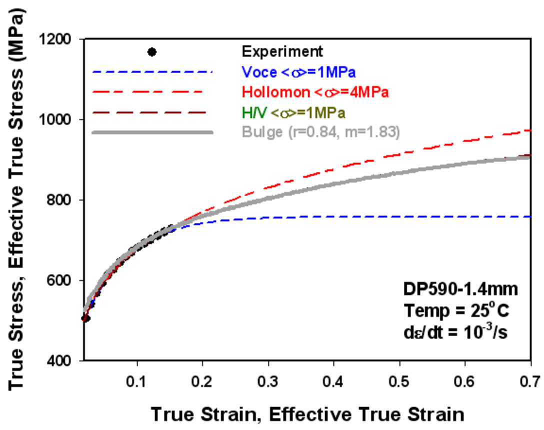

(a) DP590

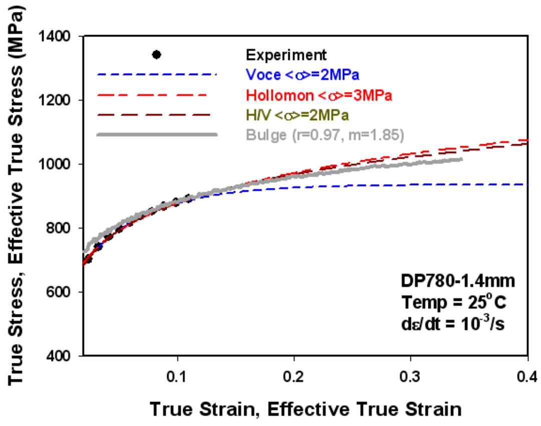

(b) DP780

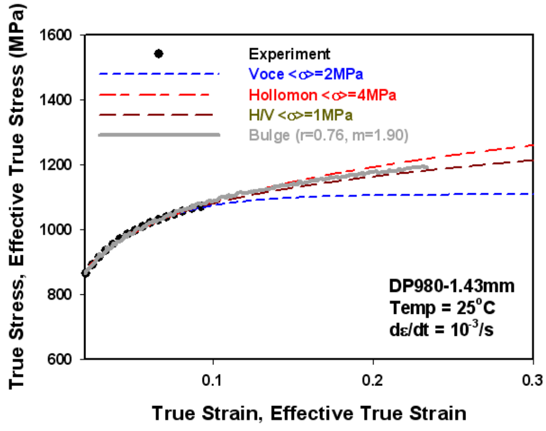

(c) DP980

Figure 4. Biaxial bulge test compared with 1-D constitutive equations.

Strain Hardening Function, $f(\varepsilon,T)$

It has been reported that the Hollomon model predicts better at room temperature conditions and the Voce model does better at elevated temperature for DP steels [1]. Therefore, a strain-hardening function $f(\varepsilon,T)$ is proposed as Eq. (2) represented by a novel linear combination of the Hollomon and Voce equations with a temperature-dependent proportion, $\alpha(T)$.

$$\begin{aligned} &f(\varepsilon,T)=\alpha(T)f_{Hollo}+(1-\alpha(T))\cdot f_{Voce} \\ &,where\ \alpha(T)=\alpha_1-\alpha_2(T-T_{RT}) \\ &f_{Hollo}=K\varepsilon^n \\ &f_{Voce}\ =y_0(1-Ae^{-B\varepsilon}) \end{aligned} \tag{2}$$

Where T is current temperature, T_{RT} is room temperature, and α_1, α_2, K, n, y_o, A, B, are material constants. The function $\alpha(T)$ allows a more Voce-like curve at higher temperatures and a more Hollomon-like curve at lower temperatures. $\alpha(T)$ and $h(T)$ (see below) are obtained by fitting the constitutive equations to tensile-test results carried out at various temperatures.

Strain-Rate Sensitivity Function, $g(\dot{\varepsilon})$

Strain-rate sensitivity is an important parameter influencing plastic instability of many materials, so it must be included in the constitutive equation for accurate failure prediction. The strain-rate sensitivity is incorporated into constitutive equations by multiplicative form, Eq. (3). It was observed that the strain-rate sensitivity index, m increased with increase of strain rate. Therefore, the strain-rate sensitivity index m is expressed as a linear form of logarithmic value of strain rate, Eq. (4).

$$\sigma=f(\varepsilon,T)_{\dot{\varepsilon}_0}\left(\frac{\dot{\varepsilon}}{\dot{\varepsilon}_0}\right)^m \quad \text{[multiplicative]} \tag{3}$$

$$m=a[\log\dot{\varepsilon}]+b \tag{4}$$

where a and b are material constants.

Temperature-Dependent Function, $h(T)$

The temperature term included in the strain-hardening function, Eq. (2), represents the change of strain-hardening curve with temperature, while the temperature function, $h(T)$, represents the change of strength with temperature as a simple multiplicative form, Eq. (5).

$$h(T) = (1 - C \cdot (T - T_{RT})) \tag{5}$$

where C is a material constant which can be found by fitting to tensile-test data at various temperatures.

The constitutive equations developed for three grades of DP steels, DP590, DP780, and DP980, are compared with the effective stress-strain curves obtained from balanced biaxial bulge tests, Figure 4.

FEM Simulations for 1-D Constitutive Laws

The proposed constitutive equations are investigated using a recently developed, thermomechanical, finite-element model (FEM), C3D8RT, of a tensile test with the same specimen geometry as in the experiments. ABAQUS Stand version 6.7 [2] is utilized for this analysis, Figure 5.

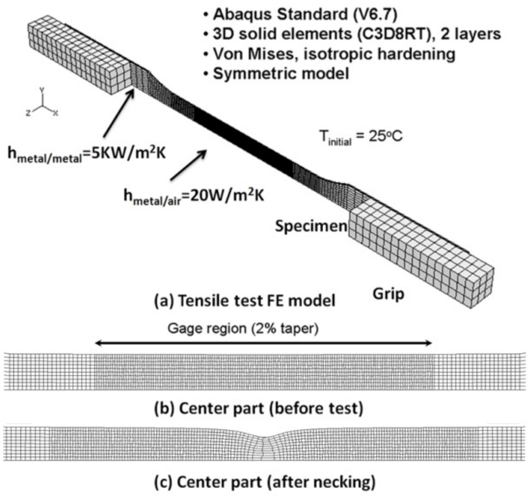
• Abaqus Standard (V6.7)
• 3D solid elements (C3D8RT), 2 layers
• Von Mises, isotropic hardening
• Symmetric model
$T_{initial}$ = 25°C
$h_{metal/metal}$=5KW/m²K
$h_{metal/air}$=20W/m²K
Specimen
Grip
(a) Tensile test FE model
Gage region (2% taper)
(b) Center part (before test)
(c) Center part (after necking)

Figure 5. FE model for tensile test.

A series of FEM simulations of tensile tests are conducted using the three constitutive equations, Hollomon, Voce, and H/V model for the three DP steels, and thermal coefficients shown in Figure 6. The results are compared in terms of total elongation where the total elongation in the simulation is determined based on a fractional load drop that is measured in the experiment.

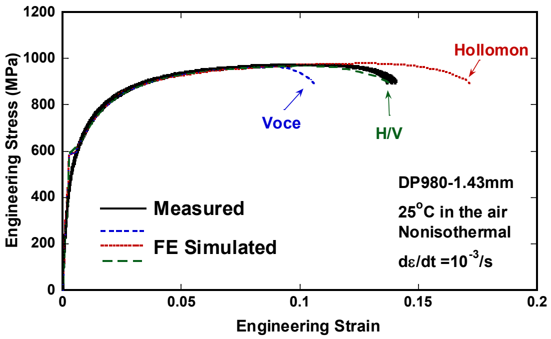

(a) 25°C

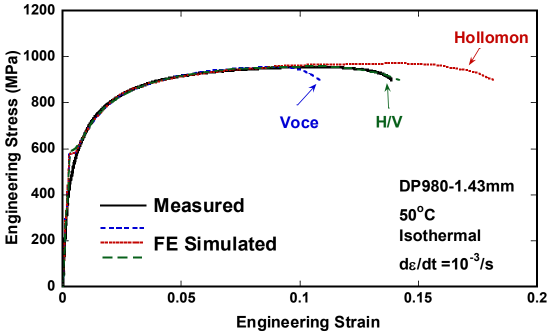

(b) 50°C

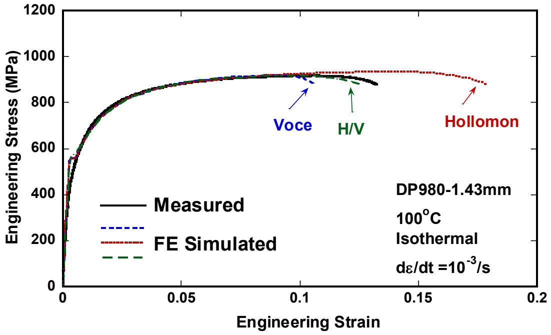

(c) 100°C

Figure 6. Comparison of FE simulation and experiments of uniaxial tensile test using different 1-D constitutive laws at various temperatures for DP980.

As shown in Figure 6, the Hollomon model predicts fracture well at room temperature but shows big error in the elevated temperatures, and vice versa for Voce. The H/V model, however, shows good agreement with the experimental results in the temperature range from 25 to 100 °C for all three materials. “Damage” localization resulting from the growth of voids is unlikely to play a significant role in tensile localization and failure for DP steels based on the comparison results between FE simulation and experiments.

3-D Constitutive Equations

Accurate 3-D constitutive equations have been developed to describe the T/C and C/T tests. The Von Mises yield surface is assumed and a non-linear kinematic hardening model, the Chaboche model, is proposed as follows,

$$\boldsymbol{\alpha} = \boldsymbol{\alpha}_1 + \boldsymbol{\alpha}_2$$

$$d\boldsymbol{\alpha}_1 = \frac{2}{3} C_1 d\boldsymbol{\varepsilon}_p - \gamma \boldsymbol{\alpha}_1 dp \tag{6}$$

$$d\boldsymbol{\alpha}_2 = \frac{2}{3} C_2 d\boldsymbol{\varepsilon}_p$$

where $\boldsymbol{\alpha}$ is the back stress, $\boldsymbol{\varepsilon}_p$ is the plastic strain, and p is the effective strain. C_1, C_2, and γ are constants. The backstress is divided into two parts, a linear component $\boldsymbol{\alpha}_1$ which represents permanent softening, and a non-linear variable for transient behavior near the re-yielding domain.

Isotropic hardening is taken as an exponential function

$$R = R_s(1 - \exp(-bp)) \tag{7}$$

where R is the yield surface size, and R_s and b are constants. Figure 2 represents a good agreement between the C/T tests and 3-D constitutive laws simulations.

Draw-Bend Springback

A draw-bend springback (DBS) test is conducted to investigate the relationship between springback and the retaining force, as shown in Figure 7. Three grades of dual phase steels, namely DP590, DP780, and DP980, are used in this study. The specimen is cut along the rolling direction for 710-mm length and 25.4-mm width. The back force is varied between 50% yield strength of the material to 110 % yield strength at regular intervals of 10%. The specimen is drawn to a distance of 127 mm at a rate of 25.4 mm per second over two roller radii, 6.4 and 11.1 mm.

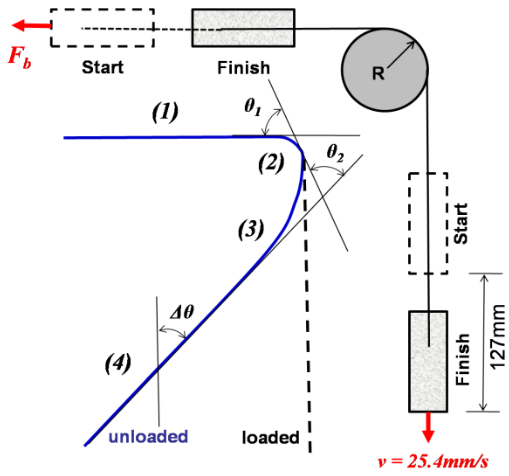

Figure 7. Schematic of the stages of the draw-bend test and unloaded specimen geometry

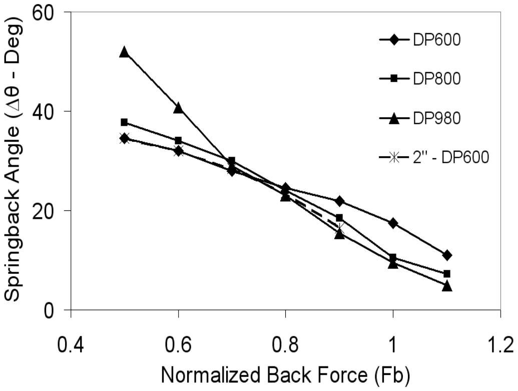

Figure 8. Springback angle obtained using R=6.4 mm.

As the normalized back-forces (F_bs) increased, the springback angle reduced (Figure 8). The reduction in springback angle increased with increasing material strength. The springback angle at high F_b's is controlled by anticlastic curvature [3]. Higher F_bs accentuate anticlastic curvature which in turn increased the moment of inertia of the specimen cross-section, thus reducing springback. At F_bs, the springback angles for increasing material strength are higher. Beyond Fb = 0.8 this trend reversed and the springback angles for increasing material strength became smaller.

AHSS (DP 590, DP 780, DP 980, and TRIP 780) show time-dependent springback at room temperature, while standard autobody steels such as draw-quality semi-killed (DQSK), aluminum-killed draw-quality (AKDQ), and high-strength low-alloy (HSLA) steels showed no such time-dependent springback up to seven years following deformation.

Springback Simulations

As schematically shown in Figure 9, 300 shell elements with 51 integration points (IP) through the thickness are used for FE simulation of

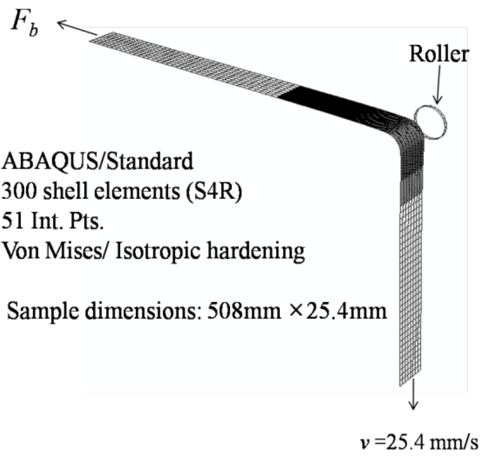
F_b
Roller
•ABAQUS/Standard
•300 shell elements (S4R)
•51 Int. Pts.
•Von Mises/ Isotropic hardening
• Sample dimensions: 508mm ×25.4mm
v =25.4 mm/s

Figure 9. Simulation of springback.

springback using ABAQUS/Standard [2]. Von Mises yield function and isotropic hardening are used as a simple material model that showed good agreement with experiments in previous works [4] for $F_b < 0.7$. As can be seen in Figure 10, simulated initial springback angle shows relatively good agreement with the experiment even though a simple material model is used.

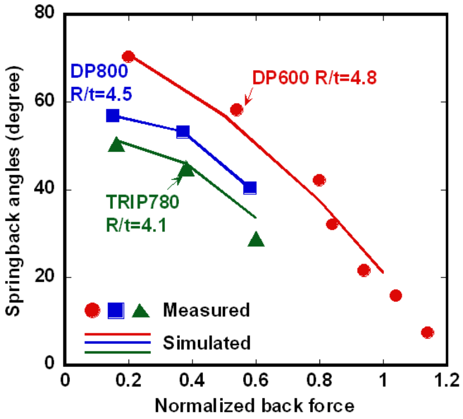

Figure 10. Comparison of the measured and simulated springback.

Formability Objective

Depending on the application and the grade, failures in AHSS are not always able to be predicted by the usual forming simulation and application of forming-limit diagrams. Such diagrams represent the forming limit based on localized deformation, or necking, which has proven successful in predicting failures for conventional sheet steels. The new type of failure, so-called "shear fracture", is observed at sharp radii where bending and unbending under tension during forming occurred [5].

The draw-bend test mimics the mechanics of deformation of sheet metal as it is drawn, stretched, bent, and straightened over a die radius entering a typical die cavity [6]. The test can produce both normal plastic localization/necking and shear fracture. For AHSS, the flow stress is affected significantly by deformation-induced heating at even modest strain rates, so the constitutive equations must take into account these effects [7]. Deformation- induced heating is usually expected to have a detrimental effect on ductility [8].

The objective of this research is to develop a FE model of the draw-bend test, and to improve predictability by taking into account thermal effect with a new 1-D constitutive equation relating flow stress to strain, strain rate, and temperature for three dual phase steels.

Thermomechanical Finite-Element Analysis for Draw-Bend Test

A thermomechanical finite element model of draw-bend tests is developed to investigate the failure mechanisms of AHSS. The model accounts for deformation heating and heat transfer and is capable of representing softening and altered strain hardening of materials measured at elevated temperatures. Such capability is required because temperatures increase much beyond room temperature during draw-bend tests by deformation heating. A symmetric 3-D solid model (C3D8RT) is used with five layers through thickness in ABAQUS 6.7 Standard. Isotropic yield and isotropic hardening are assumed for simplicity. Thermal coefficients are measured from independent experiments or obtained from the literature. The friction coefficient is based on a comparison of forces of front grip and back grip between FE simulation and draw-bend fracture test using Coulomb's friction law.

As can be seen from Figures 11–13, all three types of failure are predicted accurately (Type I—tensile, Type II—mixed, Type III—shear) and the

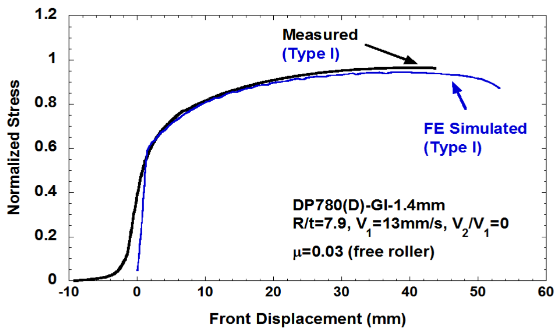

Figure 11. Thermomechanically FE simulated and measured stress-displacement curves, Type I.

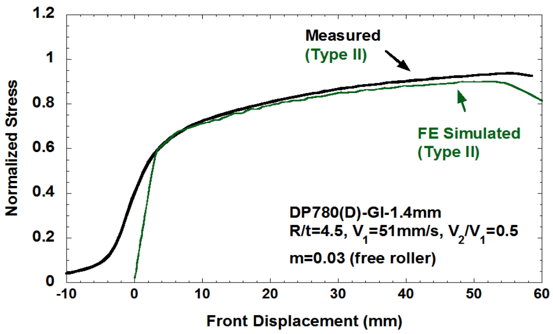

Figure 12. Thermomechanically FE simulated and measured stress-displacement curves, Type II.

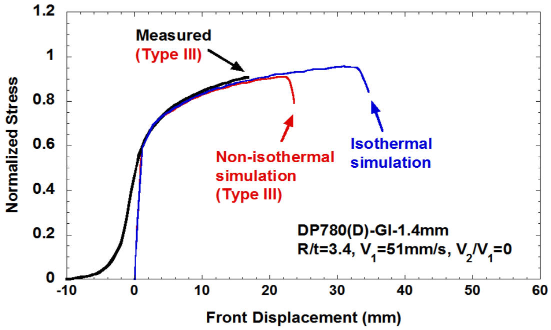

Figure 13. Thermomechanically FE simulated and measured stress-displacement curves, Type III.

draw distances to failure are predicted within 5–20 percent of the measured results. Isothermal simulations significantly over-predicted the draw distances to failure, by up to 100 percent (Figure 13).

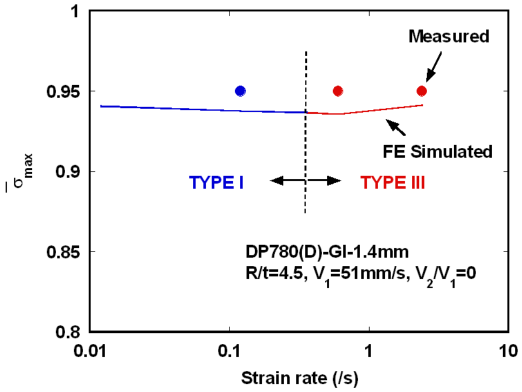

Figure 14. Comparison of simulated and measured maximum stresses at various strain rates.

The normalized maximum stresses are compared as a function of strain rates in Figure 14. While the normalized stress to failure changes little, the failure type changes from Type I to Type III (tensile localization to shear failure) as the strain rate increases. This result suggests that shear failure is a consequence of thermally assisted strain localization, in agreement with Figure 14.

Conclusions

Measure Strain Hardening

(1) T/C and C/T tests show: (a) Bauschinger effect, (b) transient behavior near re-yielding domain, and (c) permanent softening.

(2) From two-path tensile tests, directional-hardening behaviors are complicated but systematic.

Constitutive Equations

1-D and 3-D constitutive equations are developed.

1. 1-D constitutive equation has a remarkable agreement of the thermomechanical tensile test FE model simulation with experimental results. Using the proposed constitutive equation lends confidence that the constitutive equations are valid well beyond uniform elongation in tension within the temperature range of 25–100°C and predict correctly AHSS failure without damage mechanics.
2. "Damage" is unlikely to play a significant role in tensile localization and failure for DP steels based on the comparison results between FE simulation and experiments.
3. Accurate strain-hardening description beyond uniform elongation is critical.

4. 3-D constitutive law had a good agreement with T/C and C/T tests.

Springback

1. As the back-force increases, the springback angle can drop quickly with increasing material strength and this behavior is pronounced at low R/t ratios.
2. Draw restraining force has significant influence on the springback; higher forces result in less springback and consequently produce dimensional stability in the formed part.

Draw-Bend Test

A new formability test and FE model of the draw-bend tests are developed. Maps of failure type and normalized maximum sheet tensions have been measured and simulated with good accuracy as functions of R/t and strain rate for dual phase steels. Deformation induced heating and consequent material softening is a critical part of the failure process at typical strain rates. The results suggest that damage is not an important component of "shear" failures observed, at least with these alloys under these conditions.

Presentations/Publications/Patents

1. R. Padmanabhan, Jihyun Sung, H. Lim, M. C. Oliveira, L. F. Menezes, and R. H. Wagoner, "Influence of Draw Restraining Force on the Springback in Advanced High Strength Steels," International Journal of Material Forming, 3 April, 2008.
2. H. Lim, M. G. Lee, J. H. Sung, and R. H. Wagoner, "Time-Dependent Springback," International Journal of Material Forming, 3 April, 2008.
3. Ji Hoon Kim, Ji Hyun Sung, and R. H. Wagoner, "Finite Element Simulation of DP590 Draw-Bend Tests," NADDRG 2008, May 14–15, 2008, Windsor, Canada.
4. Ji Hyun Sung, Ji Hoon Kim, and R. H. Wagoner, "Constitutive Equation of AHSS," NADDRG 2008, May 14–15, 2008, Windsor, Canada.
5. H. Lim, Ji Hyun Sung, M. G. Lee, and R. H. Wagoner, "UPDATE: Time-Dependent Springback of AHSS," NADDRG 2008, May 14–5, 2008, Windsor, Canada.
6. M. Amitesh and R. H. Wagoner, "Draw Bend Failure of AHSS," NADDRG 2008, May 14–15, 2008, Windsor, Canada.

References

1. J. H. Sung, J. H. Kim, and R. H. Wagoner, "Constitutive Equation of AHSS," 2008 Spring NADDRG, May 14–15, Windsor, Canada.
2. ABAQUS, User's manual for version 6.7.1. Hibbit, Karlson & Sorensen Inc.
3. L. Geng and R. H. Wagoner, "Role of Plastic Anisotropy and its Evolution on Springback," International Journal of Mechanical Sciences 44, 123–148, 2002.
4. J. F. Wang, R. H. Wagoner, D. K. Matlock, and F. Barlat, "Anticlastic Curvature in Draw-Bend Springback," International Journal of Solids and Structures 42, 1287–1307, 2005.
5. R. H. Wagoner, "Fundamental Research Issues," Proc. Of NSF Workshop, Arlington, VA, Oct. 22–23, 2006.
6. F. F. Damborg, R. H. Wagoner, J. Danckert, and D. K. Matlock, "Stretch Bend Formability," Ph.D. Dissertation, Aalborg University, Aalborg, Denmark, 1997.
7. S. I. Kim, Y. Lee, and S. M. Byon, "Study on Constitutive Relation of AISI 4140 Steel Subject to Large Strain at Elevated Temperatures," J. Mat. Proc. Tech., 140:84–89, 2003.
8. Y. Gao and R. H. Wagoner, "A Simplified Model of Heat Generation During the Uniaxial Tensile Test." Metall. Trans. A, 18A:1001–1009, 1987.